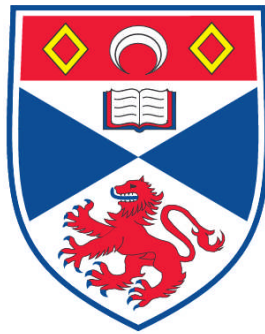


**ASPECTS OF THREE-DIMENSIONAL MHD: MAGNETIC
RECONNECTION AND ROTATING CORONAE**

Nasser Said Al-Salti

**A Thesis Submitted for the Degree of PhD
at the
University of St. Andrews**



2010

**Full metadata for this item is available in the St Andrews
Digital Research Repository**

at:

<https://research-repository.st-andrews.ac.uk/>

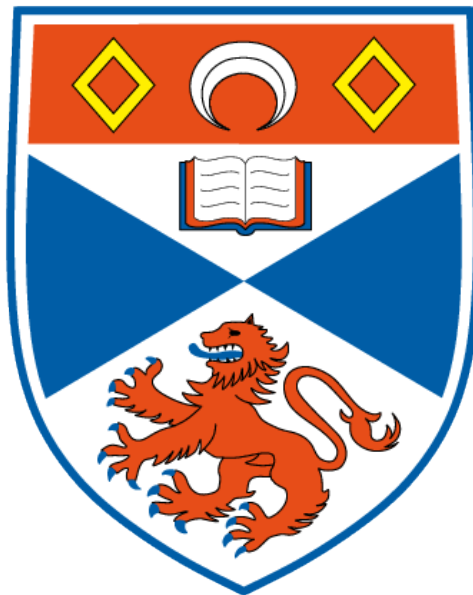
Please use this identifier to cite or link to this item:

<http://hdl.handle.net/10023/947>

This item is protected by original copyright

Aspects of Three-dimensional MHD: Magnetic Reconnection and Rotating Coronae.

Nasser Said Al-Salti



Thesis submitted for the degree of Doctor of Philosophy
of the University of St Andrews

26 April 2010

Abstract

Solutions of the magnetohydrodynamic (MHD) equations are very important for modelling laboratory, space and astrophysical plasmas, for example the solar and stellar coronae, as well as for modelling many of the dynamic processes that occur in these different plasma environments such as the fundamental process of magnetic reconnection. Our previous understanding of the behavior of plasmas and their associated dynamic processes has been developed through two-dimensional (2D) models. However, a more realistic model should be three-dimensional (3D), but finding 3D solutions of the MHD equations is, in general, a formidable task. Only very few analytical solutions are known and even calculating solutions with numerical methods is usually far from easy.

In this thesis, 3D solutions which model magnetic reconnection and rigidly rotating magnetized coronae are presented. For magnetic reconnection, a 3D stationary MHD model is used. However, the complexity of the problem meant that so far no generic analytic solutions for reconnection in 3D exist and most work consists of numerical simulations. This has so far hampered progress in our understanding of magnetic reconnection. The model used here allows for analytic solutions at least up to a certain order of approximation and therefore gives some better insight in the significant differences between 2D and 3D reconnection. Three-dimensional numerical solutions are also obtained for this model.

Rigidly rotating magnetized coronae, on the other hand, are modeled using a set of magnetohydrostatic (MHS) equations. A general theoretical framework for calculating 3D MHS solutions outside massive rigidly rotating central bodies is presented. Under certain assumptions, the MHS equations are reduced to a single linear partial differential equation referred to as the fundamental equation of the theory. As a first step, an illustrative case of a massive rigidly rotating magnetized cylinder is considered, which somehow allows for analytic solutions in a certain domain of validity. In general, the fundamental equation of the theory can only be solved numerically and hence numerical example solutions are presented. The theory is then extended to include a more realistic case of massive rigidly rotating spherical bodies. The resulting fundamental equation of the theory in this case is too complicated to allow for analytic solutions and hence only numerical solutions are obtained using similar numerical methods to the ones used in the cylindrical case.

Declaration

I, Nasser Al-Salti, hereby certify that this thesis, which is approximately 31,000 words in length, has been written by me, that it is the record of work carried out by me and that it has not been submitted in any previous application for a higher degree.

Candidate: Nasser Al-Salti **Signature:** **Date:** 26/04/2010

I was admitted as a research student in January 2006 and as a candidate for the degree of Doctor of Philosophy in January 2007; the higher study for which this is a record was carried out in the University of St Andrews between 2006 and 2010.

Candidate: Nasser Al-Salti **Signature:** **Date:** 26/04/2010

I hereby certify that the candidate has fulfilled the conditions of the Resolution and Regulations appropriate for the degree of Doctor of Philosophy in the University of St Andrews and that the candidate is qualified to submit this thesis in application for that degree.

Supervisor: Thomas Neukirch **Signature:** **Date:** 26/04/2010

In submitting this thesis to the University of St Andrews we understand that we are giving permission for it to be made available for use in accordance with the regulations of the University Library for the time being in force, subject to any copyright vested in the work not being affected thereby. We also understand that the title and the abstract will be published, and that a copy of the work may be made and supplied to any bona fide library or research worker, that my thesis will be electronically accessible for personal or research use unless exempt by award of an embargo as requested below, and that the library has the right to migrate my thesis into new electronic forms as required to ensure continued access to the thesis. We have obtained any third-party copyright permissions that may be required in order to allow such access and migration, or have requested the appropriate embargo below.

The following is an agreed request by candidate and supervisor regarding the electronic publication of this thesis:

Access to Printed copy and electronic publication of thesis through the University of St Andrews.

Date: 26/04/2010 **signature of candidate**..... **signature of supervisor**.....

Acknowledgements

“ Say (O Muhammad): Verily, my prayer, my sacrifice, my living, and my death are for Allah, the Lord of the worlds \ominus He has no partner. And of this I have been commanded, and I am the first of the Muslims \ominus ”

(Interpretation of the Holy Quran **6**: 162-163)

All praise be to God, the Lord of the worlds, the Most Gracious, the Most Merciful. May peace and blessings of God be upon all His Prophets and Messengers. The Prophet Muhammad (peace be upon him) said:

“One who does not thank people does not thank God.”

So, I would like to take this opportunity to express my sincere thanks to my supervisors, Thomas Neukirch and Gunnar Hornig, for their continuous help and support over the last four years.

I am also grateful to the Solar MHD group in St. Andrews and the MHD group in Dundee for useful discussions with very special thanks to Antonia Wilmot-Smith.

Special and very warm thanks should go to my family for their continuous encouragements, sacrifices and prayers.

Finally, I would like to thank Sultan Qaboos University, Oman, for their financial support.

Contents

Contents	i
List of Figures	iii
1 Introduction	1
1.1 The Sun: Facts and Structure	2
1.1.1 The Solar Interior	3
1.1.2 The Solar Surface: The Photosphere	4
1.1.3 The Solar Atmosphere	5
1.2 A Mathematical Tool: Magnetohydrodynamics (MHD)	6
1.2.1 Basic Equations	7
1.2.2 The Induction Equation	9
1.2.3 Magnetohydrostatics (MHS)	10
1.3 Aims and Outline	11
2 Magnetic Reconnection: an Overview	13
2.1 Introduction	13
2.2 Significance of Magnetic Reconnection	15
2.3 Two-Dimensional (2D) Magnetic Reconnection	17
2.3.1 Classical 2D Models	17
2.3.2 General Mathematical Approach	20
2.3.3 Fundamental Properties	21
2.4 Three-Dimensional (3D) Magnetic Reconnection	22
2.4.1 Comparison with reconnection in 2D	22
2.4.2 Non-null Reconnection	24
3 On The Solutions of Three-Dimensional Non-Null Magnetic Reconnection - I	26
3.1 Introduction	26

3.2	The model	27
3.3	General Method of Integration	30
3.4	Solutions	32
3.4.1	Analytical Solutions	32
3.4.2	Numerical Solutions	40
3.4.3	Total Solution Approximation	42
3.5	Summary and discussion	45
4	On The Solutions of Three-Dimensional Non-Null Magnetic Reconnection - II	47
4.1	Pure 3D Reconnection Solutions	49
4.1.1	Analytical Solutions	49
4.1.2	Numerical Solutions	52
4.1.3	Total Solution Approximation	55
4.2	Composite 3D Reconnection Solutions	58
4.2.1	Composite Solutions I: $\ \mathbf{j}_{41}\ _{\max} > \ \mathbf{j}_{42}\ _{\max}$	61
4.2.2	Composite Solutions II: $\ \mathbf{j}_{41}\ _{\max} \approx \ \mathbf{j}_{42}\ _{\max}$	68
4.2.3	Composite Solutions III: $\ \mathbf{j}_{41}\ _{\max} < \ \mathbf{j}_{42}\ _{\max}$	72
4.3	Summary	77
5	Three-Dimensional Solutions of the Magnetohydrostatic Equations: Rigidly Rotating Magnetized Coroneae in Cylindrical Geometry	78
5.1	Introduction	78
5.2	Theory	80
5.2.1	Coordinate Independent Theory	80
5.2.2	Cylindrical Geometry	83
5.3	Solution Methods and Example Solutions	88
5.3.1	Separation of Variables	88
5.3.2	Numerical Solutions of Eq. (??)	91
5.4	Summary and Discussion	98
6	Three-Dimensional Solutions of the Magnetohydrostatic Equations: Rigidly Rotating Magnetized Coroneae in Spherical Geometry	100
6.1	Introduction	100
6.2	Numerical Solutions	102
6.2.1	Example Solution I	103
6.2.2	Example Solution II	109

6.3	Summary	111
7	Summary and Future Work	114
7.1	Summary	114
7.2	Future Work	117
Appendix A	Derivation Of The Generalized Ohm's Law	120
Appendix B	Electron Parallel Compressibility Effects on Magnetic Reconnection	121
Appendix C	MATLAB Routines for Solving Equations (3.14) and (3.15)	123
Appendix D	Solutions to The Stationary Kinematic Model	128
Bibliography		130

List of Figures

1.1	Sun-Earth Connection	1
1.2	Structure of the Sun from core to outer atmosphere	2
1.3	Granulation around sunspots in the photosphere	4
1.4	The solar corona in a total eclipse and in X-rays	6
2.1	A basic picture of 2D magnetic reconnection	17
2.2	The Sweet-Parker model for 2D steady reconnection.	18
2.3	The Petschek model for 2D steady reconnection.	19
2.4	The structure of field lines near a null point in 3D.	23
3.1	The structure of \mathbf{B}_0 in 2D and 3D	29
3.2	Contour plots of the electric potential ϕ_0	33
3.3	Strength and direction of the velocity field \mathbf{v}_0	33
3.4	Contour plots of the pressure p_2 variation	34
3.5	Illustration of the current j_{2z}	35
3.6	The non-ideal region at $\ \eta_c \mathbf{j}_2\ = 0.05 \ \eta_c \mathbf{j}_2\ _{\max}$	36
3.7	Contour plots of the electric potential ϕ_1	37
3.8	Strength and direction of the velocity field \mathbf{v}_1	37
3.9	Field lines and magnitude of the magnetic field \mathbf{B}_2	38
3.10	Contour plots of the pressure p_3	39
3.11	Illustration of the current j_{3z}	39
3.12	Contour plots of the electric potential ϕ_2	39
3.13	Strength and direction of the velocity \mathbf{v}_2	40
3.14	The strength and field lines of the magnetic field \mathbf{B}_3	41
3.15	Contour plots of the pressure $p = M_A^2 p_2 + M_A^3 p_3$ variation	42
3.16	Strength and field lines of the magnetic field $\mathbf{B} = \mathbf{B}_0 + M_A^2 \mathbf{B}_2 + M_A^3 \mathbf{B}_3$	42
3.17	Illustration of the current $j_z = M_A^2 j_{2z} + M_A^3 j_{3z}$	43

3.18	Contour plots of the electric potential $\phi = \phi_0 + M_A\phi_1$	43
3.19	Strength and direction of $\mathbf{v} = \mathbf{v}_0 + M_A\mathbf{v}_1$	43
3.20	Contour plots of the electric potential $\phi = \phi_0 + M_A\phi_1 + M_A^2\phi_2$	44
3.21	Strength and direction of the velocity $\mathbf{v} = \mathbf{v}_0 + M_A\mathbf{v}_1 + M_A^2\mathbf{v}_2$	45
4.1	Contour plots of the pressure p_2 variation	48
4.2	Contour plots of the electric potential ϕ_2	50
4.3	Strength and direction of the velocity \mathbf{v}_2	51
4.4	Contour plots of the pressure p_4	53
4.5	Illustration of the current \mathbf{j}_4	53
4.6	Contour plots of the electric potential ϕ_3	53
4.7	Strength, direction and components of the velocity \mathbf{v}_3	54
4.8	Strength and field lines of the magnetic field \mathbf{B}_4	54
4.9	Strength and field lines of the magnetic field $\mathbf{B} = \mathbf{B}_0 + M_A^2\mathbf{B}_2 + M_A^4\mathbf{B}_4$	56
4.10	Contour plots of the pressure $p = M_A^2p_2 + M_A^4p_4$ variation	56
4.11	Illustration of the current $j_z = M_A^2j_{2z} + M_A^4j_{4z}$	57
4.12	Contour plots of the electric potential $\phi = M_A\phi_1 + M_A^3\phi_3$	57
4.13	Strength and direction of the velocity $\mathbf{v} = M_A\mathbf{v}_1 + M_A^3\mathbf{v}_3$	57
4.14	Contour plots of the electric potential ϕ_{32}	59
4.15	Strength, direction and components the velocity \mathbf{v}_{32}	60
4.16	Contour plots of the pressure p_{43} variation	61
4.17	Contour plots of the composite electric potential ϕ_1 I	62
4.18	Strength and direction of the composite velocity \mathbf{v}_1 I	62
4.19	Contour plots of the composite pressure p_4 I	62
4.20	Illustration of the composite current \mathbf{j}_4 I	63
4.21	Contour plots of the composite electric potential ϕ_3 I	63
4.22	Strength, direction and components of the composite velocity \mathbf{v}_3 I	65
4.23	Strength and field lines of the magnetic field \mathbf{B}_4 I	65
4.24	Contour plots of the composite pressure $p = M_A^2p_2 + M_A^4p_4$ variation I	66
4.25	Illustration of the composite current $j_z = M_A^2j_{2z} + M_A^4j_{4z}$ I	66
4.26	Contour plots of the composite electric potential $\phi = M_A\phi_1 + M_A^3\phi_3$ I	66
4.27	Strength and direction of the velocity $\mathbf{v} = M_A\mathbf{v}_1 + M_A^3\mathbf{v}_3$ I	66
4.28	Contour plots of the composite electric potential ϕ_1 II	67
4.29	Strength and direction of the composite velocity \mathbf{v}_1 II	67
4.30	Contour plots of the composite pressure p_4 II	69

4.31	Components of the composite current \mathbf{j}_4 II	69
4.32	Contour plots of the composite electric potential ϕ_3 II	69
4.33	Strength, direction and components of the composite velocity \mathbf{v}_3 II	70
4.34	Strength of the magnetic field \mathbf{B}_4 II	70
4.35	Contour plots of the composite pressure $p = M_A^2 p_2 + M_A^4 p_4$ variation II	71
4.36	Illustration of the composite current $\mathbf{j} = M_A^2 \mathbf{j}_2 + M_A^4 \mathbf{j}_4$ II	71
4.37	Contour plots of the composite electric potential $\phi = M_A \phi_1 + M_A^3 \phi_3$ II	71
4.38	Strength and direction of the velocity $\mathbf{v} = M_A \mathbf{v}_1 + M_A^3 \mathbf{v}_3$ II	71
4.39	The composite electric potential ϕ_1 and velocity \mathbf{v}_1 III	72
4.40	Contour plots of the composite pressure p_4 III	73
4.41	Illustration of composite the current \mathbf{j}_4 III	73
4.42	Contour plots of the composite electric potential ϕ_3 III	74
4.43	Strength, direction and components of the composite velocity \mathbf{v}_3 III	74
4.44	Strength and field lines of the magnetic field \mathbf{B}_4 III	75
4.45	Contour plots of the composite pressure $p = M_A^2 p_2 + M_A^4 p_4$ variation III	75
4.46	Illustration of the composite current $j_z = M_A^2 j_{2z} + M_A^4 j_{4z}$ III	76
4.47	The composite electric potential ϕ III	76
4.48	Strength and direction of the composite velocity \mathbf{v} III	76
5.1	The combined potential $V(\varpi)$	84
5.2	The critical points $\varpi_{s_+}^2$ and $\varpi_{s_-}^2$	87
5.3	Field line plots	89
5.4	Cross section plots of the pressure and density variations	90
5.5	3D field line plot and a view along the z -axis	91
5.6	Magnetic field lines plots	93
5.7	Pressure isosurface plots	95
5.8	Variation of the pressure deviation from its background in the xz -plane	96
5.9	Variation of the density deviation from its background in the xz -plane	97
6.1	3D plot of the expression $1 - \kappa(V)(\nabla V)^2$	104
6.2	Locations where the expression $1 - \kappa(V)(\nabla V)^2$ vanishes.	105
6.3	3D plots of random field lines SPH	106
6.4	Pressure isosurface plots SPH	107
6.5	Variation of the pressure deviation from its background SPH I	108
6.6	Variation of the density deviation from its background SPH I	109

6.7	Variation of the total plasma temperature SPH I	110
6.8	Variation of the pressure deviation from its background SPH II	111
6.9	Variation of the density deviation from its background SPH II	112
6.10	Variation of the total plasma temperature SPH II	112

Chapter 1

Introduction

“ It is He (The Almighty God) Who made the sun a shining glory and the moon as light, and measured out for it stages; that you might know the number of years and the count (of time). Allah did not create this but in truth. He explains His signs in detail for those who have knowledge Θ ”

(Interpretation of the Holy Quran **10**: 5)

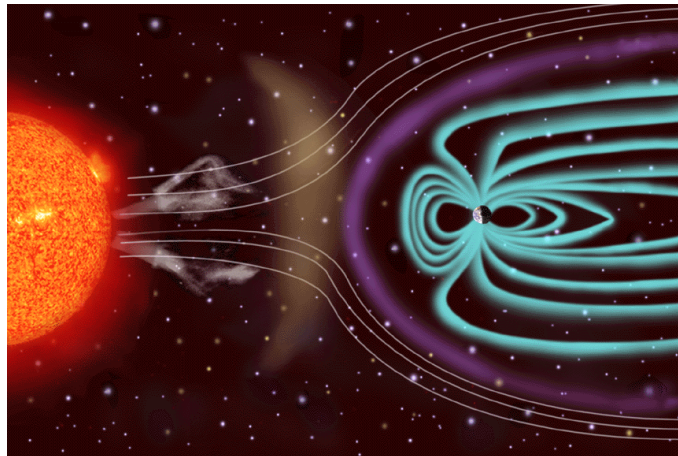


Figure 1.1: “The Sun’s magnetic field and releases of plasma directly affect Earth and the rest of the solar system. The solar wind shapes the Earth’s magnetosphere and magnetic storms are illustrated here as approaching Earth. These storms, which occur frequently, can disrupt communications and navigational equipment, damage satellites, and even cause blackouts. The white lines represent the solar wind; the purple line is the bow shock line; and the blue lines surrounding the Earth represent its protective magnetosphere. The magnetic cloud of plasma can extend to 30 million miles wide by the time it reaches earth” (SOHO).

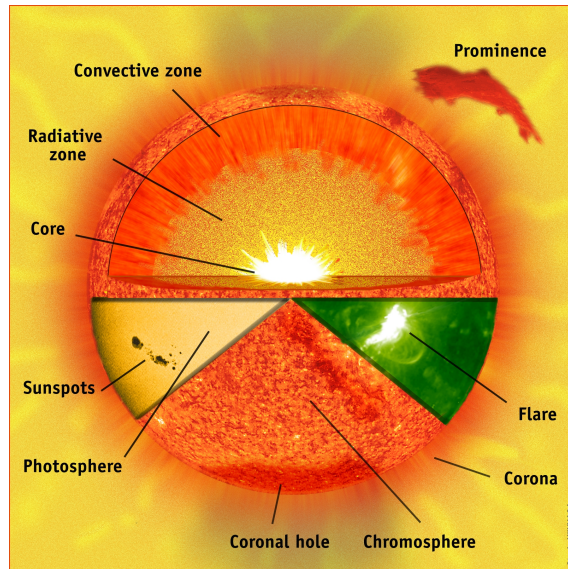


Figure 1.2: Cartoon illustrating the structure of the Sun from core to outer atmosphere (SOHO).

Almost all matter in the universe, such as stars, interstellar medium and interplanetary medium, can be described as plasma, since they are all made of ionized gases. Hence, the understanding of these plasmas, even though plasma generally does not exist on the Earth's surface, are very essential. This is because our planet the Earth is part of this universe, especially the solar system, and it interacts with its surroundings, (see Fig. 1.1). Moreover, the ionosphere, the upper atmosphere of the Earth, and the Earth's radiation belts the Van Allen belts are also found to be ionized.

One of the most widely used theoretical descriptions of plasmas is the magnetohydrodynamics (MHD) description (introduced here in Section 1.2). Much of our current understanding comes from two-dimensional models. A more realistic model, however, should be three-dimensional and hence a progress towards more realistic geometries in MHD is very crucial for our understanding. Analytical theory in three dimensions, on the other hand, is so hard and most work consists of numerical simulations. In this thesis, we aim to present solutions of three dimensional MHD models in two different areas (see Section 1.3).

The natural laboratory where one could study the properties and behavior of plasmas is our dynamic Sun. So, let us first introduce the Sun and discuss its structure and properties.

1.1 The Sun: Facts and Structure

The Sun is the closest star to us at a distance of 1.496×10^{11} m . This close proximity is indeed an advantage to scientists aiming to study not only the Sun, but plasmas in general since they

can observe examples of different plasma processes in a very close detail. The radius of the Sun is $R_{\odot} = 6.96 \times 10^8$ m, which is equal to 109 times the Earth radius and it has a mass $M_{\odot} = 1.989 \times 10^{30}$ kg of which about 72% is hydrogen, around 26% is helium and small traces of other elements such as oxygen (0.97%), carbon (0.4%) and iron (0.14%). With such a mass, which is about 330 000 times the mass of the Earth, the Sun is not just able to produce its own light, but rather it is the primary source of energy for our solar system. It has been luminous for about 4.6×10^9 years due to nuclear fusion that is taking place in its core. This source of energy is capable to keep the Sun shining for about 10 billion years, i.e., the Sun is about halfway through its lifetime.

The Sun is also found to be rotating differentially. It rotates faster at its equator with a period around 26 days. The rotation becomes slower with increasing latitude having a period about 35 days near the poles.

In structure, the Sun can be broadly defined in layers, starting from the centre and moving outward as shown in Fig. (1.2). These layers can be combined into three main regions: the solar interior, the solar surface and the solar atmosphere, which we discuss in more details in the following sections (see, e.g., Priest 1982).

1.1.1 The Solar Interior

The solar interior consists primarily of three layers: the core, the radiative zone and the convective zone. The core, where the energy from nuclear fusion is generated, has a density around 150 g/cm^3 . On the other hand side, because of its extreme temperature of more than 15×10^6 K, the core is a fluid all the way to the very centre of the Sun. These values of density and temperature are sufficient to support nuclear fusion reactions which require extremely high temperatures and densities. However, as one moves away from the solar centre in the radial direction the temperature and density start to decrease. At about $0.2R_{\odot}$, the temperature and density values can not support fusion reactions any more. This marks the end of the core of the Sun. Energy produced in the core of the Sun is transported in the form of photons to the next layer by radiation. Consequently, the layer of the solar interior surrounding the core of the Sun is known as the radiative zone, which extends out to about $0.7R_{\odot}$. In this zone, photons undergo continuous absorption and re-emission of energy as new radiation. The absorption and re-emission of energy has the effect of increasing the photon's wavelength and hence the temperature will continue to drop as we move towards the next layer, which in turn results in the absorbed energy not being released readily. Hence, another energy transport method is required since the transport of energy by radiation is slowing down significantly. Moreover, when the temperature gradients required to transport energy by radiation is higher than the adiabatic rate, the plasma becomes unstable to convection. Hence, the expected transport method now is convection, which is a very efficient method of energy transport, and

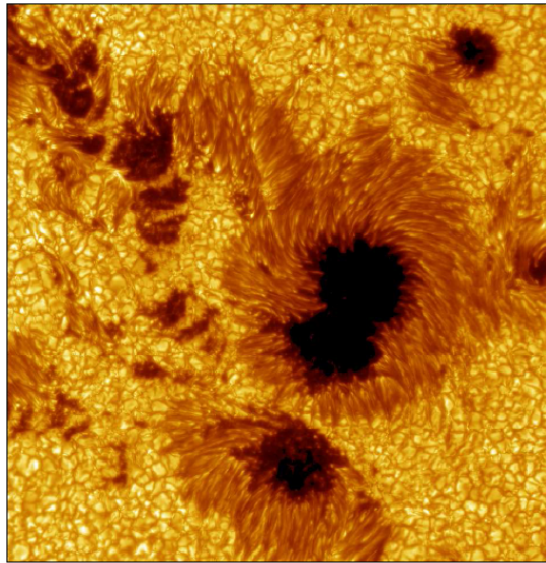


Figure 1.3: Image of granulation around sunspots in the photosphere (Swedish Solar Telescope).

we are now in the last layer of the solar interior known as the convective zone, which is just below the solar surface. The resultant large-scale convective fluid motions also give rise to small-scale motions, such as granulation, which can be observed on the solar surface. Between the radiative and convective zones, there exists a thin layer called the tachocline, which is believed to be responsible for a process known as the solar dynamo by which large-scale solar magnetic fields are generated. These fields are carried around by the plasma motion and energy is now transported much faster than by radiation. The convective zone marks the end of the solar interior, which starts from the very centre of the Sun and extends out to the solar surface.

1.1.2 The Solar Surface: The Photosphere

The next region in the structure of the Sun is the photosphere, the visible surface of the Sun, which marks the dividing line between the solar interior and the solar atmosphere. Energy is transported through the photosphere once again by radiation. The plasma there is optically thin, making a layer of only $0.07R_{\odot}$ and the temperature continues its decreasing pattern to reach about 6000 K. The properties and features of plasma in this part of the Sun and in the solar atmosphere can be observed directly in great details picking out even the very fine structures on the surface using a range of telescopes and radiation detectors, either from space or down from the Earth. One of the major observed photospheric features, which are illustrated in Fig. (1.2), are the continuously changing dark spots known as sunspots. They are regions of intense magnetic field concentration and appear dark since they are cooler than the surroundings (the rest of the photosphere) with a typical temperature of about 4000 K. The number of sunspots appear on the photosphere increases

and decreases in a regular pattern known as the 11 year solar cycle. However, in general, the minimum and maximum numbers of sunspots vary from one cycle to another, with the number peaks at the solar maximum around the mid of each cycle.

Looking more closely at the solar surface using high resolution instruments, one would observe another feature of the photosphere in the form of very fine structures called granulation as shown in Fig. (1.3). This pattern as mentioned previously is related to the convective plasma motions taking place in the convective zone. Each granular cell has a diameter of about 1000 km and a mean lifetime of about 10 minutes.

1.1.3 The Solar Atmosphere

The last three layers of the Sun are the chromosphere, the transition region and the corona. These layers are above the photosphere and hence make the solar atmosphere. Moving outward in the Sun's atmosphere, the density continues to decrease. However, the temperature starts to increase above the photosphere reaching 20000 K in the chromosphere and a temperature of about $2 \times 10^6 K$ in the corona. The chromosphere (which literally means the sphere of color) was named after its appearance as a colorful layer around the Sun during solar eclipses. It is about 2000 km thick. The $H\alpha$ emission line can be used to view the chromosphere, giving it a distinctive red color. Another interesting feature seen in $H\alpha$ are regions where plasma at chromospheric temperature is held up in the corona by the coronal magnetic field as illustrated in Fig. (1.2). This feature is known as a prominence. Between the chromosphere and the corona, there exists a thin layer of the solar atmosphere known as the transition region. This region has very large temperature gradients, since within it the temperature is increasing drastically from the chromospheric values of 20000 K to over 1 million degree Kelvin in the corona.

It is believed that the complicated structure of the coronal magnetic field with its ability to store a huge amount of energy is playing a very active role in heating up the corona. This stored energy can be released during changes in the connectivity of field lines in a process called magnetic reconnection, which is the only process that has the ability to change the topology of the magnetic field. We shall discuss the fundamental process of magnetic reconnection in more detail in Chapter 2.

The corona, the outermost layer of the solar atmosphere, can be seen when the bright solar surface is blocked either during a total solar eclipse or by using special instruments, such as a coronagraph telescope which simulates an eclipse by covering the Sun's surface. In this case, due to the very bright emissions from the photosphere and the corona itself, the corona can be observed in white light during a solar eclipse (Fig. 1.4 left). However, these very bright emissions can be easily made invisible using non-visible wavelength emissions, such as X-rays, and hence the corona could be

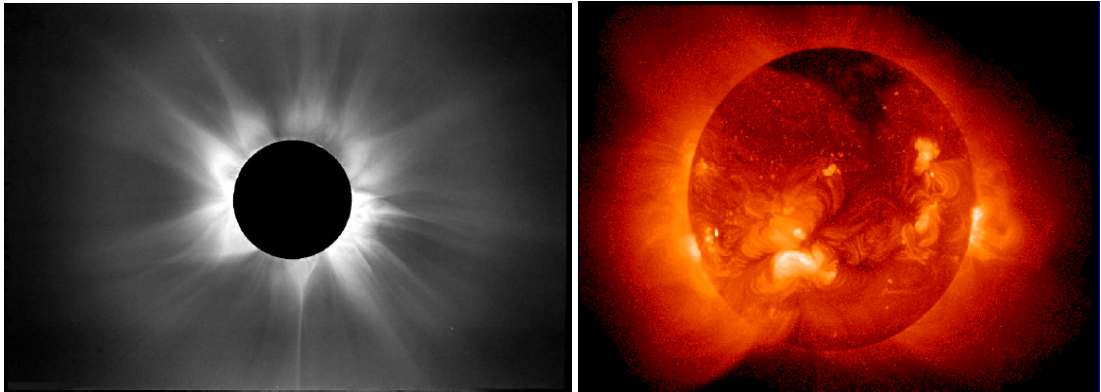


Figure 1.4: Left: the solar corona as observed in a total solar eclipse (High Altitude Observatory). Right: An X-ray image of the solar corona (Yohkoh).

observed in a very great detail as shown in Fig. (1.4 right). Most of the corona is found to consist of regions of closed loops of magnetic field lines, which are clearly seen at solar maximum. These regions appear bright in X-rays as shown in Fig. (1.4). There are other regions which appear dark in X-rays. These are regions of field lines that do not loop back to the Sun known as coronal holes. They can be seen covering both poles at solar minimum as illustrated in Figs. (1.2) and (1.4). Also, small-scale bright features called coronal bright points are observed in X-rays. They are distributed throughout the corona and have typical diameters of 22 000 km and a mean lifetime of 8 hours.

The plasma dynamics in this highly structured very active zone is dominated by its very strong complicated magnetic field. Hence, the coronal magnetic field together with the process of magnetic reconnection is found to be responsible for wide variety of dynamic processes that take place in the corona such as solar flares, see Fig. (1.2) for illustration, and coronal mass ejections (CMEs).

To mathematically model plasmas in general and the solar corona in particular along with its magnetic field and the associated fundamental process of magnetic reconnection, we shall consider the most widely used theoretical description, namely, magnetohydrodynamics (MHD). This mathematical tool is introduced in the following section.

1.2 A Mathematical Tool: Magnetohydrodynamics (MHD)

Plasmas can have different theoretical descriptions ranging from using particle dynamics through statistical mechanics to fluid mechanics. Its basic description, however, is obtained by using kinetic theory in which the governing equations are the Boltzmann equation for the distribution function and Maxwell's equations, with averaged sources, for the electric and magnetic fields.

Other plasma properties, such as the number density, velocity, pressure and temperature, can be obtained by taking different velocity moments of the distribution function (see, for example, Boyd and Sanderson 2003). However, this approach is mathematically very complicated. The fluid description, on the other hand, is relatively easier. In this description, the plasma is treated either as multiple fluids of different particle species and hence we have fluid equations for each particle species along with Maxwell's equations or it is treated as a single fluid as in MHD.

MHD is the study of the motion of electrically conducting fluids in electromagnetic fields. Many solar and laboratory plasma phenomena can indeed be described by a fluid model. Even though a plasma is not really one fluid but at least two, an ion fluid and an electron fluid, a single fluid description of a plasma is a useful model which is widely used. The advantage of the MHD model is its simplicity, compared to other models. It can be applied whether the plasma dynamics support frequent collisions between particles or not. However, the use of the MHD model is based on a number of assumptions and conditions. Firstly, to treat the plasma as a single fluid, where the effects of individual particles are ignored, requires that typical length scales of interest are much larger than typical internal plasma length scales such as the mean free path, the Debye length and the ion Larmor (gyro)-radius. The typical plasma velocities are assumed to be much less than the speed of light, c , in order to neglect the displacement current given by $(\partial \mathbf{E} / \partial t) / c^2$ in Ampere's law. It is also assumed that the plasma is quasi-neutral, so that the charge density may be neglected as well. In general, these assumptions are well satisfied in the solar corona over large enough length scales. In this next section, we present the basic equations in the MHD model (see, e.g., Roberts 1967; Priest 1982; Boyd and Sanderson 2003, for derivations of the MHD equations and detailed discussions about the MHD assumptions).

1.2.1 Basic Equations

The governing equations in the MHD model are given by the following set of fluid and electromagnetic equations:

- **Continuity Equation** (conservation of mass):

$$\frac{\partial \rho}{\partial t} + \nabla \cdot (\rho \mathbf{v}) = 0. \quad (1.1)$$

If the plasma is taken to be incompressible, Eq. (1.1) reduces to

$$\nabla \cdot \mathbf{v} = 0. \quad (1.2)$$

- **Equation of Motion** (conservation of momentum):

$$\rho \left(\frac{\partial}{\partial t} + (\mathbf{v} \cdot \nabla) \right) \mathbf{v} = \mathbf{j} \times \mathbf{B} - \nabla p + \mathbf{F}. \quad (1.3)$$

- **Energy Equation** (setting the total energy loss to zero):

$$\frac{\partial p}{\partial t} + \mathbf{v} \cdot \nabla p = -\gamma p \nabla \cdot \mathbf{v}. \quad (1.4)$$

- **Ideal Gas Law:**

$$p = \frac{\rho \mathcal{R} T}{\tilde{\mu}}. \quad (1.5)$$

- **Maxwell's Equations:**

$$\nabla \cdot \mathbf{B} = 0, \quad (1.6)$$

$$\nabla \times \mathbf{B} = \mu \mathbf{j}, \quad (1.7)$$

$$\nabla \times \mathbf{E} = -\frac{\partial \mathbf{B}}{\partial t}. \quad (1.8)$$

- **Ohm's Law:**

$$\mathbf{E} + \mathbf{v} \times \mathbf{B} = \mathbf{R} \quad (1.9)$$

where,

ρ is the mass density,

\mathbf{v} is the plasma's bulk flow velocity,

\mathbf{j} is the current density,

\mathbf{B} is the magnetic induction, usually referred to as the magnetic field,

p is the plasma pressure,

\mathbf{F} represents all other forces which may be present, such as the gravitational and viscous forces (centrifugal forces may be included if it is found convenient to use a rotating frame of reference),

γ is a specific heats ratio, usually taken to be 5/3,

$\mathcal{R} = 8.3 \times 10^3 J K^{-1} kg^{-1}$ is the gas constant,

T is the plasma temperature,

$\tilde{\mu}$ is the mean atomic weight,

$\mu = 4\pi \times 10^{-7} H m^{-1}$ is the magnetic permeability in vacuum,

\mathbf{E} is the electric field, and

\mathbf{R} represents a general non-ideal term, which includes different non-ideal effects such as collisional effects, electron-inertia effects and the Hall effects. In resistive MHD, collisional effects are assumed to be dominant and hence we have $\mathbf{R} = \eta_e \mathbf{j}$, where $\eta_e = (\sigma)^{-1}$ is the electrical resistivity, and σ is the electrical conductivity. A more general form of the non-ideal term \mathbf{R} which makes the generalized Ohm's law is discussed in Chapter 2.

1.2.2 The Induction Equation

Using the resistive form of Ohm's law together with Eqs. (1.7) and (1.8), we could eliminate the variables \mathbf{E} and \mathbf{j} to obtain the induction equation (see, e.g., Priest 1982),

$$\frac{\partial \mathbf{B}}{\partial t} = \nabla \times (\mathbf{v} \times \mathbf{B}) - \nabla \times (\eta \nabla \times \mathbf{B}),$$

where, $\eta = (\mu\sigma)^{-1}$ is the magnetic diffusivity and if it is taken to be constant (generally depends on the plasma temperature and hence expected to vary in space), we get

$$\frac{\partial \mathbf{B}}{\partial t} = \nabla \times (\mathbf{v} \times \mathbf{B}) + \eta \nabla^2 \mathbf{B}, \quad (1.10)$$

The induction equation (1.10) describes how the magnetic field \mathbf{B} evolves with time. The two terms on the right-hand side are known as the advection term, $\nabla \times (\mathbf{v} \times \mathbf{B})$, and the diffusion term, $\eta \nabla^2 \mathbf{B}$. The advection term describes how the magnetic field lines are carried along by the plasma velocity and hence the field lines are "frozen in" to the plasma if the advection term is dominant, i.e., plasma elements which are initially on the same field line remain so for all later times. On the other hand, if the diffusion term is dominant then the magnetic field lines may slip through the plasma. So, it is very important to determine the relative magnitude of these two terms in order to know when may these two different effects take place. Their relative magnitude is determined by a dimensionless number, R_m , known as the magnetic Reynold's number:

$$\begin{aligned} R_m &= \frac{|\nabla \times (\mathbf{v} \times \mathbf{B})|}{|\eta \nabla^2 \mathbf{B}|} \\ &= \frac{Lv_0}{\eta}, \end{aligned}$$

where, L is a typical length scale and v_0 is a typical plasma velocity. The magnetic Reynold's number is almost always very large on the Sun, since L and v_0 are typically very large which

means that the diffusion term is negligible and the “frozen in” condition will remain valid. However, there is an exception at locations where the typical length scales are very small and hence the non-ideal effects become important, such as localized non-ideal regions where reconnection might take place.

Another dimensionless parameter of interest in studying the behavior of plasmas is the plasma beta

$$\beta = \frac{2\mu p_0}{B_0^2},$$

which measures the ratio of the plasma pressure (p_0) to the magnetic pressure. Here, B_0 is a typical magnetic field strength. Most regions in the corona, such as active regions and coronal holes, have beta values very much less than one.

1.2.3 Magnetohydrostatics (MHS)

Magnetohydrostatics (MHS) is the study of the static equilibria of MHD equations. Many solar phenomena, such as sunspots and prominences, are observed to evolve slowly with time, i.e., they evolve in time scales much longer than the typical dynamic time scales of the plasma. Essentially, they remain in a static state for long periods of time and hence could be approximated by time-independent solutions to the MHD equations. Moreover, it is a good practice when dealing with complicated systems of equations, such as the MHD equations, to start with relatively simpler cases, such as the case of static equilibria in MHD. Nevertheless, this kind of approach provides a good understanding of the basic properties of those systems.

The governing equations in the MHS model can be derived from the MHD equations by neglecting the flow ($\mathbf{v} \equiv \mathbf{0}$) and assuming there is no time variation ($\partial/\partial t = 0$). The equation of motion is reduced to a force balance equation (see, e.g., Priest 1982)

$$\mathbf{j} \times \mathbf{B} - \nabla p + \mathbf{F} = \mathbf{0}, \quad (1.11)$$

coupled with the following equations that remain unchanged:

$$\begin{aligned} \nabla \cdot \mathbf{B} &= 0, \\ \nabla \times \mathbf{B} &= \mu \mathbf{j}, \\ p &= \frac{\rho \mathcal{R} T}{\tilde{\mu}}. \end{aligned} \quad (1.12)$$

The remaining MHD equations, on setting \mathbf{R} to zero, are automatically satisfied.

As we have already mentioned in Section 1.2.1 that \mathbf{F} represents all other forces which may be present, such as the gravitational force ($-\rho \mathbf{g}$), where the gravitational acceleration \mathbf{g} can be

derived from a potential V_g ,

$$\mathbf{g} = \nabla V_g.$$

If we are dealing with a rigidly rotating system (e.g. a rotating star) using a frame of reference rotating with the same angular velocity, say $\boldsymbol{\Omega}$, as the system itself, one may also include a centrifugal force. The centrifugal force, in this case, can also be derived from a potential given by

$$V_c = \frac{1}{2}|\boldsymbol{\Omega} \times \mathbf{r}|^2.$$

Hence, including these two forces, the force balance equation (1.11) can now be written as (see e.g. Mestel 1999)

$$\mathbf{j} \times \mathbf{B} - \nabla p - \rho \nabla V = \mathbf{0},$$

where $V = V_c + V_g$ is the combined centrifugal and gravitational potential.

The MHS equations are very important for modelling astrophysical plasmas, for example the coronae of magnetized stars. In this thesis, we aim to present three-dimensional solutions for simple rigidly rotating magnetized coronae (see Section 1.3).

Now, if we neglect the force \mathbf{F} in Eq. (1.11), then for plasmas with low beta ($\beta \ll 1$), the pressure gradient term can be also ignored compared to the Lorentz force since

$$\frac{|\nabla p|}{|\mathbf{j} \times \mathbf{B}|} = \frac{\mu p_0}{B_0^2} = \frac{\beta}{2} \ll 1.$$

Hence, under this assumption, Eq. (1.11) reduces to

$$\mathbf{j} \times \mathbf{B} = \mathbf{0},$$

i.e., there is no Lorentz force acting on the plasma and hence such a magnetic field is known as a force-free field. Ampere's law in (1.12) can now be written as

$$\nabla \times \mathbf{B} = \alpha \mathbf{B},$$

for some scalar function α , since the corresponding current density has to be parallel to the magnetic field. For the special case of $\alpha = 0$, the magnetic field is potential.

1.3 Aims and Outline

As we have already mentioned, in this thesis we aim to present three-dimensional solutions of two different MHD models and hence, the thesis could be divided in two parts. In the first part, we aim

to study the fundamental process of magnetic reconnection in 3D. In particular, a stationary MHD model is used to find solutions of 3D reconnection in the absence of null points with a localized non-ideal region building on the work started by Hornig and Priest (2003) and Wilmot-Smith et al. (2006, 2009). The solutions are presented in the form of an expansion scheme, where quantities at different orders are obtained either analytically or numerically via an integration scheme. We start with a short overview of the fundamental process of magnetic reconnection in 2D and 3D in Chapter 2. In Chapter 3, the stationary MHD model is presented and the integration scheme is introduced, which can be used to obtain variety of both analytical and numerical solutions. The same assumptions as in Wilmot-Smith et al. (2006, 2009) are used to allow for a direct comparison. The work done by Hornig and Priest (2003) and Wilmot-Smith et al. (2006, 2009) is extended further in Chapter 4.

In the other part of this thesis, we use an MHS model to calculate 3D solutions outside massive rigidly rotating central bodies. The governing equations are obtained by neglecting the flow and resistivity in the set of the resistive stationary MHD equations used in the previous model. We consider in Chapter 5 a mathematically simpler case of a rigidly rotating cylinder which somehow allows for analytical solutions. In Chapter 6, we present a more realistic case of rotating spherical bodies. However, in this case, solutions are only obtained numerically since there is no hope to find analytical solutions. Finally, a short summary is given in Chapter 7.

Chapter 2

Magnetic Reconnection: an Overview

“Have not those who disbelieve known that the heavens and the Earth were joined together as one unit of creation, then we split them asunder? And we have made from water every living thing. Will they not then believe? Θ”

(Interpretation of the Holy Quran **21**: 30)

2.1 Introduction

Magnetic reconnection is a fundamental process of structure formation in plasmas (see, for example, Biskamp 2000; Priest and Forbes 2000; Zweibel and Yamada 2009, for a review). In this process, a magnetic field changes the connectivity of its field lines. This change plays an important role in releasing free magnetic energy stored in the plasma and converting it into kinetic energy, heat and accelerated particles. This becomes possible, because the presence of a finite resistivity leads to the violation of the “frozen-in” constraint and allows field lines to break and reconnect. The “frozen-in” condition is effective when the plasma obeys the ideal Ohm’s law:

$$\mathbf{E} + \mathbf{v} \times \mathbf{B} = \mathbf{0}.$$

Deviations from the ideal MHD state are described by the generalized Ohm’s law, see Appendix A for its derivation, which is given by

$$\begin{aligned} \mathbf{E} + \mathbf{v} \times \mathbf{B} = \eta_e \mathbf{j} &+ \frac{m_e}{ne^2} \left(\frac{\partial \mathbf{j}}{\partial t} + (\mathbf{v} \cdot \nabla) \mathbf{j} + (\mathbf{j} \cdot \nabla) \mathbf{v} - \frac{1}{ne} (\mathbf{j} \cdot \nabla) \mathbf{j} \right) \\ &+ \frac{1}{ne} (\mathbf{j} \times \mathbf{B}) - \frac{1}{ne} \nabla p_e, \end{aligned} \quad (2.1)$$

where, n is the plasma number density, e is the electron charge and p_e is the electron pressure. The last three terms on the right-hand side of the generalized Ohm's law (2.1), which are not included in resistive MHD, are known as the electron inertia term, the Hall term and the pressure term, respectively. The relative significance of the non-ideal terms in the generalized Ohm's law (2.1) depends on the various plasma parameters, e.g. n , \mathbf{B} , and T , as well as on the length scales over which these parameters vary. So, in order to determine the relative importance of these terms we shall nondimensionalize Eq. (2.1) using

$$\tilde{\nabla} = L\nabla, \quad \tilde{\mathbf{v}} = \frac{\mathbf{v}}{v_0}, \quad \tilde{\mathbf{B}} = \frac{\mathbf{B}}{B_0}, \quad \tilde{\mathbf{E}} = \frac{\mathbf{E}}{v_0 B_0}, \quad \tilde{\mathbf{j}} = \frac{\mathbf{j}}{(B_0/\mu L)}, \quad \tilde{p} = \frac{p}{(B_0^2/\mu)}, \quad (2.2)$$

where L is a typical length scale, B_0 is a typical magnetic field strength and v_0 is a typical plasma velocity. We then have

$$M_A(\mathbf{E} + \mathbf{v} \times \mathbf{B}) = \eta_c \mathbf{j} + C_I \left(M_A \left(\frac{\partial \mathbf{j}}{\partial t} + (\mathbf{v} \cdot \nabla) \mathbf{j} + (\mathbf{j} \cdot \nabla) \mathbf{v} \right) - C_H (\mathbf{j} \cdot \nabla) \mathbf{j} \right) + C_H (\mathbf{j} \times \mathbf{B} - \nabla p_e) \quad (2.3)$$

where $M_A = v_0/v_A$ is the Alfvén Mach number, $v_A = B_0/\sqrt{\mu\rho}$ is the typical Alfvén speed of the plasma, $\eta_c = \eta/(Lv_A) = L_c/L$ is the inverse Lundquist number, $C_I = d_e^2/L^2$ and $C_H = d_i/L$. All over tildes have been neglected for ease of notation. The Lundquist number, or the global magnetic Reynolds number, S given by

$$S = \frac{Lv_A}{\eta} \quad (2.4)$$

is the ratio of the global Ohmic diffusion time $\tau_{diff} = L^2/\eta$ to the global Alfvén time $\tau_A = L/v_A$ and it is typically very high in the solar corona. The dimensionless numbers η_c , C_I and C_H indicate the relative magnitudes of the collisional, inertial and Hall terms, respectively. From Eq. (2.3), we note that the ideal Ohm's law is scale invariant, i.e., it doesn't define a spatial scale, whereas the other terms are associated with specific spatial scales and are important when those spatial scales are reached. The collision term $\eta_c \mathbf{j}$ is associated with a length scale $L_c = \eta/v_A$, the electron-inertia term is associated with the electron skin depth $d_e = c/\omega_{pe}$ and the Hall term is associated with the ion skin depth $d_i = c/\omega_{pi}$, where

$\omega_{pe} = \left(\frac{n_0 e^2}{m_e \epsilon_0}\right)^{\frac{1}{2}}$, is the electron plasma frequency, and

$\omega_{pi} = \left(\frac{n_0 e^2}{m_i \epsilon_0}\right)^{\frac{1}{2}}$, is the ion plasma frequency.

The isotropic pressure term, in the isothermal limit with $T_e \gg T_i$, brings in the ion sound Larmor (gyro-) radius

$$\rho_s = \frac{\sqrt{k_B T_e / m_i}}{\Omega_i},$$

where,

$\Omega_i = (eB)/m_i$ is the ion Larmor (gyro-) frequency.

The derivation of this length-scale, which doesn't follow from Ohm's law alone, is presented in Appendix B. Estimations of these length scales show that, in general, for high temperature plasmas we have

$$L_c \ll d_e, \rho_s < d_i$$

However, even though it has the largest scale-length in most plasmas environments, the Hall term by itself doesn't allow reconnection. The magnetic field lines are rather frozen in the electron fluid since Ohm's law with the Hall term as the only nonideal effect can be written as

$$\mathbf{E} + \left(\mathbf{v} - \frac{1}{ne} \mathbf{j} \right) \times \mathbf{B} = \mathbf{E} + \mathbf{v}_e \times \mathbf{B} = \mathbf{0},$$

while, in the absence of collisions, electron-inertia leads to the decoupling of the plasma motion from that of the magnetic field lines and hence allows reconnection to take place.

2.2 Significance of Magnetic Reconnection

Magnetic Reconnection plays an important role in relaxation or configuration change in virtually all plasmas. It is responsible for many dynamic processes, whether in laboratories, the Earth's magnetosphere, the Sun or in any astrophysical plasmas where magnetic fields exist (see, e.g., Priest and Forbes 2000, for a review). The importance of magnetic reconnection in these different plasma environments comes about because it is playing a fundamental role in the generation of magnetic fields in these environments and has the ability to change the magnetic field topology and hence releasing the stored magnetic energy and converting it into other different forms such as kinetic energy, heat and accelerated particles. In the following, we give some examples illustrating the role of magnetic reconnection in the above mentioned plasma environments:

Laboratory (see also, e.g., Zweibel and Yamada 2009)

- In fusion devices, such as tokamaks, magnetic reconnection is believed to disturb the plasma confinement process by causing various instabilities and oscillations, such as the sawtooth oscillations.
- In other fusion devices, such as, the reversed-field pinch, it is found to be useful in generating confining magnetic fields, since it allows the seed magnetic field to create a stronger confining field (a dynamo-like action).

- There is a number of lab experiments dedicated for the understanding of the fundamental process of magnetic reconnection, such as the Magnetic Reconnection Experiment (MRX) (Yamada et al. 1997).

The Earth's Magnetosphere (see also, e.g., Sonnerup et al. 1981; Nishida 2000))

- Reconnection on the day side of the magnetosphere between the interplanetary magnetic field and the Earth magnetic field plays a role in shaping the magnetotail and also provides a source of particles and energy to the magnetosphere.
- Reconnection of the magnetotail field lines, on other hand, is believed to accelerate plasma particles toward and away from the Earth and produce global disturbance called magnetospheric substorm.
- Terrestrial aurorae are also believed to be a result of magnetic reconnection in the Earth's magnetosphere.

The Sun (see, e.g., Priest and Forbes 2000).

- Magnetic reconnection is very essential for the solar dynamo. It allows the seed magnetic field to be restructured to generate a stronger large-scale magnetic field.
- It provides energy that powers many large-scale eruptive processes, such as solar flares and CMEs, as well as small-scale events, such as coronal bright points (see, e.g., Parnell et al. 1994).
- It is believed that reconnection plays a major part in heating the solar corona.

Astrophysical Plasmas (see also, e.g., Mestel 1999; Zweibel and Yamada 2009)

- Magnetic reconnection is very important for the generation of magnetic fields in stars, plays a major role in heating the stellar coronae and is believed to be behind many dynamic astrophysical phenomena such as stellar flares.
- It has been invoked as a heat source in warm, ionized interstellar gas and as a mechanism for the transfer of angular momentum in accretion disks.

The pivotal role of magnetic reconnection in plasma has led to a strong interest in understanding the fundamental physics of reconnection. Theoretically, very good progress has been made in understanding the fundamental process of magnetic reconnection both by analytical and numerical

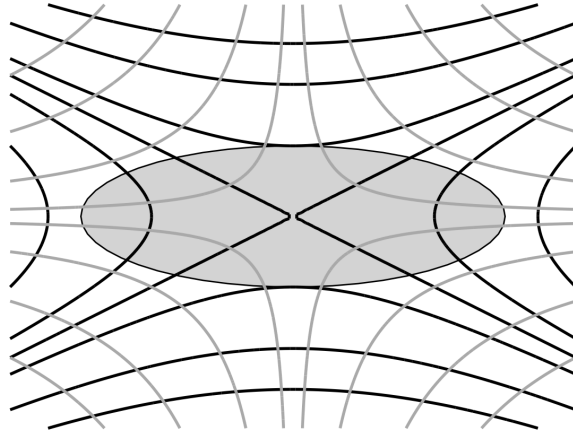


Figure 2.1: A basic picture of 2D magnetic reconnection, with magnetic field lines in black and velocity streamlines in gray.

approaches starting with the two classical models for two-dimensional reconnection, namely, the Sweet-Parker model (Sweet 1958; Parker 1957) and the Petschek model (Petschek 1964) followed by a lot of work in both two and three-dimensional magnetic reconnection (see, for example, Biskamp 2000; Priest and Forbes 2000, for a review).

2.3 Two-Dimensional (2D) Magnetic Reconnection

2.3.1 Classical 2D Models

In 2D, magnetic reconnection can only take place at X-type magnetic null points, locations where the magnetic field vanishes. The basic picture of 2D reconnection, as in Fig. (2.1), is that of field lines being frozen in and carried along with the fluid towards a non-ideal region, where an X-point is located. Then at this point, due to non-ideal effects in Ohm's law, they break and reconnect to form new field lines which move away from the non-ideal region.

This basic picture of reconnection was first formulated by Sweet (1958) and Parker (1957) resulted in a well-known reconnection mechanism called the Sweet-Parker mechanism for 2D reconnection, which is an order-of-magnitude analysis. They have presented a model for 2D steady magnetic reconnection, where the flow is taken to be incompressible. They considered two parallel, but oppositely directed, uniform magnetic fields B_i , which are carried along with an inflow velocity v_i towards a diffusion layer or a current sheet with length $2L$ and width $2l$, where a null point is located at the centre as illustrated in Fig. (2.2). The reconnected field lines then move away from the diffusion region with an outflow velocity v_o equal to the Alfvén speed $v_{A_i} = B_i/\sqrt{\mu\rho}$, since the plasma at the outflow region is accelerated to such a speed. The rate at which field lines

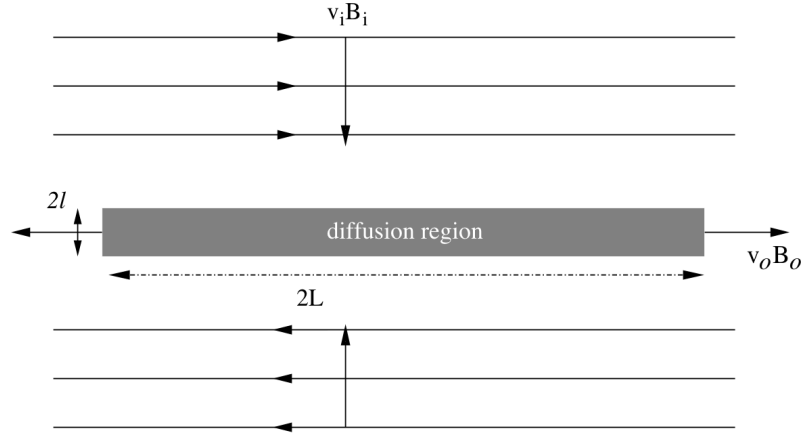


Figure 2.2: The Sweet-Parker model for 2D steady reconnection.

(or flux) pass(es) through the null point, which is how the reconnection rate is defined in 2D, is measured by the electric field at the null point. However, a dimensionless reconnection rate is represented in terms of the Alfvén Mach number which, in this case, is given by

$$M_A = \frac{v_i}{v_o} = \frac{v_i}{v_{Ai}} = \frac{1}{\sqrt{S}},$$

where S is the Lundquist number given by Eq. (2.4). The obtained reconnection rate is calculated based on the following relations:

$v_i = \eta/l$, i.e., the inflow velocity v_i can be taken to be equal to the diffusion rate η/l , since we have a steady reconnection, and

$v_i L = v_o l$, since, mass is conserved and the flow is incompressible.

However, the value of this reconnection rate is very small in astrophysical plasma ($M_A \approx 10^{-3}$ to 10^{-6}), since the Lundquist number is very high there (typically 10^6 to 10^{12}). Hence, the Sweet-Parker mechanism is too slow to explain the very fast energy release of solar flares (where $M_A \approx 0.1$), which was the main purpose of this model. The Sweet-Parker reconnection is classified as a slow reconnection model and an alternative mechanism which is fast enough to explain the energy release in solar flares is required.

Petschek (1964) presented a new mechanism for 2D steady incompressible reconnection after realizing that having a very small diffusion region will increase the reconnection rate and that the reconnection process can produce slow mode shocks. The set up of his model is illustrated in Fig. (2.3), where we have a Sweet-Parker diffusion region with a length L smaller than the global external length-scale L_e located at the centre and four slow-mode shocks attached to the four corners of the diffusion region. It is at these shocks where most of the conversion of magnetic

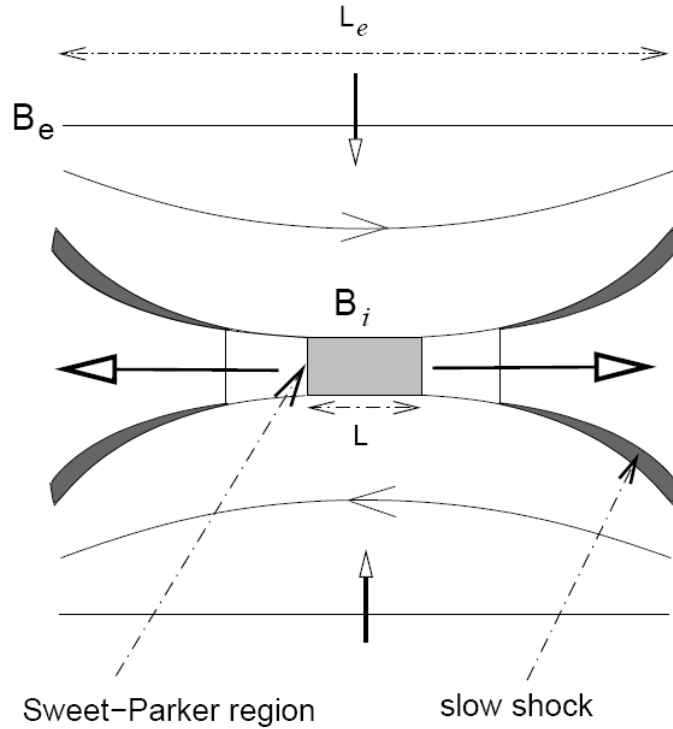


Figure 2.3: The Petschek model for 2D steady reconnection.

energy into thermal and kinetic energy is taking place. The inflow magnetic field is still oppositely directed on either side of the diffusion region, but it is no longer uniform. It is rather slightly curved. Petschek derived a family of solutions with the corresponding maximum reconnection rate given by

$$M_A = \frac{\pi}{8 \ln S}.$$

Hence, due its logarithmic dependence on the Lundquist number S , the Petschek reconnection rate is several order of magnitude greater than the Sweet-Parker rate and in most space and laboratory plasmas, we have $M_A \approx 0.1$ to 0.01 . Such a fast reconnection rate provides a good explanation of the energy release in solar flares and marks the Petschek model as the first fast reconnection model.

Later, Priest and Forbes (1986) presented a set of new models for incompressible steady-state magnetic reconnection, where Petschek-type regimes are particular cases of their presented family of reconnection regimes, which are obtained by prescribing different inflow boundary conditions. This was then followed by a lot research in 2D reconnection using both analytical and numerical techniques and not only considering collisional magnetic reconnection, but also studying other types of reconnection such as collisionless reconnection and Hall reconnection.

2.3.2 General Mathematical Approach

A general mathematical approach towards solving a 2D reconnection problem is done by considering 2.5 dimensional representations of the magnetic field and velocity given, respectively, by (see, e.g., Craig and Watson 2003)

$$\mathbf{B} = \nabla\psi(x, y, t) \times \mathbf{e}_z + b(x, y, t)\mathbf{e}_z \quad (2.5)$$

$$\mathbf{v} = \mathbf{e}_z \times \nabla\phi(x, y, t) + w(x, y, t)\mathbf{e}_z \quad (2.6)$$

which are divergence free and hence satisfy Eqs. (1.2) and (1.6). Here,

ψ is a scalar magnetic potential,

ϕ is a scalar velocity potential,

b is the z -component of the magnetic field \mathbf{B} , usually known as a guide field, and

w is the z -component of the velocity \mathbf{v} .

Substituting Eqs. (2.5) and (2.6) into Eqs. (2.3) and (1.3) and using Eqs. (1.7) and (1.8), the z -components of Eqs. (2.3) and (1.3) are then given, respectively, by

$$\psi_t + [\phi, \psi] = \eta_c \nabla^2 \psi + C_I \{ \nabla^2 \psi_t + [\phi, \nabla^2 \psi] + [b, v] \} - C_H [b, \psi] \quad (2.7)$$

$$w_t + [\phi, w] = [b, \psi] \quad (2.8)$$

The x and y -components of Eqs. (2.3) and (1.3) can be combined to give, respectively,

$$b_t + [\phi, b] + [\psi, w] = \eta_c \nabla^2 b + C_I \{ \nabla^2 b_t + [\phi, \nabla^2 b] + [b, \nabla^2 \phi] \} - C_H [\nabla^2 \psi, \psi] \quad (2.9)$$

$$\nabla^2 \phi_t + [\phi, \nabla^2 \phi] = [\psi, \nabla^2 \psi] \quad (2.10)$$

In this derivation, we have used a dimensionless form of the MHD equations, assumed ρ to be unity, set \mathbf{F} that appear in Eq. (1.3) to zero and used the Poisson bracket notation $[f, g] = f_x g_y - f_y g_x$. These four equations could be further simplified or even reduced to two equations depending on the problem being addressed. For example, if the Hall effect is to be neglected, $C_H = 0$, one can set $w = 0$ and take b to be constant. Hence, the four equations now reduced to

$$\psi_t + [\phi, \psi] = \eta_c \nabla^2 \psi + C_I \{ \nabla^2 \psi_t + [\phi, \nabla^2 \psi] \}$$

$$\nabla^2 \phi_t + [\phi, \nabla^2 \phi] = [\psi, \nabla^2 \psi]$$

which can be used to study the electron inertia effects on magnetic reconnection. To obtain a

collisional resistive solution, one can further set $C_I = 0$. Analytical solutions may be obtained by choosing appropriate representations of ψ and ϕ (see, e.g., Shivamoggi 1993; Al-Salti and Shivamoggi 2003).

Before moving to reconnection in 3D, let us finally summarize the basic properties of 2D reconnection. These properties, although many of them seem to be obvious, are very helpful in demonstrating the fundamental differences between reconnection in 2D and 3D as most of these basic properties are not present in 3D reconnection (Priest et al. 2003).

2.3.3 Fundamental Properties

- A flux transport velocity \mathbf{w} (Hornig and Schindler 1996; Hornig and Priest 2003) satisfying

$$\frac{\partial \mathbf{B}}{\partial t} - \nabla \times (\mathbf{w} \times \mathbf{B}) = 0$$

or equivalently satisfying

$$\mathbf{E} + \mathbf{w} \times \mathbf{B} = 0$$

exists everywhere in 2D except at the X-point. This velocity, within which the magnetic flux is frozen (by comparison with the ideal Ohm's law), can be given by

$$\mathbf{w} = \frac{\mathbf{E} \times \mathbf{B}}{\|\mathbf{B}\|^2},$$

which is possible in 2D since the electric field is perpendicular to the magnetic field. Moreover, the given flux transport velocity is singular at the X-point, which is indicating that a reconnection process for the transported magnetic flux is taking place (Hornig 2001).

- As we have already mentioned that reconnection in 2D and hence the change of the connectivity of the magnetic field lines takes place only at an X-type magnetic null point, that is, field lines connections are preserved everywhere, even in the diffusion region, except at the X-point where they cut and hence change their connection.
- In 2D, we have “perfect reconnection”, that is, for any field line which is going to reconnect, there exist a unique counterpart with which it will reconnect perfectly to form two new field lines.
- Fieldline mapping is discontinuous in 2D due to the fact that field lines break only at a single X-point (see Priest et al. 2003, for more details)
- The reconnection rate in 2D, as we have mentioned earlier, is defined as the rate at which magnetic field lines pass through the X-point of the magnetic field, i.e., the rate at which the magnetic flux is transferred between regions with different topology and it is given by the

value of the electric field at the X-point. However, if the electric field is normalized to some typical field, then the dimensionless Alfvén Mach number could be used instead as we have seen previously.

2.4 Three-Dimensional (3D) Magnetic Reconnection

2.4.1 Comparison with reconnection in 2D

Two-dimensional magnetic reconnection is currently fairly well understood (see, for example, Biskamp 2000; Priest and Forbes 2000, for a review) and much of recent research is focusing in three-dimensional reconnection (Hornig and Priest 2003; Linton and Priest 2003; Priest et al. 2003; De Moortel and Galsgaard 2006; Pontin and Craig 2006; Wilmot-Smith et al. 2006; Pontin and Galsgaard 2007; Parnell et al. 2008; Priest and Pontin 2009; Parnell et al. 2009). Existing models for reconnection in 3D have shown some fundamental differences between reconnection in 2D and in 3D. For example, unlike reconnection in 2D, three-dimensional magnetic reconnection can take place at null points as well as at locations where the magnetic field does not vanish (Schindler et al. 1988; Lau and Finn 1990). Hence, any definition of reconnection that uses the concept of null points or separatrices is very restrictive since 3D reconnection, in general, does not require null points nor separatrices. Schindler et al. (1988) suggested to use the more general definition that define magnetic reconnection as a change in the connectivity of the magnetic field lines due to a localized non-idealness. This change in the magnetic field line connectivity requires a non-vanishing electric field component parallel to the magnetic field in the region where the ideal MHD breaks down (Hesse and Schindler 1988). There are various other suggestions for the definition of magnetic reconnection (see, for example, Vasylunas 1975; Priest and Forbes 1989; Hornig and Rastätter 1998).

Moreover, even though both 2D and 3D reconnection can take place at null points, 2D and 3D magnetic null points are very different (Fukao 1975; Parnell et al. 1996). In 2D, in general, we have X-type and O-type null points, where reconnection is taking place only at X-type null points. On the other hand, in 3D, we have two types of field lines that are directed out of or into the null (Priest and Titov 1996). The first one is known as the spine of the null, which is a pair of field lines that are directed out of or into the null point from opposite directions and the second one is a set of field lines into or out of the null lying in a surface, called the fan plane. An example of the structure of the magnetic field near a 3D null point is shown in Fig. (2.4). In this example, the field lines of the spine are the ones directed into the null point along the z -axis and the field lines of the fan are the ones directed out of the null. Thus, when 3D null points are present, magnetic reconnection can occur in the form of the so-called fan or spine reconnection depending on whether the current is aligned with the fan or the spine of the null, respectively (Pontin et al. 2004, 2005).

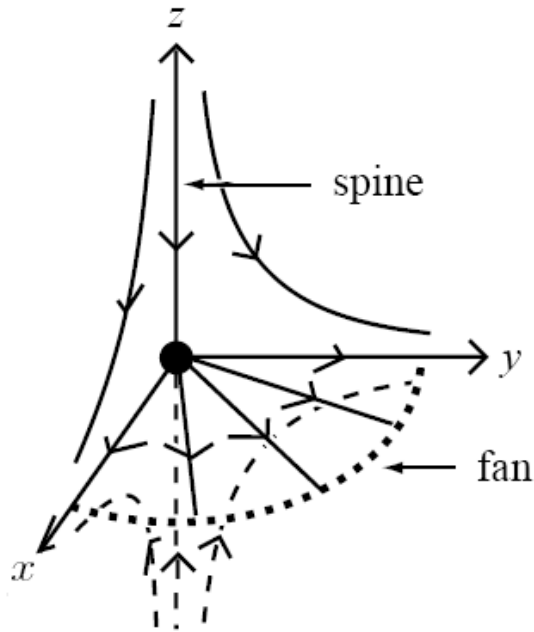


Figure 2.4: The structure of field lines near a null point in 3D.

More recently, Priest and Pontin (2009) proposed three different types of reconnection at a 3D null point to replace fan reconnection and spine reconnection. These are called torsional fan reconnection, torsional spine reconnection and spine-fan reconnection. The first two are caused by rotational motions, either of the spine or of the fan, with the current concentration being in the fan or along the spine, respectively. The third type takes place in response to a shearing of the null point with the current concentration is in both the spine and fan in the form of a localized sheet that is inclined to the fan and spine. Reconnection can also take place along the field line connecting two null points. This special field line which lies in the spine or fan of each null is called a separator and hence this type of reconnection is known as a separator reconnection (Priest and Titov 1996; Pontin and Craig 2006; Parnell et al. 2009), which can be indeed considered as a particular case of reconnection at regions of non-vanishing magnetic field (the so-called non-null magnetic reconnection). Thus, the change of connectivity of field lines can take place anywhere in the non-ideal region not just at the null points compared to 2D reconnection. In fact, field lines change their connections continually throughout the non-ideal region and hence, in general, no unique counterpart reconnecting field lines exist. However, the field line mapping is continuous everywhere except at the spine and fan of a null point, that is except at the separatrices of the magnetic field. Furthermore, unlike in 2D, a unique flux transport velocity w does not generally exist in 3D (see Priest et al. 2003, for more detail). Finally, the reconnection rate in 3D is given by the integral of the parallel electric field along the field line which maximizes this integral (see, e.g., Hesse et al. 2005).

2.4.2 Non-null Reconnection

As we have mentioned earlier that 3D reconnection can take place within regions of non-vanishing magnetic field, which is known as a non-null magnetic reconnection. A fundamental investigation of this type of reconnection was given by Schindler et al. (1988) and Hesse and Schindler (1988), where they have used the term “general magnetic reconnection”. In these two papers, they have shown that the electric field component parallel to the magnetic field plays a very important role in the non-null reconnection. In particular, they have proven that a non-vanishing electric field component parallel to the magnetic field is a requirement of this type of reconnection to occur. The non-null reconnection includes as particular cases the so-called quasi-separatrix layer reconnection (Priest and Démoulin 1995), which is also called slip-running reconnection by Aulanier et al. (2006), and separator reconnection (Priest and Titov 1996).

The main part of this thesis, namely, Chapters 3 and 4, deals with non-null magnetic reconnection, in which we build on the work started by Hornig and Priest (2003) and Wilmot-Smith et al. (2006, 2009).

Hornig and Priest (2003) have studied the process of non-null reconnection by setting up a kinematic, stationary MHD model with the non-ideal region being localized, i.e., they have presented solutions of the MHD equations with the equation of motion being neglected. They have started by prescribing an X-type linear magnetic field in the xy -plane with a uniform z -component, which resulted in a current with only a uniform z -component. This field, in 3D, gives an example of the so-called “hyperbolic flux tube” (HFT). The localization of the non-ideal region was achieved by prescribing a localized form of the resistivity, since the current is constant. This choice also helped in obtaining analytical solutions for the remaining variables. The localization parameters can be chosen so the non-ideal region is enclosed inside the HFT. The obtained solutions are expressed in terms of the coordinates x_0, y_0, s along field lines, since their expressions in the Cartesian coordinate system x, y, z are quite lengthy. However, we were able to further simplify these expressions and present them here in Appendix D, in order to have a direct comparison with the solution obtained in this thesis which are presented in Chapter 4.

This kinematic analysis allowed the authors to obtain an electric potential ϕ up to a free component ϕ_0 , which is constant along field lines. This freedom of choosing ϕ_0 allows to superimpose any ideal flow onto the obtained solutions. The authors noted that this freedom is a result of the fact that in 3D, in general, for a prescribed magnetic field, Ohm’s law can be decomposed into two parts (ideal and non-ideal):

$$\begin{aligned} -\nabla\phi_{id} + \mathbf{v}_{id} \times \mathbf{B} &= \mathbf{0}, \\ -\nabla\phi_{nonid} + \mathbf{v}_{nonid} \times \mathbf{B} &= \eta\mathbf{j}, \end{aligned}$$

The authors analyzed two different cases corresponding to two different choices of ϕ_0 . The first case, termed “pure solutions”, corresponds to $\phi_0 = 0$. The resultant velocity for this case represents a counter-rotational flow above and below the z -axis, where it vanishes. This type of flow, which only affects the plasma within the HFT, is directly related to the localization of the non-ideal term $\eta\mathbf{j}$. The second case, termed “composite solutions”, corresponds to a situation where an ideal stagnation flow is superimposed onto the rotational flow obtained in the previous case and hence, the flow pattern within the HFT depends on the relative strengths of the rotational and stagnation flow.

To investigate whether the freedom of imposing any ideal solution onto the obtained “pure solution” results because of the neglect of the equation of motion in the kinematic analysis, Wilmot-Smith et al. (2006, 2009) carried this work further by including the equation of motion in their analysis. They have represented solutions of the full stationary MHD equations in the form of expansion scheme and succeeded in obtaining analytical solutions of equations at the first few orders, whereas solutions of equations at higher orders require numerical integration. They have shown that there exists a wide variety of steady reconnection solutions in 3D and presented few examples, through which they were able to recover many features of the kinematic model, such the existence of rotational flows. Moreover, the freedom of imposing an ideal solution still showed up even when including the equation of motion. The solutions obtained by Wilmot-Smith et al. (2006), termed “particular solutions”, correspond to the pure solution case in the kinematic model, while the composite solution are presented in the second paper (Wilmot-Smith et al. 2009). However, the analytical solutions obtained by Wilmot-Smith et al. (2006) do not include the effect of the inertial term in the equation of motion, since the inertial term first appears at fourth order, where the equation needs to be solved numerically. Therefore the obtained particular solutions by Wilmot-Smith et al. (2006) appear to be similar to the pure solution obtained by Hornig and Priest (2003) as discussed in Chapter 4. Furthermore, the composite solutions obtained by Wilmot-Smith et al. (2009) correspond to a special class of ideal flow, namely, ideal plasma flows \mathbf{v} for which $\nabla \times (\mathbf{v} \cdot \nabla)\mathbf{v} = 0$. This choice, which limits the effect of the inertial term, was made in order to obtain analytical solutions for the equation of motion.

In this thesis, as described in Section 1.3, we shall carry this work further by generalizing the analytical solutions at the first few orders and examining the contribution of higher order terms which are obtained numerically.

Chapter 3

On The Solutions of Three-Dimensional Non-Null Magnetic Reconnection - I

3.1 Introduction

In this chapter, we present both analytical and numerical solutions of non-null magnetic reconnection following the work started by Hornig and Priest (2003) and Wilmot-Smith et al. (2006, 2009). As discussed earlier, Hornig and Priest (2003) used a kinematic model in their analysis and Wilmot-Smith et al. (2006, 2009) extended the work further by including the equation of motion in their model. The current work uses the last model which is detailed here in Section 3.2. Similar models were used by Priest and Forbes (1986) and Jardine (1994) for 2D and 3D stationary magnetic reconnection solutions, respectively. The solutions of the full stationary MHD equations are represented in the form of an expansion scheme and the resultant equations at different orders are solved using a general integration scheme. This integration scheme, which is introduced in Section 3.3, can be used to obtain a wide variety of 3D stationary solutions. In Section 3.4, we present a more general form of analytical solutions of equations at the first few orders. We then use numerical techniques to find higher order solutions and hence examine their contribution and get an idea about the convergence of the scheme.

The contents of this chapter have been already published and can be found in Al-Salti and Hornig (2009).

3.2 The model

We use the following set of resistive MHD equations for a stationary solution with an incompressible flow, taking ρ to be constant:

$$\mathbf{E} + \mathbf{v} \times \mathbf{B} = \frac{\mathbf{j}}{\sigma}, \quad (3.1)$$

$$\rho(\mathbf{v} \cdot \nabla)\mathbf{v} = -\nabla p + \mathbf{j} \times \mathbf{B}, \quad (3.2)$$

$$\nabla \cdot \mathbf{v} = 0, \quad (3.3)$$

$$\nabla \cdot \mathbf{B} = 0, \quad (3.4)$$

$$\nabla \times \mathbf{B} = \mu \mathbf{j}, \quad (3.5)$$

$$\nabla \times \mathbf{E} = \mathbf{0}. \quad (3.6)$$

To see the relative importance of each term in the previous set of equations, specially Eqs. (3.1) and (3.2), we shall first nondimensionalize them using (2.2). The resultant dimensionless equations are then given by

$$M_A(\mathbf{E} + \mathbf{v} \times \mathbf{B}) = \eta_c \mathbf{j}, \quad (3.7)$$

$$M_A^2(\mathbf{v} \cdot \nabla)\mathbf{v} = -\nabla p + \mathbf{j} \times \mathbf{B}, \quad (3.8)$$

$$\nabla \cdot \mathbf{v} = 0, \quad (3.9)$$

$$\nabla \cdot \mathbf{B} = 0, \quad (3.10)$$

$$\nabla \times \mathbf{B} = \mathbf{j}, \quad (3.11)$$

$$\nabla \times \mathbf{E} = \mathbf{0}, \quad (3.12)$$

where, all over tildes have been neglected for ease of notation. The standard method of solving these equations would be to start with the time-dependent set of equations, choose a certain domain, implement ad-hoc boundary conditions and solve the equations with a standard (e.g. finite differences) code, hoping that with sufficient damping a stationary state is eventually achieved. Due to the lack of mathematical theory concerning the permissible boundary conditions, the typical situation is that the boundary conditions overdetermine the solution, a problem which in most codes is handled by a high resistivity, viscosity, damping or smoothing on the boundaries. The lack of well defined boundary conditions, and the subsequent lack of confidence as to how generic the obtained solutions are, has led us to follow a different approach. With the expansion scheme explained below and the integration scheme discussed in Section 3.3, we do not have to prescribe detailed boundary conditions but we rather choose the lowest order structure of the solution we are looking for. This approach is much more suitable to investigate reconnection if the exact boundary conditions are unknown. While there is still a comparatively large freedom of matching boundary

conditions, due to free functions which appear in the integration scheme, the solution is essentially determined by the prescribed lowest order terms of the solution and the condition that the scheme converges.

Numerical simulations have shown typical values of the Alfvén Mach number of 0.1 in magnetic reconnection (see, e.g., Shay et al. 1999; Huba and Rudakov 2004). We therefore assume here $M_A < 1$, so that the inertial term in the equation of motion is small and hence one could seek solutions for slow flows, $v_0 < v_A$, by expanding the variables in terms of M_A , i.e., we look for solutions in the form of the following expansions:

$$\begin{aligned}
\mathbf{B} &= \mathbf{B}_0 + M_A \mathbf{B}_1 + M_A^2 \mathbf{B}_2 + M_A^3 \mathbf{B}_3 + \cdots, \\
\mathbf{v} &= \mathbf{v}_0 + M_A \mathbf{v}_1 + M_A^2 \mathbf{v}_2 + M_A^3 \mathbf{v}_3 + \cdots, \\
\mathbf{j} &= \mathbf{j}_0 + M_A \mathbf{j}_1 + M_A^2 \mathbf{j}_2 + M_A^3 \mathbf{j}_3 + \cdots, \\
\mathbf{E} &= \mathbf{E}_0 + M_A \mathbf{E}_1 + M_A^2 \mathbf{E}_2 + M_A^3 \mathbf{E}_3 + \cdots \\
&= -\nabla \phi_0 - M_A \nabla \phi_1 - M_A^2 \nabla \phi_2 - M_A^3 \nabla \phi_3 + \cdots, \\
p &= p_0 + M_A p_1 + M_A^2 p_2 + M_A^3 p_3 + \cdots.
\end{aligned}$$

Substituting these expansions into Eqs. (3.7) and (3.8) and collecting terms of powers of M_A , we obtain

$$\begin{aligned}
\text{Order 0} & \left\{ \begin{array}{l} -\nabla p_0 + \mathbf{j}_0 \times \mathbf{B}_0 = \mathbf{0} \\ \mathbf{j}_0 = \mathbf{0} \end{array} \right. \\
\text{Order 1} & \left\{ \begin{array}{l} -\nabla p_1 + \mathbf{j}_1 \times \mathbf{B}_0 = \mathbf{0} \\ -\nabla \phi_0 + \mathbf{v}_0 \times \mathbf{B}_0 = \eta_c \mathbf{j}_1 \end{array} \right. \\
\text{Order 2} & \left\{ \begin{array}{l} -\nabla p_2 + \mathbf{j}_2 \times \mathbf{B}_0 = (\mathbf{v}_0 \cdot \nabla) \mathbf{v}_0 - \mathbf{j}_1 \times \mathbf{B}_1 \\ -\nabla \phi_1 + \mathbf{v}_1 \times \mathbf{B}_0 = \eta_c \mathbf{j}_2 - \mathbf{v}_0 \times \mathbf{B}_1 \end{array} \right. \\
\text{Order 3} & \left\{ \begin{array}{l} -\nabla p_3 + \mathbf{j}_3 \times \mathbf{B}_0 = ((\mathbf{v}_0 \cdot \nabla) \mathbf{v}_1 + (\mathbf{v}_1 \cdot \nabla) \mathbf{v}_0) - (\mathbf{j}_1 \times \mathbf{B}_2 + \mathbf{j}_2 \times \mathbf{B}_1) \\ -\nabla \phi_2 + \mathbf{v}_2 \times \mathbf{B}_0 = \eta_c \mathbf{j}_3 - (\mathbf{v}_0 \times \mathbf{B}_2 + \mathbf{v}_1 \times \mathbf{B}_1) \end{array} \right. \\
& \vdots \\
\text{Order } n & \left\{ \begin{array}{l} -\nabla p_n + \mathbf{j}_n \times \mathbf{B}_0 = \sum_{i=0}^{n-2} (\mathbf{v}_i \cdot \nabla) \mathbf{v}_{n-(i+2)} - \sum_{k=1}^{n-1} \mathbf{j}_k \times \mathbf{B}_{n-k} = \mathbf{Q}_{n-1} \\ -\nabla \phi_{n-1} + \mathbf{v}_{n-1} \times \mathbf{B}_0 = \eta_c \mathbf{j}_n - \sum_{k=1}^{n-1} \mathbf{v}_{k-1} \times \mathbf{B}_{n-k} = \mathbf{R}_n \end{array} \right. , \quad n \geq 4
\end{aligned}$$

We should notice that at any given order n , there is a coupling between Ohm's law and the equation of motion through \mathbf{j}_n . So, in general at the n -th order, we will first need to solve the equation of motion for p_n and \mathbf{j}_n and then substitute \mathbf{j}_n into Ohm's law and solve for ϕ_{n-1} and \mathbf{v}_{n-1} . It can also be easily seen that taking p_0 to be constant, say $p_0 = p_{00}$ satisfies the equation of motion

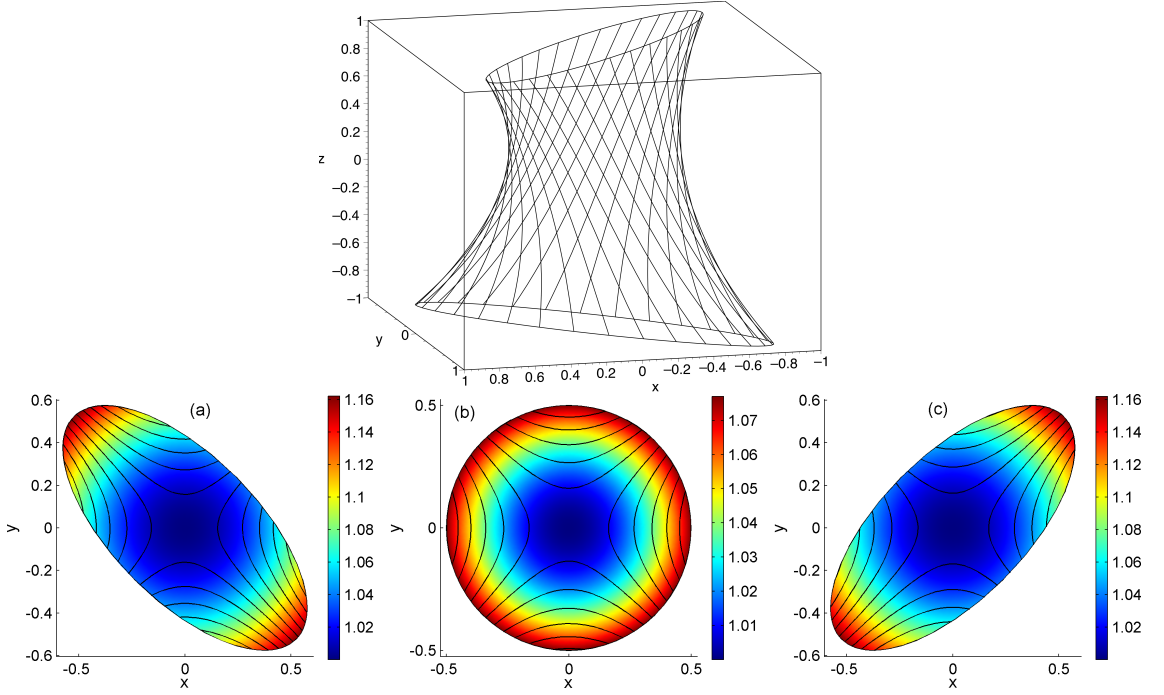


Figure 3.1: Field lines illustrating the structure of \mathbf{B}_0 in 3D (HFT) (top) and their projection in 2D at (a) $z = -0.5$, (b) $z = 0$ and (c) $z = 0.5$ inside the HFT (bottom), with the background colour representing its strength.

at zeroth order, since $\mathbf{j}_0 = \mathbf{0}$ and that the lowest-order magnetic field, \mathbf{B}_0 , is potential, since $\nabla \times \mathbf{B}_0 = \mathbf{j}_0 = \mathbf{0}$. So, it is not really necessary to assume that the zeroth-order current, \mathbf{j}_0 , is zero or that the lowest-order magnetic field, \mathbf{B}_0 , is potential as in Wilmot-Smith et al. (2006, 2009). It rather comes directly as a property of this expansion scheme. One suitable choice of \mathbf{B}_0 , as in Wilmot-Smith et al. (2006, 2009), which allows for analytical solutions, is

$$\mathbf{B}_0 = b_0(ky, kx, 1), \quad (3.13)$$

where $k > 0$. This magnetic field, which clearly satisfies the solenoidal constraint (3.10), was used as an example for a “hyperbolic flux tube” (HFT) by Titov et al. (2002). The basic state is an X-type current-free equilibrium in the xy plane, superimposed on a uniform field in the z -direction. An illustration of such a field in 2D and 3D is shown in Fig. (3.1).

The equations, $\mathbf{X}(\mathbf{x}_0, s)$, of the field line passing through a point \mathbf{x}_0 can be then obtained by solving

$$\frac{\partial \mathbf{X}(s)}{\partial s} = \mathbf{B}_0(\mathbf{X}(s)),$$

where the parameter s is related to the distance l along the field line by

$$ds = \frac{dl}{\|\mathbf{B}_0\|}.$$

The components of $\mathbf{X}(\mathbf{x}_0, s)$ and its inverse mapping $\mathbf{X}_0(\mathbf{x}, s)$ are then given by

$$\begin{aligned} X &= x_0 \cosh(b_0 k s) + y_0 \sinh(b_0 k s), \\ Y &= y_0 \cosh(b_0 k s) + x_0 \sinh(b_0 k s), \\ Z &= b_0 s + z_0, \\ X_0 &= x \cosh(b_0 k s) - y \sinh(b_0 k s), \\ Y_0 &= y \cosh(b_0 k s) - x \sinh(b_0 k s), \\ Z_0 &= -b_0 s + z. \end{aligned}$$

3.3 General Method of Integration

One can easily see that, at any given order, Ohm's law and the equation of motion have the same structure, namely

$$-\nabla F + \mathbf{G} \times \mathbf{B}_0 = \mathbf{H}. \quad (3.14)$$

Taking the dot product of (3.14) with \mathbf{B}_0 , we get

$$\begin{aligned} -\nabla F \cdot \mathbf{B}_0 &= \mathbf{H} \cdot \mathbf{B}_0 \\ \Rightarrow -\frac{\partial F}{\partial s} &= \mathbf{H} \cdot \mathbf{B}_0 \\ \Rightarrow F &= -\int \mathbf{H} \cdot \mathbf{B}_0 ds + F_0(x_0, y_0), \end{aligned}$$

while taking the cross product of (3.14) with \mathbf{B}_0 leads to

$$\begin{aligned} -(\nabla F \times \mathbf{B}_0) - \mathbf{G}_\perp \|\mathbf{B}_0\|^2 &= \mathbf{H} \times \mathbf{B}_0 \\ \Rightarrow \mathbf{G}_\perp &= -\frac{(\nabla F + \mathbf{H}) \times \mathbf{B}_0}{\|\mathbf{B}_0\|^2} \\ \Rightarrow \mathbf{G} &= \mathbf{G}_\perp - \alpha \mathbf{B}_0, \end{aligned}$$

where α is used to ensure that \mathbf{G} is divergence free. Hence,

$$\alpha = \int \nabla \cdot \mathbf{G}_\perp ds + \alpha_0(x_0, y_0).$$

Here, $F_0(x_0, y_0)$ and $\alpha_0(x_0, y_0)$ are free functions resulting from the starting plane of integration which can be used to match boundary conditions. Thus, solving the equation of motion at the n -th

order

$$-\nabla p_n + \mathbf{j}_n \times \mathbf{B}_0 = \mathbf{Q}_{n-1}$$

for p_n and \mathbf{j}_n , we get

$$p_n(x_0, y_0, s) = - \int \mathbf{Q}_{n-1} \cdot \mathbf{B}_0 ds + p_{n0}(x_0, y_0),$$

$$\mathbf{j}_n = \mathbf{j}_{n\perp} - \lambda_n \mathbf{B}_0,$$

where,

$$\mathbf{j}_{n\perp} = \frac{(-\nabla p_n - \mathbf{Q}_{n-1}) \times \mathbf{B}_0}{\|\mathbf{B}_0\|^2},$$

$$\lambda_n = \int \nabla \cdot \mathbf{j}_{n\perp} ds + \lambda_{n0}(x_0, y_0).$$

Similarly, solving Ohm's law at the same order

$$-\nabla \phi_{n-1} + \mathbf{v}_{n-1} \times \mathbf{B}_0 = \mathbf{R}_n$$

for ϕ_{n-1} and \mathbf{v}_{n-1} gives

$$\phi_{n-1}(x_0, y_0, s) = - \int \mathbf{R}_n \cdot \mathbf{B}_0 ds + \phi_{n-1,0}(x_0, y_0),$$

$$\mathbf{v}_{n-1} = \mathbf{v}_{n-1,\perp} - \mu_{n-1} \mathbf{B}_0,$$

where,

$$\mathbf{v}_{n-1,\perp} = \frac{(-\nabla \phi_{n-1} - \mathbf{R}_n) \times \mathbf{B}_0}{\|\mathbf{B}_0\|^2},$$

$$\mu_{n-1} = \int \nabla \cdot \mathbf{v}_{n-1,\perp} ds + \mu_{n-1,0}(x_0, y_0).$$

These integrals are evaluated analytically for the first few orders, whereas higher order solutions require numerical integration, which is carried out in MATLAB along 146740 field lines of \mathbf{B}_0 . The required gradients are then calculated using the FastRBFTM Interpolation Toolbox (see Appendix C for more details).

Unlike standard approaches where one looks for solutions by prescribing boundary conditions on a given domain which in most cases have an impact on the structure of the reconnection region, this approach allows us to rather prescribe certain properties of the solutions, such as stagnation flows, through the freedom of choosing the low-order quantities (\mathbf{B}_0 , ϕ_0 , p_0 etc) and the free functions p_{n0} , ϕ_{n0} , λ_{n0} and μ_{n0} . Therefore, it is not surprising that by using this approach one can obtain a variety of solutions and could hopefully control the convergence of the expansion

scheme.

We are only left with finding \mathbf{B}_n which can be obtained by solving Ampere's law at the n -th order, namely

$$\nabla \times \mathbf{B}_n = \mathbf{j}_n, \quad (3.15)$$

which is solved numerically using COMSOL Multiphysics 3.3a with MATLAB, a numerical software package that implements finite element analysis to solve partial differential equations for various physics and engineering applications. Equation (3.15) is solved in a hyperbolic domain, namely, the HFT shown in Fig. (3.1), together with the following boundary condition:

$$\mathbf{n} \cdot \mathbf{B}_n = 0,$$

and a mesh size of 146740 elements (see Appendix C for more details). Here \mathbf{n} is a normal vector.

3.4 Solutions

3.4.1 Analytical Solutions

Since our present work, as a first attempt, builds on the work done by Wilmot-Smith et al. (2006, 2009), we shall consider the same assumptions they have used. A more general approach will be left for future work. One of these assumptions is to set $\mathbf{B}_1 = 0$, and hence $\mathbf{j}_1 = 0$. This assumption has been used by Wilmot-Smith et al. (2006, 2009), to allow for a direct comparison between their solutions and the ones in Hornig and Priest (2003), since it reduces Ohm's law at first order to an ideal equation, whereas Ohm's law at second order remains non-ideal as shown below. With this assumption, the equation of motion at first order reduces to $\nabla p_1 = \mathbf{0}$, and hence is satisfied by taking p_1 to be constant, say $p_1 = p_{10}$, and Ohm's law at the same order becomes

$$-\nabla \phi_0 + \mathbf{v}_0 \times \mathbf{B}_0 = \mathbf{0}. \quad (3.16)$$

Using the general method of integration discussed in the previous section, we have

$$\phi_0 = \phi_0(x_0, y_0).$$

One obvious choice, related to reconnection, is to start with a stagnation flow at the zeroth order. For this purpose, we choose ϕ_0 to be

$$\phi_0 = \frac{\varphi_0}{\Lambda^2} x_0 y_0.$$

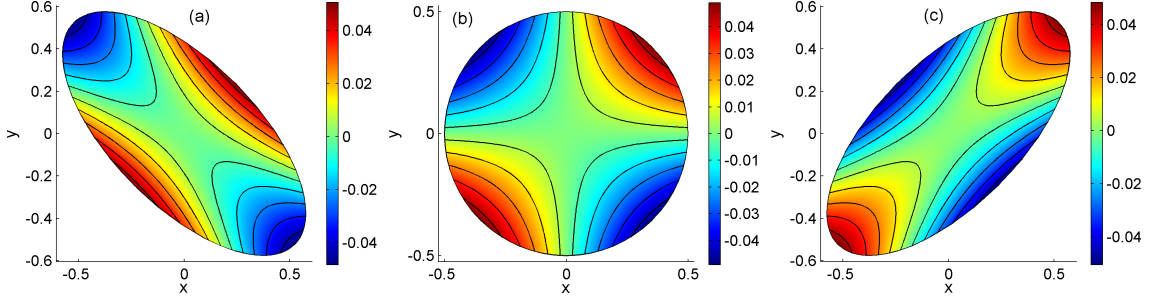


Figure 3.2: Contour plots of the electric potential ϕ_0 at (a) $z = -0.5$, (b) $z = 0$ and (c) $z = 0.5$.

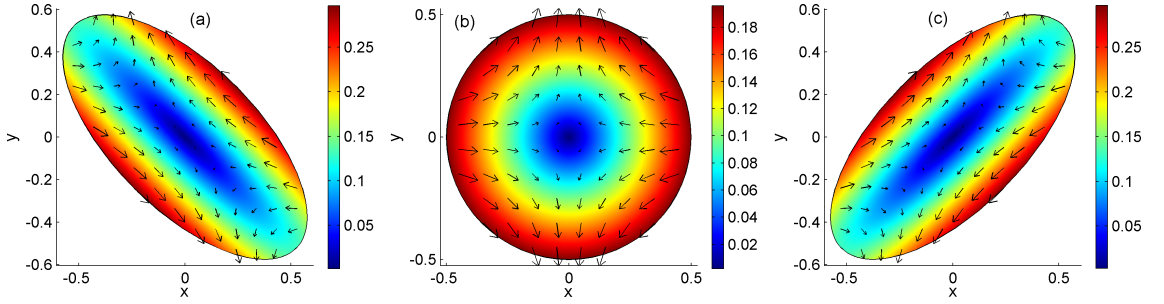


Figure 3.3: Strength and direction of the velocity field \mathbf{v}_0 for the case of $\mu_0 = 0$ at (a) $z = -0.5$, (b) $z = 0$ and (c) $z = 0.5$.

Setting $Z_0 = 0$ and using the inverse field line mappings to express ϕ_0 in terms of x , y , and z gives

$$\phi_0(x, y, z) = \frac{\varphi_0}{2\Lambda^2} (2xy \cosh(2kz) - (x^2 + y^2) \sinh(2kz)) \quad (3.17)$$

Contours of ϕ_0 , which are streamlines for \mathbf{v}_0 , are shown in Fig. (3.2).

The components of \mathbf{v}_0 perpendicular and parallel to \mathbf{B}_0 are then given by

$$\begin{aligned} \mathbf{v}_{0\perp} &= -\frac{\nabla\phi_0 \times \mathbf{B}_0}{\|\mathbf{B}_0\|^2}, \\ \mathbf{v}_{0\parallel} &= \left(\mu_0(x_0, y_0) - \frac{\varphi_0(x^2 - y^2) \sinh(2kz)}{\Lambda^2 \|\mathbf{B}_0\|^2} \right) \mathbf{B}_0, \end{aligned}$$

which are combined to give

$$\begin{aligned} \mathbf{v}_0 &= \left(\frac{\varphi_0}{\Lambda^2 b_0} (y \sinh(2kz) - x \cosh(2kz)) + kb_0 y \mu_0 \right) \hat{\mathbf{x}} \\ &+ \left(\frac{\varphi_0}{\Lambda^2 b_0} (y \cosh(2kz) - x \sinh(2kz)) + kb_0 x \mu_0 \right) \hat{\mathbf{y}} \\ &+ b_0 \mu_0 \hat{\mathbf{z}}. \end{aligned} \quad (3.18)$$

Setting $\mu_0 = 0$, this velocity reduces to the one obtained by Wilmot-Smith et al. (2009), which

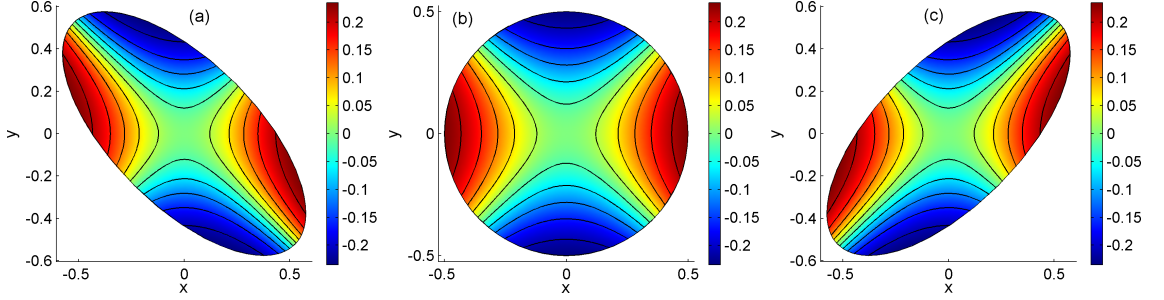


Figure 3.4: Contour plots of the pressure p_2 variation for the choice of $p_{20} = -\frac{\lambda^2 k j_{20} b_0}{2} \tanh\left(\frac{x^2 - y^2}{\lambda^2}\right)$ at (a) $z = -0.5$, (b) $z = 0$ and (c) $z = 0.5$.

represents a stagnation flow as shown in Fig. (3.3) and as expected.

The equations at second order become

$$-\nabla p_2 + \mathbf{j}_2 \times \mathbf{B}_0 = (\mathbf{v}_0 \cdot \nabla) \mathbf{v}_0, \quad (3.19)$$

$$-\nabla \phi_1 + \mathbf{v}_1 \times \mathbf{B}_0 = \eta_c \mathbf{j}_2. \quad (3.20)$$

Again, using the general method of integration, we get

$$p_2 = p_{20}(x_0, y_0) - \frac{\varphi_0^2}{2\Lambda^4 b_0^2} (x^2 + y^2),$$

$$\mathbf{j}_{2\perp} = -\frac{(\nabla p_2 + (\mathbf{v}_0 \cdot \nabla) \mathbf{v}_0) \times \mathbf{B}_0}{\|\mathbf{B}_0\|^2} = -\frac{\nabla p_{20} \times \mathbf{B}_0}{\|\mathbf{B}_0\|^2},$$

$$\mathbf{j}_{2\parallel} = \left(\lambda_{20} - \frac{k(2C1 \cosh(kz) + k^2(x^2 - y^2)(C2 \cosh(kz) - C3 \sinh(kz)) \sinh(2kz))}{(k^2(x^2 + y^2) \cosh(2kz) - 2k^2 xy \sinh(2kz) - 1) \|\mathbf{B}_0\|^2} \right) \mathbf{B}_0,$$

where

$$C1 = x \frac{\partial p_{20}}{\partial x_0} - y \frac{\partial p_{20}}{\partial y_0},$$

$$C2 = y \frac{\partial p_{20}}{\partial x_0} + x \frac{\partial p_{20}}{\partial y_0},$$

$$C3 = x \frac{\partial p_{20}}{\partial x_0} + y \frac{\partial p_{20}}{\partial y_0}.$$

For the following choice of p_{20} :

$$p_{20}(x_0, y_0) = f(x_0^2 - y_0^2) = f(x^2 - y^2),$$

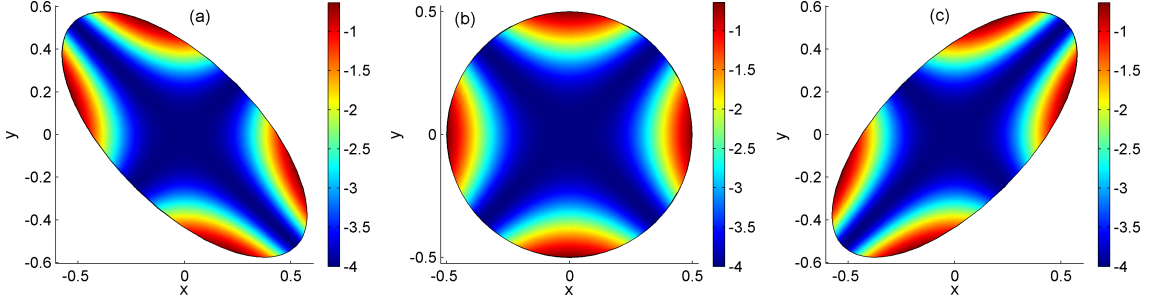


Figure 3.5: Illustration of the current $j_{2z} = \frac{j_{20}}{\cosh^2\left(\frac{x^2-y^2}{\lambda^2}\right)}$ at (a) $z = -0.5$, (b) $z = 0$ and (c) $z = 0.5$.

the component of \mathbf{j}_2 parallel to \mathbf{B}_0 becomes

$$\mathbf{j}_{2\parallel} = \left(\lambda_{20}(x_0, y_0) - \frac{2f'(x^2 - y^2)}{k \|\mathbf{B}_0\|^2} \right) \mathbf{B}_0,$$

and hence the current at second order is given by

$$\mathbf{j}_2 = kb_0\lambda_{20}(y\hat{x} + x\hat{y}) + \left(b_0\lambda_{20} - \frac{2f'(x^2 - y^2)}{b_0k} \right) \hat{z}. \quad (3.21)$$

The solutions used by Wilmot-Smith et al. (2009) for p_2 and j_2 can be obtained here by taking

$$\begin{aligned} f(x^2 - y^2) &= p_{200} - \frac{\lambda^2 k j_{20} b_0}{2} \tanh\left(\frac{x^2 - y^2}{\lambda^2}\right), \\ \lambda_{20} &= 0, \end{aligned} \quad (3.22)$$

where, p_{200} and j_{20} are constants. The resultant solutions are illustrated in Figs. (3.4) and (3.5).

Now for Eq. (3.20), we seek solutions such that the non-ideal term $\eta_c \mathbf{j}_2$ is localized. This localization can be achieved through a localization in three dimensions of either the resistivity η_c or the current \mathbf{j}_2 or through a localization of both terms. Keeping the current \mathbf{j}_2 , given by Eq. (3.21), arbitrary, we have to localize the resistivity η_c . This can be achieved by prescribing a localized form for $\mathbf{E}_1 \cdot \mathbf{B}_0$, such as

$$\mathbf{E}_1 \cdot \mathbf{B}_0 = e_{10} b_0 \exp\left(-\frac{b_0^2 s^2}{L^2} - \frac{x_0^2 + y_0^2}{l^2}\right), \quad (3.23)$$

where $l, L > 0$. Physically one could think of this as an anomalous resistivity caused by a micro-instability which is localized in a current sheet. We can then determine η_c by taking the scalar product of Eq. (3.20) with \mathbf{B}_0 . Hence, we have

$$\eta_c = \frac{-\nabla\phi_1 \cdot \mathbf{B}_0}{\mathbf{j}_2 \cdot \mathbf{B}_0} = \frac{\mathbf{E}_1 \cdot \mathbf{B}_0}{\mathbf{j}_2 \cdot \mathbf{B}_0},$$

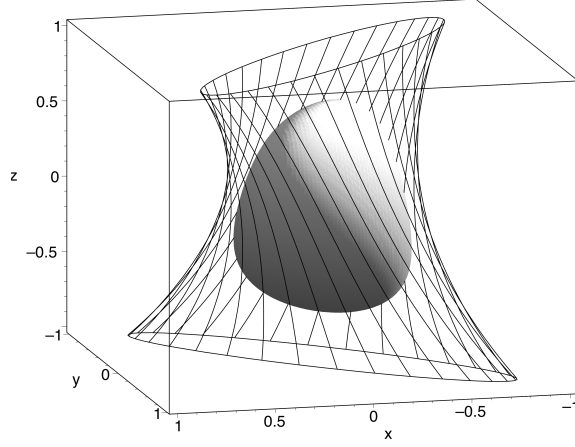


Figure 3.6: The non-ideal region at $\|\eta_c \mathbf{j}_2\| = 0.05 \|\eta_c \mathbf{j}_2\|_{\max}$ enclosed in the HFT, with $\lambda_{20} = 0$.

which, on substituting for $\mathbf{E}_1 \cdot \mathbf{B}_0$, setting $Z_0 = 0$, and using the inverse field line mappings, can be written in terms of x , y , and z . Thus, defining

$$\gamma^2 = (x^2 + y^2) \cosh(2kz) - 2xy \sinh(2kz),$$

we have

$$\eta_c = \frac{kb_0 e_{10} \exp\left(-\frac{z^2}{L^2} - \frac{\gamma^2}{l^2}\right)}{k\lambda_{20} \|\mathbf{B}_0\|^2 - 2f'(x^2 - y^2)}. \quad (3.24)$$

Progress now depends on the choice of the free functions f or λ_{20} . For simplicity and to allow for more analytic solutions, we shall set λ_{20} to zero. An example of the resultant non-ideal region, which is now independent of the choice of f , is shown in Fig. (3.6). Substituting for η_c and \mathbf{j}_2 into Eq. (3.20) and using the general method of integration to solve for ϕ_1 , we get

$$\phi_1 = \phi_{10}(x_0, y_0) - \frac{\sqrt{\pi}}{2} L e_{10} \exp\left(-\frac{\gamma^2}{l^2}\right) \operatorname{erf}\left(\frac{z}{L}\right). \quad (3.25)$$

The freedom of choosing $\phi_{10}(x_0, y_0)$ allows us to superimpose an ideal plasma flow on the solution of the first-order velocity \mathbf{v}_1 , since the corresponding Ohm's law, Eq. (3.20), can be decomposed into ideal and non-ideal parts as follow:

$$\begin{aligned} -\nabla\phi_{id} + \mathbf{v}_{id} \times \mathbf{B}_0 &= \mathbf{0}, \\ -\nabla\phi_{nonid} + \mathbf{v}_{nonid} \times \mathbf{B}_0 &= \eta_c \mathbf{j}_2, \end{aligned}$$

with $\phi_{id} = \phi_{10}(x_0, y_0)$. Hence, it is again not necessary to assume that $\mathbf{B}_1 = \mathbf{0}$, as in Wilmot-Smith et al. (2006, 2009), in order to decompose Ohm's law into ideal and non-ideal equations. In general, this decomposition of Ohm's law is valid at any order n , since we always have the freedom of including an ideal electric potential $\phi_{n-1,0}$, the source of an ideal plasma flow, as

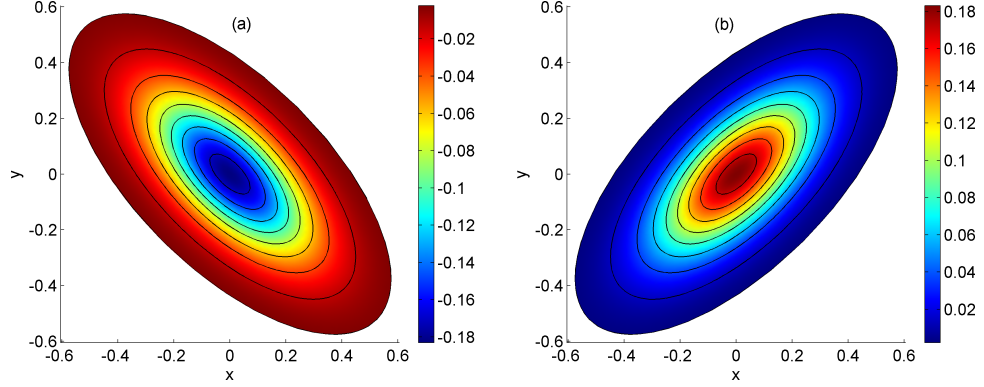


Figure 3.7: Contour plots of the electric potential ϕ_1 , with $\phi_{10}(x_0, y_0) = 0$, at (a) $z = -0.5$ and (b) $z = 0.5$, where ϕ_1 vanishes at the $z = 0$ plane.

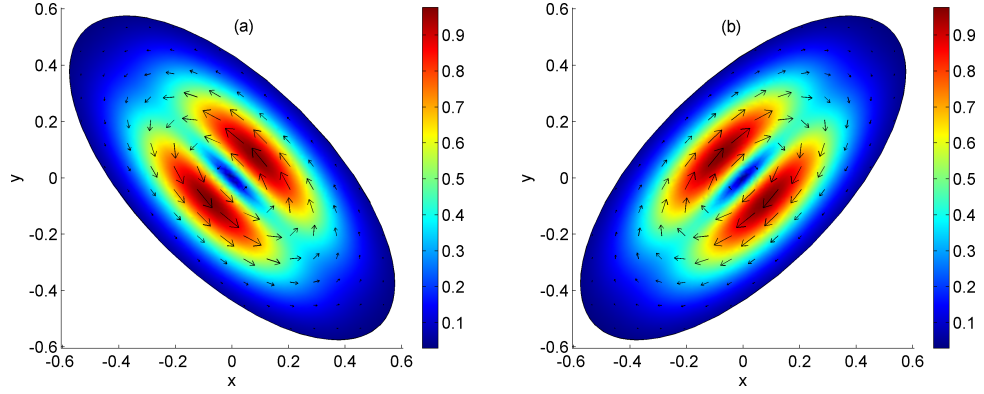


Figure 3.8: Strength and direction of the velocity field \mathbf{v}_1 for the case of $\mu_{10} = 0$ at (a) $z = -0.5$ and (b) $z = 0.5$. The velocity field \mathbf{v}_1 vanishes at $z = 0$ for this case.

shown in Section 3.3. But, since we have already started with an ideal flow at zeroth order, we shall consider $\phi_{10}(x_0, y_0) = 0$. With this choice, Eq. (3.25) reduces to the one obtained by Wilmot-Smith et al. (2006). Contours of the resultant ϕ_1 , which are streamlines for \mathbf{v}_1 , are shown in Fig. (3.7). The corresponding plasma velocity at first order is then given by

$$\begin{aligned} \mathbf{v}_1 = & \left(\frac{2\phi_{11}}{b_0 l^2} (y \cosh(2kz) - x \sinh(2kz)) + kb_0 y \mu_{10} \right) \hat{\mathbf{x}} \\ & + \left(\frac{2\phi_{11}}{b_0 l^2} (y \sinh(2kz) - x \cosh(2kz)) + kb_0 x \mu_{10} \right) \hat{\mathbf{y}} \\ & + b_0 \mu_{10} \hat{\mathbf{z}}, \end{aligned} \quad (3.26)$$

where

$$\phi_{11} = -\frac{\sqrt{\pi}}{2} L e_{10} \exp\left(-\frac{\gamma^2}{l^2}\right) \operatorname{erf}\left(\frac{z}{L}\right). \quad (3.27)$$

Again the first-order velocity obtained by Wilmot-Smith et al. (2006) can be recovered here by

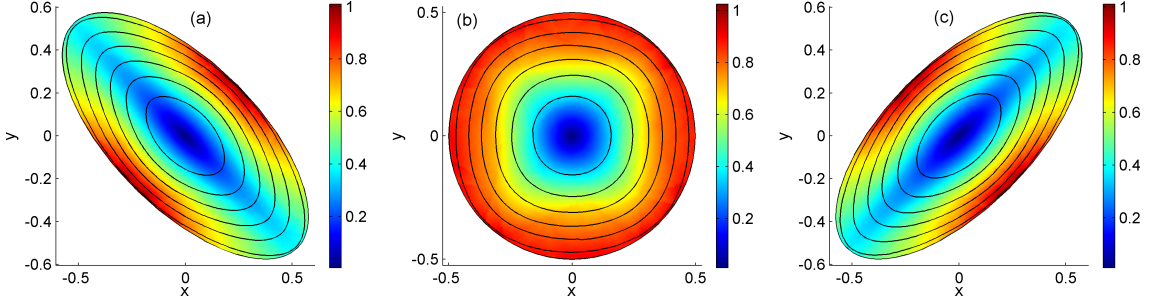


Figure 3.9: Projection of field lines and magnitude of the magnetic field \mathbf{B}_2 at (a) $z = -0.5$, (b) $z = 0$ and (c) $z = 0.5$.

taking μ_{10} to be zero. The velocity \mathbf{v}_1 , which represents the lowest order effect of reconnection on the ideal flow \mathbf{v}_0 , represents a counter-rotational flow above and below the $z = 0$ plane, where it vanishes. In Hornig and Priest (2003) the existence of such a flow has been demonstrated analytically and was later found in numerical simulations as well (see, e.g, Pontin et al. 2005). An illustration of such a flow is shown in Fig. (3.8).

Solutions to equations at higher orders require numerical integration. Hence, we will solve some of them numerically in the following section using the general method of integration discussed in Section 3.3. Higher order numerical solutions will be calculated using particular analytical solutions obtained by choosing $f(x^2 - y^2)$ and λ_{20} to be given by (3.22) and setting μ_0 and μ_{10} to zero. These particular solutions, which will be also used to calculate approximations of the total solutions in Section 3.4.3, can be summarized as follow:

$$\begin{aligned}
 p_0 &= p_{00}, & p_1 &= p_{10}, & p_2 &= p_{200} - \frac{\lambda^2 k j_{20} b_0}{2} \tanh\left(\frac{x^2 - y^2}{\lambda^2}\right) - \frac{\varphi_0^2}{2\Lambda^4 b_0^2} (x^2 + y^2), \\
 \mathbf{j}_0 &= \mathbf{j}_1 = \mathbf{0}, & \mathbf{j}_2 &= \frac{j_{20}}{\cosh^2\left(\frac{x^2 - y^2}{\lambda^2}\right)} \hat{\mathbf{z}}, \\
 \phi_0 &= \frac{\varphi_0}{2\Lambda^2} (2xy \cosh(2kz) - (x^2 + y^2) \sinh(2kz)), \\
 \phi_1 &= -\frac{\sqrt{\pi}}{2} L e_{10} \exp\left(-\frac{\gamma^2}{l^2}\right) \operatorname{erf}\left(\frac{z}{L}\right), \\
 \mathbf{v}_0 &= \frac{\varphi_0}{b_0 \Lambda^2} ((y \sinh(2kz) - x \cosh(2kz)) \hat{\mathbf{x}} + (y \cosh(2kz) - x \sinh(2kz)) \hat{\mathbf{y}}), \\
 \mathbf{v}_1 &= \frac{2\phi_1}{b_0 l^2} ((y \cosh(2kz) - x \sinh(2kz)) \hat{\mathbf{x}} + (y \sinh(2kz) - x \cosh(2kz)) \hat{\mathbf{y}}),
 \end{aligned}$$

with the resistivity η_c given by

$$\eta_c = \frac{e_{10}}{j_{20}} \exp\left(-\frac{z^2}{L^2} - \frac{\gamma^2}{l^2}\right) \cosh^2\left(\frac{x^2 - y^2}{\lambda^2}\right). \quad (3.28)$$

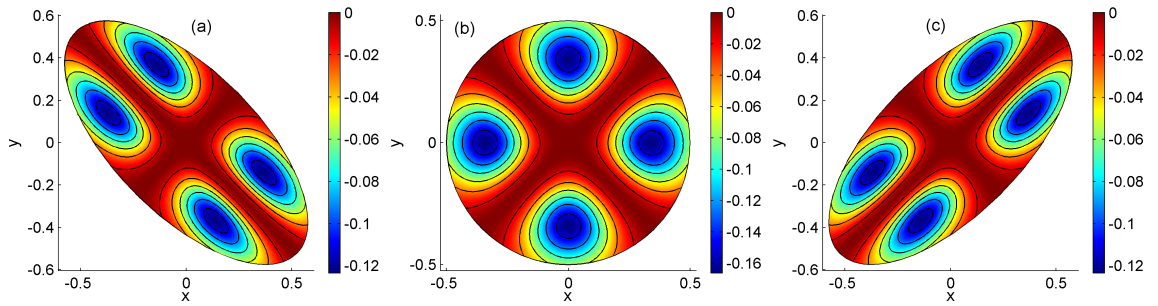


Figure 3.10: Contour plots of the pressure p_3 at (a) $z = -0.5$, (b) $z = 0$ and (c) $z = 0.5$.

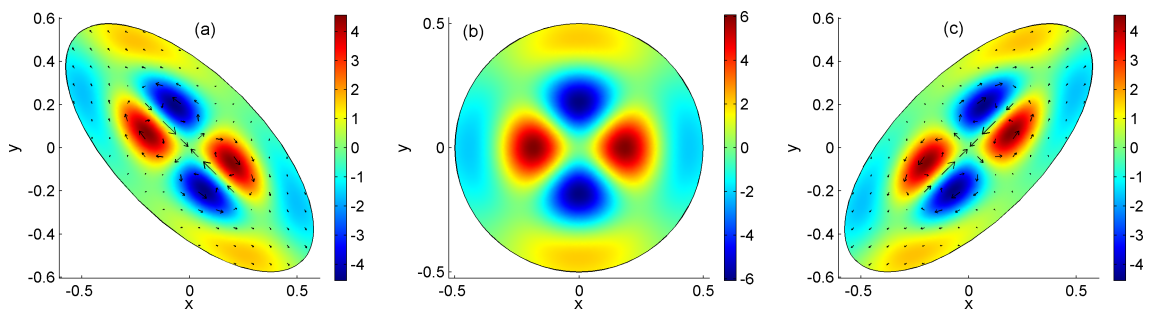


Figure 3.11: Illustration of the current j_{3z} at (a) $z = -0.5$, (b) $z = 0$ and (c) $z = 0.5$, with the arrows representing the direction of \mathbf{v}_2 , which vanishes at $z = 0$.

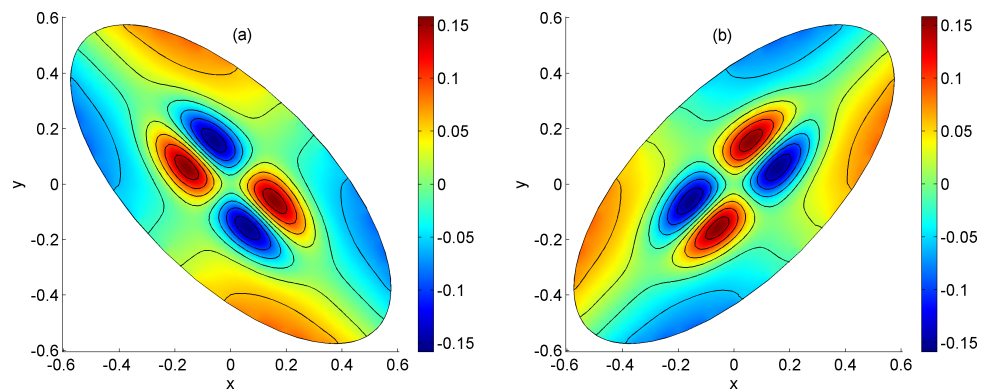


Figure 3.12: Contour plots of the electric potential ϕ_2 at (a) $z = -0.5$ and (b) $z = 0.5$. Here, we have $\phi_2 = 0$ at $z = 0$.

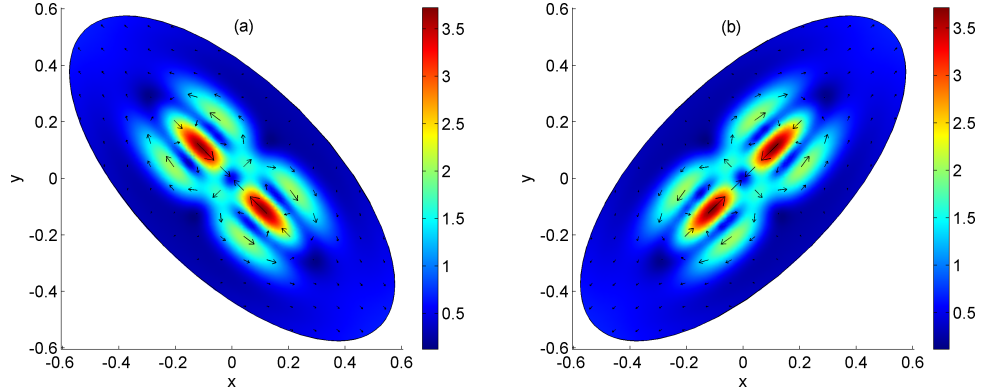


Figure 3.13: Strength and direction of the velocity \mathbf{v}_2 , at (a) $z = -0.5$ and (b) $z = 0.5$, where \mathbf{v}_2 vanishes at the $z = 0$ plane.

3.4.2 Numerical Solutions

Based on the particular solutions listed at the end of the previous section and using the general method of integration discussed in Section 3.3, we present numerical solutions to Ampere's law at second order and equations at third order. We start by solving the following Ampere's law:

$$\begin{aligned}\nabla \times \mathbf{B}_2 &= \mathbf{j}_2, \\ \mathbf{n} \cdot \mathbf{B}_2 &= 0,\end{aligned}$$

for \mathbf{B}_2 . The resulting magnetic field \mathbf{B}_2 has closed field lines as shown in Fig. (3.9). At third order, we have

$$-\nabla p_3 + \mathbf{j}_3 \times \mathbf{B}_0 = (\mathbf{v}_0 \cdot \nabla) \mathbf{v}_1 + (\mathbf{v}_1 \cdot \nabla) \mathbf{v}_0, \quad (3.29)$$

$$-\nabla \phi_2 + \mathbf{v}_2 \times \mathbf{B}_0 = \eta_c \mathbf{j}_3 - (\mathbf{v}_0 \times \mathbf{B}_2), \quad (3.30)$$

which are coupled by \mathbf{j}_3 . So, we will first solve Eq. (3.29) for p_3 and \mathbf{j}_3 . Then, substitute for \mathbf{j}_3 into Eq. (3.30) and solve for ϕ_2 and \mathbf{v}_2 . Solutions to these equations are illustrated in Figs. (3.10) - (3.13). Figure (3.10) shows four regions with the same pressure concentration both above and below the plane $z = 0$, where they have their maximum absolute value. This is due to the appearance of the two inertial terms in the right-hand side of Eq. (3.29), specially the term including gradients of the components of \mathbf{v}_1 which is related to the localization of the non-ideal region. The effect of these terms, or more specifically the effect of the localization of the non-ideal region, also appears in \mathbf{j}_3 , whose structure is dominated by its z -component, j_{3z} , which involves higher order gradients of \mathbf{v}_1 components. An illustration of the structure of j_{3z} is shown in Fig. (3.11), where we have four regions of strong current concentration, two positive and two negative, both above and below the plane $z = 0$, where they have their maximum value too.

There are also weaker current concentrations, at the same locations where we have the pressure concentrations, due to pressure gradients. The arrows, shown in Fig. (3.11), indicate the direction of the velocity \mathbf{v}_2 , which show that rotational flows are present around those regions of strong current concentration. A stagnation flow is also present at the centre away from the $z = 0$ plane, where \mathbf{v}_2 vanishes. In Fig. (3.12), contours of ϕ_2 , which represent a projection of the streamlines of \mathbf{v}_2 , are shown. They confirm the presence of rotational flows around regions of strong current concentration. The background plot in Fig. (3.12) represents the structure of ϕ_2 , in which the four regions of strong concentration appears again, but with opposite signs to the ones in the profile of j_{3z} , since they results from the integration of the resistive term, $(-\eta\mathbf{j}_3)$. We also see four other regions of strong ϕ_2 concentration towards the boundary as a result of integrating the advection term, $\mathbf{v}_0 \times \mathbf{B}_2$. The strength and direction of the velocity \mathbf{v}_2 are illustrated in Fig. (3.13). Finally,

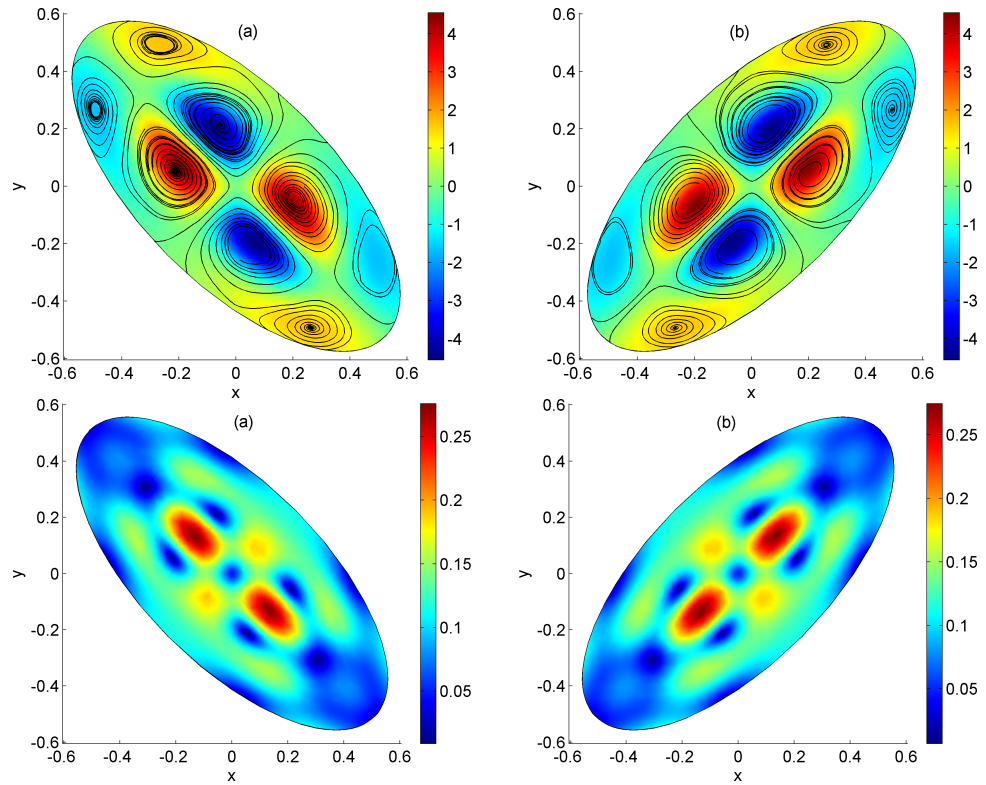


Figure 3.14: Projection of field lines of the magnetic field \mathbf{B}_3 where the background color indicates the magnitude of the current j_{3z} (top) and the strength of \mathbf{B}_3 (bottom) at (a) $z = -0.5$ and (b) $z = 0.5$.

we solve Ampere's law at third order:

$$\begin{aligned}\nabla \times \mathbf{B}_3 &= \mathbf{j}_3, \\ \mathbf{n} \cdot \mathbf{B}_3 &= 0,\end{aligned}$$

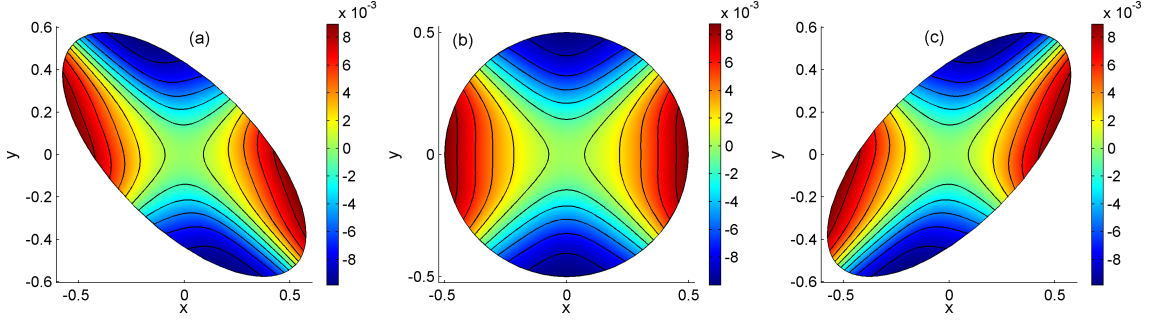


Figure 3.15: Contour plots of the pressure $p = M_A^2 p_2 + M_A^3 p_3$ variation at (a) $z = -0.5$, (b) $z = 0$ and (c) $z = 0.5$.

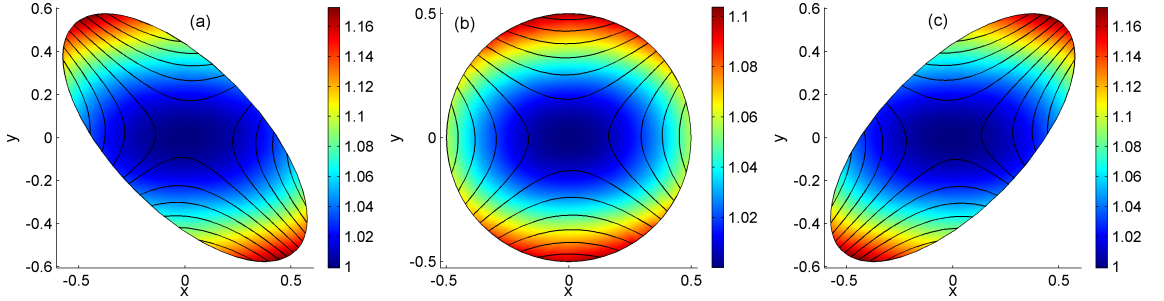


Figure 3.16: Projection of field lines of the magnetic field $\mathbf{B} = \mathbf{B}_0 + M_A^2 \mathbf{B}_2 + M_A^3 \mathbf{B}_3$ at (a) $z = -0.5$, (b) $z = 0$ and (c) $z = 0.5$, where the background colour represents its strength.

for \mathbf{B}_3 . An illustration of field lines of the resulting magnetic field \mathbf{B}_3 is shown in Fig. (3.14), where the background plot in the top panels indicates j_{3z} profile.

3.4.3 Total Solution Approximation

Now, we shall combine the obtained analytical and numerical solutions of equations at different orders of M_A to calculate an approximation of the total solution for each variable using $M_A = 0.2$. For the case of $M_A = 0.1$, it is very hard to see the contribution of higher order terms, if any, since the solutions are dominated by the lowest order terms. The total pressure approximation, $p = p_0 + M_A p_1 + M_A^2 p_2 + M_A^3 p_3 + \mathcal{O}(M_A^4)$ is shown in Fig. (3.15), which shows that the third order pressure contribution $M_A^3 p_3$ is small compared with the second order pressure contribution $M_A^2 p_2$ which gives an indication of the convergence of the scheme for the pressure p , and we still have the freedom of adding the constant pressures p_0 and p_1 . Figure (3.16) illustrates some field lines of the total magnetic field approximation, $\mathbf{B} = \mathbf{B}_0 + M_A^2 \mathbf{B}_2 + M_A^3 \mathbf{B}_3 + \mathcal{O}(M_A^4)$, at three different planes. The field is still dominated by the zeroth-order contribution \mathbf{B}_0 which indicates that the expansion may converge quickly for the magnetic field \mathbf{B} , provided that we can use the free parameters of the scheme to make higher terms small. The z -component of the approximated

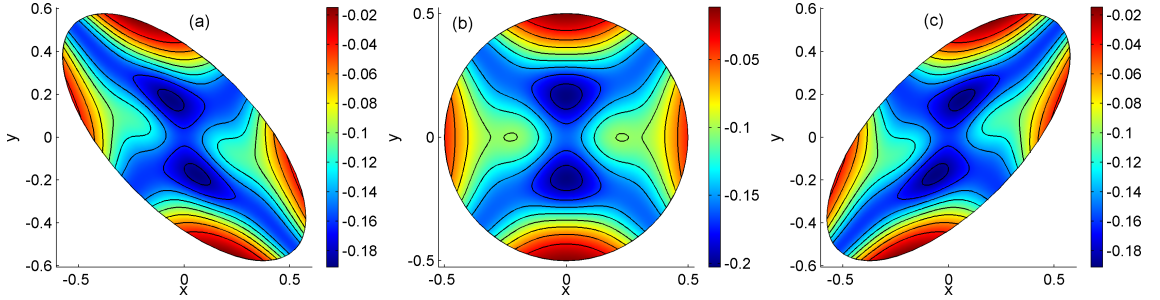


Figure 3.17: Illustration of the current $j_z = M_A^2 j_{2z} + M_A^3 j_{3z}$ at (a) $z = -0.5$, (b) $z = 0$ and (c) $z = 0.5$.

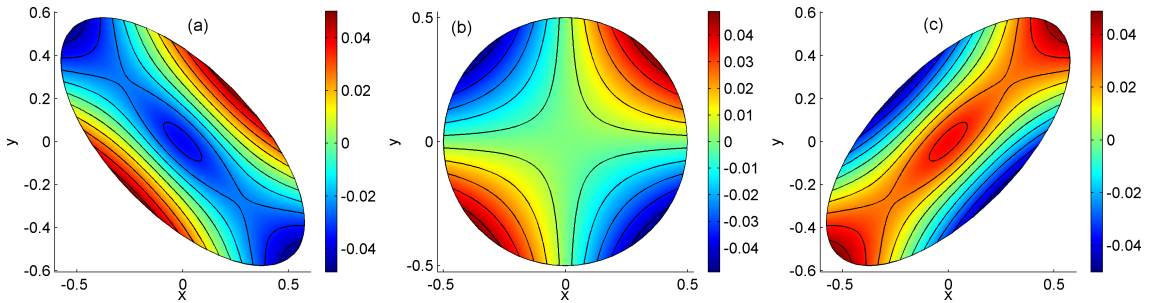


Figure 3.18: Contour plots of the electric potential $\phi = \phi_0 + M_A \phi_1$, at (a) $z = -0.5$, (b) $z = 0$ and (c) $z = 0.5$.

total current, $j_z = M_A^2 j_{2z} + M_A^3 j_{3z} + \mathcal{O}(M_A^4)$ is shown in Fig. (3.17). Here, two regions with strong negative current concentration appear in the total current which come as a contribution from the current at third order, j_{3z} , see Fig. (3.11), whereas regions with positive current concentration that appear in j_{3z} are dominated by the second-order current component j_{2z} which is negative. These four extrema of j_{3z} together with j_{2z} lead to a total current with a saddle-type structure at $x = y = 0$, as shown in Fig. (3.17). This is the first difference which we found here in comparison with two-dimensional models where the current maximum is usually at the X -point of the field (see, e.g., Priest and Forbes 1986; Baty et al. 2006).

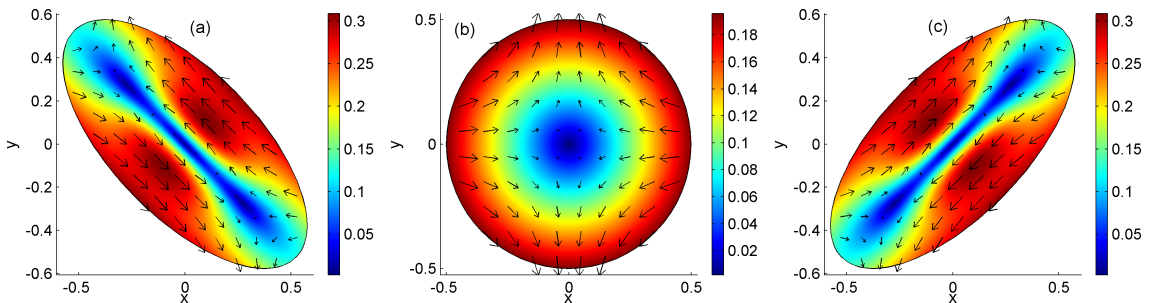


Figure 3.19: Strength and direction of $\mathbf{v} = \mathbf{v}_0 + M_A \mathbf{v}_1$ at (a) $z = -0.5$, (b) $z = 0$ and (c) $z = 0.5$.

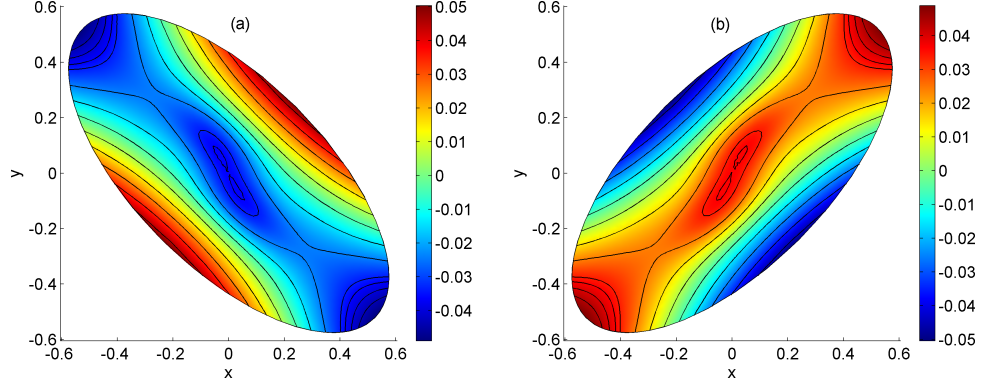


Figure 3.20: Contour plots of the electric potential $\phi = \phi_0 + M_A\phi_1 + M_A^2\phi_2$ at (a) $z = -0.5$ and (b) $z = 0.5$. At $z = 0$, $\phi = \phi_0 + \mathcal{O}(M_A^3)$ since $\phi_1 = \phi_2 = 0$ there.

Now, combining the zeroth-order component ϕ_0 together with the first-order component ϕ_1 , the resultant solution $\phi = \phi_0 + M_A\phi_1$ shows another important feature of 3D reconnection, which does not appear in 2D, namely, the existence of two stagnation points together with an O -type flow. Such a flow structure is illustrated in Fig. (3.18) which shows contour plots of $\phi = \phi_0 + M_A\phi_1$, which are streamlines for $\mathbf{v} = \mathbf{v}_0 + M_A\mathbf{v}_1$, at three particular planes. At the $z = 0$ plane, we still have a stagnation point at the centre, but as we move along z in both directions, we can see the appearance of an O -point in the centre and two new X -points. The strength and direction of the velocity of this flow are shown in Fig. (3.19). This effect results from the increasing strength of the counter rotating flows, defined by ϕ_1 , with distance from the symmetry plane $z = 0$. If strong enough, this rotational flow can dominate over the background stagnation flow, defined by ϕ_0 . The size of the islands depends on the relative strength of the rotational flow, which in turn depends on the distance from the $z = 0$ plane and on the non-ideal term $\eta_c \mathbf{j}_2$, compared with the strength of the stagnation flow.

While the magnitude of the second order velocity contribution $M_A^2\mathbf{v}_2$ is small compared with that of \mathbf{v}_0 and $M_A\mathbf{v}_1$, it still can play a role in the vicinity of the z -axis where $\mathbf{v}_0 = \mathbf{v}_1 = \mathbf{0}$. As an example of the fine structure in the reconnection region we include here plots of $\phi = \phi_0 + M_A\phi_1 + M_A^2\phi_2$ and $\mathbf{v} = \mathbf{v}_0 + M_A\mathbf{v}_1 + M_A^2\mathbf{v}_2$ in Figs. (3.20) and (3.21), respectively, which show the possibility for a formation of multiple X and O type flows. This phenomenon, which is reminiscent of the dynamics of non-stationary reconnection in two dimensions, occurs here in a stationary flow as a result of dimensionality of the problem.

Finally, even though these solutions are obtained for the case of low plasma beta, $\beta \ll 1$, they are also valid for high plasma beta, $\beta \gg 1$, since we still have the freedom of adding constant pressures at zeroth and first orders, p_0 and p_1 .

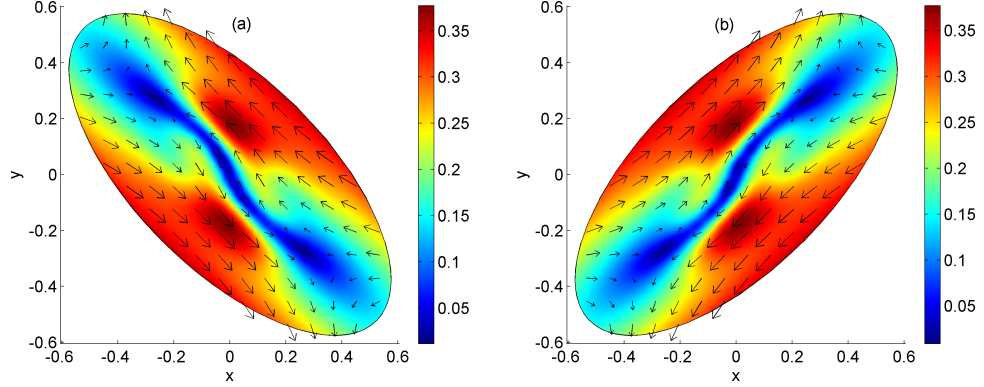


Figure 3.21: Strength and direction of the velocity $\mathbf{v} = \mathbf{v}_0 + M_A \mathbf{v}_1 + M_A^2 \mathbf{v}_2$ at (a) $z = -0.5$ and (b) $z = 0.5$. At $z = 0$, $\mathbf{v} = \mathbf{v}_0 + \mathcal{O}(M_A^3)$ since $\mathbf{v}_1 = \mathbf{v}_0 = \mathbf{0}$ there.

3.5 Summary and discussion

We have presented solutions of a stationary incompressible resistive MHD model for 3D magnetic reconnection in the absence of null points. The dimensionless form of the stationary MHD equations, specially Ohm's Law and the equation of motion, showed the appearance of the Alfvén Mach number, M_A , and hence, on assuming that $M_A < 1$, solutions were obtained in terms of powers of M_A in the form of expansion scheme. A basic state of an X-type current-free equilibrium magnetic field in the xy plane, superimposed on a uniform magnetic field in the z -direction has been assumed which in 3D has a form known as “hyperbolic flux tube” and a localized non-ideal region has been achieved through a localization of the resistivity η_c . The localization parameters, namely the parameters L and l which are related to the length of the non-ideal region in the z -direction and to the width of the non-ideal region in the $z = 0$ plane, respectively, were chosen such that the non-ideal region is completely enclosed in the HFT. Unlike reconnection in 2D, a wide variety of 3D reconnection solutions were obtained via an integration scheme which allowed us to prescribe certain properties of the solutions, such as stagnation flows and parallel electric fields, through the freedom of choosing its free functions and prescribing the low-level terms. General analytical solutions were obtained for equations at the first few orders, whereas solutions to equations at some higher orders were obtained numerically. The obtained solutions show important differences between 3D reconnection solutions and the commonly used 2D models such as the appearance of saddle-type current structures and the existence of multiple X and O -point type flows in the reconnection region. These features are related to the localization of the non-ideal region. Finally, the system has been solved up to third order to minimize numerical errors resulting from evaluating the required gradients. However, the outlined integration scheme can still be used to obtain solutions at all higher orders. We have succeeded in controlling the magnitude of the obtained solutions at higher orders in such a way that the solutions at lower orders are dominant as seen in the approximations of the total solutions and, in principal, the same can be

done for solutions at even higher orders since at each order we have enough free functions through which one could be able to control the magnitude of the corresponding solutions and hence the convergence of the expansion scheme.

Even though, the analytical solutions of equations at the first few orders are dominating the overall structure of the obtained total solution approximations, the contribution of numerical solutions of equations at some higher order has added new features to the reconnection solutions, such as those of the flow and current structures. This is due to the appearance of the inertial terms in the equations at higher orders, which were not included by Wilmot-Smith et al. (2009) since solutions require numerical integration and of course were not included by Hornig and Priest (2003), where only a kinematic model was considered. Hence, in the next chapter, we will extend the kinematic solutions obtained by Hornig and Priest (2003) towards solutions of the full set of MHD equations.

Chapter 4

On The Solutions of Three-Dimensional Non-Null Magnetic Reconnection - II

In the previous chapter, we started by including a stagnation flow at the zeroth order. But, as we have previously mentioned, the integration scheme discussed in Section 3.3 allows us to include an ideal electric potential at any order and hence superimpose any ideal plasma flow at that order. Thus, we shall make use of this property to introduce a further simplification to the expansion scheme by setting the zeroth-order velocity, \mathbf{v}_0 , to zero and hence examining the resulting solutions. The solutions obtained by Wilmot-Smith et al. (2006) for this case do not include the effect of the inertial term in the equation of motion, since they are only obtained up to third order, while the inertial term first appears at fourth order. That is why those solutions are very similar to the ones obtained by Hornig and Priest (2003) for the stationary kinematic model. Hence, to have a better generalization of the solutions obtained in the kinematic model and to see the effect of the inertial term on the reconnection solutions, the system has to be solved at least up to fourth order, which we shall consider in this chapter.

The material in this chapter based on Al-Salti et al. (2010).

Now, Ohm's law at first order (3.16), on using $\mathbf{v}_0 = 0$, reduces to $-\nabla\phi_0 = \mathbf{0}$, which can be satisfied by taking ϕ_0 to be constant, and the equation of motion at second order (3.19) becomes

$$-\nabla p_2 + \mathbf{j}_2 \times \mathbf{B}_0 = \mathbf{0}. \quad (4.1)$$

Using the general method of integration, Eq. (4.1) reduces to $-\mathbf{B}_0 \cdot \nabla p_2 = 0$, that is p_2 is constant along fields of \mathbf{B}_0 , and hence

$$p_2 = p_{20}(x_0, y_0). \quad (4.2)$$

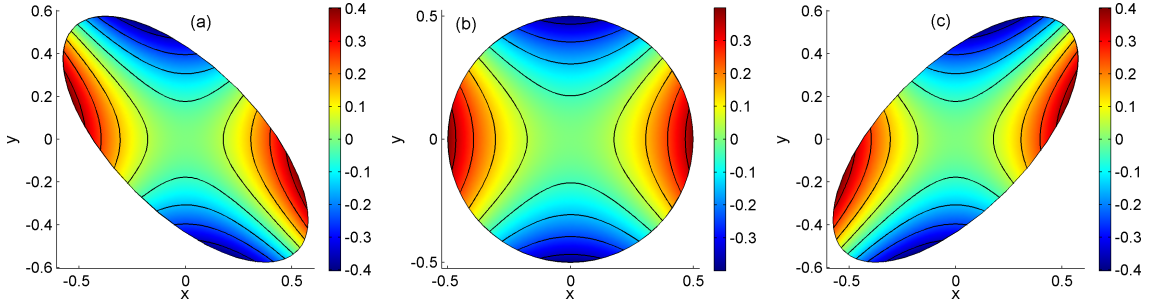


Figure 4.1: Contour plots of the pressure p_2 variation for the choice of $p_{20} = -\frac{k}{2}b_0j_{20}(x^2 - y^2)$ at (a) $z = -0.5$, (b) $z = 0$ and (c) $z = 0.5$.

Again, choosing p_{20} to be

$$p_{20}(x_0, y_0) = f(x_0^2 - y_0^2) = f(x^2 - y^2),$$

the expression (3.21) is still valid for the second-order current \mathbf{j}_2 for this case. However, to allow for a direct comparison with the solutions obtained in the kinematic model, we shall choose $f(x^2 - y^2)$ and λ_{20} in such a way that the second-order current \mathbf{j}_2 has only a constant z -component. For this purpose, we choose

$$\begin{aligned} f(x^2 - y^2) &= p_{200} - \frac{k}{2}b_0j_{20}(x^2 - y^2), \\ \lambda_{20} &= 0, \end{aligned} \quad (4.3)$$

where, p_{200} and j_{20} are constants. The resultant second-order pressure, p_2 is illustrated in Fig. (4.1) and the current at the same order reduces to

$$\mathbf{j}_2 = j_{20}\hat{\mathbf{z}}. \quad (4.4)$$

Hence, Ampere's law at second order becomes

$$\nabla \times \mathbf{B}_2 = j_{20}\hat{\mathbf{z}},$$

which can be satisfied by taking \mathbf{B}_2 to be

$$\mathbf{B}_2 = j_{20}(k_1y, k_2x, k_3), \quad (4.5)$$

where k_1 , k_2 and k_3 are constants with $k_2 - k_1 = 1$.

Ohm's law at the second order (3.20), on the other hand, remains unchanged, since it does not depend on the zeroth-order velocity, \mathbf{v}_0 . Substituting (4.3) into Eq. (3.24), we get the following

expression for η_c :

$$\eta_c = \frac{e_{10}}{j_{20}} \exp\left(-\frac{z^2}{L^2} - \frac{\gamma^2}{l^2}\right),$$

with

$$\gamma^2 = (x^2 + y^2) \cosh(2kz) - 2xy \sinh(2kz),$$

But, the way in which η_c is defined makes the non-ideal term $\eta_c \mathbf{j}_2$ independent of the choice of the function f . Hence, we shall use the same diffusion region shown in Fig. (3.6). The electric potential at first order, ϕ_1 , is still given by (3.25), which can be written as

$$\phi_1 = \phi_{11} + \phi_{10}(x_0, y_0),$$

where ϕ_{11} is given by (3.27). Ohm's law (3.20) can then be decomposed into two equations, namely,

$$-\nabla\phi_{11} + \mathbf{v}_{11} \times \mathbf{B}_0 = \eta_c \mathbf{j}_2, \quad (4.6)$$

$$-\nabla\phi_{10} + \mathbf{v}_{10} \times \mathbf{B}_0 = \mathbf{0}, \quad (4.7)$$

with $\mathbf{v}_1 = \mathbf{v}_{11} + \mathbf{v}_{10}$. In the following sections, we will examine solutions obtained by considering two different ideal plasma flows, \mathbf{v}_{10} . This can be obtained by prescribing the electric potential ϕ_{10} , the source of these ideal flows, taking $\phi_{10} = 0$ in Section 4.1 and then considering a stagnation-type flow in Section 4.2. These two cases, respectively, correspond to the pure and composite solutions discussed by Hornig and Priest (2003) in their kinematic model.

4.1 Pure 3D Reconnection Solutions

4.1.1 Analytical Solutions

We first start by setting ϕ_{10} to zero and hence Eq. (4.7) can be satisfied by taking $\mathbf{v}_{10} = \mathbf{0}$. The expression for the plasma velocity at first order, \mathbf{v}_1 , is then given by (3.27). Now, on substituting $\mathbf{v}_0 = \mathbf{0}$, the equation of motion at third order becomes

$$-\nabla p_3 + \mathbf{j}_3 \times \mathbf{B}_0 = \mathbf{0}. \quad (4.8)$$

which is similar to the equation of motion at the previous order, Eq. (4.1), and hence could be solved by taking

$$p_3 = g(x^2 - y^2), \quad (4.9)$$

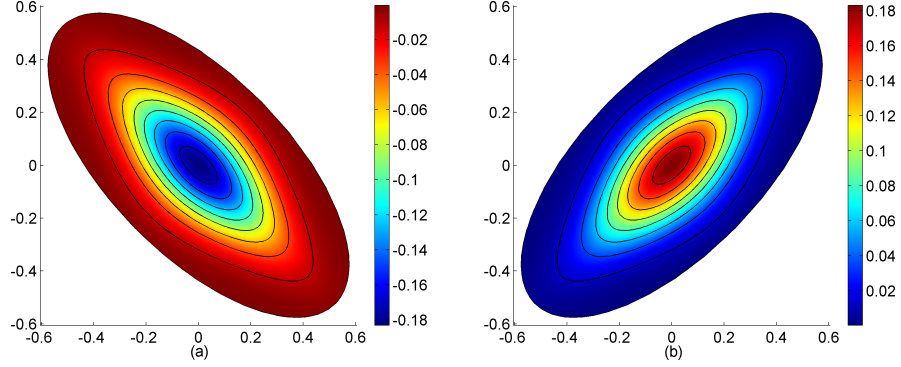


Figure 4.2: Contour plots of the electric potential ϕ_2 at (a) $z = -0.5$ and (b) $z = 0.5$, with $j_{20} = j_{30} = -4$. At $z = 0$, $\phi_2 = \phi_{20} = \text{constant}$.

$$\mathbf{j}_3 = kb_0\lambda_{30}(y\hat{\mathbf{x}} + x\hat{\mathbf{y}}) + \left(b_0\lambda_{30} - \frac{2g'(x^2 - y^2)}{b_0k}\right)\hat{\mathbf{z}}, \quad (4.10)$$

and Ohm's law at the same order reduces to

$$-\nabla\phi_2 + \mathbf{v}_2 \times \mathbf{B}_0 = \eta_c\mathbf{j}_3, \quad (4.11)$$

which is also similar to Ohm's law at the previous order (3.20). Thus, due to the similarity of the equations at second and third orders and depending on the choice of $g(x^2 - y^2)$, the solutions of the equations at third order (p_3 , \mathbf{j}_3 , ϕ_2 and \mathbf{v}_2) may or may not add new features to the reconnection solutions. For illustration, we shall consider here the following choice of $g(x^2 - y^2)$:

$$g(x^2 - y^2) = p_{30} - \frac{\lambda^2 k j_{30} b_0}{2} \tanh\left(\frac{x^2 - y^2}{\lambda^2}\right),$$

where, p_{30} and j_{30} are constants. The current at third order, \mathbf{j}_3 , on taking $\lambda_{30} = 0$, becomes

$$\mathbf{j}_3 = j_{3z}\hat{\mathbf{z}} = \frac{j_{30}}{\cosh^2\left(\frac{x^2 - y^2}{\lambda^2}\right)}\hat{\mathbf{z}}, \quad (4.12)$$

and hence the numerical solution obtained in Section (3.4.2) for the magnetic field \mathbf{B}_2 can be used here for \mathbf{B}_3 . Using the general method of integration, solutions to Ohm's law (4.11), on taking ϕ_{20} to be constant, are then given by

$$\phi_2 = \phi_{20} - \frac{j_{3z}\sqrt{\pi}}{2j_{20}} Le_{10} \exp\left(-\frac{\gamma^2}{l^2}\right) \text{erf}\left(\frac{z}{L}\right),$$

$$\mathbf{v}_2 = \left(\frac{2j_{3z}\phi_{11}}{j_{20}b_0} \left(\frac{(y \cosh(2kz) - x \sinh(2kz))}{l^2} - \frac{2y \tanh\left(\frac{x^2 - y^2}{\lambda^2}\right)}{\lambda^2}\right) + kb_0y\mu_{20}\right)\hat{\mathbf{x}}$$

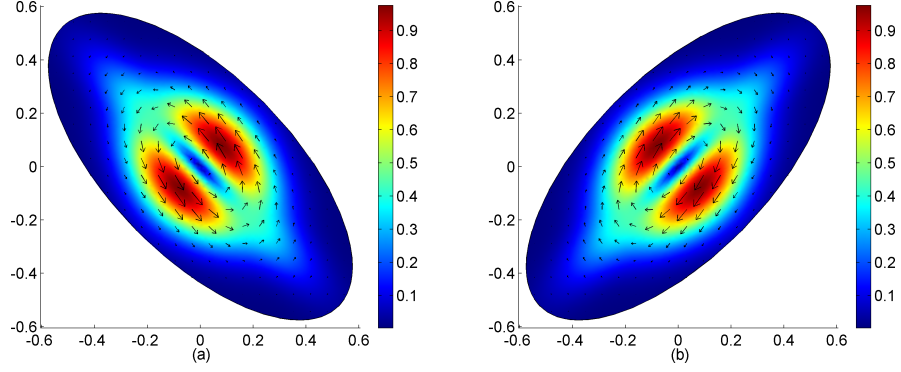


Figure 4.3: Strength and direction of the velocity \mathbf{v}_2 , for the case of $j_{20} = j_{30} = -4$ and $\mu_{10} = \mu_{20} = 0$, at (a) $z = -0.5$ and (b) $z = 0.5$. For this case, \mathbf{v}_2 vanishes at $z = 0$.

$$\begin{aligned}
 & + \left(\frac{2j_{3z}\phi_{11}}{j_{20}b_0} \left(\frac{(y \sinh(2kz) - x \cosh(2kz))}{l^2} - \frac{2x \tanh\left(\frac{(x^2 - y^2)}{\lambda^2}\right)}{\lambda^2} \right) + kb_0x\mu_{20} \right) \hat{\mathbf{y}} \\
 & + b_0\mu_{20}\hat{\mathbf{z}},
 \end{aligned}$$

which can be rewritten as

$$\phi_2 = \frac{j_{3z}}{j_{20}}\phi_1 + \phi_{20}, \quad (4.13)$$

$$\mathbf{v}_2 = \frac{j_{3z}}{j_{20}}\mathbf{v}_1 + \mathbf{v}_{21}, \quad (4.14)$$

where,

$$\begin{aligned}
 \mathbf{v}_{21} & = \left(kb_0y \left(\mu_{20} - \frac{j_{3z}}{j_{20}}\mu_{10} \right) - \frac{4j_{3z}\phi_1}{b_0j_{20}\lambda^2}y \tanh\left(\frac{(x^2 - y^2)}{\lambda^2}\right) \right) \hat{\mathbf{x}} \\
 & + \left(kb_0x \left(\mu_{20} - \frac{j_{3z}}{j_{20}}\mu_{10} \right) - \frac{4j_{3z}\phi_1}{b_0j_{20}\lambda^2}x \tanh\left(\frac{(x^2 - y^2)}{\lambda^2}\right) \right) \hat{\mathbf{y}} \\
 & + b_0 \left(\mu_{20} - \frac{j_{3z}}{j_{20}}\mu_{10} \right) \hat{\mathbf{z}}.
 \end{aligned} \quad (4.15)$$

These solutions are illustrated in Figs. (4.2) and (4.3). Figure (4.2) shows contour plots of the electric potential ϕ_2 , which are streamlines for \mathbf{v}_2 . Here, as in the previous order, we still have a counter-rotational flow above and below the $z = 0$ plane, with only a minor difference, namely, that the factor (j_{3z}/j_{20}) appeared in Eqs. (4.13) and (4.14) has the effect of narrowing the velocity field lines away from the z -axis. The strength and direction of this flow are shown in Fig. (4.3). Here we should notice that, even though the obtained solutions of equations at third order are qualitatively similar to the previous-order solutions, their magnitude can still be controlled independently by j_{30} . Thus, for simplicity and to improve the convergence of the expansion scheme,

we shall set j_{30} to zero and hence the solutions of the equations at third order become

$$\mathbf{j}_3 = \mathbf{B}_3 = \mathbf{v}_2 = \mathbf{0}, \quad p_3 = p_{30}, \quad \phi_2 = \phi_{20}. \quad (4.16)$$

By doing so, we can then solve the equations at all remaining odd orders ($m = 5, 7, 9, \dots$) by taking

$$\mathbf{j}_m = \mathbf{B}_m = \mathbf{v}_{m-1} = \mathbf{0}, \quad p_m = p_{m0}, \quad \phi_{m-1} = \phi_{m-1,0}, \quad (4.17)$$

since they all reduce to

$$\begin{aligned} -\nabla p_m + \mathbf{j}_m \times \mathbf{B}_0 &= \mathbf{0}, \\ -\nabla \phi_{m-1} + \mathbf{v}_{m-1} \times \mathbf{B}_0 &= \eta_c \mathbf{j}_m. \end{aligned}$$

Here, p_{m0} and $\phi_{m-1,0}$ are constants. Solutions to equations at the remaining higher even orders require numerical integration, which we will discuss in the following section. But, let us finally list the obtained analytical solutions as follow:

$$\begin{aligned} \mathbf{B} &= b_0 (ky\hat{\mathbf{x}} + kx\hat{\mathbf{y}} + \hat{\mathbf{z}}) + M_A^2 j_{20} (k_1 y\hat{\mathbf{x}} + k_2 x\hat{\mathbf{y}} + k_3 \hat{\mathbf{z}}) + \mathcal{O}(M_A^4) \\ p &= p_{00} + M_A p_{10} + M_A^2 \left(p_{200} - \frac{k}{2} b_0 j_{20} (x^2 - y^2) \right) + M_A^3 p_{30} + \mathcal{O}(M_A^4) \\ \mathbf{j} &= M_A^2 j_{20} \hat{\mathbf{z}} + \mathcal{O}(M_A^4) \\ \phi &= -M_A \frac{\sqrt{\pi}}{2} L e_{10} \exp\left(-\frac{\gamma^2}{l^2}\right) \operatorname{erf}\left(\frac{z}{L}\right) + M_A^2 \phi_{20} + \mathcal{O}(M_A^3) \\ \mathbf{v} &= M_A \frac{2\phi_1}{b_0 l^2} ((y \cosh(2kz) - x \sinh(2kz)) \hat{\mathbf{x}} + (y \sinh(2kz) - x \cosh(2kz)) \hat{\mathbf{y}}) + \mathcal{O}(M_A^3). \end{aligned}$$

Here, we have set μ_{10} to zero. Comparing these solutions to the ones of the kinematic model, listed in Appendix D, we can easily see the similarity between them, with only minor differences. Hence, with the above solutions approximation of the full resistive stationary MHD equations, we can observe many features, if not all, of the stationary kinematic model presented by Hornig and Priest (2003), which confirms that the kinematic solutions can indeed be used in a certain limit to represent solutions to the full stationary resistive MHD equations.

4.1.2 Numerical Solutions

Using the analytical solutions discussed in the previous section and the general method of integration presented in Section 3.3, we present numerical solutions to the following equations at fourth order:

$$-\nabla p_4 + \mathbf{j}_4 \times \mathbf{B}_0 = (\mathbf{v}_1 \cdot \nabla) \mathbf{v}_1 - (\mathbf{j}_2 \times \mathbf{B}_2), \quad (4.18)$$

$$-\nabla \phi_3 + \mathbf{v}_3 \times \mathbf{B}_0 = \eta_c \mathbf{j}_4 - (\mathbf{v}_1 \times \mathbf{B}_2), \quad (4.19)$$

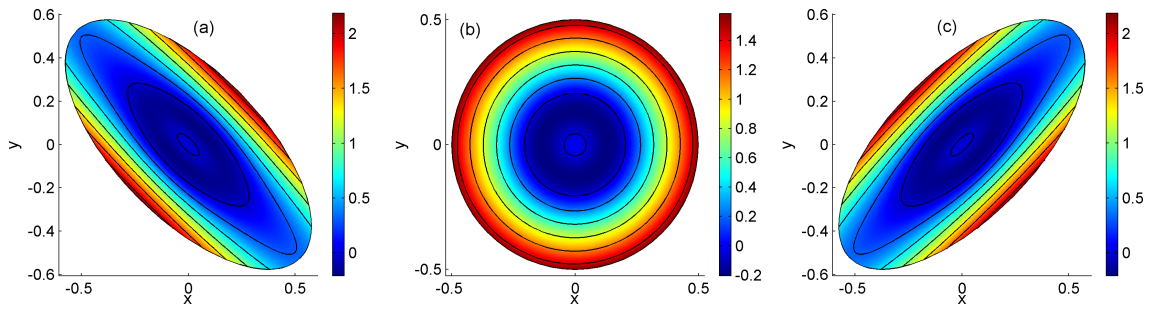


Figure 4.4: Contour plots of the pressure p_4 at (a) $z = -0.5$, (b) $z = 0$ and (c) $z = 0.5$.

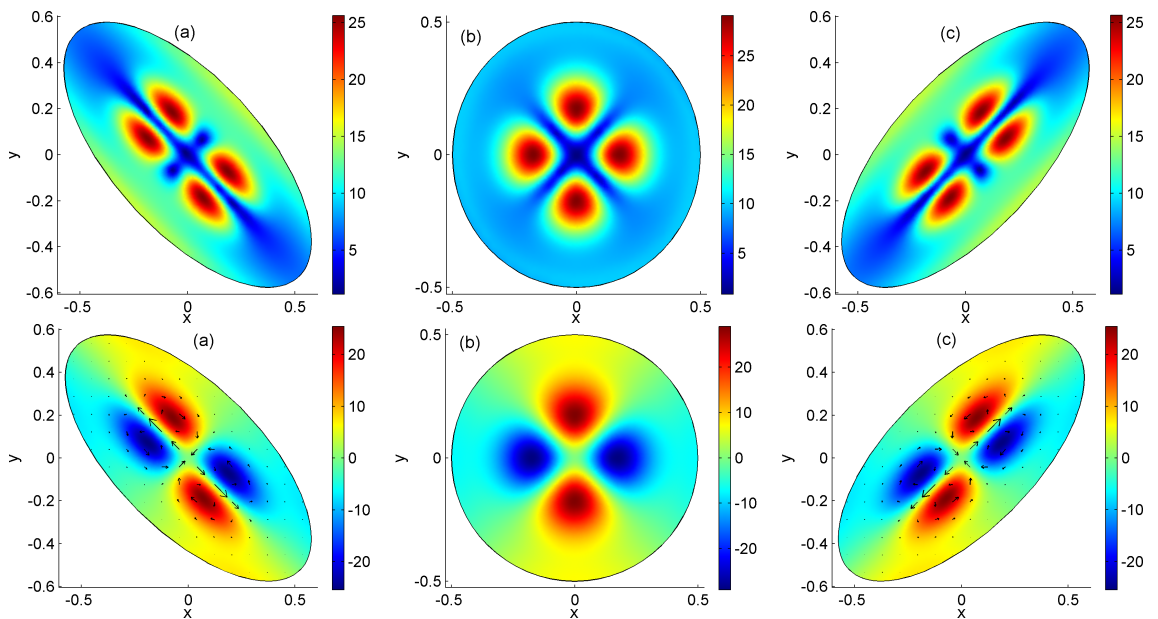


Figure 4.5: Illustration of the magnitude of the current \mathbf{j}_4 (top) and its z -component, j_{4z} , with the arrows representing the direction of \mathbf{v}_3 (bottom) at (a) $z = -0.5$, (b) $z = 0$ and (c) $z = 0.5$. Note that $\mathbf{v}_3 = \mathbf{0}$ at $z = 0$.

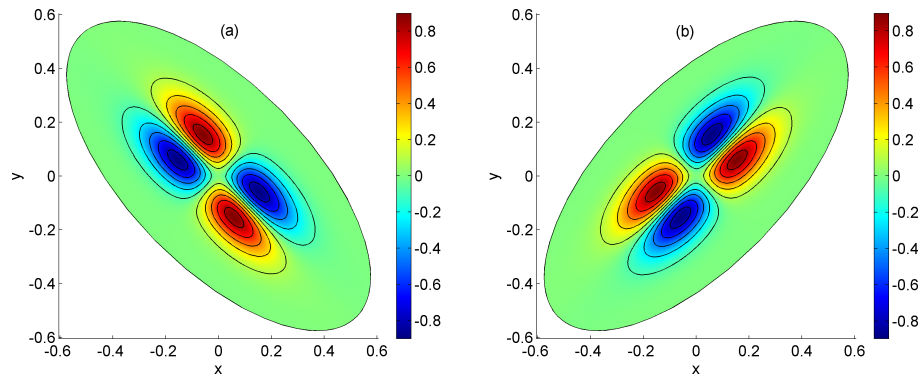


Figure 4.6: Contour plots of the electric potential ϕ_3 at (a) $z = -0.5$ and (b) $z = 0.5$, where ϕ_3 vanishes at the $z = 0$ plane.

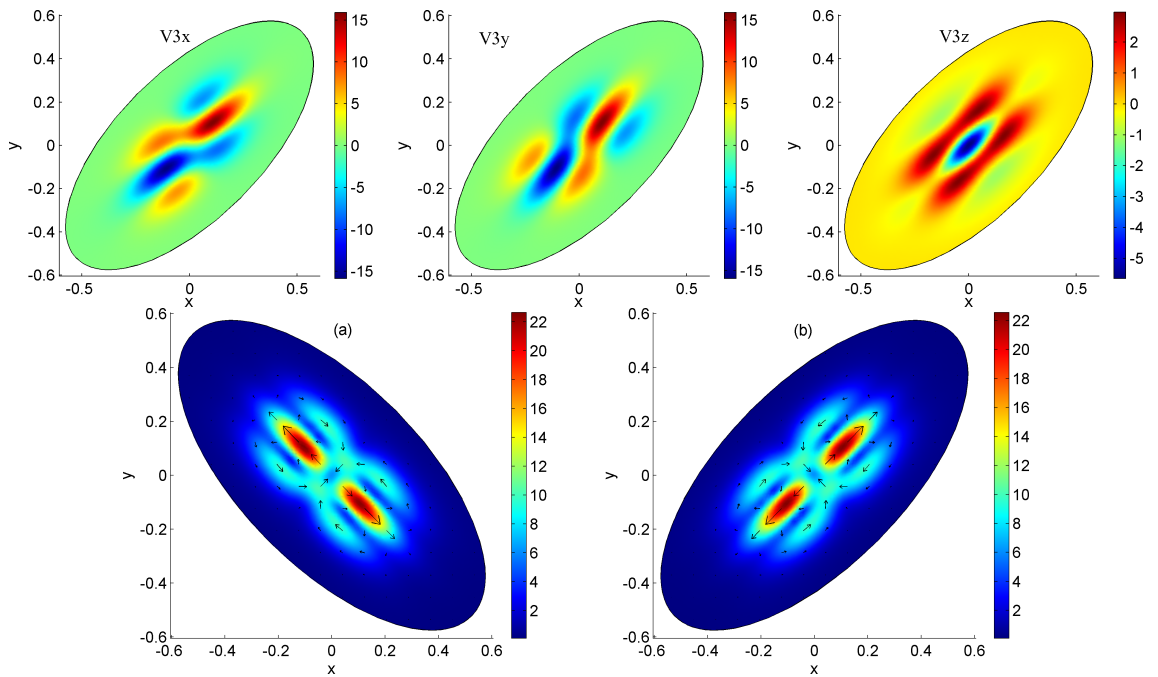


Figure 4.7: The x, y, z components of the velocity \mathbf{v}_3 at $z = 0.5$ (top) and its strength and direction, at (a) $z = -0.5$ and (b) $z = 0.5$ (bottom), where $\mathbf{v}_3 = \mathbf{0}$ at $z = 0$.

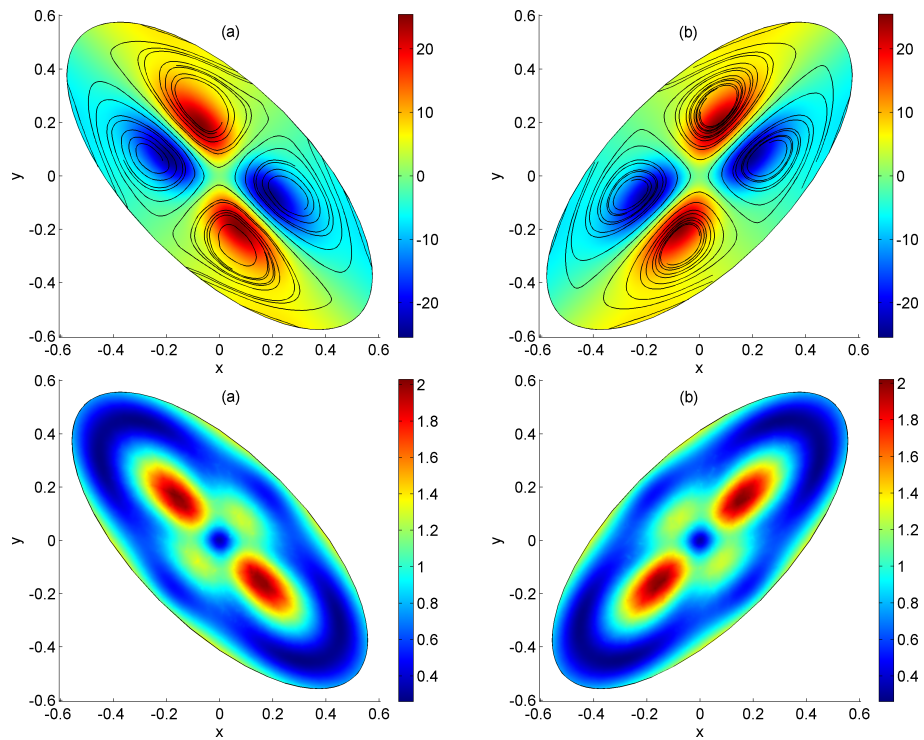


Figure 4.8: Projection of field lines of the magnetic field \mathbf{B}_4 where the background color indicates the magnitude of the current j_{4z} (top) and the strength of \mathbf{B}_4 (bottom) at (a) $z = -0.5$ and (b) $z = 0.5$.

$$\begin{aligned}\nabla \times \mathbf{B}_4 &= \mathbf{j}_4, \\ \mathbf{n} \cdot \mathbf{B}_4 &= 0.\end{aligned}\tag{4.20}$$

We now see the first appearance of the inertial term in Eq. (4.18) and we also see the coupling of these equations through \mathbf{j}_4 . Hence, we start by solving Eq. (4.18) for p_4 and \mathbf{j}_4 and then substitute for \mathbf{j}_4 into Eqs. (4.19) and (4.20) and solve for ϕ_3 , \mathbf{v}_3 and \mathbf{B}_4 . The resultant solutions are illustrated in Figs. (4.4) - (4.8). Figure (4.4) shows contour plots of the pressure p_4 variations, where we see both the inertial term, $(\mathbf{v}_1 \cdot \nabla) \mathbf{v}_1$, and the Lorentz-force term, $(\mathbf{j}_2 \times \mathbf{B}_2)$, have contributed to the pressure structure. The effect of the inertial term is limited to the vicinity of the z -axis with its maximum contribution at the plane $z = 0$, while the Lorentz-force term has its maximum contribution towards the boundary both above and below the plane $z = 0$, where it has its minimum contribution. The current \mathbf{j}_4 structure, on the other hand, is dominated by gradients of the inertial term that contains the first-order velocity, \mathbf{v}_1 , which in turn is related to the localization of the non-ideal region. These gradients result in the appearance of four regions of strong current concentration in the dominant component of the current, j_{4z} , again two positive and two negative, both above and below the plane $z = 0$, where they have their maximum value. Those four regions, which are a bit stretched here, are similar to the ones appeared in the third-order current structure, presented in Section 3.4.2, but with opposite signs. The effect of gradients of the Lorentz-force term is very small and only limited to regions very close the boundary. An illustration of the current structure at fourth order is shown in Fig. (4.5), which clearly shows that the major contribution to the magnitude of \mathbf{j}_4 comes from its z -component. The arrows appearing in Fig. (4.5) represent the direction of the velocity field \mathbf{v}_3 , which vanishes at $z = 0$. These arrows show the presence of a stagnation flow at the centre and rotational flows around those region of current concentration. The presence of these flows is confirmed in Fig. (4.6) that shows contours of the electric potential ϕ_3 , which represent a projection of streamlines for the velocity \mathbf{v}_3 . Unlike the advection term $\mathbf{v}_0 \times \mathbf{B}_2$ that contributed to the structure of ϕ_2 as presented in Section 3.4.2, the background plot in Fig. (4.6) shows that, the advection term $\mathbf{v}_1 \times \mathbf{B}_2$ appeared in Eq. (4.19) does not contribute to the structure of ϕ_3 , which is dominated by the resistive term $\eta_c \mathbf{j}_4$. The components, strength and direction of the corresponding velocity field \mathbf{v}_3 are shown in Fig. (4.7), which shows that the major contribution to the magnitude of \mathbf{v}_3 comes from its x and y -components. Finally, in Fig. (4.8), we show an illustration of field lines and strength of the magnetic field \mathbf{B}_4 , where we see the appearance of two regions of strong magnetic field concentration both above and below the $z = 0$ plane, where they have their maximum.

4.1.3 Total Solution Approximation

We have now solved the system analytically up to third order and solutions to the equations at fourth order were obtained numerically. Solutions to equations at fifth order are also given by

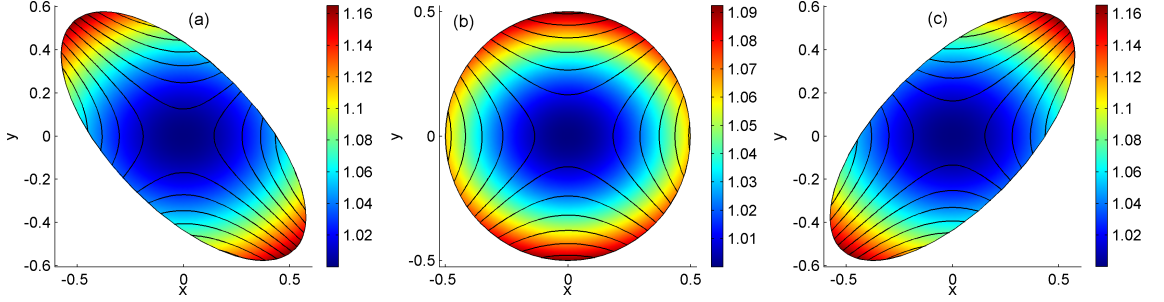


Figure 4.9: Projection of field lines of the magnetic field $\mathbf{B} = \mathbf{B}_0 + M_A^2 \mathbf{B}_2 + M_A^4 \mathbf{B}_4$ at (a) $z = -0.5$, (b) $z = 0$ and (c) $z = 0.5$, where the background colour represents its strength.

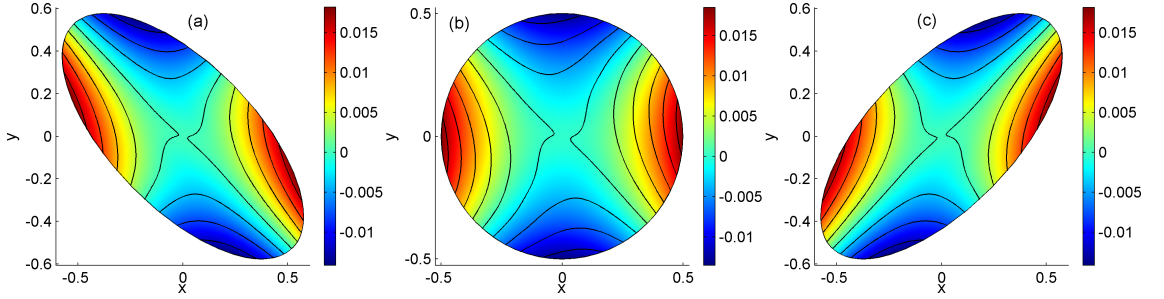


Figure 4.10: Contour plots of the pressure $p = M_A^2 p_2 + M_A^4 p_4$ variation at (a) $z = -0.5$, (b) $z = 0$ and (c) $z = 0.5$.

(4.17). Hence, to obtain an approximation of the total solution of each variable and to examine contribution of solutions at higher orders, we shall now combine the obtained solutions of equations at different order of M_A using again $M_A = 0.2$. The magnetic field approximation, $\mathbf{B} = \mathbf{B}_0 + M_A^2 \mathbf{B}_2 + M_A^4 \mathbf{B}_4 + \mathcal{O}(M_A^6)$, is shown in Fig. (4.9), which shows that the magnetic field is dominated by its zeroth-order term, \mathbf{B}_0 . Figure (4.10) shows a contour plot of the total pressure approximation, $p = p_0 + M_A p_{10} + M_A^2 p_2 + M_A^3 p_{30} + M_A^4 p_4 + M_A^5 p_{50} + \mathcal{O}(M_A^6)$, where we can clearly see that the fourth-order pressure term, $M_A^4 p_4$, has contributed to the total pressure. This contribution, which results from appearance of the inertial term $(\mathbf{v}_1 \cdot \nabla) \mathbf{v}_1$ in Eq. (4.18), is only limited to the vicinity of the z -axis, where the second order pressure $p_2 = 0$. The overall pressure structure is dominated by the second-order pressure contribution, $M_A^2 p_2$, and we still have the freedom to add the constant pressures at zeroth, first, third and fifth orders, p_0 , p_{10} , p_{30} and p_{50} , respectively. The effect of this inertial term is also seen in the structure of the approximated total current. It has led to a saddle-type current structure at $x = y = 0$, as shown in Fig. (4.11), which illustrates the structure of the z -component of the approximated total current, $j_z = M_A^2 j_{2z} + M_A^4 j_{4z} + \mathcal{O}(M_A^6)$ in three different planes. Here we see that the magnitude of the second-order term $M_A^2 j_{2z}$ dominates the one of the fourth-order contribution $M_A^4 j_{4z}$ resulting into four negative current extrema, two stronger ones and two weaker ones.

Figure (4.12) shows contours of the total electric potential approximation $\phi = M_A \phi_1 + M_A^2 \phi_{20} +$

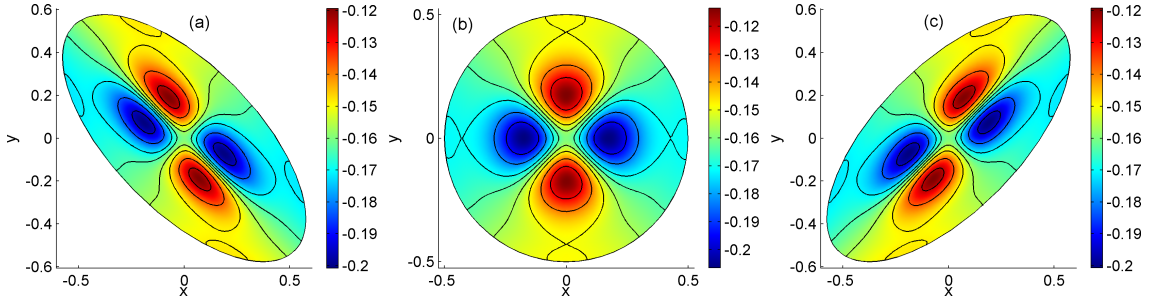


Figure 4.11: Illustration of the current $j_z = M_A^2 j_{2z} + M_A^4 j_{4z}$ at (a) $z = -0.5$, (b) $z = 0$ and (c) $z = 0.5$.

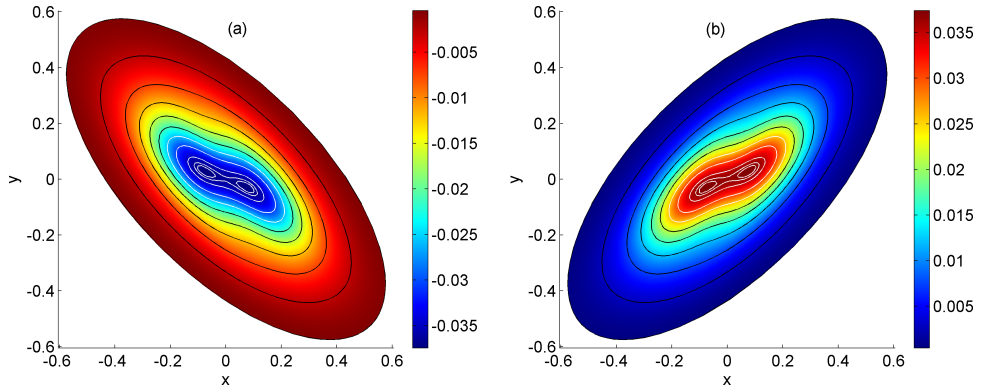


Figure 4.12: Contour plots of the electric potential $\phi = M_A \phi_1 + M_A^3 \phi_3$ at (a) $z = -0.5$ and (b) $z = 0.5$. At $z = 0$, $\phi = 0$ since $\phi_1 = \phi_3 = 0$ there.

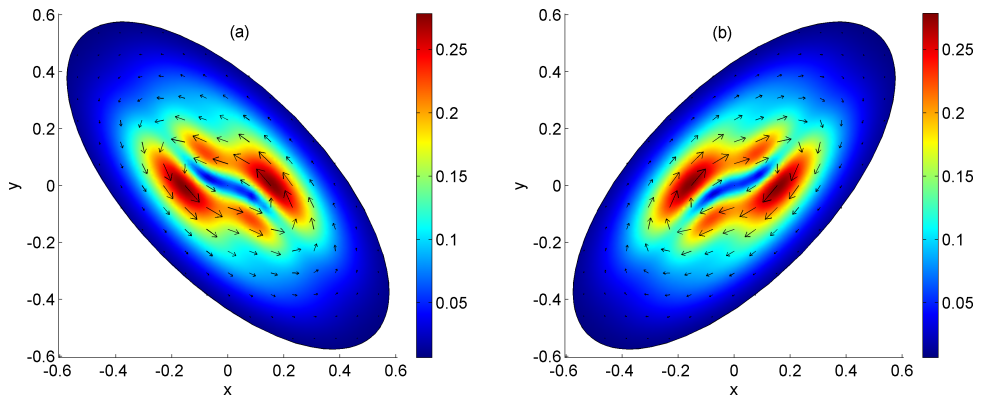


Figure 4.13: Strength and direction of the velocity $\mathbf{v} = M_A \mathbf{v}_1 + M_A^3 \mathbf{v}_3$ at (a) $z = -0.5$ and (b) $z = 0.5$. At $z = 0$, $\mathbf{v} = \mathbf{0}$ since $\mathbf{v}_3 = \mathbf{v}_1 = \mathbf{0}$ there.

$M_A^3\phi_3 + M_A^4\phi_{40} + \mathcal{O}(M_A^5)$, which represent a projection of streamlines for the total velocity approximation $\mathbf{v} = M_A\mathbf{v}_1 + M_A^3\mathbf{v}_3 + \mathcal{O}(M_A^5)$, where we have rotational flows everywhere except in the vicinity of the z -axis where $\mathbf{v}_1 = \mathbf{0}$. There we see the appearance of a stagnation flow, which comes as contribution from the third-order term $M_A^3\mathbf{v}_3$. Here we still have the freedom of including the constant electrical potentials at second and fourth order, ϕ_{20} and ϕ_{40} , respectively. The strength and direction of the total velocity approximation are shown in Fig. (4.13). Away from the z -axis, we still have counter-rotational flow above and below the $z = 0$ plane, where the flow vanishes since $\mathbf{v}_1 = \mathbf{v}_3 = \mathbf{0}$ at $z = 0$. But, as we have mentioned earlier, the integration scheme allows us to include an ideal electric potential at any order and hence superimpose an ideal plasma flow. Thus, we can superimpose a stagnation flow in the $z = 0$ plane through the freedom of choosing the ideal electric potential ϕ_{30} .

4.2 Composite 3D Reconnection Solutions

In the previous section, we have examined solutions resulting from choosing $\phi_{10} = 0$ and setting the corresponding velocity \mathbf{v}_{10} to zero as well. But, in general, we can superimpose any non-zero ideal flow on the first-order velocity obtained in the pure solution case. This corresponds to the composite solution case in the kinematic model. One possible choice, which is of particular interest in magnetic reconnection, is to superimpose a stagnation flow. For this purpose, we choose

$$\phi_{10} = \frac{\varphi_0}{\Lambda^2} x_0 y_0.$$

This choice is similar to the one chosen by Hornig and Priest (2003) and hence allows for a direct comparison with their composite solution case. Setting $Z_0 = 0$ and using the inverse field line mappings, we can express ϕ_{10} in terms of x , y , and z and then use the general method of integration to solve Eq. (4.7) for \mathbf{v}_{10} . The composite solutions for the first-order electric potential and velocity, ϕ_1 and \mathbf{v}_1 , respectively, are then given by

$$\begin{aligned} \phi_1 &= \phi_{11} + \phi_{10} \\ &= -\frac{\sqrt{\pi}}{2} L e_{10} \exp\left(-\frac{\gamma^2}{l^2}\right) \operatorname{erf}\left(\frac{z}{L}\right) + \frac{\varphi_0}{2\Lambda^2} (2xy \cosh(2kz) - (x^2 + y^2) \sinh(2kz)), \end{aligned} \quad (4.21)$$

$$\mathbf{v}_1 = \mathbf{v}_{11} + \mathbf{v}_{10} + \mu_{10} \mathbf{B}_0, \quad (4.22)$$

where,

$$\mathbf{v}_{11} = \frac{2\phi_{11}}{b_0 l^2} ((y \cosh(2kz) - x \sinh(2kz)) \hat{\mathbf{x}} + (y \sinh(2kz) - x \cosh(2kz)) \hat{\mathbf{y}}),$$

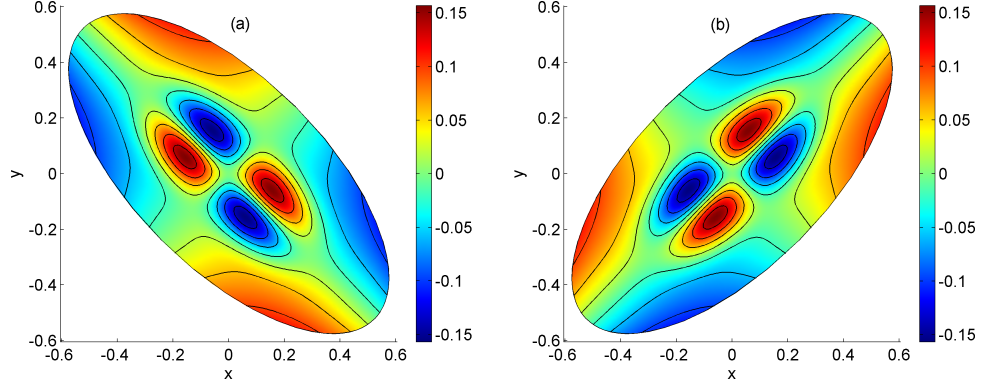


Figure 4.14: Contour plots of the electric potential ϕ_{32} at (a) $z = -0.5$ and (b) $z = 0.5$, where $\phi_{32} = 0$ at $z = 0$.

$$\mathbf{v}_{10} = \frac{\varphi_0}{b_0 \Lambda^2} ((y \sinh(2kz) - x \cosh(2kz)) \hat{\mathbf{x}} + (y \cosh(2kz) - x \sinh(2kz)) \hat{\mathbf{y}}).$$

The composite velocity \mathbf{v}_1 consists of two different types of flows, a rotational flow represented by \mathbf{v}_{11} and a stagnation flow represented by \mathbf{v}_{10} . Depending on the relative strength of these two flows, we might have different types of composite solutions for equations at fourth order and hence different total composite solution approximations, which we discuss in the following sections. Again, the first-order composite electric potential and velocity ϕ_1 and \mathbf{v}_1 , respectively, are similar to the ones obtained by Hornig and Priest (2003) for the kinematic model presented here in Appendix D.

The equations at third order, Eqs. (4.8) and (4.11), remain the same and hence can still be satisfied by (4.16). Similarly, the equations at all remaining odd orders ($m = 5, 7, 9, \dots$) can be solved by (4.17), whereas solutions to equations at the remaining higher even orders, in general, require numerical integration. Equations at fourth order, Eqs. (4.18) and (4.19), can be easily satisfied by dividing them into the following three systems of equations:

$$\begin{aligned} \text{System (1)} & \begin{cases} -\nabla p_{41} + \mathbf{j}_{41} \times \mathbf{B}_0 = (\mathbf{v}_{11} \cdot \nabla) \mathbf{v}_{11} - (\mathbf{j}_2 \times \mathbf{B}_2) \\ -\nabla \phi_{31} + \mathbf{v}_{31} \times \mathbf{B}_0 = \eta_e \mathbf{j}_{41} - (\mathbf{v}_{11} \times \mathbf{B}_2), \end{cases} \\ \text{System (2)} & \begin{cases} -\nabla p_{42} + \mathbf{j}_{42} \times \mathbf{B}_0 = (\mathbf{v}_{11} \cdot \nabla) \mathbf{v}_{10} + (\mathbf{v}_{10} \cdot \nabla) \mathbf{v}_{11} \\ -\nabla \phi_{32} + \mathbf{v}_{32} \times \mathbf{B}_0 = \eta_e \mathbf{j}_{42} - (\mathbf{v}_{10} \times \mathbf{B}_2), \end{cases} \\ \text{System (3)} & \begin{cases} -\nabla p_{43} + \mathbf{j}_{43} \times \mathbf{B}_0 = (\mathbf{v}_{10} \cdot \nabla) \mathbf{v}_{10} \\ -\nabla \phi_{33} + \mathbf{v}_{33} \times \mathbf{B}_0 = \eta_e \mathbf{j}_{43}, \end{cases} \end{aligned}$$

where,

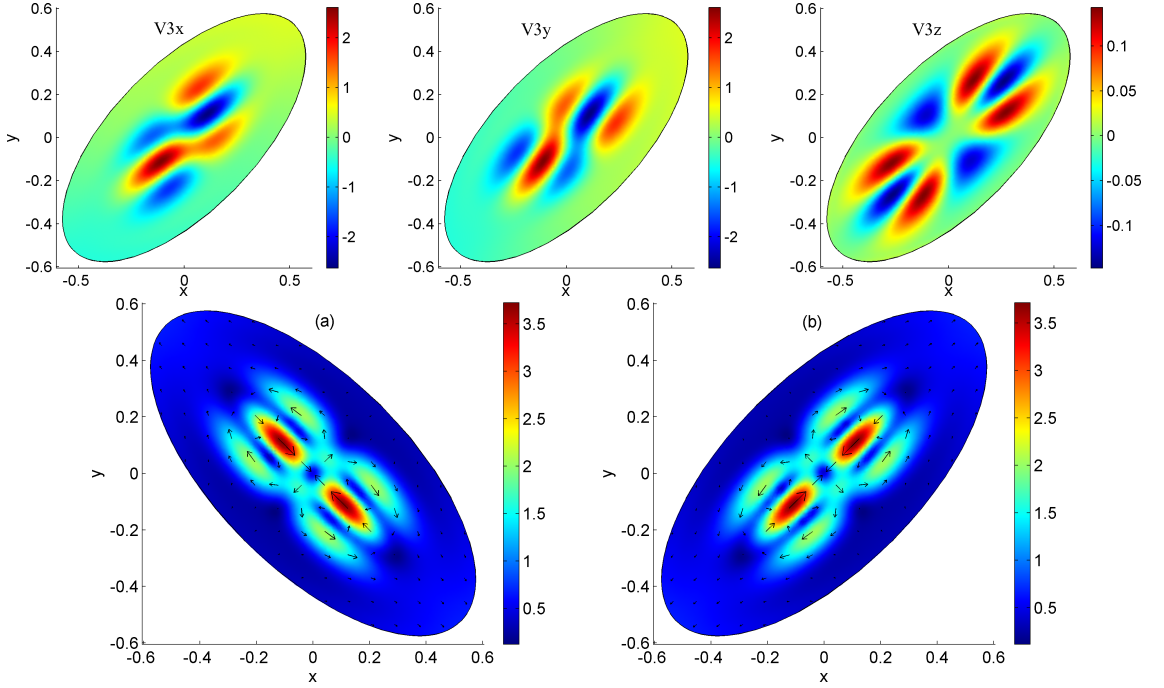


Figure 4.15: Components of the velocity \mathbf{v}_{32} at $z = 0.5$ (top) and its strength and direction, at (a) $z = -0.5$ and (b) $z = 0.5$ (bottom), where \mathbf{v}_{32} vanishes at $z = 0$.

$$\begin{aligned}
 p_4 &= p_{41} + p_{42} + p_{43}, \\
 \mathbf{j}_4 &= \mathbf{j}_{41} + \mathbf{j}_{42} + \mathbf{j}_{43}, \\
 \phi_3 &= \phi_{31} + \phi_{32} + \phi_{33}, \\
 \mathbf{v}_3 &= \mathbf{v}_{31} + \mathbf{v}_{32} + \mathbf{v}_{33}.
 \end{aligned} \tag{4.23}$$

The reason for this is that we already have solutions to these three systems of equations. System (1) can be satisfied by the numerical solutions obtained in Section 4.1.2, since it is similar to equations at fourth order discussed there and System (2) is similar to equations at third order presented in Section 3.4.2, but with a different second-order magnetic field \mathbf{B}_2 . Thus, the equation of motion in System (2) can be satisfied by the corresponding numerical solutions obtained in Section 3.4.2. Substituting the obtained solution for \mathbf{j}_{42} into Ohm's law in System (2) and using Eq. (4.5) for \mathbf{B}_2 , we can now use the general method of integration to solve for ϕ_{32} and \mathbf{v}_{32} . The obtained solutions are illustrated in Figs. (4.14) and (4.15). Comparing the obtained numerical solutions for System (1) and System (2), we can easily see that some of them have common structures but with different signs and magnitudes. For example, the z -component of both \mathbf{j}_{41} and \mathbf{j}_{42} , has four regions with strong current concentration, but with opposite signs and different magnitudes as shown in Figs. (4.5) and (3.11), respectively. Moreover, magnitudes of the solutions of System (1) are proportional to the strength of the rotational flow represented by \mathbf{v}_{11} , whereas the ones of System (2) are proportional to the strength of the stagnation flow represented by \mathbf{v}_{10} as well as the strength of the rotational flow. Thus, varying the strength of the stagnation flow, while keeping a

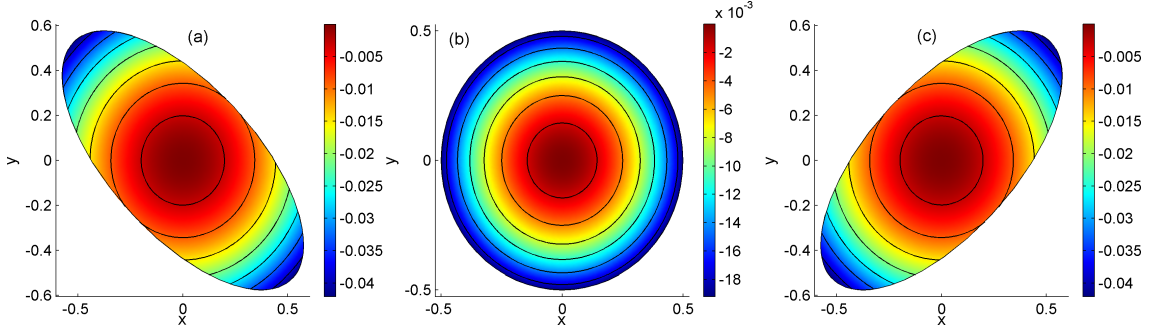


Figure 4.16: Contour plots of the pressure p_{43} variation at (a) $z = -0.5$, (b) $z = 0$ and (c) $z = 0.5$.

fixed rotational flow strength, will lead at some point to a cancelation of these common structures. In the following sections, we consider three examples of composite solutions, which correspond to three different cases relating the magnitudes of \mathbf{j}_{41} and \mathbf{j}_{42} . These different cases are achieved by only varying the strength of the stagnation flow.

Finally, System (3) can be solved analytically, since it is similar to equations at second order discussed in Section 3.4.1. The expressions for p_{43} and \mathbf{j}_{43} can then be written as

$$p_{43} = p_{430}(x^2 - y^2) - \frac{\varphi_0^2}{2\Lambda^4 b_0^2}(x^2 + y^2), \quad (4.24)$$

$$\mathbf{j}_{43} = kb_0\lambda_{430}(y\hat{\mathbf{x}} + x\hat{\mathbf{y}}) + \left(b_0\lambda_{430} - \frac{2p'_{430}(x^2 - y^2)}{b_0k} \right) \hat{\mathbf{z}}, \quad (4.25)$$

where $p_{430}(x^2 - y^2)$ and $\lambda_{430}(x_0, y_0)$ are free functions. Depending on the choice of these free functions, we could then solve for ϕ_{33} and \mathbf{v}_{33} . For simplicity, we shall take p_{430} to be constant and set λ_{430} to zero. Hence, we have $\mathbf{j}_{43} = \mathbf{0}$ and Ohm's law in System (3) can be satisfied by taking ϕ_{33} to be constant and \mathbf{v}_{33} to be zero. The pressure p_{43} variation for this choice of p_{430} is illustrated in Fig. (4.16).

4.2.1 Composite Solutions I: $\|\mathbf{j}_{41}\|_{\max} > \|\mathbf{j}_{42}\|_{\max}$

We start by considering a case where the magnitude of \mathbf{j}_{41} is greater than the one of \mathbf{j}_{42} , which corresponds to a situation where the rotational flow is stronger than the stagnation flow away from the $z = 0$ plane. Contours of the corresponding composite electric potential ϕ_1 , which are streamlines for the composite velocity \mathbf{v}_1 , are illustrated in Fig. (4.17) at three different planes. At the $z = 0$ plane, $\mathbf{v}_{11} = \mathbf{0}$ and thus we only have a stagnation flow. But, at a distance from the symmetry plane $z = 0$, we see that both types of flows have contributed to the flow structure, namely, we have a rotational flow towards the z -axis surrounded by two stagnation flows. The

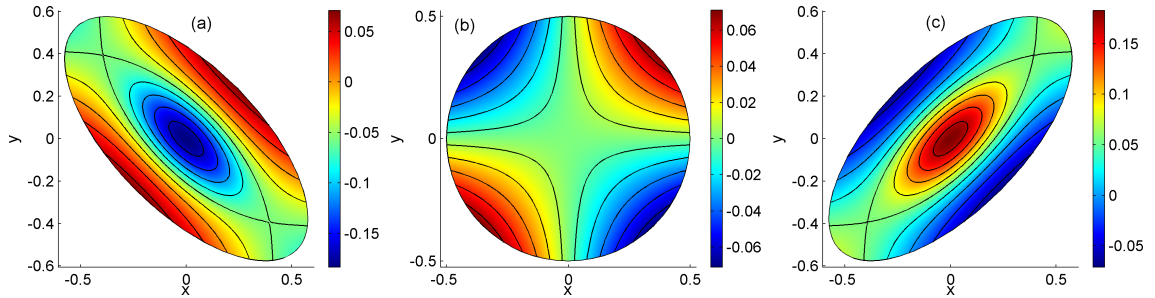


Figure 4.17: Contour plots of the composite electric potential ϕ_1 , at (a) $z = -0.5$, (b) $z = 0$ and (c) $z = 0.5$

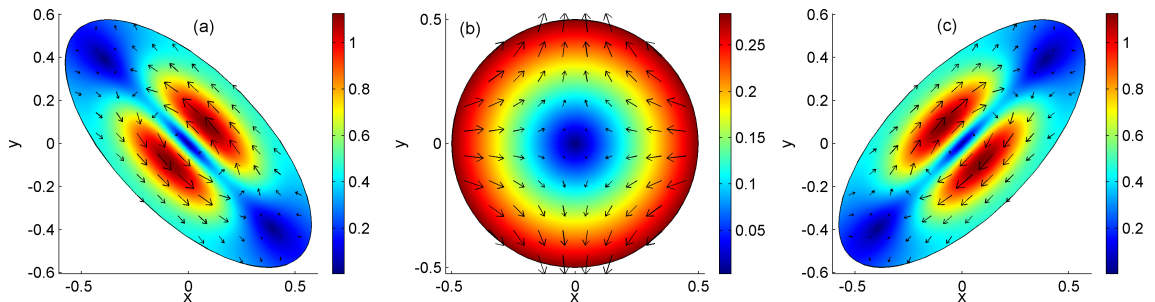


Figure 4.18: Strength and direction of the composite velocity \mathbf{v}_1 at (a) $z = -0.5$, (b) $z = 0$ and (c) $z = 0.5$.

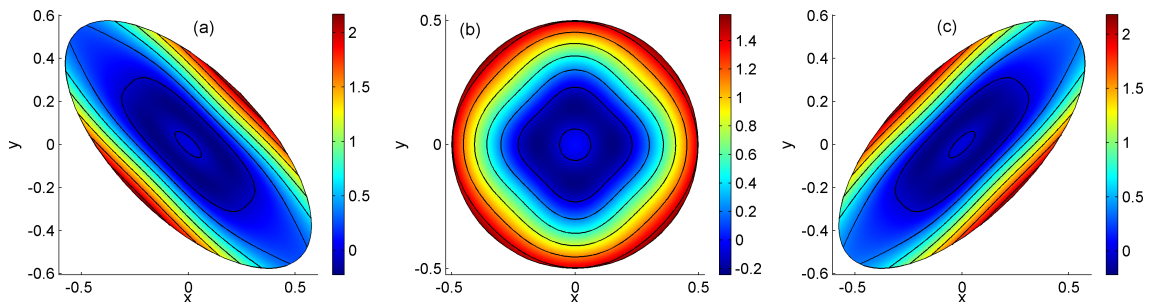


Figure 4.19: Contour plots of the composite pressure p_4 at (a) $z = -0.5$, (b) $z = 0$ and (c) $z = 0.5$.

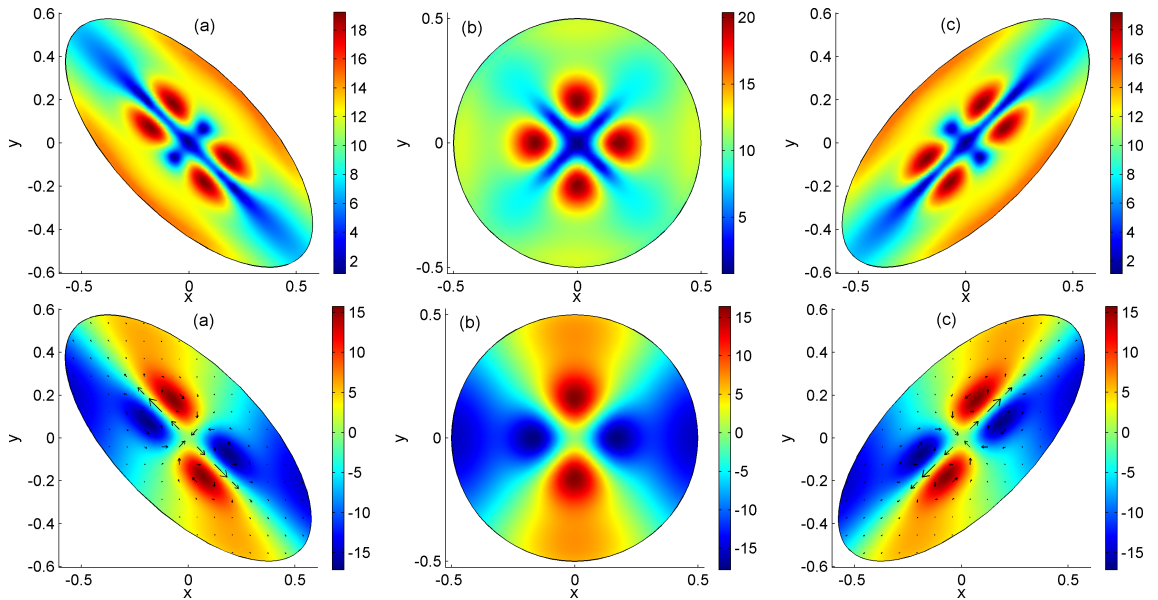


Figure 4.20: Illustration of the magnitude of the composite current \mathbf{j}_4 (top) and its z -component, j_{4z} , with the arrows representing the direction of \mathbf{v}_3 (bottom) at (a) $z = -0.5$, (b) $z = 0$ and (c) $z = 0.5$. Note that $\mathbf{v}_3 = \mathbf{0}$ at $z = 0$.

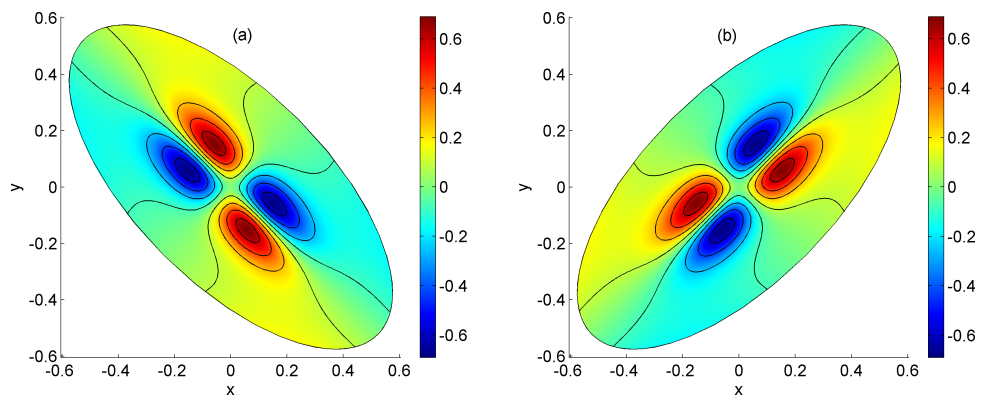


Figure 4.21: Contour plots of the composite electric potential ϕ_3 at (a) $z = -0.5$ and (b) $z = 0.5$, where ϕ_3 vanishes at the $z = 0$ plane.

strength and direction of the corresponding composite velocity \mathbf{v}_1 are shown in Fig. (4.18), which confirms the appearance of a counter-rotational flow above and below the $z = 0$ plane, where we only have a stagnation flow. It also confirms that, at distance from the $z = 0$ plane, the strength of the rotational flow is greater than the one of the stagnation flow. Using (4.23), the composite solutions to equations at fourth order are illustrated in Figs. (4.19) - (4.22), which show that the overall structures of these solutions are still dominated by solutions of System (1), which correspond to the pure solution case. Solutions to equations in System (2) have mainly two effects. The first one is to reduce the magnitude of the pure case solutions, except for the pressure p_4 , which almost has the same magnitude as the one of the pure case, p_{41} . But, the effect of the pressure p_{43} is clearly seen in the structure of p_4 , which altered the shape of contours of p_{41} as shown in Fig. (4.19). The second effect of solutions to equations in System (2) is to introduce new structures towards the boundary, as seen in Figs. (4.20) - (4.22). The current concentrations toward the boundary represent the effect of the gradients of the pressure p_{42} and the weaker contributions toward the boundary in the electric potential ϕ_3 and the velocity \mathbf{v}_3 are due to the appearance of the advection term $\mathbf{v}_{01} \times \mathbf{B}_2$ in Ohm's law at fourth order. The effect of the pressure p_{43} , which its magnitude is proportional to the strength of the stagnation flow, is limited to the vicinity of the z -axis with a maximum contribution at the $z = 0$ plane. This effect plays an important role in minimizing the contribution of the fourth-order pressure p_4 in comparison with the one of the second-order pressure p_2 , which help improving the convergence of the expansion scheme for the pressure p as we will see in the total pressure approximation. At fourth order, we only left with solving the following Ampere's law:

$$\begin{aligned}\nabla \times \mathbf{B}_4 &= \mathbf{j}_4, \\ \mathbf{n} \cdot \mathbf{B}_4 &= 0,\end{aligned}$$

for \mathbf{B}_4 . Field lines and strength of the resultant magnetic field are illustrated in Fig. (4.23), which is similar to the one in the pure case, but with less magnitude and extra contribution towards the boundary.

Now, to calculate an approximation of the total composite solution for each variable for this case, we shall combine the obtained solutions at different orders of M_A , again using $M_A = 0.2$. The obtained total composite solution approximations are illustrated in Figs. (4.24) - (4.27). The total magnetic field approximation for the composite solution case is similar to the one of the pure solution case, since the zeroth and second order magnetic fields \mathbf{B}_0 and \mathbf{B}_2 , respectively, are the same for both cases and the fourth order magnetic field contribution $M_A^4 \mathbf{B}_4$ is even smaller for this case. The total composite pressure approximation, $p = p_{00} + M_A p_{10} + M_A^2 p_2 + M_A^3 p_{30} + M_A^4 p_4 + M_A^5 p_{50} + \mathcal{O}(M_A^6)$ is shown in Fig. (4.24), which shows that contribution of the fourth-order pressure term, $M_A^4 p_4$, is still limited to the vicinity of the z -axis, where the second order pressure $p_2 = 0$, and it is smaller than the contribution of the one in the pure solution case. Figure (4.25)

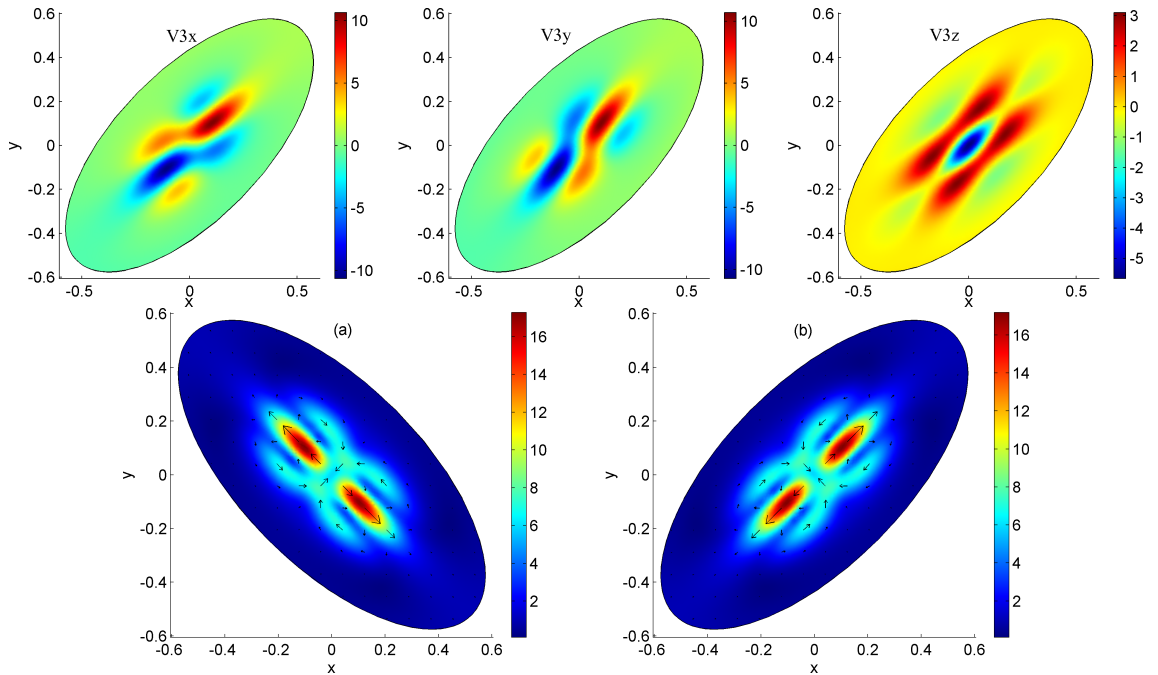


Figure 4.22: Components of the composite velocity \mathbf{v}_3 at $z = 0.5$ (top) and its strength and direction, at (a) $z = -0.5$ and (b) $z = 0.5$ (bottom), where $\mathbf{v}_3 = 0$ at $z = 0$.

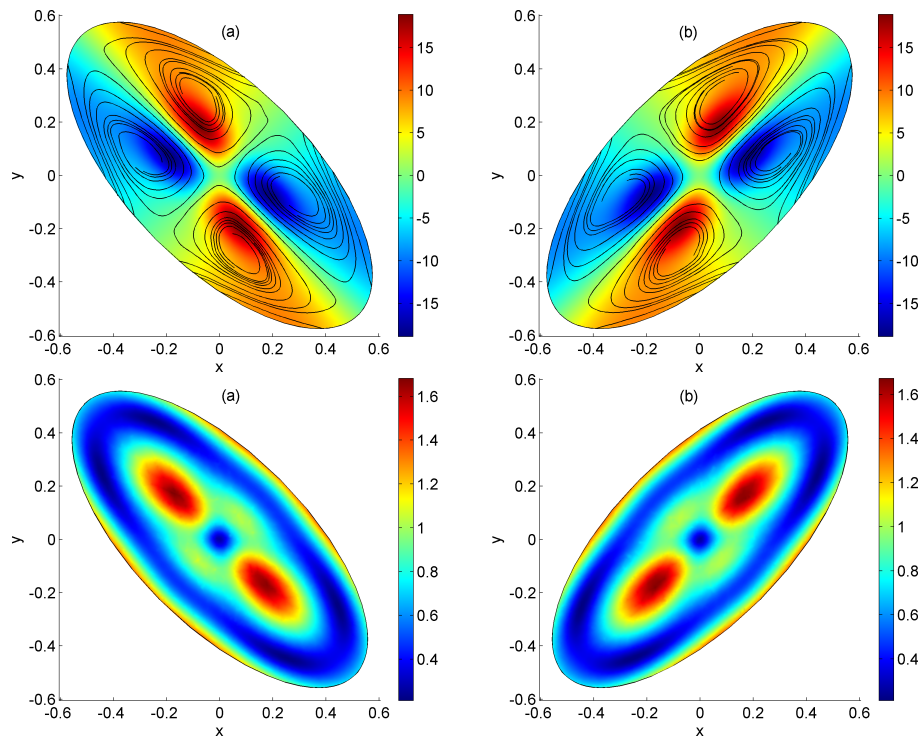


Figure 4.23: Projection of field lines of the magnetic field \mathbf{B}_4 where the background color indicates the magnitude of the current j_{4z} (top) and the strength of \mathbf{B}_4 (bottom) at (a) $z = -0.5$ and (b) $z = 0.5$.

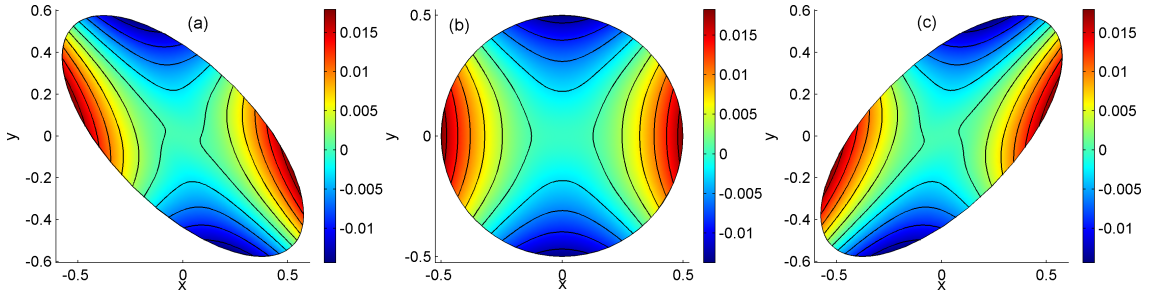


Figure 4.24: Contour plots of the composite pressure $p = M_A^2 p_2 + M_A^4 p_4$ variation at (a) $z = -0.5$, (b) $z = 0$ and (c) $z = 0.5$.

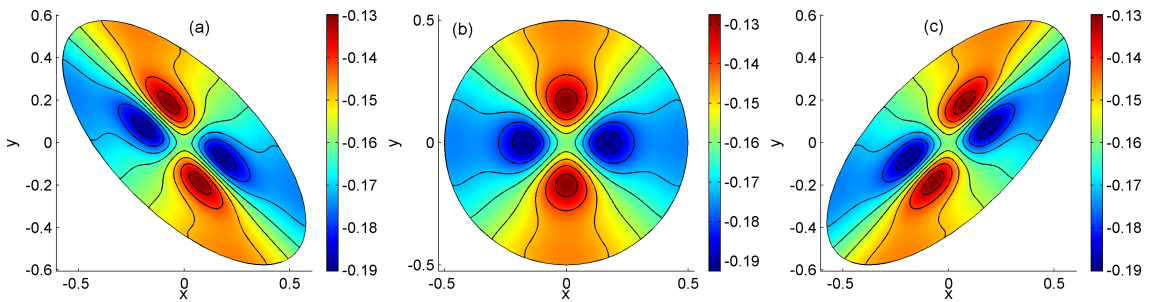


Figure 4.25: Illustration of the z -component of the composite current, $j_z = M_A^2 j_{2z} + M_A^4 j_{4z}$ at (a) $z = -0.5$, (b) $z = 0$ and (c) $z = 0.5$.

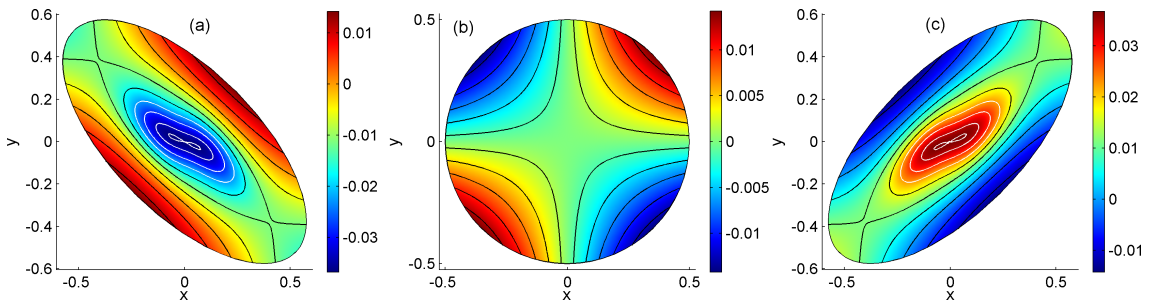


Figure 4.26: Contour plots of the composite electric potential $\phi = M_A \phi_1 + M_A^3 \phi_3$ at (a) $z = -0.5$, (b) $z = 0$ and (c) $z = 0.5$.

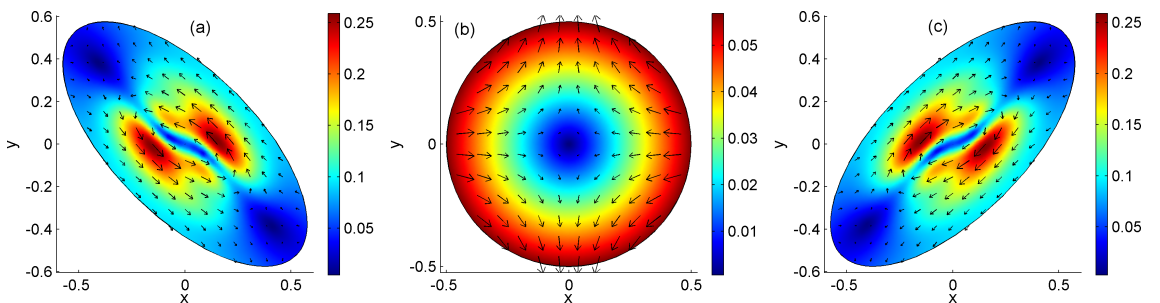


Figure 4.27: Strength and direction of the velocity $\mathbf{v} = M_A \mathbf{v}_1 + M_A^3 \mathbf{v}_3$ at (a) $z = -0.5$, (b) $z = 0$ and (c) $z = 0.5$.

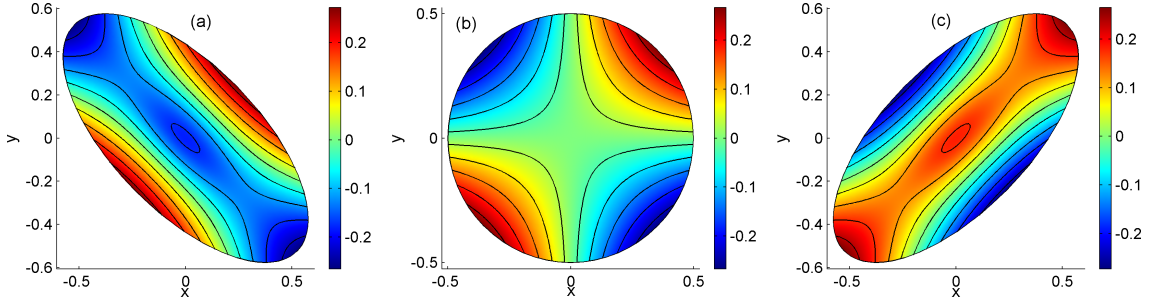


Figure 4.28: Contour plots of the composite electric potential ϕ_1 , at (a) $z = -0.5$, (b) $z = 0$ and (c) $z = 0.5$

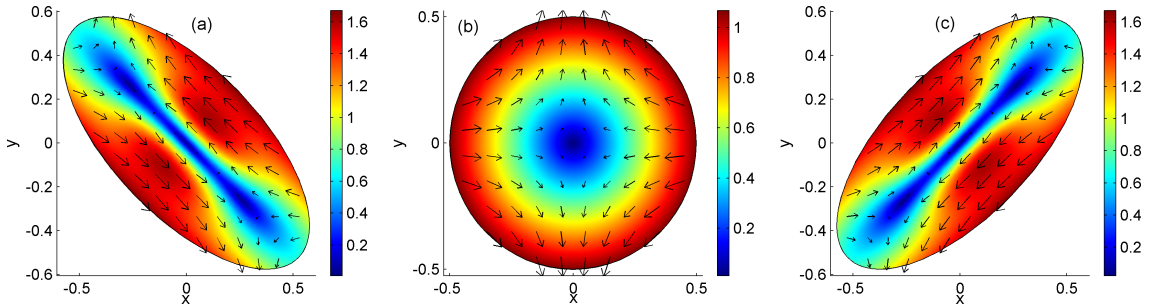


Figure 4.29: Strength and direction of the composite velocity \mathbf{v}_1 at (a) $z = -0.5$, (b) $z = 0$ and (c) $z = 0.5$.

illustrates the structure of the z -component of the approximated total composite current, $j_z = M_A^2 j_{2z} + M_A^4 j_{4z} + \mathcal{O}(M_A^6)$, which still shows the appearance of a saddle-type current structure at $x = y = 0$, but with less deviation from the dominant constant second order current contribution $M_A^2 j_{2z}$ compared with the pure solution case. Contours of the total composite electric potential approximation $\phi = M_A \phi_1 + M_A^2 \phi_{20} + M_A^3 \phi_3 + M_A^4 \phi_{40} + \mathcal{O}(M_A^5)$, which represent a projection of streamlines for the total composite velocity approximation $\mathbf{v} = M_A \mathbf{v}_1 + M_A^3 \mathbf{v}_3 + \mathcal{O}(M_A^5)$, are shown in Fig. (4.26), where we can see that the third order velocity contribution $M_A^3 \mathbf{v}_3$ is still playing a role in the vicinity of the z -axis where $\mathbf{v}_1 = \mathbf{0}$. This contribution of $M_A^3 \mathbf{v}_3$ together with the composite first-order velocity contribution $M_A \mathbf{v}_1$ has led to a formation of multiple X and O -type flows in the reconnection region at distances from the $z = 0$ plane, where we only have a stagnation flow. The strength and direction of the total composite velocity approximation are shown in Fig. (4.27) which shows that, away from the z -axis, we still have counter-rotational flow above and below the $z = 0$ plane and that the magnitude of this velocity is smaller than the one in the pure solution case.

4.2.2 Composite Solutions II: $\|\mathbf{j}_{41}\|_{\max} \approx \|\mathbf{j}_{42}\|_{\max}$

Here we shall increase the strength of the stagnation flow to lead to a situation where the maximum contributions of the currents \mathbf{j}_{41} and \mathbf{j}_{42} are almost equal in magnitude which might in turn lead to a cancelation of the four regions of strong current concentration. The corresponding first order composite electric potential and velocity for this case are illustrated in Figs. (4.28) and (4.29), which show that we still have counter-rotational flows toward the z -axis surrounded by two stagnation flows with the stagnation flow being stronger than the rotational one. Composite solutions to equations at fourth order, including Ampere's law, are illustrated in Figs. (4.30) - (4.34). Figure (4.30) shows that the contribution of p_{42} and p_{43} , which are proportional to the strength of the stagnation flow, are clearly seen especially at the $z = 0$ plane, with the latter is strong enough to minimize the magnitude of the pressure p_4 in the vicinity of the z -axis, which now almost equal to zero. Hence, this effect will limit the contribution of the fourth-order pressure in the total pressure approximation, since it used to contribute only in the vicinity of the z -axis. The current, \mathbf{j}_4 , structure is illustrated in Fig. (4.31), which shows that now all components of \mathbf{j}_4 have contributed to its magnitude and that the four regions of current concentrations become very weak as expected. The current structure is now dominated by gradients of the pressure p_{32} , since the inertial terms have the effect of cancelling one another. Similarly, the four regions of strong electric potential, ϕ_3 , concentration that appeared in the previous cases as a result of integrating the resistive term $\eta_c \mathbf{j}_4$ are now about to disappear, since the current \mathbf{j}_4 has almost no such a structure and hence, the structure of ϕ_3 is dominated by the the advection term $\mathbf{v}_{01} \times \mathbf{B}_2$, which contributes only towards the boundary as shown in Fig. (4.32). With such a structure, we do not expect the third-order electric potential, ϕ_3 , to contribute to the total electric potential approximation, since it has a contribution only in the vicinity of the z -axis in the previous cases. Figure (4.33) illustrates the velocity field \mathbf{v}_3 , which shows that the third-order velocity is now very weak, compared to the previous cases, with only an X -point in the centre. Finally, the magnetic field at fourth order for this case is shown in Fig. (4.34), which shows that the two regions of magnetic field concentration presented in the previous cases have now disappeared and that the maximum strength of \mathbf{B}_4 is now towards the boundary.

Now, combining the obtained analytical and numerical solutions at different orders of M_A gives a total composite solution approximation for each variable up to fifth order. These solutions are illustrated in Figs. (4.35) - (4.38), which show that the solutions for this case are dominated by the lowest order terms everywhere including the vicinity of the z -axis, except for the current where we still have a contribution from the fourth order term $M_A^4 \mathbf{j}_4$. But, this contribution is small compared to the previous cases and only limited towards the boundary, where the current has it maximum deviation from the dominant constant second order current contribution $M_A^2 \mathbf{j}_2$. Therefore, in this case, i.e., the case where the stagnation flow is slightly stronger than the rotational flow (taken here $\|\mathbf{v}_{10}\|_{\max} \approx 1.5 \|\mathbf{v}_{11}\|_{\max}$), the analytical lowest order solutions or equivalently, the kine-

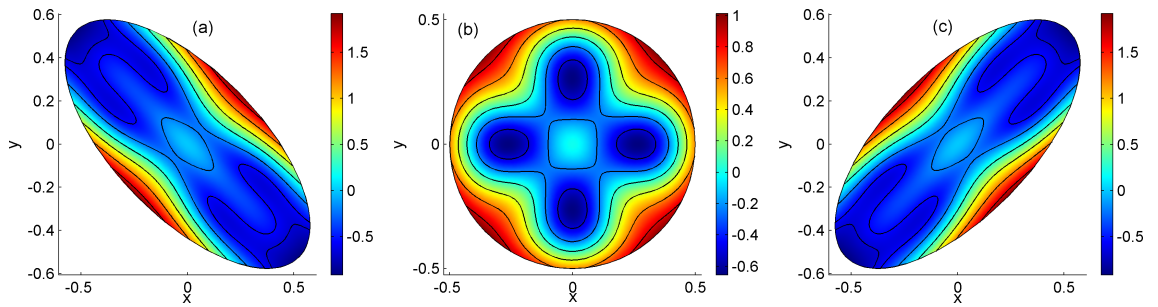


Figure 4.30: Contour plots of the composite pressure p_4 at (a) $z = -0.5$, (b) $z = 0$ and (c) $z = 0.5$.

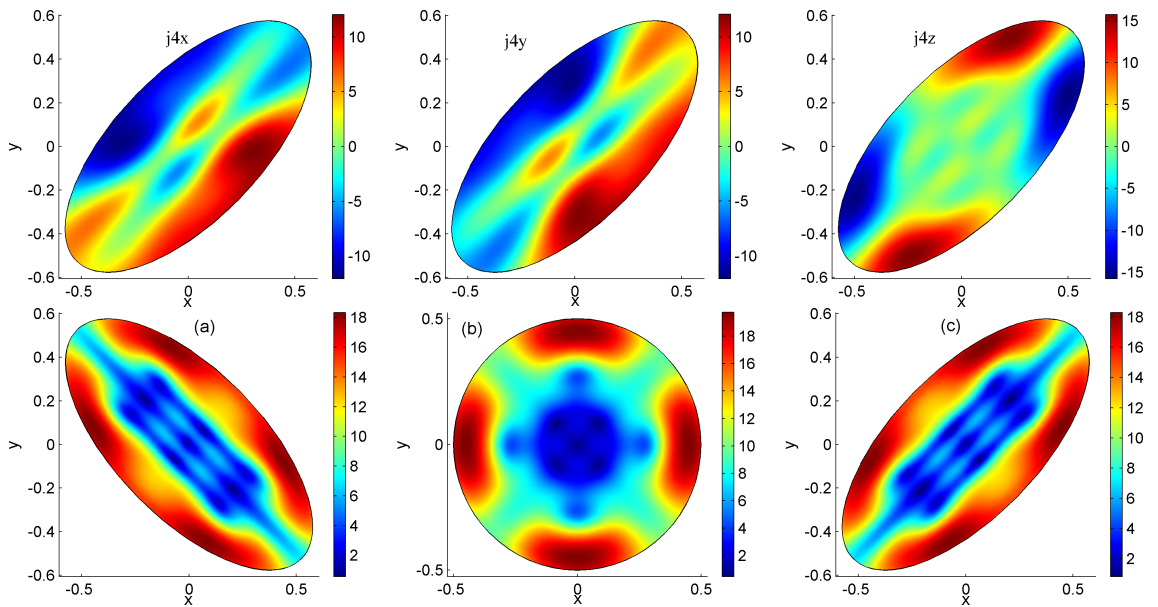


Figure 4.31: Components of the composite current \mathbf{j}_4 at $z = 0.5$ (top) and its magnitude at (a) $z = -0.5$, (b) $z = 0$ and (c) $z = 0.5$ (bottom).

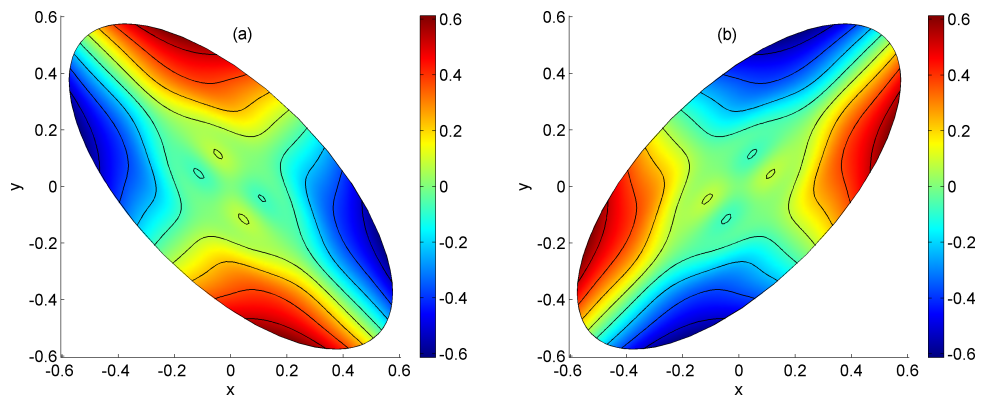


Figure 4.32: Contour plots of the composite electric potential ϕ_3 at (a) $z = -0.5$ and (b) $z = 0.5$, where $\phi_3 = 0$ at $z = 0$.

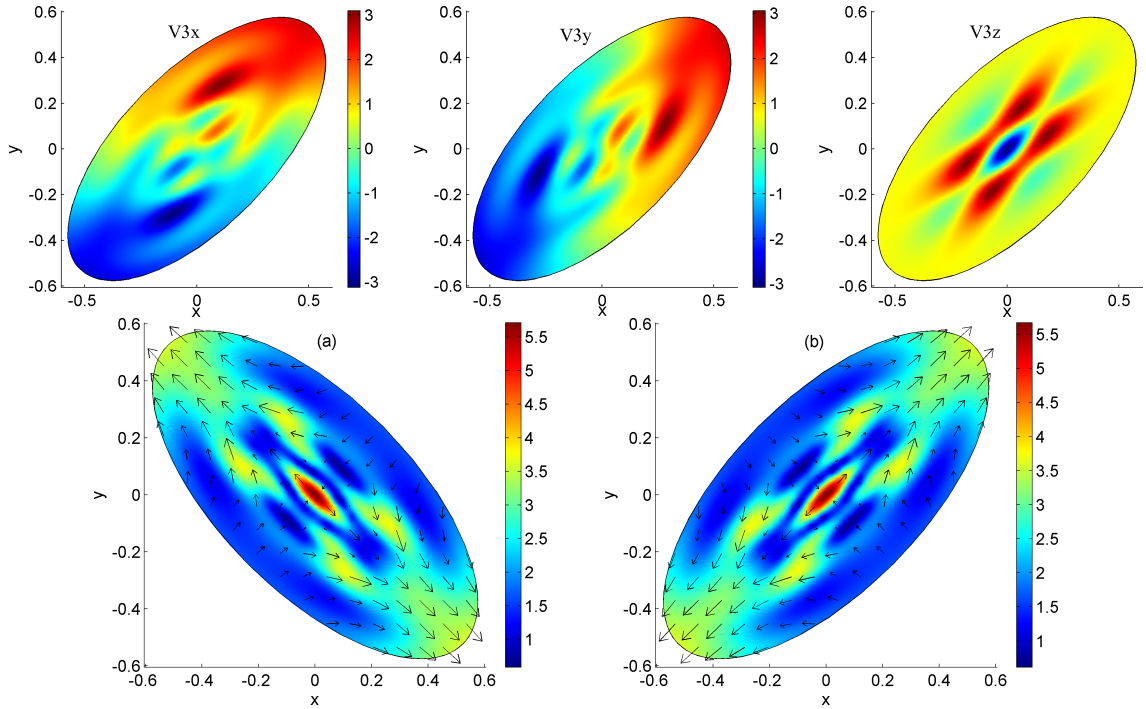


Figure 4.33: Components of the composite velocity \mathbf{v}_3 at $z = 0.5$ (top) and its strength and direction, at (a) $z = -0.5$ and (b) $z = 0.5$ (bottom). Here, $\mathbf{v}_3 = \mathbf{0}$ at $z = 0$.

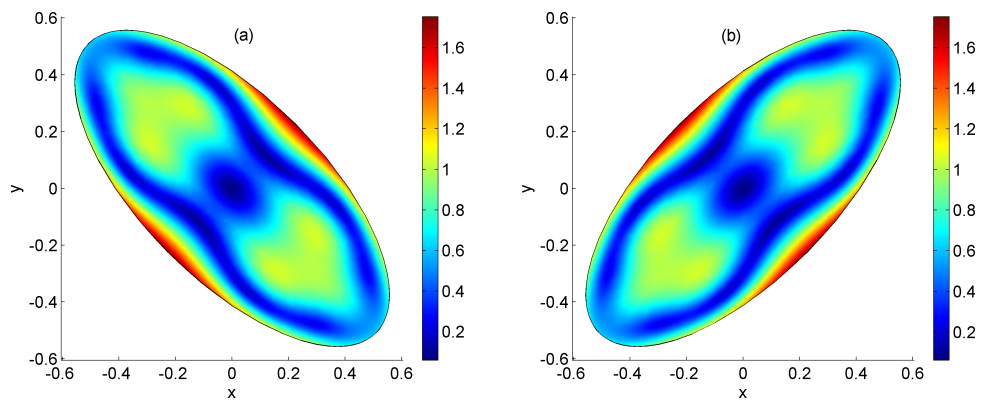


Figure 4.34: Strength of the magnetic field B_4 at (a) $z = -0.5$ and (b) $z = 0.5$.

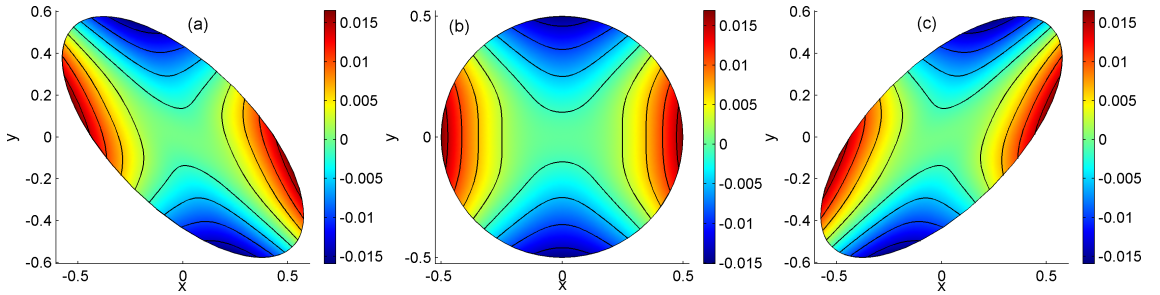


Figure 4.35: Contour plots of the composite pressure $p = M_A^2 p_2 + M_A^4 p_4$ variation at (a) $z = -0.5$, (b) $z = 0$ and (c) $z = 0.5$.

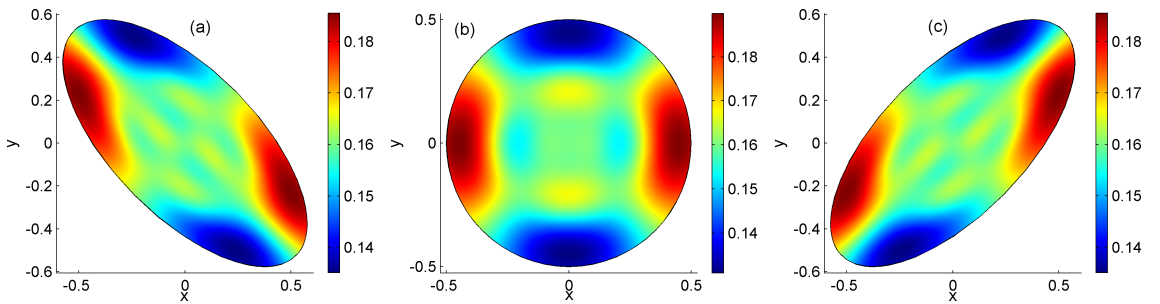


Figure 4.36: Illustration of the composite current $\mathbf{j} = M_A^2 \mathbf{j}_2 + M_A^4 \mathbf{j}_4$ at (a) $z = -0.5$, (b) $z = 0$ and (c) $z = 0.5$.

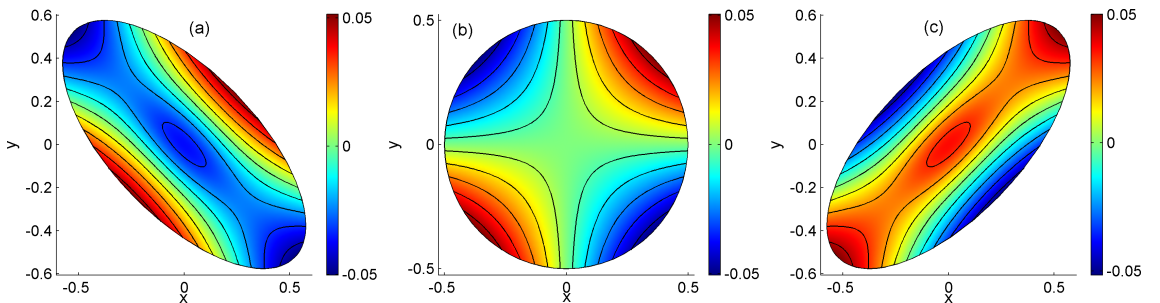


Figure 4.37: Contour plots of the composite electric potential $\phi = M_A \phi_1 + M_A^3 \phi_3$ at (a) $z = -0.5$, (b) $z = 0$ and (c) $z = 0.5$.

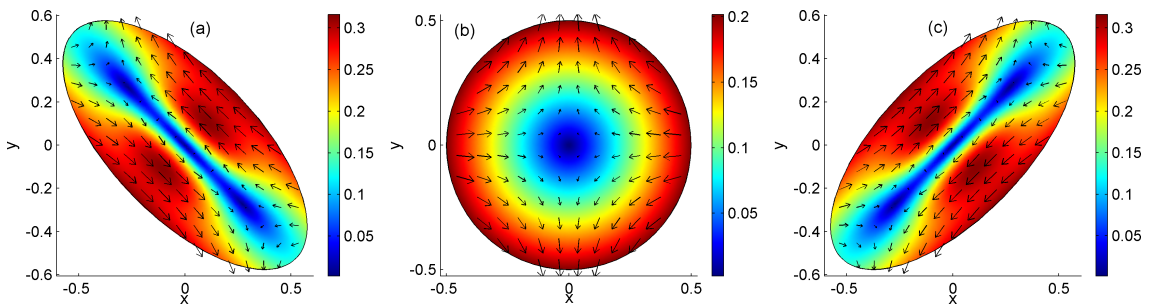


Figure 4.38: Strength and direction of the velocity $\mathbf{v} = M_A \mathbf{v}_1 + M_A^3 \mathbf{v}_3$ at (a) $z = -0.5$, (b) $z = 0$ and (c) $z = 0.5$.

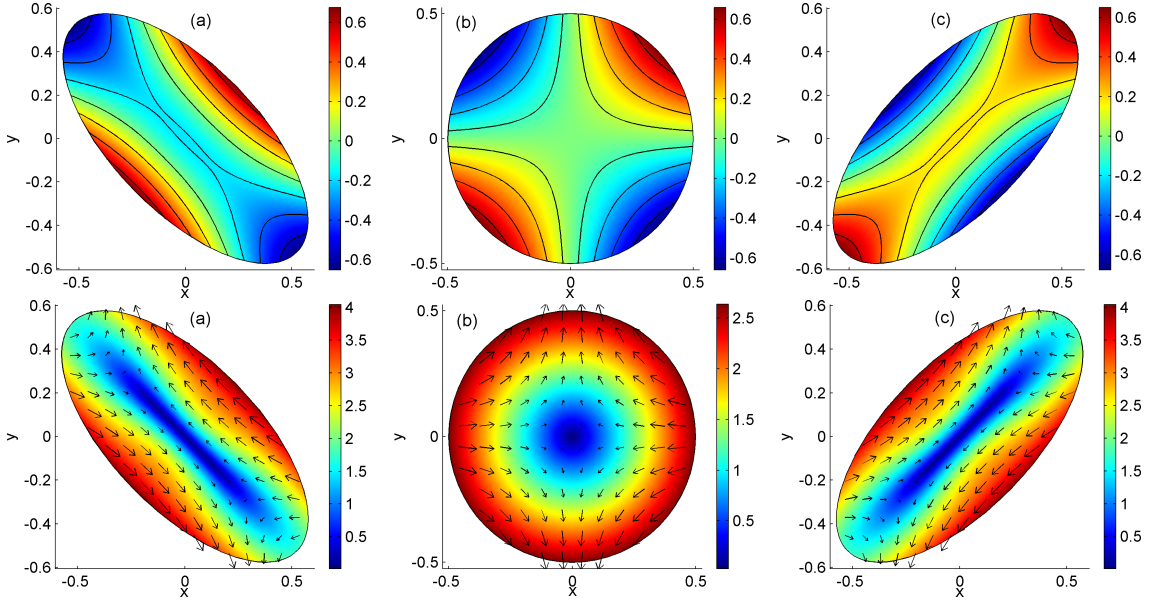


Figure 4.39: Contour plots of the composite electric potential ϕ_1 (top) and the strength and direction of the composite velocity \mathbf{v}_1 (bottom), at (a) $z = -0.5$, (b) $z = 0$ and (c) $z = 0.5$.

matic solutions are very good approximations to the solutions of the full resistive MHD equations provided that the contribution of the remaining higher order solutions are very small, which is, in principal, possible due to the freedom we have in the expansion and integration schemes.

4.2.3 Composite Solutions III: $\|\mathbf{j}_{41}\|_{\max} < \|\mathbf{j}_{42}\|_{\max}$

The last example of composite solutions we present is the one related to a situation where the magnitude of \mathbf{j}_{41} is less than the one of \mathbf{j}_{42} . This could be achieved by increasing the strength of the stagnation flow to a situation where it is much stronger than the one of the rotational flow. The corresponding composite electric potential and velocity at first order for this case are illustrated in Fig. (4.39), which confirms that the rotational flow is now very weak and that stagnation flows dominate the flow structure. Solutions to equations at fourth order, which are now dominated by solutions of System (2) are illustrated in Figs. (4.40) - (4.44). Figure (4.40) shows that the fourth order pressure, p_4 , structure is now dominated by p_{42} and p_{43} , since their magnitudes are proportional to the strength of the stagnation flow. The four regions of current concentration are now back to the structure of \mathbf{j}_4 , which is dominated by its z -component, as shown in Fig. (4.41). These four regions have different signs from the ones in the first example of composite solutions presented in Section 4.2.1 and we also have other four regions of current concentration toward the boundary, since the fourth-order current is now dominated by \mathbf{j}_{42} . Similarly, the four regions of electrical potential concentration resulting from the integration of the resistive term $\eta_c \mathbf{j}_4$ also appear in the structure of the third-order electrical potential ϕ_3 as well as the other four regions

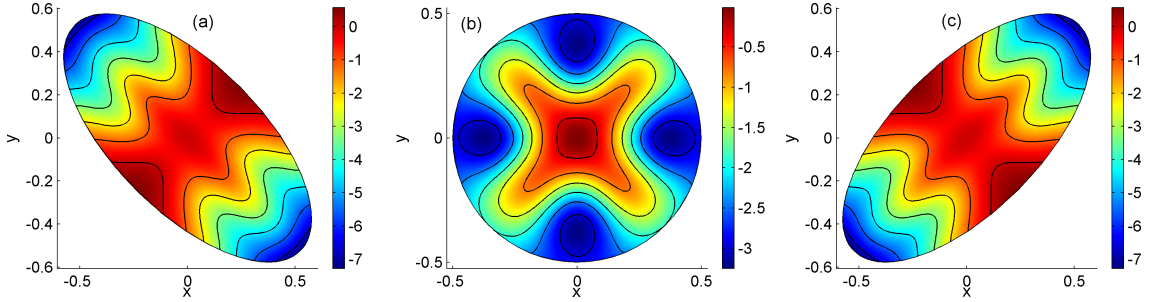


Figure 4.40: Contour plots of the composite pressure p_4 at (a) $z = -0.5$, (b) $z = 0$ and (c) $z = 0.5$.

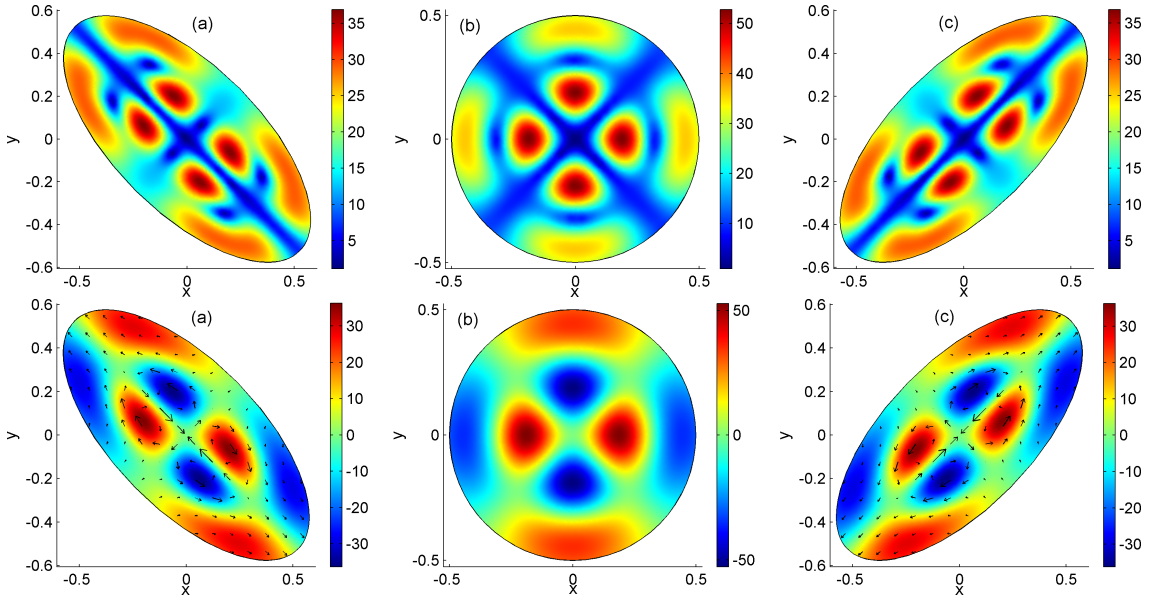


Figure 4.41: Illustration of the magnitude of composite the current \mathbf{j}_4 (top) and its z -component, j_{4z} , with the arrows representing the direction of \mathbf{v}_3 (bottom) at (a) $z = -0.5$, (b) $z = 0$ and (c) $z = 0.5$. Note that $\mathbf{v}_3 = \mathbf{0}$ at $z = 0$.

toward the boundary which come as a result of integrating the advection term $\mathbf{v}_{01} \times \mathbf{B}_2$, as shown in Fig. (4.42). The corresponding velocity at third order, \mathbf{v}_3 , is illustrated in Fig. (4.43), which has a similar structure to \mathbf{v}_{32} and which is now strong enough to contribute to the total velocity approximation. Figure (4.44) illustrates field lines and strength of the fourth-order magnetic field \mathbf{B}_4 , which now has a more complicated structure than the one of \mathbf{B}_3 presented in Section 3.4.2, since the four regions of the current \mathbf{j}_4 concentration toward the boundary have almost the same strength as the ones toward the centre, whereas the current \mathbf{j}_3 has weaker structures toward the boundary than those toward the centre.

Finally, the total composite solution approximation for each variable for this case are illustrated in Figs. (4.45) - (4.48), which show that solutions to equations at fourth order have now contributed

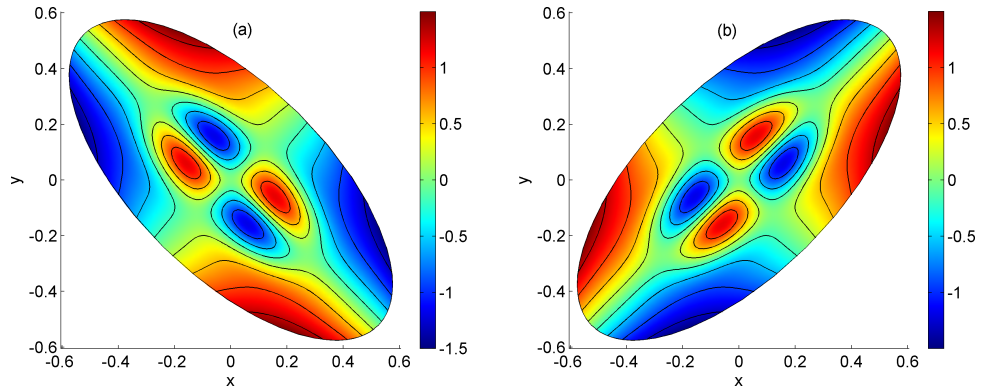


Figure 4.42: Contour plots of the composite electric potential ϕ_3 at (a) $z = -0.5$ and (b) $z = 0.5$, where ϕ_3 vanishes at the $z = 0$ plane.

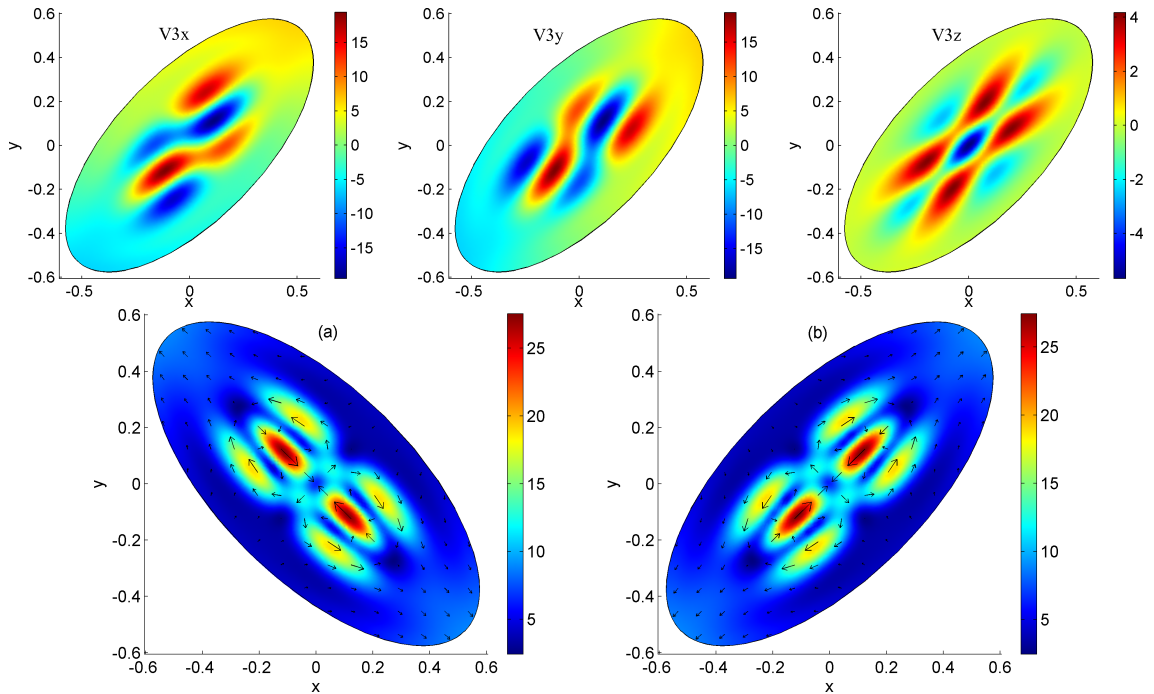


Figure 4.43: Components of the composite velocity \mathbf{v}_3 at $z = 0.5$ (top) and its strength and direction, at (a) $z = -0.5$ and (b) $z = 0.5$ (bottom), where $\mathbf{v}_3 = \mathbf{0}$ at $z = 0$.

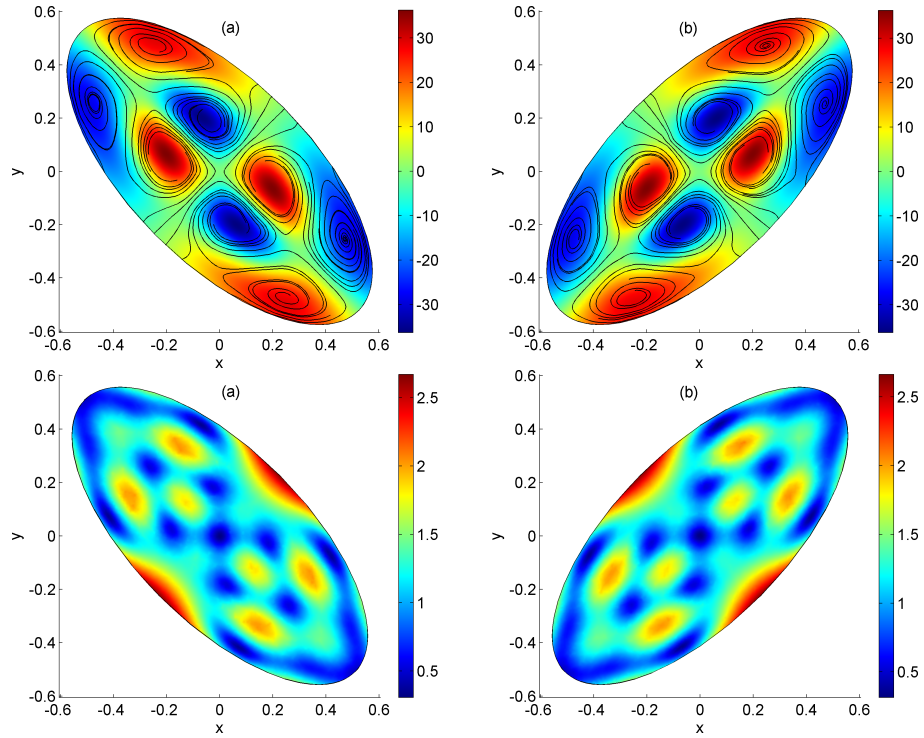


Figure 4.44: Projection of field lines of the magnetic field \mathbf{B}_4 where the background color indicates the magnitude of the current j_{4z} (top) and the strength of \mathbf{B}_4 (bottom) at (a) $z = -0.5$ and (b) $z = 0.5$.

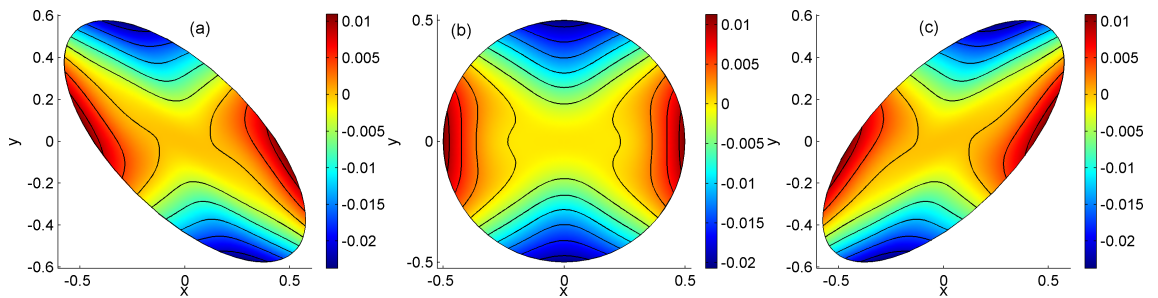


Figure 4.45: Contour plots of the composite pressure $p = M_A^2 p_2 + M_A^4 p_4$ variation at (a) $z = -0.5$, (b) $z = 0$ and (c) $z = 0.5$.

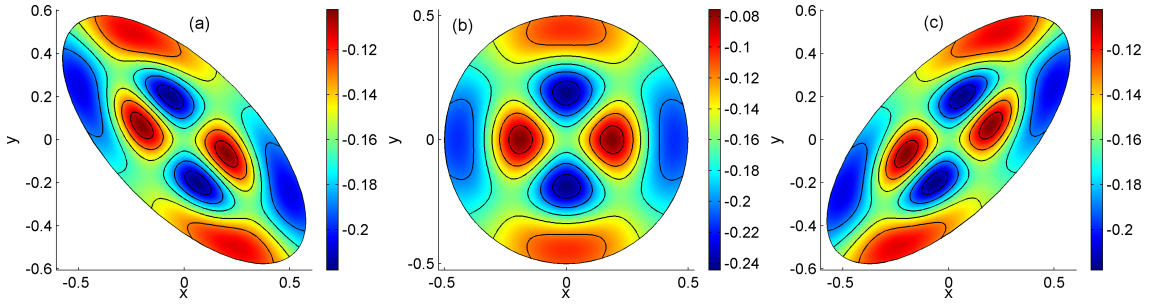


Figure 4.46: Illustration of the composite current $j_z = M_A^2 j_{2z} + M_A^4 j_{4z}$ at (a) $z = -0.5$, (b) $z = 0$ and (c) $z = 0.5$.

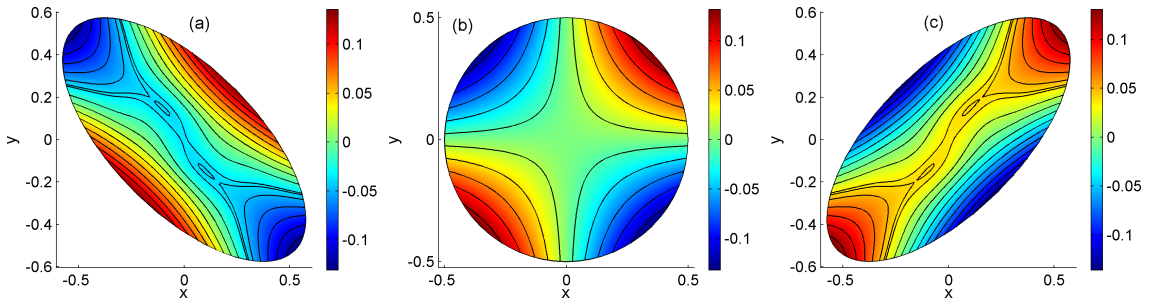


Figure 4.47: Contour plots of the composite electric potential $\phi = M_A \phi_1 + M_A^3 \phi_3$ at (a) $z = -0.5$, (b) $z = 0$ and (c) $z = 0.5$.

to the total composite solution approximations. Figure (4.46) shows that we have a total current with a saddle-type structure at $x = y = 0$ similar to the one in Section 4.2.1, but with different orientation. We also have a total flow with very fine structures of multiple X and O -points as shown in Figs. (4.47) and (4.48).

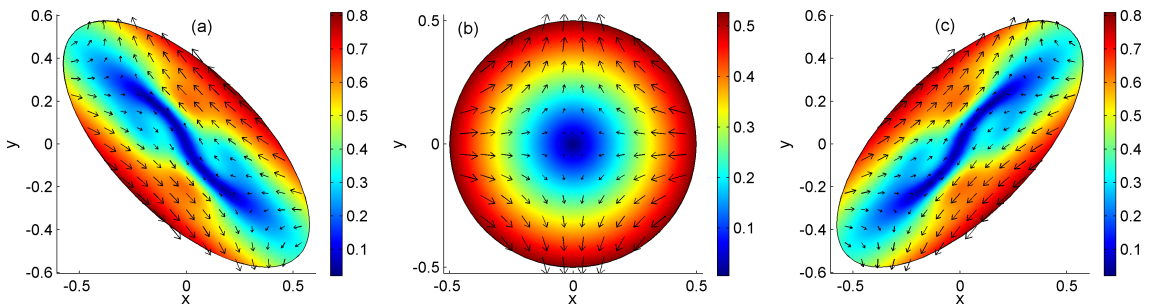


Figure 4.48: Strength and direction of the composite velocity $\mathbf{v} = M_A \mathbf{v}_1 + M_A^3 \mathbf{v}_3$ at (a) $z = -0.5$, (b) $z = 0$ and (c) $z = 0.5$.

4.3 Summary

We have used the stationary MHD model presented in Chapter 3 to extend the kinematic model presented by Hornig and Priest (2003). Solutions to equations at different orders were obtained using the integration scheme discussed in Section 3.3. In order to have a proper extension of the kinematic model, the system were solved up to fifth order since the inertial term in the equation of motion first appeared at fourth order. Lower-order analytical solutions were chosen to have specific forms in order to allow for a direct comparison with the solutions obtained in the kinematic model. Up to second order, the obtained analytical solutions for both cases of pure and composite solutions agree very well with the corresponding solutions in the kinematic model which confirms that in a certain limit the kinematic solutions satisfy the full stationary MHD equations. However, by including numerical solutions of equations at higher orders, solutions of the full stationary MHD equations started to deviate from the kinematic ones specially close to the z -axis. This is due to including the equation of motion in the analysis or in particular the appearance of the inertial term in equations at higher order. The inertial term clearly affects the current density, which in turn modifies the plasma velocity. For example, in the case of pure solutions, the inertial term has led to a current density with a saddle point at $x = y = 0$, which in turn resulted in the appearance of a stagnation flow in the vicinity of the z -axis along with rotational flows away from the z -axis. This flow structure is different from the one presented in the kinematic model for the pure solution case where we have rotational flows everywhere away from the $z = 0$ plane.

In the composite solution case, where we have superimposed a stagnation flow on the rotational flow obtained in the pure solution case, the structure of the solutions were found to depend on the relative magnitude of these two different types of flow. Thus, to illustrate this, we have presented three examples of composite solutions obtained by only varying the strength of the superimposed stagnation flow in such a way that the corresponding inertial term in the equation of motion results in three different current structures which in turn leads to different flow structures. We have found that when the maximum strength of the stagnation flow is slightly greater than the one of the rotational flow, the effect of the higher order terms is, in general, negligible and the obtained solutions are dominated by the lower order analytical solutions, which are similar to the kinematic solutions, whereas when the stagnation flow is much stronger than the rotational flow or when the rotational flow is dominant, higher order contributions become very important specially in the vicinity of the z -axis. For example, they have led to the appearance of saddle-type current structure and the existence of fine structures of multiple X and O -point type flows in the reconnection region.

Chapter 5

Three-Dimensional Solutions of the Magnetohydrostatic Equations: Rigidly Rotating Magnetized Coronae in Cylindrical Geometry

“ Blessed is He (The Almighty God) Who has placed constellations in the sky, and has placed therein a lamp (the Sun), and a moon giving light \ominus And it is He Who has made the night and the day in succession, for such who desires to remember or desires to show his gratitude \ominus ”

(Interpretation of the Holy Quran **25**: 61-62)

5.1 Introduction

In the previous two chapters, we have considered a stationary magnetohydrodynamic (MHD) model, where both flow and resistivity were present, since they play very important roles in the process of magnetic reconnection. In this chapter and the following one, we will consider a situation where the flow and non-ideal resistive terms can be neglected. Hence, the governing equations in the stationary MHD model will reduce to a set of magnetohydrostatic (MHS) equations as shown in Section 1.2.3. This is relevant to many astrophysical applications, such as rotating coronae, which we discuss here. However, finding three-dimensional (3D) solutions of the MHS equations, i.e. solutions with no spatial symmetry, is a formidable task. Only very few analytical solutions are known and even using numerical methods for calculating 3D MHS solutions is usually far from straightforward (e.g. Wiegelmann and Neukirch 2006; Wiegelmann et al. 2007).

Analytic solutions have been found for a number of different cases.¹ If external forces like the gravitational force or the centrifugal force can be neglected, force balance between the Lorentz force and the pressure gradient has to be achieved. A small number of analytical solutions in Cartesian and cylindrical coordinates have been found (e.g. Woolley 1976, 1977; Shivamoggi 1986; Salat and Kaiser 1995; Kaiser and Salat 1996, 1997) and some of them have been generalized to include field-aligned incompressible flows (Petrie and Neukirch 1999).

The case where external forces cannot be neglected is often the more relevant for astrophysical applications. In particular, three-dimensional solutions of the MHS equations in the presence of an external gravitational field have been found for this case, both in Cartesian (e.g. Low 1982, 1984, 1985, 1992, 1993a,b; Neukirch 1997; Neukirch and Rastätter 1999; Petrie and Neukirch 2000) and in spherical coordinates (e.g. Osherovich 1985a,b; Bogdan and Low 1986; Neukirch 1995).

For the case of the presence of external forces, a systematic method for calculating a special class of 3D MHS equilibria has been developed in a series of papers by Low (1985, 1991, 1992, 1993a,b, 2005) and Bogdan and Low (1986). The method is applicable to all external forces derived from a potential and assumes a special form for the electric current density to allow analytical progress. In the simplest possible case, the MHS equations reduce to a linear partial differential equation for the magnetic field. It has been shown that in Cartesian and spherical geometry, the fundamental equation is very similar to a Schrödinger equation (Neukirch 1995; Neukirch and Rastätter 1999). Therefore standard methods such as expansion in terms of orthogonal function systems (e.g. Rudenko 2001) or Green's functions (e.g. Petrie and Neukirch 2000) can be used for finding solutions, and this method has been used to model, for example, the solar corona (e.g. Zhao and Hoeksema 1993, 1994; Zhao et al. 2000; Ruan et al. 2008) and stellar coronae (e.g. Lanza 2008).

While the method has been mainly used to find 3D MHS solutions for the case of an external gravitational potential, Low (1991) has also developed the method for rigidly rotating systems subject to centrifugal forces. For those cases the system is stationary only in the frame of reference rotating with the same angular velocity as the system itself. Recently, Neukirch (2009) has presented a couple of 3D MHS solutions for rigidly rotating magnetospheres in cylindrical geometry, again using the simplest case leading to a linear differential equation for the magnetic field.

In the present contribution we extend the theory to the case where both gravitational and centrifugal force are taken into account. This case is, for example, relevant for the coronal structure of fast rotating stars (e.g. Jardine and Unruh 1999; Jardine 2004; Jardine and van Ballegooijen 2005; Ryan et al. 2005; Townsend and Owocki 2005; Townsend et al. 2005; ud-Doula et al. 2006), in particular for the closed field line region. Often, however, potential magnetic fields are used for models derived from stellar surface data (e.g. Jardine et al. 1999, 2001, 2002; Donati et al. 2006,

¹We explicitly exclude force-free fields from this discussion.

2008; Morin et al. 2008), while there is observational evidence for the non-potentiality of some measured surface magnetic fields (e.g. Hussain et al. 2002). Recently, Mackay and van Ballegoijen (2006) and Yeates et al. (2008) developed a numerical technique to produce sequences of quasi-static non-linear force-free equilibria from time series of observed magnetograms. While this technique was so far only applied to the Sun, it could in principle also be applied to other stars if magnetic field data with a sufficiently high time cadence are obtained. The theory presented in this chapter could improve the potential field models and, in its simplest form, is not computationally more demanding than potential field models.

As in Neukirch (2009), we will present the theory in a general form following Low (1991), but then investigate the somewhat artificial, but illustrative case of a massive rigidly rotating central cylinder. This is done merely for mathematical convenience as it is much easier to impose boundary conditions on a cylindrical boundary. A full solution of the problem would also include a stellar wind on open field line regions and the need to solve a free boundary problem to determine the transition from open to closed field regions. A solution to this problem is beyond the scope of this thesis and we neglect flows altogether. Instead, for the solutions presented in this chapter, we impose boundary conditions on an imaginary outer boundary, similar to the source surface used for potential field models. For this case, we determine solutions using standard numerical methods. In future work, one could as a first step towards solving the full problem, assume that the open field line regions are potential and thus try to determine the boundary between open and closed field line regions.

This chapter is organized as follows. In Section 5.2 we present a brief derivation of the underlying theory, followed by illustrative example solutions in Section 5.3. We conclude with a summary and discussion in Section 5.4.

The result of this chapter can be found in Al-Salti and Neukirch (2009) and Al-Salti et al. (2010).

5.2 Theory

5.2.1 Coordinate Independent Theory

Before moving on to the special case of a massive rigidly rotating cylinder, we briefly outline the basic theory in a coordinate independent form. In this way, the equations derived below are applicable to other cases as well, such as massive rigidly rotating spheres or ellipsoids (stars), or even synchronously rotating double stars, using e.g. the Roche potential.

We basically follow Low (1991) in our outline and refer the reader to his paper for more details (see also Neukirch 2009). The MHS equations in the co-rotating frame of reference are given by

(see Section 1.2.3)

$$\mathbf{j} \times \mathbf{B} - \nabla p - \rho \nabla V = \mathbf{0}, \quad (5.1)$$

$$\nabla \times \mathbf{B} = \mu_0 \mathbf{j}, \quad (5.2)$$

$$\nabla \cdot \mathbf{B} = 0, \quad (5.3)$$

where \mathbf{B} is the magnetic field, \mathbf{j} is the current density, p is the pressure, ρ is the plasma density and V is the combined centrifugal and gravitational potential. We make the assumption that

$$\mu_0 \mathbf{j} = \nabla F \times \nabla V, \quad (5.4)$$

where F is a free function. Substituting this form of the current density \mathbf{j} into the force balance equation (5.1) leads to

$$\begin{aligned} \frac{1}{\mu_0} (\nabla F \times \nabla V) \times \mathbf{B} - \nabla p - \rho \nabla V &= \frac{1}{\mu_0} (\mathbf{B} \cdot \nabla F) \nabla V - \frac{1}{\mu_0} (\mathbf{B} \cdot \nabla V) \nabla F - \nabla p - \rho \nabla V \\ &= \mathbf{0}. \end{aligned}$$

Thus, one finds that

$$p(\varpi, \phi, z) = p(F, V), \quad (5.5)$$

and

$$\left(\frac{\partial p}{\partial F} \right)_V = -\frac{1}{\mu_0} (\mathbf{B} \cdot \nabla V), \quad (5.6)$$

$$\rho = -\left(\frac{\partial p}{\partial V} \right)_F + \frac{1}{\mu_0} (\mathbf{B} \cdot \nabla F). \quad (5.7)$$

Further progress can be made by making an appropriate choice for the free function F . Choosing

$$F(\varpi, \phi, z) = \kappa(V) \mathbf{B} \cdot \nabla V, \quad (5.8)$$

with $\kappa(V)$ a free function, as suggested by Low (1991), leads to a linear relation between magnetic field and current density given by

$$\mu_0 \mathbf{j} = \kappa(V) \nabla (\mathbf{B} \cdot \nabla V) \times \nabla V.$$

Using Eqs. (5.6) and (5.8), we have the following expression

$$p = p_0(V) - \frac{1}{2\mu_0} \kappa(V) (\mathbf{B} \cdot \nabla V)^2 \quad (5.9)$$

for the plasma pressure. Here, $p_0(V)$ is an arbitrary function which represents a hydrostatic background atmosphere. Equation (5.9) can be used, along with Eq. (5.8), to find an expression for the

term $\left(\frac{\partial p}{\partial V}\right)_F$, which can be then substituted into Eq. (5.7) to give the following expression

$$\rho = -\frac{dp_0}{dV} + \frac{1}{2\mu_0} \frac{d\kappa}{dV} (\mathbf{B} \cdot \nabla V)^2 + \frac{1}{\mu_0} \kappa(V) \mathbf{B} \cdot \nabla(\mathbf{B} \cdot \nabla V) \quad (5.10)$$

for the plasma density. An expression for the plasma temperature can be obtained if we assume that the plasma satisfies the equation of state of an ideal gas,

$$T = \frac{\mu p}{\mathcal{R} \rho}, \quad (5.11)$$

where \mathcal{R} is the universal gas constant and μ is the mean molecular weight.

We are now only left with finding an expression for the magnetic field. This can be achieved by realizing that the current density given by Eq. (5.4) can be written as

$$\mu_0 \mathbf{j} = \nabla \times (F \nabla V),$$

which on substituting into Ampère's law (5.2), integrating and using Eq. (5.8) leads to

$$\mathbf{B} = \nabla U + \kappa(V) (\mathbf{B} \cdot \nabla V) \nabla V.$$

Multiplying this equation by ∇V , one can find an expression for the term $\mathbf{B} \cdot \nabla V$ to be

$$\mathbf{B} \cdot \nabla V = \frac{\nabla U \cdot \nabla V}{1 - \kappa(V) (\nabla V)^2}. \quad (5.12)$$

Hence, the magnetic field is given by

$$\mathbf{B} = \nabla U + \frac{\kappa(V)}{1 - \kappa(V) (\nabla V)^2} (\nabla U \cdot \nabla V) \nabla V, \quad (5.13)$$

where the function U that appears due to the integration is a pseudo-potential which determines \mathbf{B} , since the expression for \mathbf{B} is modified by the presence of currents in the system, represented by the factor $1/(1 - \kappa(\nabla V)^2)$, compared to a potential field in which only the gradient of U would appear. This pseudo-potential is determined by substituting (5.13) into the solenoidal constraint (5.3):

$$\nabla \cdot \left(\nabla U + \frac{\kappa(V)}{1 - \kappa(V) (\nabla V)^2} (\nabla U \cdot \nabla V) \nabla V \right) = 0. \quad (5.14)$$

Equation (5.14) is a single partial differential equation for the pseudo-potential U and it is the fundamental equation for the linear case of the theory presented here. An alternative form of this equation is

$$\nabla \cdot (\mathbf{M} \cdot \nabla U) = 0, \quad (5.15)$$

with the 3×3 matrix \mathbf{M} defined as

$$\mathbf{M} = \mathbf{I} + \frac{\kappa(V)}{1 - \kappa(V)(\nabla V)^2} \nabla V \nabla V. \quad (5.16)$$

Here \mathbf{I} is the 3×3 unit matrix. Equation (5.15) is particularly useful if ∇V has more than one non-vanishing component. This would, for example, be the case for the combined gravitational and centrifugal potential outside a massive rigidly rotating sphere. Then, Eq. (5.14) is usually not fully separable.

5.2.2 Cylindrical Geometry

To illustrate how the theory presented above can be used, we treat in this chapter the somewhat artificial, but mathematically simpler case of a cylinder of radius R , infinite length and uniform mass per unit length M , rotating rigidly with angular velocity Ω about its symmetry axis. We use a co-rotating cylindrical coordinate system ϖ, ϕ, z with the z -axis aligned with the rotation axis. The external gravitational potential (normalized to 0 at $\varpi = R$) of such a cylinder is given by

$$\Psi = 2GM \ln(\varpi/R), \quad (5.17)$$

and the combined potential V by

$$V = -\frac{\Omega^2}{2} \varpi^2 + 2GM \ln(\varpi/R). \quad (5.18)$$

Using Eq. (5.13), the components of \mathbf{B} in cylindrical coordinates are

$$B_\varpi = \frac{1}{1 - \kappa(V)(V')^2} \frac{\partial U}{\partial \varpi}, \quad (5.19)$$

$$B_\phi = \frac{1}{\varpi} \frac{\partial U}{\partial \phi}, \quad (5.20)$$

$$B_z = \frac{\partial U}{\partial z}, \quad (5.21)$$

with

$$V' = \frac{dV}{d\varpi}. \quad (5.22)$$

Defining

$$\xi(\varpi) = \kappa(V)(V')^2, \quad (5.23)$$

one can rewrite Eq. (5.14) as

$$\frac{1}{\varpi} \frac{\partial}{\partial \varpi} \left(\frac{\varpi}{1 - \xi(\varpi)} \frac{\partial U}{\partial \varpi} \right) + \frac{1}{\varpi^2} \frac{\partial^2 U}{\partial \phi^2} + \frac{\partial^2 U}{\partial z^2} = 0, \quad (5.24)$$

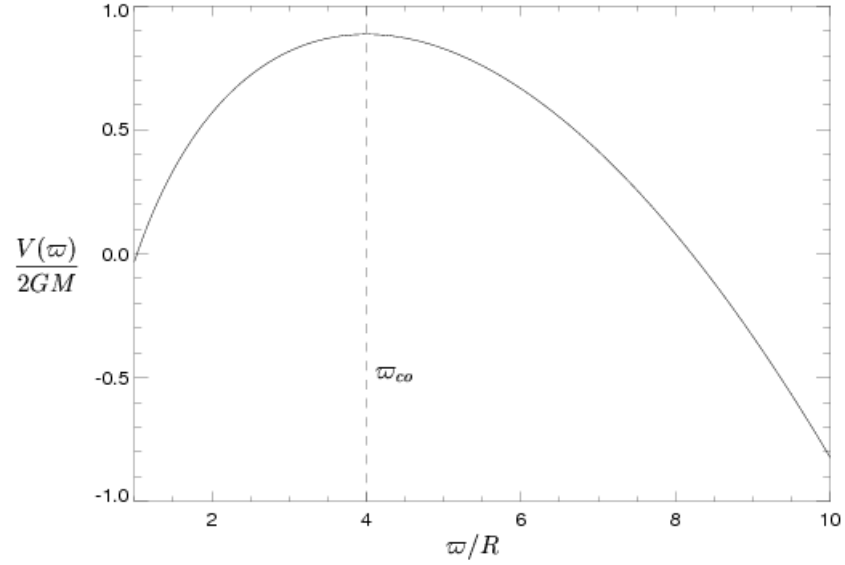


Figure 5.1: The combined potential $V(\varpi)$ for a co-rotation radius $\varpi_{co} = 4.0$.

which or, alternatively, Eq. (5.14) is the fundamental equation to be solved.

The pressure and density are then given by

$$p = p_0(V) - \frac{1}{2\mu_0} \kappa(V) V'^2 B_\varpi^2 \quad (5.25)$$

and

$$\rho = -\frac{dp_0}{dV} + \frac{1}{2\mu_0} \frac{d\kappa}{dV} V'^2 B_\varpi^2 + \frac{1}{\mu_0} \kappa(V) V'' B_\varpi^2 + \frac{1}{\mu_0} \kappa(V) V' \mathbf{B} \cdot \nabla B_\varpi. \quad (5.26)$$

While formally, Eqs. (5.19) to (5.26) are identical to the case $M \rightarrow 0$ (only centrifugal forces) investigated by Neukirch (2009), an important difference is that the combined potential (5.18) does not have a one-to-one mapping to the radial coordinate ϖ as the gravitational potential or the centrifugal potential on their own have. Instead, $V(\varpi)$ has a maximum (see Fig. 5.1) at the co-rotation radius given by

$$\varpi_{co} = \frac{\sqrt{2GM}}{|\Omega|}, \quad (5.27)$$

which is calculated from

$$V'(\varpi) = -\Omega^2 \varpi + \frac{2GM}{\varpi} = 0.$$

A test particle in a circular and planar orbit around the cylinder would have an orbital angular velocity which is equal to Ω so that it would co-rotate with the cylinder. More importantly, though, for a rigidly rotating plasma on the cylindrical surface with radius equalling the co-rotation radius,

the outward centrifugal force is exactly balancing the inward gravitational force, as the expression

$$-\rho \nabla V = -\rho V' \mathbf{e}_\varpi$$

for the combination of the two forces shows. Since V' vanishes at ϖ_{co} , the combined force is zero for $\varpi = \varpi_{co}$. For distances from the cylinder larger than the co-rotation radius the centrifugal force will be bigger than the gravitational force ($V' < 0$) and thus the combined force will be pointing outward. Obviously, overall force balance will have to include the Lorentz force and pressure gradient. The Lorentz force is crucial to be able to obtain force balance beyond the co-rotation radius.

In Neukirch (2009) the expression $\kappa(V)V'^2$ was generally replaced by a function $\xi(\varpi)$. Due to the one-to-one mapping between the centrifugal potential and the radial variable ϖ , it was possible to choose the function $\xi(\varpi)$ instead of $\kappa(V)$. This is not generally possible for the combined potential discussed here. Although defining a function $\xi(\varpi) = \kappa(V)V'^2$ is of course possible, choosing $\xi(\varpi)$ instead of $\kappa(V)$ will generally lead to problems, for example to possible singularities of $\kappa(V)$ at the co-rotation radius, because

$$\kappa(V(\varpi)) = \frac{\xi(\varpi)}{V'^2(\varpi)}. \quad (5.28)$$

Obviously the denominator vanishes at ϖ_{co} and $\kappa(V)$ will only be non-singular if $\xi(\varpi)$ goes to zero with the same or a higher power of $(\varpi - \varpi_{co})$ at the co-rotation radius. This excludes any simple choice such as $\xi(\varpi) = \xi_0 = \text{constant}$, which was one of the examples used in Neukirch (2009).

Singularities in $\kappa(V)$ in turn lead to singularities of density and temperature as well. If we express the density in terms of $\xi(\varpi)$ instead of $\kappa(V)$ we first obtain

$$\rho = -\frac{dp_0}{dV} + \frac{1}{2\mu_0} \frac{d\kappa}{dV} V'^2 B_\varpi^2 + \frac{1}{\mu_0} \kappa(V) V'' B_\varpi^2 + \frac{1}{\mu_0} \kappa(V) V' \mathbf{B} \cdot \nabla B_\varpi. \quad (5.29)$$

Using

$$\begin{aligned} \frac{d\xi}{d\varpi} &= \frac{d}{d\varpi} (\kappa(V)V'^2) \\ &= \frac{d\kappa}{dV} V'^3 + 2\kappa(V)V' V'', \end{aligned}$$

we can rewrite Eq. (5.29) in the form

$$\rho = -\frac{dp_0}{dV} + \frac{1}{V'} \frac{1}{2\mu_0} \frac{d\xi}{d\varpi} B_\varpi^2 + \frac{1}{V'} \frac{1}{\mu_0} \xi(\varpi) (\mathbf{B} \cdot \nabla B_\varpi), \quad (5.30)$$

which makes the possible singularity at $\varpi = \varpi_{co}$ ($V' = 0$) obvious. The pressure, on the other

hand, is always non-singular since

$$p = p_0(V) - \frac{1}{2\mu_0}\kappa(V)V'^2 B_{\varpi}^2 = p_0(V) - \frac{1}{2\mu_0}\xi(\varpi)B_{\varpi}^2. \quad (5.31)$$

But even if a singularity of $\kappa(V)$ and ρ could be avoided for a suitable choice of $\xi(\varpi)$ (going through 0 quadratically at ϖ_{co}), the inverse mapping from ϖ to V would not be well-defined across ϖ_{co} , and therefore a given function $\xi(\varpi)/V'^2(\varpi)$ cannot generally be expressed as a function of V . This has to borne in mind when we considering Eq. (5.24) in which $\xi(\varpi)$ should merely be regarded as an abbreviation for $\kappa(V)V'^2$, but not as an independent free function as, for example, in Neukirch (2009).

As already stated above, Eq. (5.14) or, alternatively, Eq. (5.24) is the fundamental equation that has to be solved. It is straightforward to see that for

$$1 - \kappa(V)V'^2 = 1 - \xi(\varpi) > 0, \quad (5.32)$$

Eq. (5.24) is elliptic, whereas in the case

$$1 - \kappa(V)V'^2 = 1 - \xi(\varpi) < 0, \quad (5.33)$$

it is hyperbolic, while having singularities at any radius ϖ_s where $\kappa(V)V'^2 = 1$. Obviously, none of the singularities coincides with the co-rotation radius (at $\varpi = \varpi_{co}$, we have $1 - \kappa(V)V'^2 = 1$). The singularities, i.e. the transition from an elliptic to a hyperbolic equation or vice versa can only occur for $\kappa(V)$ positive. For example, assuming for simplicity that $\kappa > 0$ is constant, the critical points occur at

$$\varpi_{s\pm}^2 = \frac{\varpi_{co}^2}{2} \left[\left(\frac{\varpi_{co}^2}{(2GM)^2\kappa} + 2 \right) \pm \sqrt{\left(\frac{\varpi_{co}^2}{(2GM)^2\kappa} + 2 \right)^2 - 4} \right]. \quad (5.34)$$

The critical point defined by ϖ_{s+}^2 is beyond the co-rotation radius, whereas the one given by ϖ_{s-}^2 is within the co-rotation radius (see Fig. 5.2). The inner singularity lies inside the central cylinder, if

$$(2GM)^2\kappa < \frac{\varpi_{co}^4 R^2}{(\varpi_{co}^2 - R^2)^2},$$

where of course $R^2 < \varpi_{co}^2$. One should note, however, that Eq. (5.34) only applies if $\kappa =$ constant. If κ depends on V (and thus on ϖ), even the possibility of more than two critical points exists in principle.

The case $\kappa(V)$ positive generally corresponds to a stretching of magnetic field compared to a potential field ($\kappa = 0$), as it can be seen from Eq. (5.19). A thought experiment where one starts

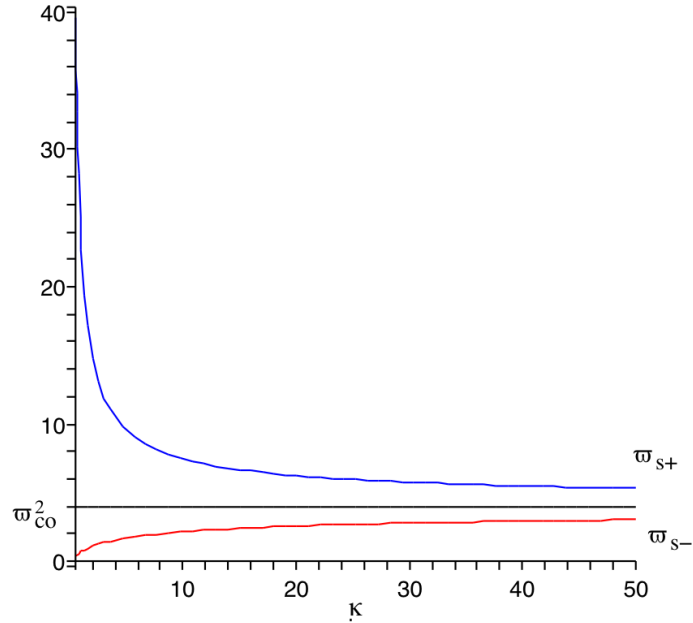


Figure 5.2: The critical points ϖ_{s+}^2 (blue) and ϖ_{s-}^2 (red) for a co-rotation radius $\varpi_{co} = 2.0$.

with $\kappa = 0$ (potential field) and then slowly increases κ shows that the radial component of the magnetic field will increase due to the decrease of $1 - \kappa V'^2$, if one assumes that to lowest order U does not change too rapidly with changing κ . Furthermore, it is relatively straightforward to see that the radial component of the Lorentz force will be directed inwards for magnetic fields which have the same general behavior as a dipole field close to the equator ($z = 0$). This is exactly what is expected of stretched magnetic fields acting to confine plasma pulled away from the cylinder by the centrifugal force.

In this chapter we will only consider Eq. (5.24) for cases where it is elliptic. We shall follow a common approach used in solar and stellar applications and in addition to the inner cylindrical boundary define an artificial outer boundary. This is similar to the source surface used in many global potential magnetic field models of the solar corona (the so-called potential field source surface or PFSS models). It should be noted, however, that because the magnetic fields calculated in this chapter are non-potential, we impose slightly different boundary conditions from those usually imposed on a source surface when potential fields are used.

5.3 Solution Methods and Example Solutions

In this section we discuss possible solution methods and a few illustrative example solutions. We first nondimensionalise all quantities and equations using

$$\begin{aligned}\tilde{\nabla} &= R\nabla, & \tilde{\omega} &= \frac{\varpi}{R}, & \tilde{\mathbf{B}} &= \frac{\mathbf{B}}{B_0}, & \tilde{V} &= \frac{V}{2GM}, \\ \tilde{\mathbf{j}} &= \frac{\mathbf{j}}{(B_0/\mu_0 R)}, & \tilde{p} &= \frac{p}{B_0^2/\mu_0}, & \tilde{\rho} &= \frac{\rho}{B_0^2/(2\mu_0 GM)},\end{aligned}$$

where B_0 is a typical magnetic field value. The dimensionless combined centrifugal and gravitational potential is given by

$$V = -\frac{1}{2\varpi_{co}^2}(\varpi^2 - \varpi_{co}^2 \ln(\varpi^2)), \quad (5.35)$$

where, $\varpi_{co} = \frac{\sqrt{2GM}/|\Omega|}{R}$ is the dimensionless co-rotation radius and the cylinder radius in these dimensionless coordinates is 1.

5.3.1 Separation of Variables

In the case when it is elliptic, Eq. (5.24) is very similar to Laplace's equation and admits separable solutions (see also Neukirch 2009) of the form

$$U(\varpi, \phi, z) = F_{mk}(\varpi) \exp(im\phi) \exp(ikz). \quad (5.36)$$

If we substitute (5.36) into (5.24) we find that the radial function $F_{mk}(\varpi)$ satisfies the equation

$$\frac{1}{\varpi} \frac{d}{d\varpi} \left(\frac{\varpi}{1 - \xi(\varpi)} \frac{dF_{mk}}{d\varpi} \right) - \left(\frac{m^2}{\varpi^2} + k^2 \right) F_{mk} = 0. \quad (5.37)$$

This ordinary second order differential equation will have two linearly independent solutions, $F_{mk}^{(1)}(\varpi)$ and $F_{mk}^{(2)}(\varpi)$, say. Since the partial differential equation for U is linear, the solutions for different m and k may be superposed to generate other solutions,

$$U(\varpi, \phi, z) = \sum_{m=-\infty}^{\infty} \exp(im\phi) \int_{-\infty}^{\infty} dk [A_m(k) F_{mk}^{(1)}(\varpi) + B_m(k) F_{mk}^{(2)}(\varpi)] \exp(ikz). \quad (5.38)$$

Here the $A_m(k)$ and $B_m(k)$ are complex coefficients, which are determined by the boundary conditions, e.g. Dirichlet or von Neumann conditions in the elliptic case.

As already discussed above, we are not allowed to choose the function $\xi(\varpi)$ in the present case, if the domain includes the co-rotation radius. However, to illustrate the method and for use as a test case for the numerical method used later, we show a few plots for an analytical solution which

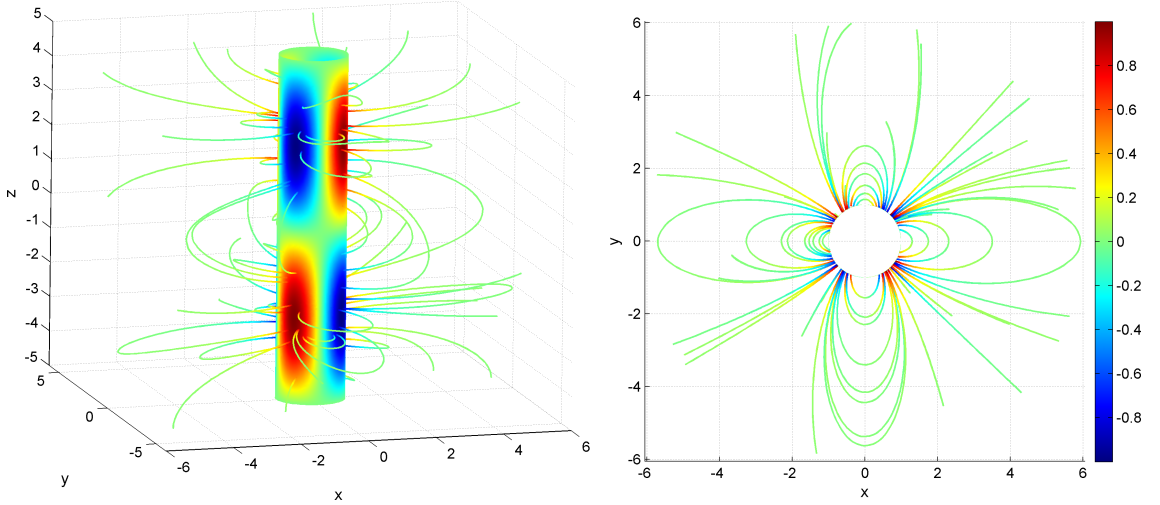


Figure 5.3: Field line plots for the example solution. The left panel shows a side view, the right panel a view along the z -axis. The colours on the boundary represent the radial magnetic field component, B_ϖ on that boundary.

can be obtained for $\xi(\varpi) = \xi_0 = \text{constant}$ (see e.g. Neukirch 2009). In this case Eq. (5.37) takes a form of a modified Bessel's equation:

$$\varpi^2 \frac{d^2 F_{mk}}{d\varpi^2} + \varpi \frac{dF_{mk}}{d\varpi} - (1 - \xi_0)(k^2 \varpi^2 + m^2) F_{mk} = 0, \quad (5.39)$$

with the general solutions given by

$$F_{mk}(\varpi) = A_m(k) I_\nu(k\sqrt{1 - \xi_0} \varpi) + B_m(k) K_\nu(k\sqrt{1 - \xi_0} \varpi), \quad (5.40)$$

where $I_\nu(x)$ and $K_\nu(x)$ are modified Bessel functions (Abramowitz and Stegun 1965), $\nu = m\sqrt{1 - \xi_0}$. $A_m(k)$ and $B_m(k)$ are constants which would usually be determined by the boundary conditions.

For this illustrative example we have chosen the parameter values

$$\xi_0 = 3/4,$$

$$m = \pm 2,$$

$$k = \pi/5$$

which leads to

$$\sqrt{1 - \xi_0} = 1/2,$$

$$\nu = m\sqrt{1 - \xi_0} = \pm 1$$

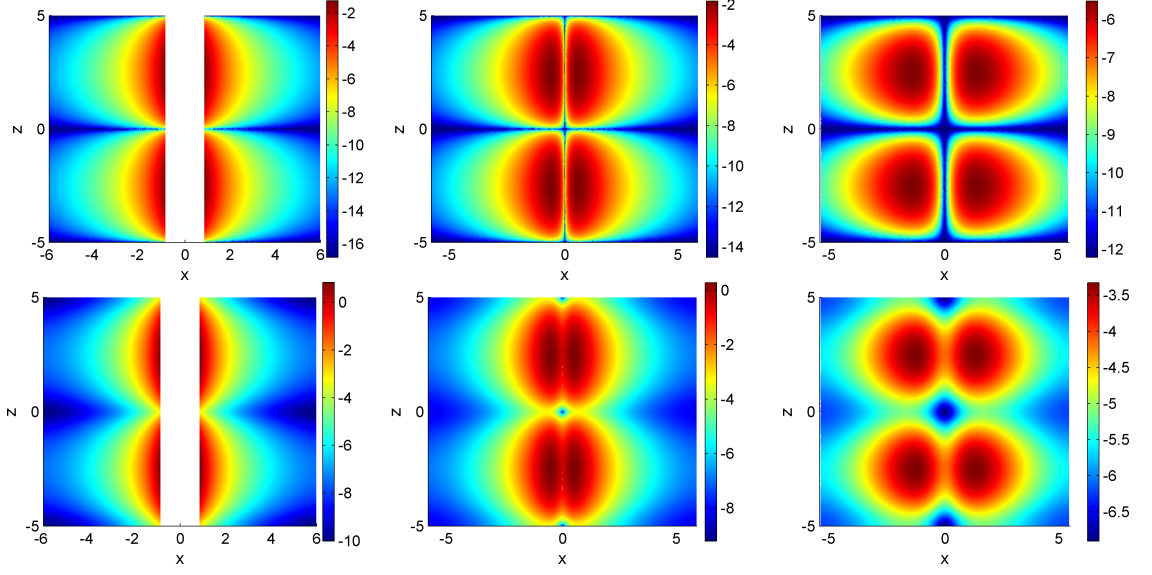


Figure 5.4: Cross section plots of the pressure (top panels) and density (bottom panels) variations in the xz -plane at $y = 0.5$, $y = 1$, and $y = 2.5$, respectively.

and we set $A_m(k) = B_m(k) = 0$, except for $B_{\pm 2}(k)$ which we choose so that the pseudo-potential is given by

$$U = B_0 K_1(\pi \varpi/10) \sin(2\phi) \sin(\pi z/5). \quad (5.41)$$

The magnetic field components are then given by

$$\begin{aligned} B_\varpi &= -\frac{2\pi}{5} B_0 [K_0(\pi \varpi/10) + \frac{10}{\pi \varpi} K_1(\pi \varpi/10)] \sin(2\phi) \sin(\pi z/5), \\ B_\phi &= \frac{2 B_0}{\varpi} K_1(\pi \varpi/10) \cos(2\phi) \sin(\pi z/5), \\ B_z &= \frac{\pi B_0}{5} K_1(\pi \varpi/10) \sin(2\phi) \cos(\pi z/5). \end{aligned} \quad (5.42)$$

The reason we choose K_ν instead of I_ν is that K_ν decreases with increasing argument, which means that the magnetic field strength decreases with increasing distance from the z -axis. In Fig. (5.3) we show a three-dimensional plot of magnetic field lines from two different viewing angles. The boundary colours represent the radial magnetic field component, B_ϖ . The non-symmetric nature of the magnetic field is obvious from the plot. The pressure is given by

$$p = p_0(V) - \frac{\xi_0}{2} B_\varpi^2 = p_0(V) - \frac{3}{8} B_\varpi^2, \quad (5.43)$$

which as discussed above is non-singular at the co-rotation radius. The density, however, is given by

$$\rho = -\frac{dp_0}{dV} + \frac{\xi_0}{V'} \mathbf{B} \cdot \nabla B_\varpi = -\frac{dp_0}{dV} + \frac{3\varpi_{co}^2 \varpi}{4(\varpi_{co}^2 - \varpi^2)} \mathbf{B} \cdot \nabla B_\varpi, \quad (5.44)$$

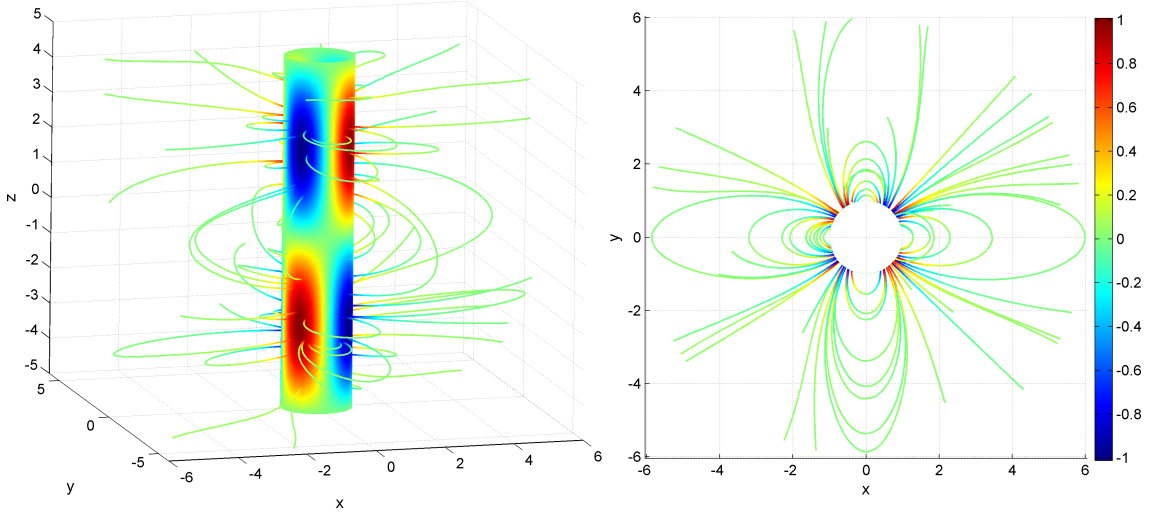


Figure 5.5: 3D field line plot (left panel) and a view along the z -axis (right) for the numerical solution of the $\xi(\varpi) = \xi_0 = 3/4$ case. The similarity of the plots with Fig. 5.3 is obvious.

and here the singularity at the co-rotation radius ϖ_{co} is obvious. We therefore consider this solution only for $\varpi < \varpi_{co}$. It should be noted that when $\xi(\varpi)$ is chosen directly, the value of the co-rotation radius affects the solution only through the presence of V' in the density. As the co-rotation radius is the only parameter in which the angular velocity Ω appears, choosing $\xi(\varpi)$ instead of $\kappa(V)$ basically eliminates the rotation rate from the problem. Again this is a feature of the solutions which is not necessarily wanted if one wants to study the effect of increasing Ω on the solutions. Plots of the pressure and density contours are shown in Fig. (5.4). Note that in these plots we only show the deviations from the cylindrically symmetrical background pressure and density.

5.3.2 Numerical Solutions of Eq. (5.14)

In general, finding analytical solutions of Eqs. (5.14) or (5.24) will be impossible even for simple choices of the function $\kappa(V)$. Thus, numerical methods will have to be used to find solutions. Since Eq. (5.14) is a simple linear partial differential equation, standard numerical methods can be used to solve it. Here we use an adaptive mesh finite element method from the COMSOL Multiphysics 3.4 package with MATLAB to solve Eq. (5.14).

To check the accuracy of our numerical method, we have first solved Eq. (5.14) for the constant ξ case presented in Section 5.3.1, using the same parameter values, as well as boundary conditions that are consistent with the analytical solution. We solve Eq. (5.14) for U using a Cartesian coordinate system x, y, z , on a numerical domain, which is bounded by an inner cylinder of radius 1, an outer cylinder of radius $\varpi_o = 6$, and which extends from -5 to 5 in the z -direction.

The outer boundary ϖ_o is assumed to be smaller than the co-rotation radius in this case to avoid singularities in the density. The components of \mathbf{B} in Cartesian coordinates for this case are given by

$$\begin{aligned} B_x &= \frac{\partial U}{\partial x} + \frac{\xi_0 x (x \frac{\partial U}{\partial x} + y \frac{\partial U}{\partial y})}{(1 - \xi_0)(x^2 + y^2)}, \\ B_y &= \frac{\partial U}{\partial y} + \frac{\xi_0 y (x \frac{\partial U}{\partial x} + y \frac{\partial U}{\partial y})}{(1 - \xi_0)(x^2 + y^2)}, \\ B_z &= \frac{\partial U}{\partial z}. \end{aligned}$$

The exact boundary conditions used for this case are

- $\mathbf{n} \cdot \mathbf{B} = B_{\varpi, analytical}(x, y, z)$ on the inner boundary ($\varpi = \sqrt{x^2 + y^2} = 1$), where $B_{\varpi, analytical}(\varpi, \phi, z)$ is the expression given in (5.42),
- $U(x, y, z) = U_{analytical}(x, y, z)$ on the outer boundary ($\varpi = \sqrt{x^2 + y^2} = 6$), where $U_{analytical}(\varpi, \phi, z)$ is given by Eq. (5.41) and
- $\mathbf{n} \cdot \mathbf{B} = 0$ at $z = \pm 5$.

The mesh size used for this calculation consists of 261996 elements.

A magnetic field line plot for the numerical solution obtained is shown in Fig. (5.5), which shows good agreement with the analytical solution. The only noticeable difference is the structure of the field lines towards $z = \pm 5$ which is due to the effect of the boundary condition at $z = \pm 5$ for the numerical solution. Having thus convinced ourselves that the numerical tool gives satisfactory results, we have considered the simplest possible choice of $\kappa(V)$, which is

$$\kappa(V) = \kappa_0 = \text{constant} \quad (5.45)$$

as an example for a case where κ is chosen directly. The components of \mathbf{B} for this case, which are now more complicated, are given by

$$\begin{aligned} B_x &= \frac{\partial U}{\partial x} + \frac{\kappa_0(\varpi_{co}^2 - \varpi^2)^2 x (x \frac{\partial U}{\partial x} + y \frac{\partial U}{\partial y})}{\varpi^2(\varpi_{co}^4 \varpi^2 - \kappa_0(\varpi_{co}^2 - \varpi^2)^2)} \\ B_y &= \frac{\partial U}{\partial y} + \frac{\kappa_0(\varpi_{co}^2 - \varpi^2)^2 y (x \frac{\partial U}{\partial x} + y \frac{\partial U}{\partial y})}{\varpi^2(\varpi_{co}^4 \varpi^2 - \kappa_0(\varpi_{co}^2 - \varpi^2)^2)} \\ B_z &= \frac{\partial U}{\partial z}. \end{aligned}$$

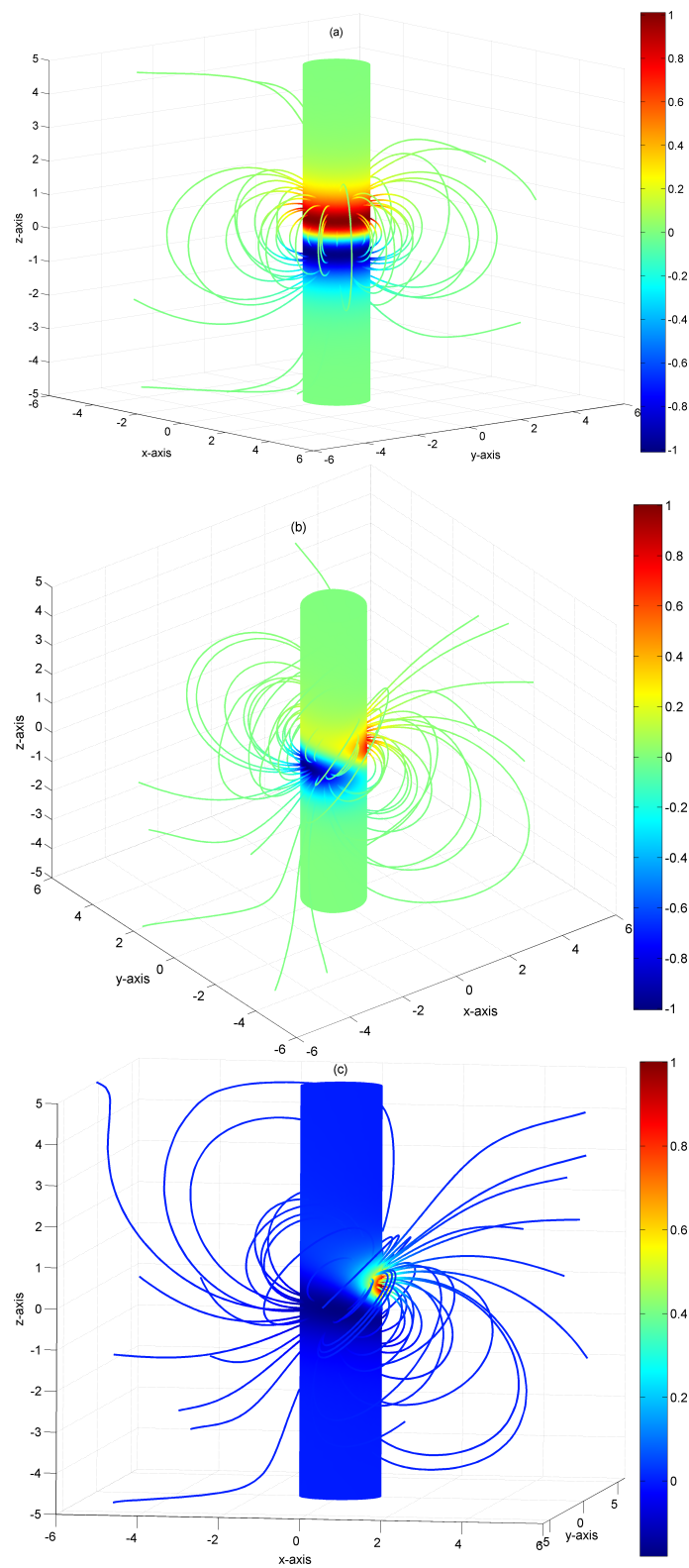


Figure 5.6: Magnetic field lines plots for the three cases of (a) aligned rotator, (b) oblique rotator and (c) displaced dipole.

The corresponding pressure and density are given by

$$\begin{aligned} p &= p_0(V) - \frac{\kappa_0}{2}(\mathbf{B} \cdot \nabla V)^2 \\ &= p_0(V) - \frac{\kappa_0}{2} \left(\frac{\varpi_{co}^2(\varpi_{co}^2 - \varpi^2)(x\frac{\partial U}{\partial x} + y\frac{\partial U}{\partial y})}{\varpi_{co}^4\varpi^2 - \kappa_0(\varpi_{co}^2 - \varpi^2)^2} \right)^2, \end{aligned} \quad (5.46)$$

$$\begin{aligned} \rho &= -\frac{dp_0}{dV} + \kappa_0\mathbf{B} \cdot \nabla(\mathbf{B} \cdot \nabla V) \\ &= -\frac{dp_0}{dV} + \kappa_0\varpi_{co}^2\mathbf{B} \cdot \nabla \left[\frac{(\varpi_{co}^2 - \varpi^2)(x\frac{\partial U}{\partial x} + y\frac{\partial U}{\partial y})}{\varpi_{co}^4\varpi^2 - \kappa_0(\varpi_{co}^2 - \varpi^2)^2} \right], \end{aligned} \quad (5.47)$$

which show that by choosing $\kappa(V)$, the density remains non-singular at the co-rotation radius. Hence, we can now calculate solutions in a domain including and extending beyond the co-rotation radius.

We have calculated numerical solutions to Eq. (5.14) using as boundary conditions on the surface of the central cylinder ($\varpi = \sqrt{x^2 + y^2} = 1$) a magnetic dipole field ($\mathbf{n} \cdot \mathbf{B} = \mathbf{B}_{dip}$) for the three cases of the

- (a) magnetic dipole moment at the origin and aligned with the rotation axis (aligned rotator),
- (b) magnetic dipole moment at the origin, but inclined with respect to the rotation axis (oblique rotator) and
- (c) magnetic dipole moment not located at the origin and inclined with respect to the rotation axis (displaced dipole).

These three cases are similar to the cases discussed by Neukirch (2009). We use the same domain and mesh size as in the previous example, with the outer boundary conditions given by $U(x, y, z) = U_o(x, y, z)$ at $\sqrt{x^2 + y^2} = 6$, where $U_o(x, y, z)$ satisfies $\nabla U_o = \mathbf{B}_{dip}$ and $\mathbf{n} \cdot \mathbf{B} = 0$ at $z = \pm 5$.

Numerical solutions for the case of $\kappa = \frac{3}{4}$ and $\varpi_{co} = 3.5$ are illustrated in Figs. (5.6) - (5.9), where the letters (a), (b) and (c) above each plot indicate the three different boundary conditions mentioned above. For the oblique rotator case the magnetic dipole moment is in the xz -plane at an angle of $\frac{\pi}{4}$ with the x -axis. For the displaced dipole case the magnetic moment is again in the xz -plane, but now at $x = 0.3$, making an angle of $\frac{\pi}{4}$ with the x -axis. In the plots showing pressure and density, we only show the three-dimensional deviation from background pressure and density. It turns out that both the three-dimensional pressure deviation and the three-dimensional density deviation are negative, which means that these terms will reduce any background pressure and density to lower values.

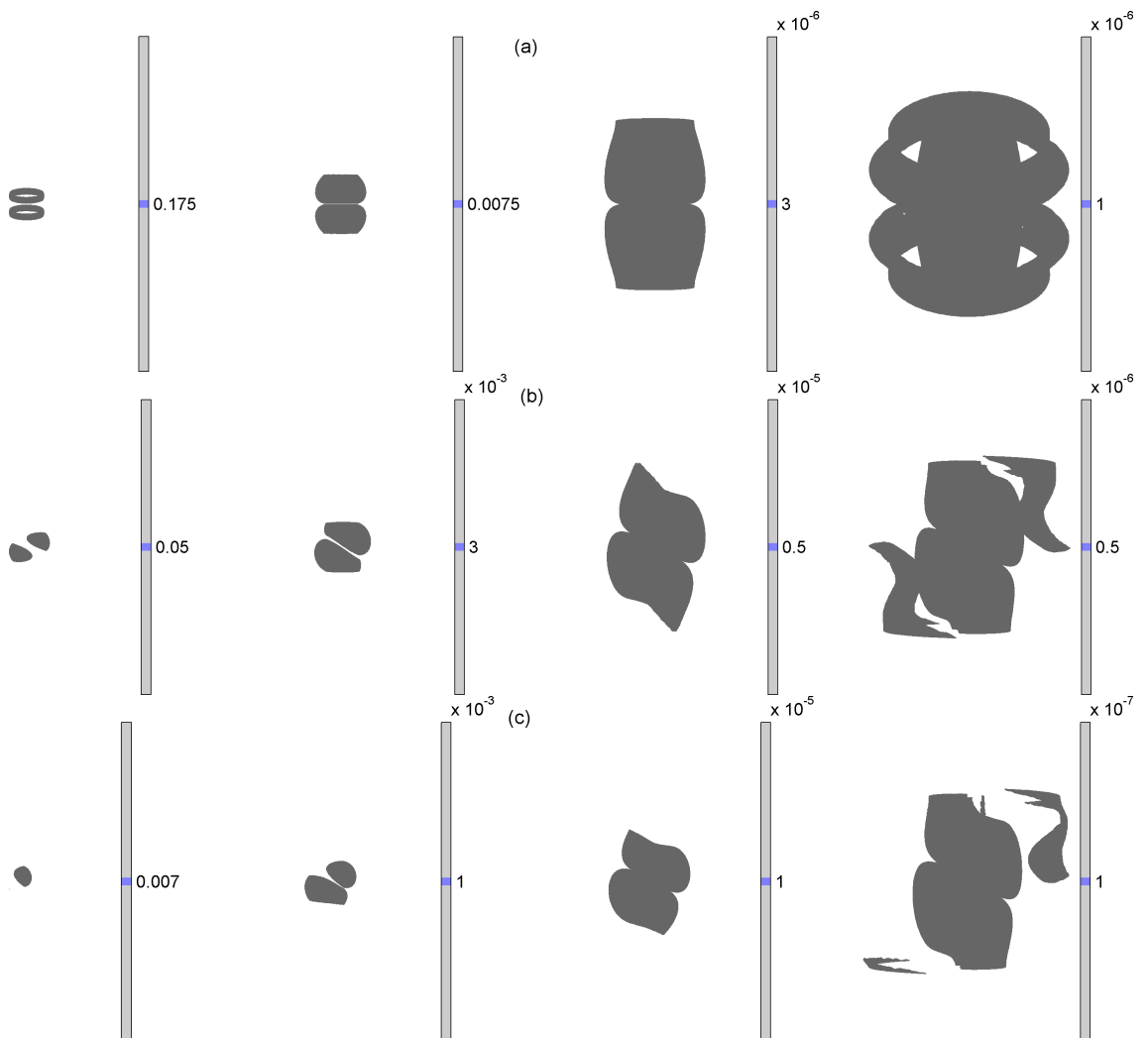


Figure 5.7: Pressure isosurface plots for the aligned rotator case (top panels), the oblique rotator case (middle panels) and the displaced dipole case (bottom panels). The transition from rotational symmetric isosurfaces in the aligned rotator case to asymmetric isosurfaces in the other two case can be seen very clearly.

Figure (5.6) shows magnetic field line plots, with the colour contours on the central cylinder indicating the strength of the radial magnetic field component, B_{ϖ} , for the three different boundary conditions. As is to be expected, the change of boundary conditions has a clear effect on the structure of the magnetic field, which is clearly symmetric for the aligned rotator case, but becomes non-symmetric for the other two cases. This is also visible in Fig. (5.7), where we show isosurfaces of the three-dimensional deviation of the pressure from the background pressure. One can see that one has smaller isosurfaces close to the inner boundary where the magnetic field (and thus the pressure deviation) is strong, whereas the isosurfaces become more extended as one moves away from the cylinder and the magnetic field becomes weaker.

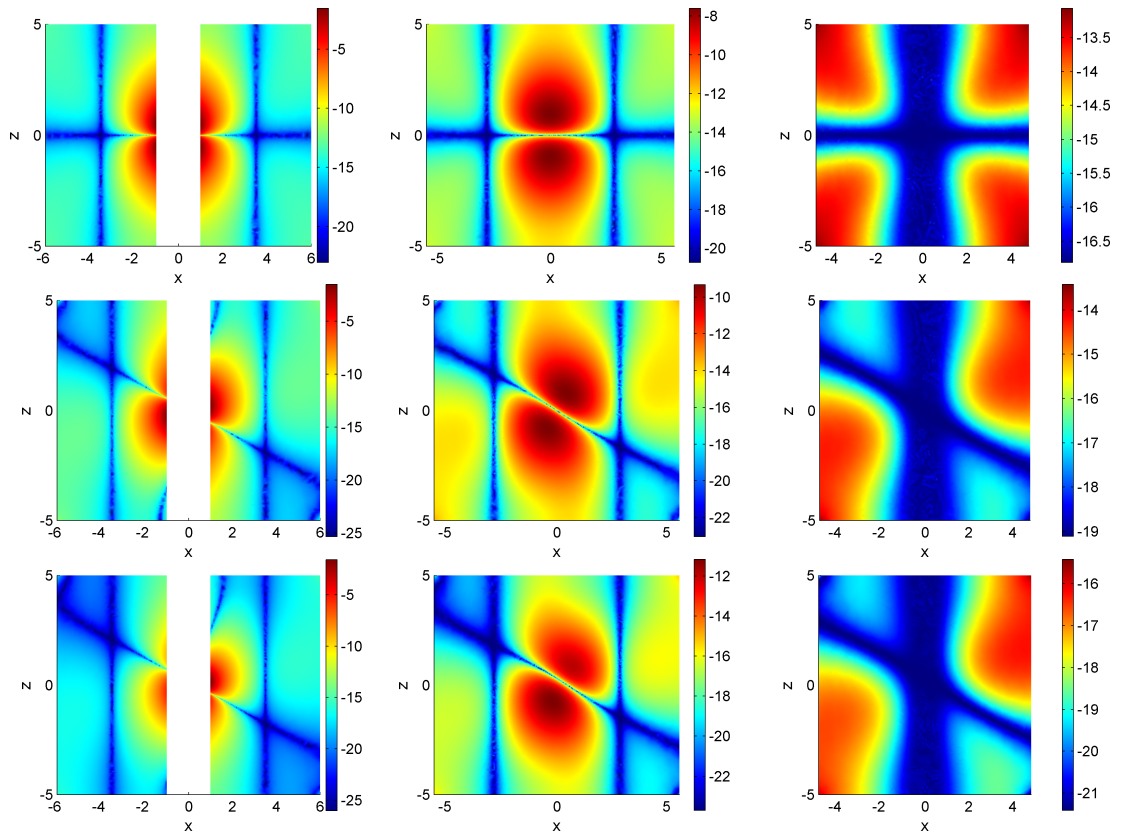


Figure 5.8: Variation of the pressure deviation from the background pressure in the xz -plane at $y = 0$ (through the central cylinders), $y = \pm 2$, and $y = \pm 3.5$ (touching the co-rotation cylinder), respectively. Shown is the logarithm of the pressure. The increasing asymmetry from top to bottom is obvious.

It can be clearly seen that for the case of aligned rotator (top panels in Fig. 5.7), the pressure isosurfaces are symmetric, whereas this symmetry is broken for the other two cases. In particular, the symmetry with respect to the x -axis and the z -axis is broken, but for the oblique rotator case (middle panels in Fig. 5.7) a notion of symmetry about the dipole axis remains. The least symmetric case, at least in terms of pressure isosurfaces, is the displaced dipole case (lower panels in Fig. 5.7). Figures (5.8) and (5.9) show cross section plots of the variation of the 3D pressure

and density deviations from the background pressure and density in planes parallel to the xz -plane for different y -values. These plots show that there is some symmetry of the pressure and density deviations about the y -axis for all three cases, but clearly show symmetry about the x and z -axes only for the aligned rotator case. The intersection between the planes shown in Fig. (5.8) and the cylindrical surface with radius equal to the co-rotation radius coincides with the dark vertical features in the plots. In the rightmost panels ($y = \pm 3.5$), the plane basically touches the co-rotation cylinder and thus one only sees a single broad vertical feature. It can be easily seen from Eq. (5.46) that the total pressure is equal to the background pressure at the co-rotation radius, i.e. $p = p_0(V)$ at $\varpi = \varpi_{co}$. The dark vertical features in Fig. (5.8) thus correspond to a vanishing three-dimensional pressure deviation, whereas no corresponding feature exists for the three-dimensional density deviation (Fig. 5.9). The pressure deviation vanishes also at locations where the radial component of the magnetic field B_ϖ is zero as it can be easily seen (e.g. from Eq. 5.25). These locations are represented by the other dark features in Fig. (5.8). The pressure and density cross-section plots confirm the increasing degree of asymmetry when going from the aligned rotator case over the oblique rotator case to the displace dipole moment case.

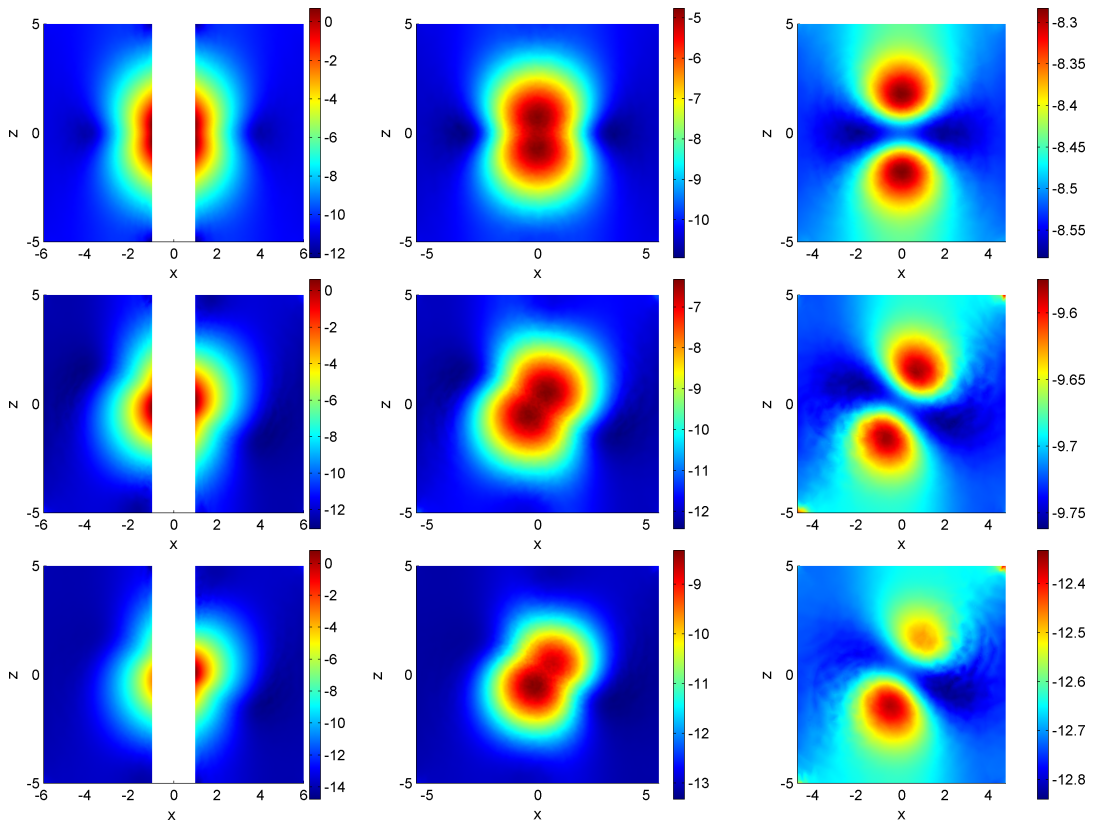


Figure 5.9: Variation of the density deviation from the background density in the xz -plane at $y = 0$ (through the central), $y = \pm 2$, and $y = \pm 3.5$ (touching the co-rotation cylinder), respectively. Shown is the logarithm of the density. The density deviation is largest close to the cylinder.

5.4 Summary and Discussion

We have presented a relatively simple (semi-)analytical approach which allows the modelling of three-dimensional rigidly rotating magnetized corone or magnetospheres around massive central objects. In this chapter, we have restricted our analysis for illustrative purposes to the simpler, but less realistic case of cylindrical geometry. The possibility of extending the theory to other geometries will be discussed below.

The theory contains free functions $\kappa(V)$ and $p_0(V)$, where V is the combined gravitational and centrifugal potential in the co-rotating frame of reference. Whereas the function $\kappa(V)$ implicitly determines the current density in the corona, $p_0(V)$ is an independent background pressure. Alternatively the derivative $dp_0/dV = -\rho_0(V)$ can be chosen, where $\rho_0(V)$ is a background density. The background pressure can then be determined by integration, if an equation of state and/or a temperature profile is assumed.

The function $\kappa(V)$ appears in the theory in the combination $\kappa(V)V'^2$ and, in the cylindrical geometry used in this chapter, a new function ξ of the radial coordinate, ϖ , can be defined as $\xi(\varpi) = \kappa(V)V'^2$. As it has been shown before (Neukirch 2009) for the case of V being just the centrifugal potential (no gravitational force), analytical solutions of the theory can in principle be found if $\xi(\varpi)$ is chosen to have a convenient form. However, for the case of a combined centrifugal and gravitational potential, as presented above, the direct choice of a function $\xi(\varpi)$ instead of deriving it from a chosen function $\kappa(V)$ generally leads to singularities, in particular of the density, at the co-rotation radius.

One can avoid these problems by choosing $\kappa(V)$ instead of $\xi(\varpi)$. In this case, however, the fundamental equation is usually too complicated to allow for analytical solutions to be found, but the equation is still sufficiently simple that standard numerical methods can be used to solve it. We have presented an example of an analytical solution to be able to test our numerical method, and the numerical solution shows good agreement with the analytical solution on its domain of validity inside the co-rotation radius. We have then presented numerical solutions for the case of $\kappa(V) = \kappa_0 = \text{constant}$ for three different types of boundary conditions on the surface of the central cylinder: a magnetic dipole field generated by a dipole moment located at the origin, aligned with the rotation axis (aligned rotator), a magnetic dipole field generated by a dipole moment located at the origin, but at an angle with the rotation axis (oblique rotator) and a magnetic dipole moment displaced from the origin, with the dipole moment not aligned with the rotation axis. These three cases were used to illustrate the transition from a rotationally symmetric corona to an asymmetric corona for the simple geometry of a magnetic dipole field.

A similar theory can also be developed for rotating spherical massive bodies. The combined gravitational and centrifugal potential for a body of mass M_0 whose rotation axis is aligned with

the z -axis has the form (using spherical coordinates r , θ and ϕ)

$$V(r, \theta) = -\frac{1}{2}\Omega^2 r^2 \sin^2 \theta - \frac{GM_0}{r}. \quad (5.48)$$

Due to the dependence of V on two of the coordinates in this case, Eq. (5.14) has a much more complicated form when written down explicitly since B_r and B_θ depend on both $\partial U/\partial r$ and $\partial U/\partial \theta$, giving rise to mixed second derivatives in Eq. (5.14). It is highly unlikely that the resulting Eq. (5.14) has any analytical solutions, but this still has to be investigated in detail. Despite its more complicated form, solving Eq. (5.14) using similar numerical methods as we have used for the cylindrical case should not be a major problem. This will be done in the next chapter.

Chapter 6

Three-Dimensional Solutions of the Magnetohydrostatic Equations: Rigidly Rotating Magnetized Coronae in Spherical Geometry

“ And a sign for them is the night. We withdraw therefrom the day, and behold, they are in darkness \ominus And the Sun runs on its fixed course for a period (appointed). That is the Decree of the All-Mighty, the All-Knowing \ominus And the Moon, We have measured for it mansions (to traverse) till it returns like the old dried curved date stalk \ominus It is not for the Sun to overtake the Moon, nor does the night outstrip the day. They all float, each in (its own) orbit \ominus ”

(Interpretation of the Holy Quran **36**: 37-40)

6.1 Introduction

In the previous chapter, we have illustrated the presented theory of 3D MHS equilibria around rigidly rotating massive central bodies by considering a special case of a rigidly rotating cylinder which allows for analytical solutions. Those analytical solutions are valid only for a certain range of radii and only possible for special choices of the free functions of the theory as discussed previously. For general choice of the free functions of the theory, 3D MHS solutions can be only obtained numerically. In this chapter, we shall use the same numerical techniques used in the cylindrical case to obtain 3D MHS solutions outside massive rigidly rotating central spherical bodies. The theory has obvious applications to rotating magnetized stars.

The material in this chapter based on Al-Salti and Neukirch (2010).

We use spherical coordinates r , θ and ϕ and consider a spherical body with radius r_0 and mass M_0 rotating rigidly with angular velocity Ω . The rotation axis is assumed to be aligned with the z -axis. The combined gravitational and centrifugal potential for this body, as already mentioned earlier, is given by

$$V = V(r, \theta) = -\frac{1}{2}\Omega^2 r^2 \sin^2 \theta - \frac{GM_0}{r}. \quad (6.1)$$

Using Eq. (5.13), we have the following components of the magnetic field \mathbf{B} in spherical coordinates:

$$B_r = \frac{\partial U}{\partial r} + \frac{\kappa(V)}{1 - \kappa(V)(\nabla V)^2} \left(\frac{\partial U}{\partial r} \frac{\partial V}{\partial r} + \frac{1}{r^2} \frac{\partial U}{\partial \theta} \frac{\partial V}{\partial \theta} \right) \frac{\partial V}{\partial r}, \quad (6.2)$$

$$B_\theta = \frac{1}{r} \left[\frac{\partial U}{\partial \theta} + \frac{\kappa(V)}{1 - \kappa(V)(\nabla V)^2} \left(\frac{\partial U}{\partial r} \frac{\partial V}{\partial r} + \frac{1}{r^2} \frac{\partial U}{\partial \theta} \frac{\partial V}{\partial \theta} \right) \frac{\partial V}{\partial \theta} \right], \quad (6.3)$$

$$B_\phi = \frac{1}{r \sin \theta} \frac{\partial U}{\partial \phi}, \quad (6.4)$$

where,

$$\begin{aligned} \frac{\partial V}{\partial r} &= -\Omega^2 r \sin^2 \theta + \frac{GM_0}{r^2}, \\ \frac{\partial V}{\partial \theta} &= \frac{-\Omega^2 r^2}{2} \sin 2\theta, \\ (\nabla V)^2 &= \frac{\Omega^4}{r^4} \left[r^3 \sin^2 \theta \left(r^3 - \frac{2GM_0}{\Omega^2} \right) + \frac{G^2 M_0^2}{\Omega^4} \right]. \end{aligned}$$

It can be easily seen that the dependence of the combined gravitational and centrifugal potential V on r and θ results in magnetic field components, namely B_r and B_θ , that depend on both $\partial U/\partial r$ and $\partial U/\partial \theta$ as shown in Eqs. (6.2) and (6.3). This dependence on first-order derivatives gives rise to mixed second-order derivatives in the fundamental equation (5.14), which can be rewritten as

$$\nabla \cdot \left(\nabla U + \frac{\kappa(V)}{1 - \kappa(V)(\nabla V)^2} \left(\frac{\partial U}{\partial r} \frac{\partial V}{\partial r} + \frac{1}{r^2} \frac{\partial U}{\partial \theta} \frac{\partial V}{\partial \theta} \right) \nabla V \right) = 0. \quad (6.5)$$

Hence, analytical solutions are highly unlikely to be obtained for the pseudo-potential U in the spherical case. Nevertheless, Eq. (6.5) can still be solved by the same numerical method used in the cylindrical case, which we will carry out in the next section.

The corresponding plasma pressure p , density ρ and temperature T can be obtained by using Eqs. (5.9) - (5.11), namely,

$$p = p_0(V) - \frac{1}{2\mu_0} \kappa(V) (\mathbf{B} \cdot \nabla V)^2, \quad (6.6)$$

$$\rho = -\frac{dp_0}{dV} + \frac{1}{2\mu_0} \frac{d\kappa}{dV} (\mathbf{B} \cdot \nabla V)^2 + \frac{1}{\mu_0} \kappa(V) \mathbf{B} \cdot \nabla(\mathbf{B} \cdot \nabla V), \quad (6.7)$$

$$T = \frac{\mu p}{\mathcal{R}\rho}, \quad (6.8)$$

where the term $\mathbf{B} \cdot \nabla V$ in the spherical case is

$$\mathbf{B} \cdot \nabla V = \frac{1}{1 - \kappa(V)(\nabla V)^2} \left(\frac{\partial U}{\partial r} \frac{\partial V}{\partial r} + \frac{1}{r^2} \frac{\partial U}{\partial \theta} \frac{\partial V}{\partial \theta} \right).$$

6.2 Numerical Solutions

As for the cylindrical case, we will solve the fundamental equation (5.14) for U numerically using a Cartesian coordinate system x, y, z . The corresponding combined gravitational and centrifugal potential V and its gradient are given by

$$V = V(x, y, z) = -\frac{\Omega^2}{2} (x^2 + y^2) - \frac{GM_0}{\sqrt{x^2 + y^2 + z^2}}$$

$$\nabla V = \frac{\Omega^2}{r^3} \left[x \left(\frac{GM_0}{\Omega^2} - r^3 \right) \hat{\mathbf{x}} + y \left(\frac{GM_0}{\Omega^2} - r^3 \right) \hat{\mathbf{y}} + \frac{GM_0}{\Omega^2} z \hat{\mathbf{z}} \right].$$

Hence,

$$(\nabla V)^2 = \frac{\Omega^4}{r^6} \left[\left(r^3 - \frac{GM_0}{\Omega^2} \right)^2 (x^2 + y^2) + \frac{G^2 M_0^2}{\Omega^4} z^2 \right] = 0$$

only in the $z = 0$ plane at the co-rotation radius given by

$$r_{co} = \sqrt[3]{\frac{GM_0}{\Omega^2}}. \quad (6.9)$$

Unlike the cylindrical case, here a test particle in a circular orbit around the sphere would have an angular velocity which is equal to Ω , so that it would co-rotate with the sphere only in the equatorial plane.

We look for solutions in the domain $r_0 \leq r = \sqrt{x^2 + y^2 + z^2} \leq r_{out}$ using the same boundary condition as in the cylindrical case, namely, we use a magnetic dipole field for the three cases of aligned rotator (a), oblique rotator (b) and displaced dipole (c).

The components of \mathbf{B} for this case are given by

$$B_x = \frac{\partial U}{\partial x} + f_\kappa(r_{co}^3 - r^3)x \left[(r_{co}^3 - r^3) \left(x \frac{\partial U}{\partial x} + y \frac{\partial U}{\partial y} \right) + r_{co}^3 z \frac{\partial U}{\partial z} \right],$$

$$B_y = \frac{\partial U}{\partial y} + f_\kappa(r_{co}^3 - r^3)y \left[(r_{co}^3 - r^3) \left(x \frac{\partial U}{\partial x} + y \frac{\partial U}{\partial y} \right) + r_{co}^3 z \frac{\partial U}{\partial z} \right],$$

$$B_z = \frac{\partial U}{\partial z} + f_\kappa r_{co}^3 \left[(r_{co}^3 - r^3) \left(x \frac{\partial U}{\partial x} + y \frac{\partial U}{\partial y} \right) + r_{co}^3 \frac{\partial U}{\partial z} \right],$$

where,

$$f_\kappa = \frac{\Omega^4 \kappa(V)}{r^6 - \Omega^4 \kappa(V) [(r_{co}^3 - r^3)^2 (x^2 + y^2) + r_{co}^6 z^2]}.$$

Alternatively, one may solve Eq. (5.15), namely,

$$\nabla \cdot (\mathbf{M} \cdot \nabla U) = 0, \quad (6.10)$$

where, the 3×3 matrix \mathbf{M} for the spherical case is given by

$$\mathbf{M} = \begin{bmatrix} 1 + f_\kappa (r_{co}^3 - r^3) x^2 & f_\kappa (r_{co}^3 - r^3) xy & f_\kappa (r_{co}^3 - r^3) xz \\ M_{12} & 1 + f_\kappa (r_{co}^3 - r^3) y^2 & f_\kappa (r_{co}^3 - r^3) yz \\ M_{13} & M_{23} & 1 + f_\kappa (r_{co}^3 - r^3) z^2 \end{bmatrix}. \quad (6.11)$$

As already discussed in the cylindrical case, the fundamental equation (5.14) or alternatively Eq. (5.15) has a singularity when $1 - \kappa(V)(\nabla V)^2 = 0$, which may only occur for $\kappa(V) > 0$. For the spherical case, this singularity, if it exists, occurs at locations where

$$r^6 - \Omega^4 \kappa(V) [(r_{co}^3 - r^3)^2 (x^2 + y^2) + r_{co}^6 z^2] = 0$$

or equivalently,

$$r^4 - \Omega^4 \kappa(V) [r^3 (r^3 - 2r_{co}^3) \sin^2 \theta + r_{co}^6] = 0$$

Unlike the cylindrical case, it is quite difficult to obtain an explicit expression for the locations of this singularity in the spherical case. However, for a given function $\kappa(V)$, we could easily plot the expression $1 - \kappa(V)(\nabla V)^2$ and identify its zeros, if they exist, in a given domain.

In the following, we will consider two examples of numerical solutions corresponding to the same choice of the free function $\kappa(V)$. However, in the first example, we will only present solutions in a domain up to the co-rotation radius, whereas in the second example the co-rotation radius is within our domain as a result of increasing the angular velocity Ω .

6.2.1 Example Solution I

As an illustrative example, we shall again consider the simplest possible choice of $\kappa(V)$, which is

$$\kappa(V) = \kappa_0 = \text{constant}. \quad (6.12)$$

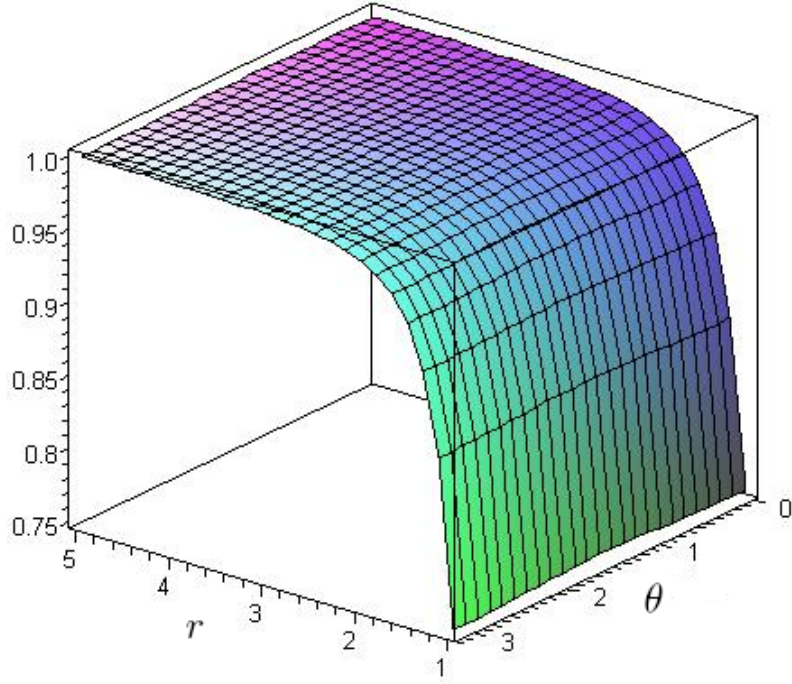


Figure 6.1: 3D plot of the expression $1 - \kappa(V)(\nabla V)^2$ in the domain $1 \leq r = \sqrt{x^2 + y^2 + z^2} \leq 5$.

The corresponding plasma pressure and density are then given by

$$\begin{aligned}
 p &= p_0(V) - \frac{\kappa_0}{2\mu_0} (\mathbf{B} \cdot \nabla V)^2 \\
 &= p_0(V) - \frac{\kappa_0}{2\mu_0} \left(\frac{\Omega^2 r^3 \left[(r_{co}^3 - r^3) \left(x \frac{\partial U}{\partial x} + y \frac{\partial U}{\partial y} \right) + r_{co}^3 z \frac{\partial U}{\partial z} \right]}{r^6 - \Omega^4 \kappa(V) \left[(r_{co}^3 - r^3)^2 (x^2 + y^2) + r_{co}^6 z^2 \right]} \right)^2, \quad (6.13)
 \end{aligned}$$

$$\begin{aligned}
 \rho &= -\frac{dp_0}{dV} + \frac{\kappa_0}{\mu_0} \mathbf{B} \cdot \nabla (\mathbf{B} \cdot \nabla V) \\
 &= -\frac{dp_0}{dV} + \frac{\kappa_0}{\mu_0} \mathbf{B} \cdot \nabla \left(\frac{\Omega^2 r^3 \left[(r_{co}^3 - r^3) \left(x \frac{\partial U}{\partial x} + y \frac{\partial U}{\partial y} \right) + r_{co}^3 z \frac{\partial U}{\partial z} \right]}{r^6 - \Omega^4 \kappa(V) \left[(r_{co}^3 - r^3)^2 (x^2 + y^2) + r_{co}^6 z^2 \right]} \right). \quad (6.14)
 \end{aligned}$$

Taking $\kappa_0 = \frac{1}{4}$, $r_0 = 1$, $r_{out} = 5$ and $r_{co} = 5$, the expression $1 - \kappa(V)(\nabla V)^2$ is always positive in our domain $1 \leq r = \sqrt{x^2 + y^2 + z^2} \leq 5$, as shown in Fig. (6.1). Locations where it vanishes, which correspond to singularities in Eq. (5.14), are clearly out side our domain, as shown in Fig. (6.2). Numerical solutions for this case, showing the dimensionless quantities, are illustrated in Figs. (6.3) - (6.6), where the three different boundary conditions mentioned previously are represented by the letters (a), (b) and (c), namely, aligned rotator: along the z -axis (a), oblique rotator: at an angle of $\frac{\pi}{4}$ between the x -axis and the z -axis (b) and displaced dipole: at $x = 0.3$

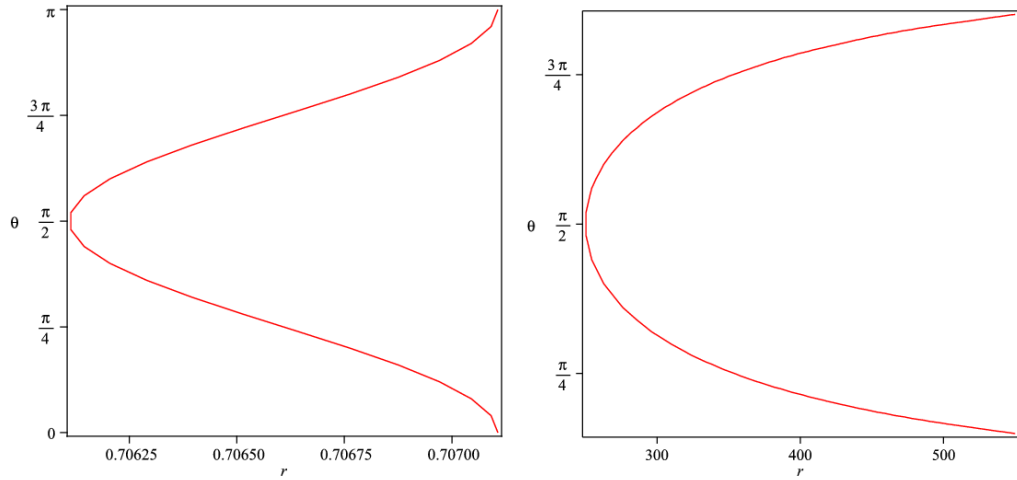


Figure 6.2: Locations where the expression $1 - \kappa(V)(\nabla V)^2$ vanishes.

with an angle of $\frac{\pi}{4}$ from the x -axis (c). These boundary conditions are similar to the one used in the cylindrical case and hence the obtained solutions for this case will have similar features to the ones obtained in the cylindrical case as expected.

Three dimensional plots of magnetic field lines for the three different boundary conditions are shown in Fig. (6.3), where the colour contours on the central sphere represent the strength of the radial magnetic field component B_r . The structure of the magnetic field is clearly affected by the change of boundary conditions, which have resulted in a symmetric magnetic field for the aligned rotator case and a non-symmetric ones for the other two cases. Figure (6.4) shows isosurfaces of the three-dimensional pressure deviation from the background pressure, where the effect of the strength of the magnetic field on the structure of the pressure deviation isosurfaces can be clearly seen. Close to the boundary of the spherical body, where the magnetic field (and thus the pressure deviation) is strong, it can be easily seen that one has smaller isosurfaces than away from the spherical body where the magnetic field is weaker. Moreover, the effect of the change of the boundary conditions is also visible in the symmetry of these isosurfaces, where one has symmetric isosurfaces only for the case of aligned rotator (top panels in Fig. 6.4). This increasing degree of asymmetry when changing the boundary conditions from the case of aligned rotator over the case of oblique rotator to the case of displace dipole is also confirmed in Figs. (6.5) and (6.6), which show cross section plots of the variation of the three-dimensional pressure and density deviations from their background ones in different planes parallel to the xz -plane. One can clearly see that symmetry of the pressure and density deviations present for the case of aligned rotator about the x and z -axes is broken for the other two cases. However, these cross section plots show some symmetry about the y -axis for all three cases. Moreover, for the case of aligned rotator (top panels in Fig. 6.5), one could easily see the appearance of almost-vertical dark features. These features, which correspond to a vanishing pressure deviation, clearly does not pass through the co-rotation

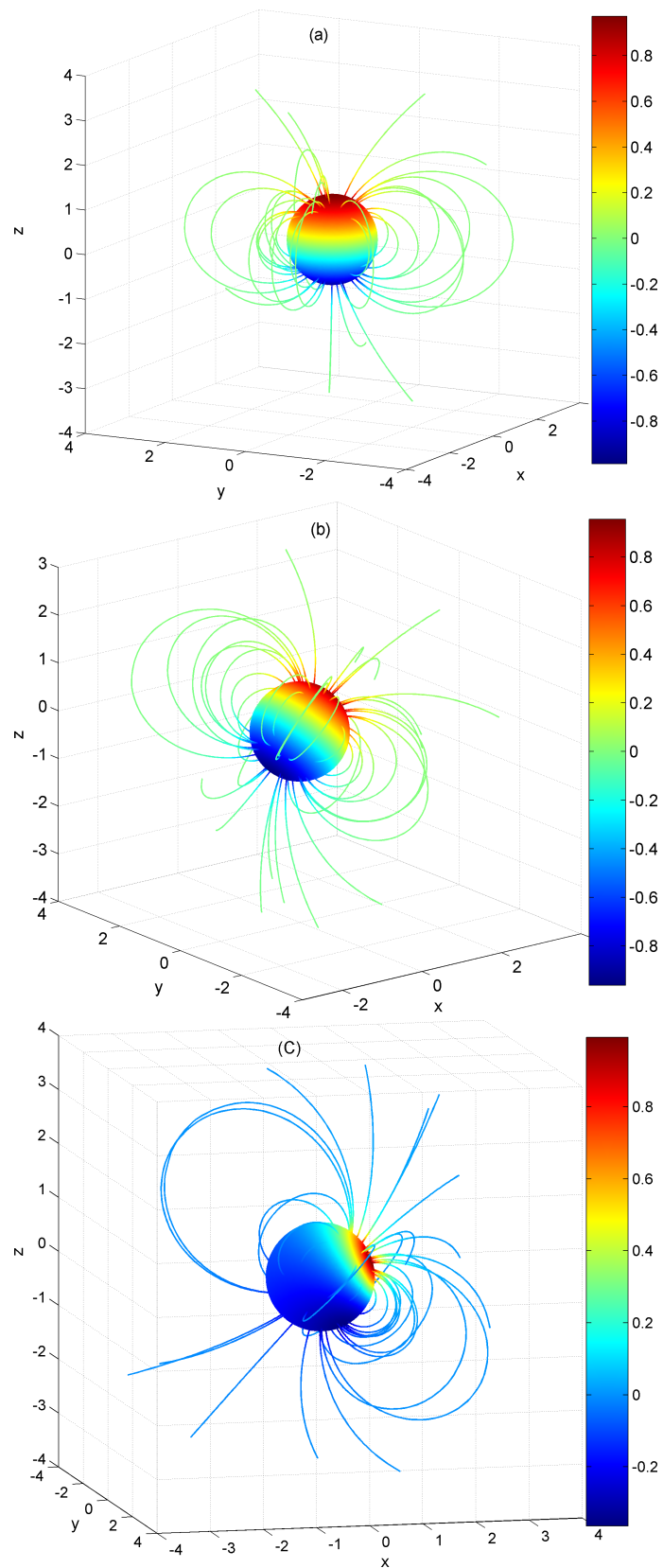


Figure 6.3: Three-dimensional plots of random field lines for the three cases of aligned rotator (a), oblique rotator (b) and displaced dipole (c).

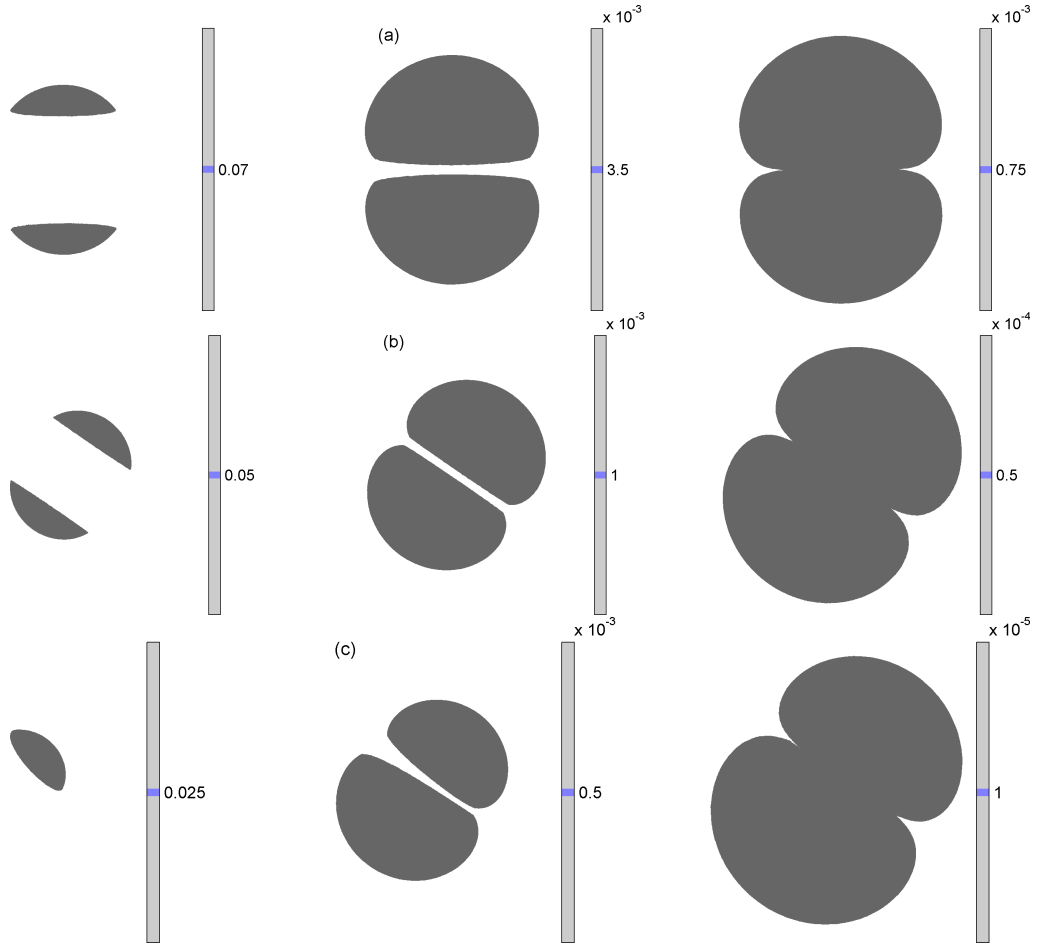


Figure 6.4: Pressure isosurface plots for the aligned rotator case (top panels), the oblique rotator case (middle panels) and the displaced dipole case (bottom panels). Showing is the absolute value of the pressure deviation from the background pressure.

radius. However, for the other two cases (middle and bottom panels in Fig. 6.5), they appear close to the outer boundary due to the change in the boundary conditions.

Furthermore, the resultant three dimensional pressure and density deviations, as for the cylindrical case, are always negative and the previous plots only show their absolute values. Hence, in order to calculate the plasma temperature, its required to include background pressure and density, which of course will be reduced to lower values by these deviations. However, as it can be clearly seen from Eqs. (6.13) and (6.14), we only need to find a background pressure $p_0(V)$. One way to find $p_0(V)$ is to consider a constant background temperature, say, T_0 and use the dimensionless equation of state and a force balance equation, namely,

$$\begin{aligned} p_0 &= \rho_0 T_0, \\ \nabla p_0 &= -\rho_0 \nabla V. \end{aligned}$$

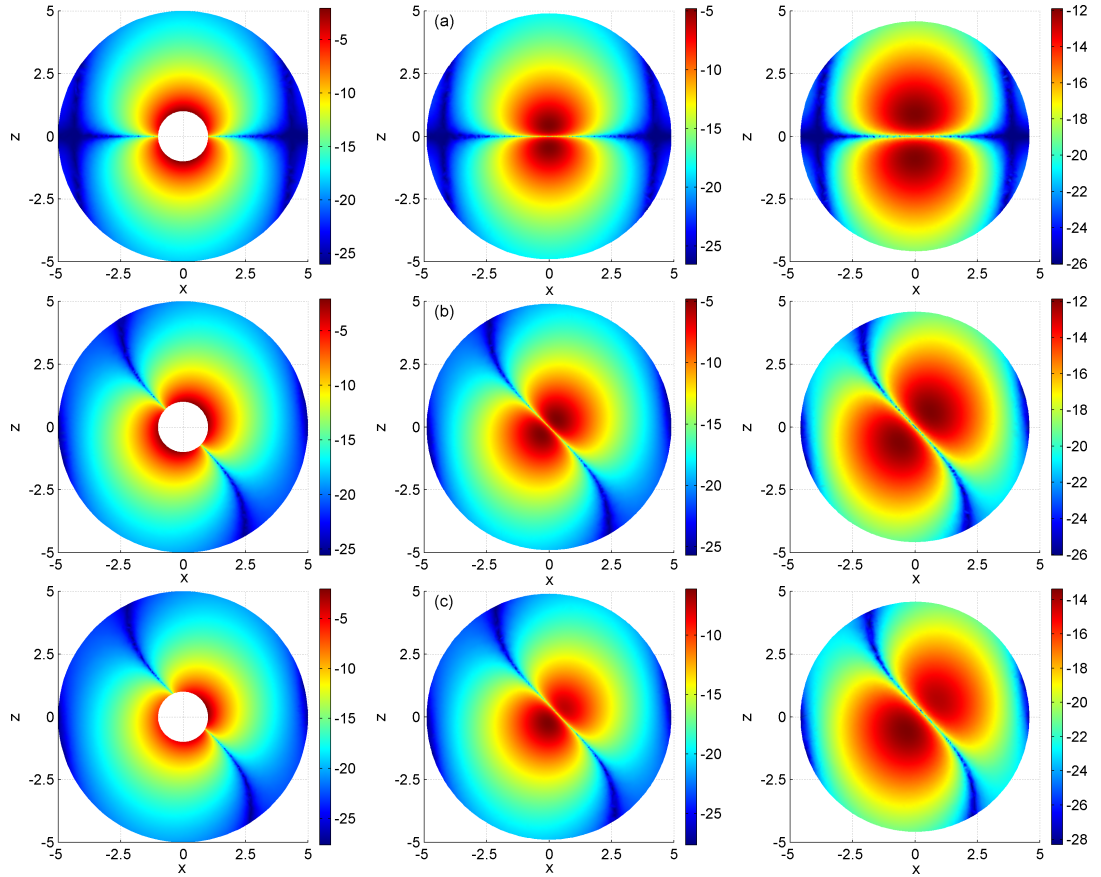


Figure 6.5: Variation of the pressure deviation from the background pressure in the xz -plane at $y = 0$ (through the central sphere), $y = \pm 1$ (touching the central sphere), and $y = \pm 2$, respectively. Shown is the logarithm of the pressure.

This system of equations can be satisfied by taking

$$p_0(V) = p_{00} \exp\left(-\frac{V}{T_0}\right), \quad (6.15)$$

where p_{00} is constant, which will be used to ensure that the total pressure and density are positive. Setting the background temperature T_0 to 0.1, it is enough to take $p_{00} = 10^{-5}$ in order to have a positive total pressure and density. The resultant total temperature is illustrated in Fig. (6.7), which shows cross section plots of the plasma temperature in planes parallel to the xz -plane for different y -values. Similar to the plasma pressure and density, the temperature is affected by the change of boundary conditions leading to a symmetry about the x -axis and z -axis only for the aligned rotator case. Moreover, there is only a small deviation of the plasma temperature from its background with its maximum deviation close to the spherical body, where the pressure and density have their maximum deviations as well.

In this section, we have only obtained solutions in a domain up to the co-rotation radius. Solutions

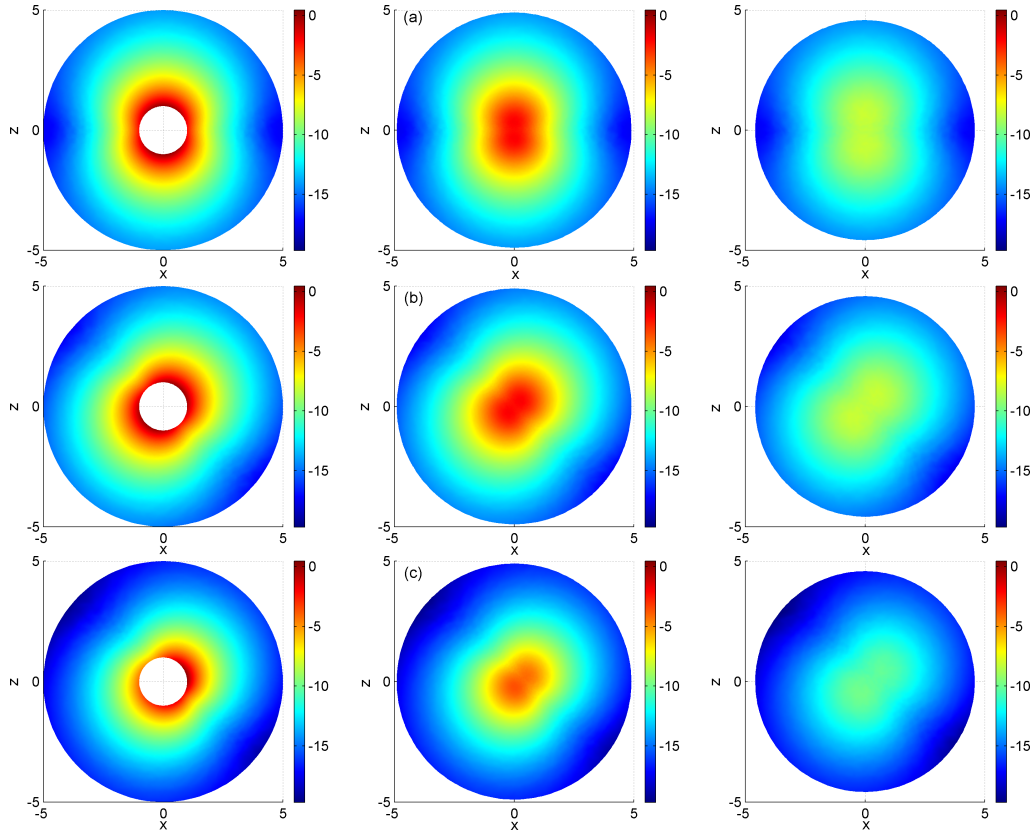


Figure 6.6: Variation of the density deviation from the background density in the xz -plane at $y = 0$ ((through the central sphere), $y = \pm 1$ (touching the central sphere), and $y = \pm 2$, respectively. Shown is the logarithm of the density.

in a domain extended beyond the co-rotation radius are presented in the next section, where we discuss the effect of increasing the angular velocity Ω on the solutions.

6.2.2 Example Solution II

Here, we consider the same choice of the free function $\kappa(V)$ discussed in the previous section, namely, taking $\kappa(V)$ to be constant. However, we will now change the angular velocity Ω aiming to study the effect of increasing Ω on the solutions. One obvious effect of increasing Ω , as it can be clearly seen from Eq. (6.9), is to reduce the co-rotation radius. Thus, we shall increase Ω in such way that it leads to a co-rotation radius $r_{co} = 2.5$. We use the same domain and boundary conditions as in the previous example. Hence, we could now study the behavior of the solutions beyond the co-rotation radius as well, since our domain is now clearly extending beyond the co-rotation radius.

The expression $1 - \kappa(V)(\nabla V)^2$ is still always positive in the domain $1 \leq r = \sqrt{x^2 + y^2 + z^2} \leq$

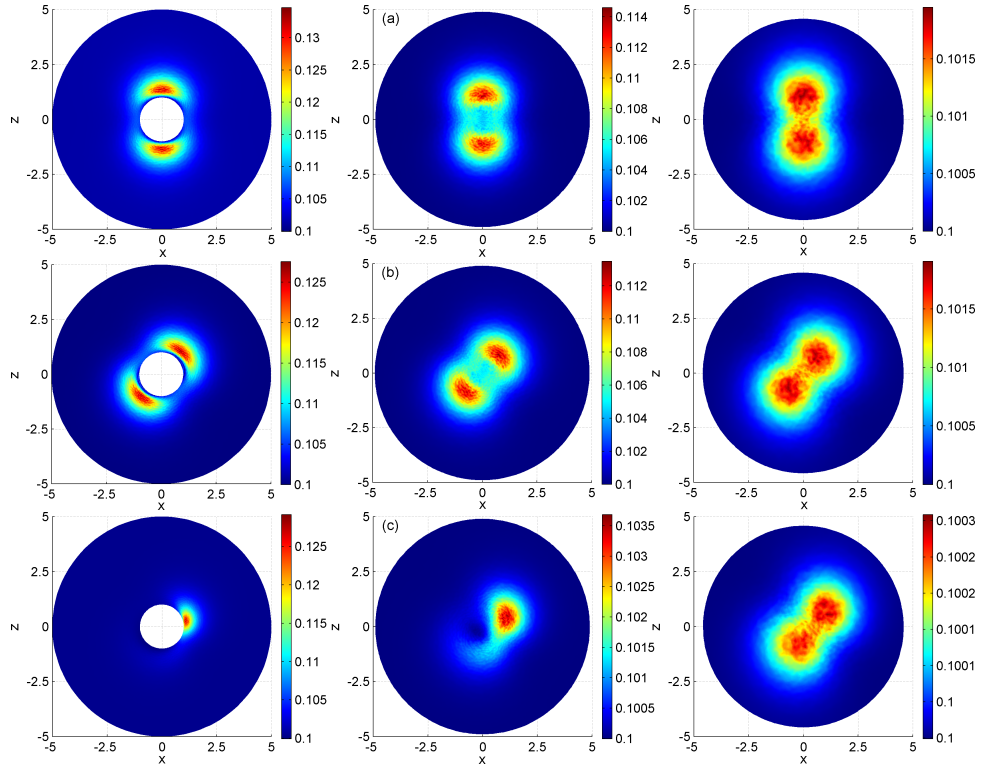


Figure 6.7: Variation of the total plasma temperature in the xz -plane at $y = 0$ (through the central sphere), $y = \pm 1$ (touching the central sphere), and $y = \pm 2$, respectively. The temperature deviation from its background is largest close to the spherical body.

5, and hence any singularities in Eq. (5.14), if exist, are clearly out side our domain. The resultant solutions for this case are illustrated in Figs. (6.8) - (6.10). Figure (6.8) shows cross section plots of the pressure deviation from its background again at different planes parallel to the xz -plane for the three different types of boundary conditions. These plots show that, as one moves away from the spherical body towards the co-rotation radius, the pressure deviation is decreasing faster than it is in the previous example. This is because the co-rotation radius is now closer to the spherical body due to the increase in the angular velocity. Moreover, the pressure deviation is negligible beyond the co-rotation radius and the dark features in Fig. (6.8) correspond to a vanishing pressure deviation. The location and structure of these dark features are clearly affected by the change of the boundary conditions. For example, in the leftmost panels ($y = \pm 1$), one can easily see that the two dark features bounding the region of strong pressure deviation from left and right do not cross the co-rotation radius for the case of aligned rotator, whereas for the other two cases they are clearly passing through the co-rotation radius. Some of these dark features occur only within the co-rotation radius and start to reduce as one moves towards the co-rotation radius until one only left with a single dark feature as shown in the rightmost panels ($y = \pm 2.5$).

The effect of increasing the angular velocity Ω on the variation of the plasma density and tem-

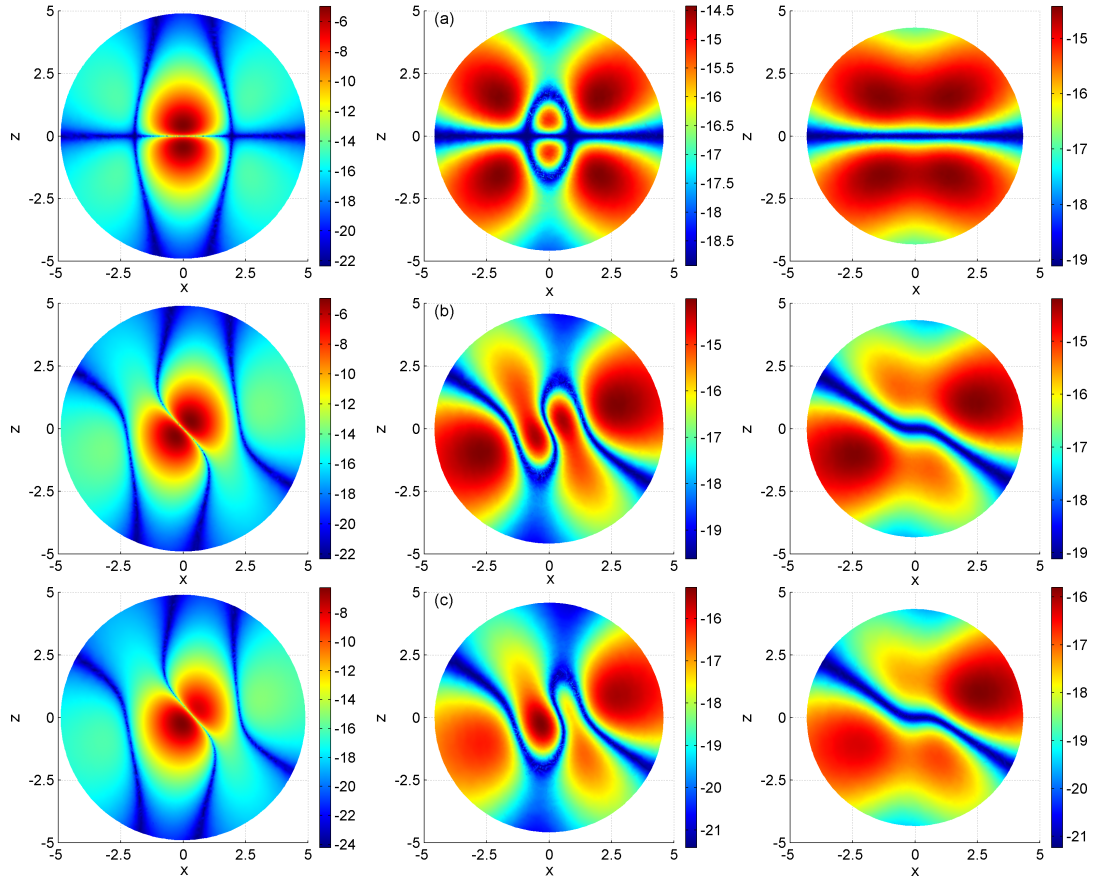


Figure 6.8: Variation of the pressure deviation from the background pressure in the xz -plane at $y = \pm 1$ (touching the central sphere), $y = \pm 2$, and $y = \pm 2.5$, respectively. Shown is the logarithm of the pressure.

perature is shown in Figs. (6.9) and (6.10), which show cross section plots of the variation of the density deviation from its background and the total temperature variation, respectively, for the three different types of boundary conditions at a plane touching the spherical body and parallel to the xz -plane. Here, we can clearly see that the rate at which these quantities are varying is fast compared to the one in the previous example, where the angular velocity is smaller.

6.3 Summary

In this chapter, we have applied the theory for calculating three-dimensional solutions of the magnetohydrostatic equations presented in the previous chapter to the case of massive rigidly rotating spherical body. In this case (using spherical coordinates r , θ and ϕ), the combined gravitational and centrifugal potential V depends on two coordinates, namely, r and θ . Due to this dependence, the fundamental equation of the theory (5.14) has now a much more complicated form than it is in

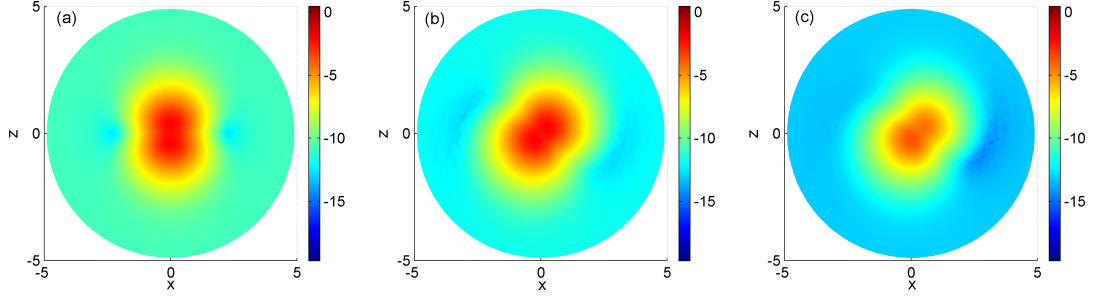


Figure 6.9: Variation of the density deviation from the background density in the xz -plane at $y = \pm 1$ (touching the central sphere) for the three different boundary conditions. Shown is the logarithm of the density.

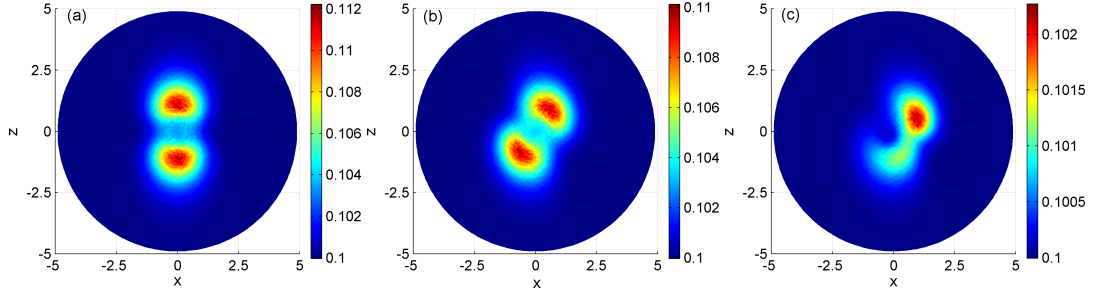


Figure 6.10: Variation of the total plasma temperature in the xz -plane at $y = \pm 1$ (touching the central sphere) for the three different boundary conditions.

the cylindrical case, since in the spherical case it includes mixed second-order derivatives. Hence, obtaining analytical solutions for the resulting Eq. (6.5) is highly unlikely to be achieved. However, Eq. (6.5) can still be solved numerically using similar numerical methods to the ones used for the cylindrical case. So, we have carried this out presenting numerical solutions for the case of $\kappa(V) = \kappa_0 = \text{constant}$ as an illustrative example. We have used the same boundary conditions as the ones used in the cylindrical case, namely, we have used a magnetic dipole field for the three cases of aligned rotator, oblique rotator and displaced dipole.

The obtained numerical solutions for the case of constant κ using spherical geometry have similar features to the ones obtained for the same case using cylindrical geometry with only minor differences. One of these differences is that the locations of vanishing three dimensional pressure deviation from its background are now more complicated than they are in the cylindrical case. In the cylindrical case the pressure deviation vanishes at the co-rotation radius, ϖ_{co} , or when the radial component of the magnetic field, B_{ϖ} is zero. At the co-rotation radius, locations of vanishing pressure deviation represented by dark vertical features are not affected by the change of the boundary conditions, which has an effect only at locations where $B_{\varpi} = 0$, whereas in the spherical case, all locations of vanishing pressure deviations are affected by the change of the boundary conditions.

In this case, we have also used a specific background pressure $p_0(V)$ with the background temperature being constant and assuming that the background pressure, density, and temperature satisfy the equation of state of an ideal gas. We have then calculated the background density using $\rho_0(V) = -dp_0/dV$ and the total plasma temperature using the equation of state. The maximum deviations of the pressure, density and temperature from their background profiles were found to be close to the spherical body similar to the cylindrical case.

Finally, we have presented numerical solutions for the same case, i.e. the constant κ case, but with increasing the angular velocity Ω . The obtained solutions show that, as one moves away from the spherical body, the different plasma quantities are now varying much faster compared to the previous case with smaller angular velocity.

Chapter 7

Summary and Future Work

“ And they ask you (O Muhammad) concerning the Spirit; Say: ”The Spirit is one of the things, the knowledge of which is only with my Lord. And of knowledge, you (mankind) have been given only a little.Θ”

(Interpretation of the Holy Quran 17: 85)

7.1 Summary

Solutions of the magnetohydrodynamic (MHD) equations are very important for modelling laboratory, space and astrophysical plasmas. Realistic models should be three dimensional and hence a progress towards more realistic geometries in MHD is very important for our understanding of plasmas in these different environments. However, only few analytical solutions of the MHD equations exist in three dimensions and most work consists of numerical simulations.

In this thesis, we have presented both analytical and numerical solutions of three dimensional MHD models in two different areas. In Chapters 3 and 4, we have used a stationary incompressible resistive MHD model for three-dimensional magnetic reconnection in the absence of null points. This work builds on and extends the work started by Hornig and Priest (2003) and Wilmot-Smith et al. (2006, 2009). In Chapters 5 and 6, we have presented three-dimensional solutions of the magnetohydrostatic (MHS) equations outside massive rigidly rotating central bodies using a theory developed by Low (1991) and extending the work done by Neukirch (2009).

In Chapter 3, solutions of the stationary MHD equations were obtained in the form of an expansion scheme in terms of powers of the Alfvén Mach number, M_A , with a localized non-ideal region. The lowest order magnetic field was found to be potential since the current density at zeroth order

is zero. A basic state of an X-type equilibrium magnetic field in the xy plane, superimposed on a uniform magnetic field in the z -direction was then used, which in 3D has a form known as “hyperbolic flux tube”. In order to have a localized non-ideal region, a localized form of the resistivity η_c was assumed. This form also allowed for analytical solutions at least for the first few orders. The localization parameters, namely the parameters L and l which are related to the length of the non-ideal region in the z -direction and to the width of the non-ideal region in the $z = 0$ plane, respectively, were chosen such that the non-ideal region is completely enclosed in the HFT. We have also used the same assumptions as in Wilmot-Smith et al. (2009) to allow for direct comparison.

Solutions of equations at different orders were obtained via an integration scheme which allowed us to prescribe certain properties of the solutions, such as stagnation flows and parallel electric fields, through the freedom of choosing its free functions and prescribing the low-level terms. Hence, unlike reconnection in 2D, a wide variety of 3D reconnection solutions can be obtained. General analytical solutions were then obtained for equations at the first few orders, from which the analytical solutions obtained by Wilmot-Smith et al. (2009) can be recovered by taking special choices of the free parameters included in these general solutions. Solutions of equations at higher orders, on the other hand, can only be obtained numerically. Example numerical solutions at higher orders were then calculated using the integration scheme along with a particular set of the analytical solutions obtained at lower orders. The obtained analytical and numerical solutions of equations at different orders were finally combined to calculate an approximation of the total solution for each variable.

The obtained total solution approximations show important differences between 3D reconnection solutions and the commonly used 2D models such as the appearance of saddle-type current structures and the existence of multiple X and O -point type flows in the reconnection region. The results of this chapter have been published in Al-Salti and Hornig (2009).

In Chapter 4, we have extended the kinematic non-null reconnection solutions obtained by Hornig and Priest (2003) using the stationary MHD model and the integration scheme presented in Chapter 3. The velocity at zeroth order was taken to be zero in order to allow for direct comparison with the kinematic solutions. We have also considered the two cases discussed by Hornig and Priest (2003), namely, the case of pure solutions, where no ideal velocity is superimposed and the case of composite solutions, which corresponds to a situation where a stagnation flow is superimposed on the rotational flow obtained in the pure solution case. The obtained analytical solutions of equations up to second order are very similar to the kinematic ones for both cases. This is because these solutions do not include the effect of the inertial term in the equation of motion, which first appears at fourth order. We then solved the equations at some higher orders numerically and combined the obtained numerical solutions and the analytical solutions of equations at lower order. The resultant solutions showed some deviations from the kinematic ones in the vicinity of the

z -axis, where for example, a stagnation flow appeared together with a rotational flow for the case of pure solutions compared to only a rotational flow in the kinematic model. The current density for this case also deviated from the constant current in the kinematic case to have a saddle point at $x = y = 0$.

For the case of composite solutions, we found that the relative magnitude of the rotational flow and the superimposed stagnation flow has an important effect on the structure of the obtained solutions. This has been illustrated with three different cases of composite solutions. The most important effect was found when the maximum strength of the stagnation flow is slightly greater than the one of the rotational flow. In this case, we found that the obtained total solution approximations are similar to the kinematic ones, since the contribution from higher order terms is, in general, negligible. The results of this chapter is currently in preparation for later publication (Al-Salti and Hornig 2010).

The results of Chapters 3 and 4 have shown that it is very important to include both X -type and O -type flows when modelling magnetic reconnection in the solar corona (for example, reconnection in solar flares). This is because our results show that these two types of flows do exist in the process of reconnection and their relative strength plays a very important role in determining the structure of the reconnection solutions.

In Chapter 5, we have started by presenting a coordinate independent theoretical framework for calculating three-dimensional MHS solutions outside massive rigidly rotating central bodies. The theory was simplified using a special form of the current density, which contains a free function $\kappa(V)$, where V is the combined gravitational and centrifugal potential in the co-rotating frame of reference. The MHS equations was then reduced to a single partial differential equation, referred to as the fundamental equation of the theory, for a pseudo-potential U . The theory also contains another free function, namely, a background pressure $p_0(V)$. We have then considered a special case of massive rigidly rotating magnetized cylinder. Introducing a new function $\xi(\varpi) = \kappa(V)V'^2$ allows somehow for analytical solutions. However, choosing $\xi(\varpi)$ instead of $\kappa(V)$ generally leads to possible singularities of $\kappa(V)$ at the co-rotation radius, which in turn lead to singularities of the plasma density and hence temperature. These problems can be easily avoided by directly choosing $\kappa(V)$, however, it is highly unlikely to find analytical solutions of the fundamental equation of the theory in this case even for simple choices of $\kappa(V)$ and hence numerical techniques need to be used.

A more realistic case of massive rigidly rotating spherical body was considered in Chapter 6. However, the resultant fundamental equation in this case is too complicated to allow for analytical solutions to be found and hence solutions can be only obtained numerically. As illustrative examples, the two cases of rotating cylinder and spherical body were solved for the simplest choice $\kappa(V) = \kappa_0 = \text{constant}$ using the same numerical method. This numerical method was first tested

using an example of analytical solutions, which were obtained by taking $\xi(\varpi)$ to be constant in the cylindrical case. The obtained numerical solutions for this case agree very well with the analytical solutions on their domain of validity.

Numerical solutions for the constant κ case were obtained using three different types of boundary conditions on the surface of the central body: a magnetic dipole field generated by a dipole moment located at the origin, aligned with the rotation axis (aligned rotator), a magnetic dipole field generated by a dipole moment located at the origin, but at an angle with the rotation axis (oblique rotator) and a magnetic dipole moment displaced from the origin, with the dipole moment not aligned with the rotation axis. The resultant numerical solutions for the two cases of rotating cylinder and spherical body show only minor differences. For examples, locations of vanishing three-dimensional pressure deviation from its background are more complicated in the spherical case than the cylindrical one. This is due to the dependence of the combined gravitational and centrifugal potential in more than one coordinate in the spherical case.

The obtained three-dimensional pressure and density deviations from their background profiles were found to be negative with the maximum deviations close to the central body. Hence, in order to calculate the plasma temperature, we have first calculated a background pressure assuming a constant background temperature and using the equation of state. This has been done only for the spherical case. The obtained temperature also shows a maximum deviation close to the spherical body.

Finally, we have studied the effect of increasing the angular velocity and found that the higher the angular velocity the smaller the co-rotation radius and hence the faster the variation of different plasma quantities as one moves away from the central body. The results of Chapters 5 and 6 can be found in Al-Salti et al. (2010) and Al-Salti and Neukirch (2010).

The importance of the method presented in Chapters 5 and 6 lies in the fact that it allows a relatively simple way of obtaining models for the closed magnetic field regions of the coronae of fast rotating stars. We showed that solutions can be found numerically with a standard package for solving elliptic partial differential equations. So, it should be possible in the future to use this method without dramatically increasing the demands on computational resources to improve upon potential field models of rotating magnetospheres and coronae.

7.2 Future Work

In Chapters 3 and 4, we have used a stationary MHD model in which the resistive term was the only non-ideal effect included in Ohm's law. Other non-ideal terms such as the electron inertia and the Hall terms, in principle, may also be included. However, one would first have to examine whether

the expansion scheme used in the resistive case is still valid or not when other non-ideal terms are included. If so, one can then examine the effects of these terms on the non-null reconnection.

The shape of the non-ideal region used in this model is a slightly deformed ball. In a realistic plasma, one would expect a much more elongated region, however, this would require a higher numerical resolution than we currently have and might also make the visualization of the fine structures that appeared in the obtained solutions more difficult. Nevertheless, if a higher resolution can be achieved, it would be good to examine the effect of using a more elongated non-ideal region on the reconnection solutions as the new situation will now involve stronger gradients. Moreover, the non-ideal region was localized by only imposing a localized resistivity, which was used in order to allow for analytical solutions. However, a more realistic way of localizing the non-ideal region would be through a localization of both the current density and the resistivity. This might make it difficult to make analytical progress, but numerical solutions can be easily obtained using the described integration scheme and provided that the required resolution can be achieved as well.

In Chapters 5 and 6, we have illustrated a theory for calculating three-dimensional MHS solutions outside massive rigidly rotating central bodies by considering the two cases of rotating magnetized cylinder and spherical body. However, as we have already mentioned, the theory is also applicable to other cases such as synchronously rotating stars, using e.g. the Roche potential. Another possible future application is to model the closed field region of the coronae of fast rotating stars using measured surface magnetic fields.

The theory also contains free functions $\kappa(V)$ and $p_0(V)$, where V is the combined gravitational and centrifugal potential in the co-rotating frame of reference. In our illustrative examples we have considered particular choices of these functions. However, in the future, one could also include different choices of these functions and hence investigate their effects on the solutions.

Moreover, for the solutions obtained in this thesis, we have imposed a boundary condition on an imaginary outer boundary. A full solution of the problem, however, would also include a stellar wind on open field line regions and the need to solve a free boundary problem to determine the transition from open to closed field regions. Hence, one could as a first step towards solving the full problem, assume that the open field line regions are potential and thus try to determine the boundary between open and closed field line regions. This is beyond the scope of the present thesis.

Finally, the governing MHS equations were simplified using a special form of the current density, which has led to a single linear partial differential equation for a pseudo-potential U . Obviously, it would be interesting to study the effect of using different forms of the current density. For example, one can use a more general form which ensures that the current density is divergence free

such that

$$\mu_0 \mathbf{j} = \nabla F \times \nabla G,$$

where both F and G are free functions.

Appendix A: Derivation Of The Generalized Ohm's Law

Let the momentum-balance equations of ions and electrons be given, respectively by,

$$nm_i \left(\frac{\partial}{\partial t} + (\mathbf{v}_i \cdot \nabla) \right) \mathbf{v}_i = -\nabla p_i + ne(\mathbf{E} + \mathbf{v}_i \times \mathbf{B}) - ne\eta_e \mathbf{j} \quad (1)$$

$$nm_e \left(\frac{\partial}{\partial t} + (\mathbf{v}_e \cdot \nabla) \right) \mathbf{v}_e = -\nabla p_e - ne(\mathbf{E} + \mathbf{v}_e \times \mathbf{B}) + ne\eta_e \mathbf{j} \quad (2)$$

where $\mathbf{v}_e = \mathbf{v}_i - \mathbf{j}/ne$. Multiplying Eq. (1) by e/m_i and Eq. (2) by e/m_e we get

$$ne \left(\frac{\partial}{\partial t} + (\mathbf{v}_i \cdot \nabla) \right) \mathbf{v}_i = -e \frac{\nabla p_i}{m_i} + \frac{ne^2}{m_i} (\mathbf{E} + \mathbf{v}_i \times \mathbf{B}) - \frac{ne^2}{m_i} \eta_e \mathbf{j}$$

$$ne \left(\frac{\partial}{\partial t} + (\mathbf{v}_e \cdot \nabla) \right) \mathbf{v}_e = -e \frac{\nabla p_e}{m_e} - \frac{ne^2}{m_e} (\mathbf{E} + \mathbf{v}_e \times \mathbf{B}) + \frac{ne^2}{m_e} \eta_e \mathbf{j}$$

These two equations can then be combined to give

$$\begin{aligned} \frac{\partial \mathbf{j}}{\partial t} + \left((\mathbf{v} \cdot \nabla) \mathbf{j} + (\mathbf{j} \cdot \nabla) \mathbf{v} - \frac{1}{ne} (\mathbf{j} \cdot \nabla) \mathbf{j} \right) \\ = -e \left(\frac{\nabla p_i}{m_i} - \frac{\nabla p_e}{m_e} \right) + ne^2 \left(\frac{1}{m_i} + \frac{1}{m_e} \right) (\mathbf{E} + \mathbf{v} \times \mathbf{B}) \\ - \frac{e}{m_e} (\mathbf{j} \times \mathbf{B}) - ne^2 \left(\frac{1}{m_i} + \frac{1}{m_e} \right) \eta_e \mathbf{j}, \end{aligned}$$

where, $\mathbf{v} = \mathbf{v}_i$. Further more, assuming that $p_i \approx p_e$, the last equation leads to the Generalized Ohm's Law,

$$\mathbf{E} + \mathbf{v} \times \mathbf{B} = \eta_e \mathbf{j} + \frac{m_e}{ne^2} \left(\frac{\partial \mathbf{j}}{\partial t} + (\mathbf{v} \cdot \nabla) \mathbf{j} + (\mathbf{j} \cdot \nabla) \mathbf{v} - \frac{1}{ne} (\mathbf{j} \cdot \nabla) \mathbf{j} \right) + \frac{1}{ne} (\mathbf{j} \times \mathbf{B} - \nabla p_e) \quad (3)$$

since $m_i \gg m_e$.

Appendix B: Electron Parallel Compressibility Effects on Magnetic Reconnection

One of the problems that shows the appearance of the the ion sound Larmor (gyro-) radius is the study of the electron parallel compressibility effects on magnetic reconnection (see, e.g., Kleva et al. (1995); Shivamoggi (2007)). Here we consider a 2D, incompressible, two-fluid model with the electrons assumed to be isothermal. Hence the generalized Ohm's law (3) can now be written as

$$\mathbf{E} + \mathbf{v} \times \mathbf{B} = \eta_e \mathbf{j} + \frac{m_e}{ne^2} \left(\frac{\partial \mathbf{j}}{\partial t} + (\mathbf{v} \cdot \nabla) \mathbf{j} + (\mathbf{j} \cdot \nabla) \mathbf{v} \right) + \frac{1}{ne} \mathbf{j} \times \mathbf{B} - \frac{k_B T_e}{ne} \nabla n, \quad (4)$$

where, k_B is the Boltzmann constant and T_e is the electron-fluid Temperature. Let the corresponding magnetic field be given by

$$\mathbf{B} = \nabla \psi \times \mathbf{e}_z + B_z \mathbf{e}_z \quad (5)$$

where B_z is assumed to be a large uniform guide field (low- β approximation) which justifies taking the plasma flow to be incompressible. Hence, the current density and electric field are given, respectively, by

$$\mathbf{j} = -\frac{1}{\mu} \nabla^2 \psi \mathbf{e}_z \quad (6)$$

$$\mathbf{E} = -\psi_t \mathbf{e}_z - \nabla \phi \quad (7)$$

The corresponding velocity is then given by

$$\mathbf{v} = \frac{1}{B_z} (\mathbf{e}_z \times \nabla \phi), \quad (8)$$

since the plasma motion is dominated by the $\mathbf{E} \times \mathbf{B}$ drift velocity.

If we assume that the electron number density, n_e , is initially uniform and for static equilibrium we have $n_e = n_i = n_0$. Then, any variations in n_e must be balanced by variations in the ion number density, n_i , since the plasma must remain quasineutral (i.e $n_e \approx n_i \approx n$). Thus, to find an expression for the number density, n , we will use the ion continuity equation,

$$\frac{\partial n_i}{\partial t} + \nabla \cdot (n_i \mathbf{v}_i) = 0 \quad (9)$$

Assuming $n_i = n_0 + \delta n_i$ where, $\delta n_i \ll 1$. Eq. (9) gives

$$\frac{dn_i}{dt} = -n_0(\nabla \cdot \mathbf{v}_i) \quad (10)$$

The variation in the ion density is then generated by the polarization drift since the $\mathbf{E} \times \mathbf{B}$ drift velocity is divergence free. Hence, Eq. (10) leads to

$$n \approx n_i = n_0 - \frac{n_0 m_i}{e B^2} (\nabla \cdot \mathbf{E}) \quad (11)$$

Using Eq. (11), Eq. (4) becomes

$$\mathbf{E} + \mathbf{v} \times \mathbf{B} = \eta_e \mathbf{j} + \frac{m_e}{n_0 e^2} \left[\frac{\partial \mathbf{j}}{\partial t} + (\mathbf{v} \cdot \nabla) \mathbf{j} + (\mathbf{j} \cdot \nabla) \mathbf{v} \right] + \frac{1}{n_0 e} \mathbf{j} \times \mathbf{B} + \varrho_s^2 \nabla (\nabla \cdot \mathbf{E}) \quad (12)$$

where $\varrho_s = \frac{(k_B T_e m_i)^{\frac{1}{2}}}{e B} = \frac{(k_B T_e / m_i)^{\frac{1}{2}}}{\Omega_i}$ is the ion sound Larmor (gyro)-radius and $\Omega_i = \frac{e B}{m_i}$ is the ion Larmor (gyro)-frequency. Thus, when the electron is taken to be isothermal, electron parallel compressibility introduces a new microscopic scale-length, ϱ_s .

Taking the dot product of Eq. (12) with \mathbf{B} and using Eqs. (5) - (8), we get

$$(\psi - d_e^2 \nabla^2 \psi)_t + [\phi, \psi - d_e^2 \nabla^2 \psi] = \eta \nabla^2 \psi + \varrho_s^2 [\nabla^2 \phi, \psi] \quad (13)$$

Similarly, taking the curl of the equation of motion

$$\rho \left(\frac{\partial}{\partial t} + (\mathbf{v} \cdot \nabla) \right) \mathbf{v} = \mathbf{j} \times \mathbf{B} - \nabla p$$

and using Eqs. (5), (6) and (8), we get

$$\nabla^2 \phi_t + [\phi, \nabla^2 \phi] = [\psi, \nabla^2 \psi] \quad (14)$$

In these derivations, we have replaced ϕ by $B_z \phi$, ψ by $\sqrt{\mu \rho} \psi$ and, again, used the Poisson bracket notation $[f, g] = f_x g_y - f_y g_x$.

Appendix C: MATLAB Routines for Solving Equations (3.14) and (3.15)

Here we present MATLAB routines for solving equations at higher orders using the integration scheme introduced in Section 3.3.

- **Calculating points along the field line connecting a given point (x, y, z) and its mapping on the $z = 0$ plane.**

Input: x, y, z coordinates of a set of points.

Output: a structure array containing the coordinates and number of points along field lines going from the $z = 0$ plane to the given points and the distance between the last two points in each field line along the z -axis.

```
%=====M-File begins=====
function Bpoints=PalongB(x,y,z)

j0 = 1;
k = k0;
% the parameter in  $\mathbf{B}_0 = (ky, kx, 1)$   $ds = ds0$ ; % step size

clear sizeX0 dz0 Mx0 My0 Mz0

for j = 1:max(size(x))
clear x0 y0 z0

x0(1) = x(j).*cosh(k*z(j))-y(j).*sinh(k*z(j));
y0(1) = y(j).*cosh(k*z(j))-x(j).*sinh(k*z(j));
z0(1) = 0;

for i = 1:fix(0.5 + abs(z(j))/ds)

z0(i+1) = sign(z(j))*ds*(i-0.5);
y0(i+1) = y0(1).*cosh(k*z0(i+1))+x0(1).*sinh(k*z0(i+1));
x0(i+1) = x0(1).*cosh(k*z0(i+1))+y0(1).*sinh(k*z0(i+1));

end
```

```

z0(fix(0.5 + abs(z(j))/ds)+2) = z(j);
y0(fix(0.5 + abs(z(j))/ds)+2) = y(j);
x0(fix(0.5 + abs(z(j))/ds)+2) = x(j);

sizeX0(j) = max(size(x0)); % gives the number of points along each field line
dz0(j) = abs((z0(end)-z0(end-1))); % difference between the z-coordinates of last two points

% Including each coordinate of the computed points in one matrix
Mx0(j0:j0+sizeX0(j)-1) = x0;
My0(j0:j0+sizeX0(j)-1) = y0;
Mz0(j0:j0+sizeX0(j)-1) = z0;
j0=j0+sizeX0(j);

end

Bpoints{1} = [Mx0;My0;Mz0]; Bpoints{2} = sizeX0; Bpoints{3} = dz0; % Output
return
%=====M-File ends=====

```

- **Evaluating the corresponding integrals presented in Section 3.3.**

Input: z coordinates of points at the end of each field line, points along each field line and the interpolant of the integrand if it has only numerical values.

Output: values of the integral at points at the end of the given field lines.

```

%=====M-File begins=====
function FFF=IFFF(zO,Bpoints,RBFIF)

ds=ds; % step size

%-----
% This is to evaluate the integrand on points along fieldlines using FastRBF interpolation
(described below) if it has only numerical values, where RBFIF is the resultant interpolant.

Mxyz = Bpoints{1};
IFS = fastrbf_pointeval(RBFIF,Mxyz,Eacc); % Eacc = evaluation accuracy (optional)
IF = IFS.Value;
%-----
% This is to evaluate integrands with analytical expressions.

x = Bpoints{1}(1,:); y = Bpoints{1}(2,:); z = Bpoints{1}(3,:);
IF = IFS(x,y,z)
%-----

sizeX0 = Bpoints{2}; dz0 = Bpoints{3};
i0 = 1;

for j = 1:max(size(zO))

```

```

FFF(j) = sign(zO(j))*(sum(IF(i0:i0+sizeX0(j)-2))*ds+IF(i0+sizeX0(j)-1)*dz0(j)-IF(i0)*ds);
i0 = i0+sizeX0(j);
end
return
%=====M-File ends=====

```

Note: the previous two M-Files can be combined in a single M-File if necessary.

- **Interpolating 3D data and calculating gradients using the FastRBF method.**

```

%=====M-File begins=====
clear Data3D
Data3D.Location = XYZ; % data points XYZ = [x; y; z]
Data3D.Value = FXYZ; % values of the function at the data points
Data3D = fastrbf_unique(Data3D);
RBFFXYZ = fastrbf_fit(Data3D,Facc); % Facc= fitting accuracy
FXYZS = fastrbf_pointeval(RBFFXYZ,NXYZ,'gradient');
FXYZN = FXYZS.Value; % function values at a set of points NXYZ
GradFXYZN = FXYZS.Gradients; % gradient of the function at NXYZ
clear Data3D
%=====M-File ends=====

```

For more information see the FastRBF manual at:

http://www.farfieldtechnology.com/download/toolbox/FastRBF_matlab.pdf

- **Solving Ampere's law at the n -th order, Eq. (3.15), for B_n .**

Here we use the 3D magnetostatic mode in the AC/DC model of the COMSOL Multiphysics 3.3a with MATLAB.

```

%=====M-File begins=====
fclear fem
clear a b
a = 0.2; b = 1;
fbinaryfile = 'HFT.mphm'; % a file containing the HFT
% Geometry
g1 = fbinary('g1','draw',fbinaryfile);
% Analyzed geometry
clear s
s.objs = g1;
s.name = 'HFT';
fem.draw = struct('s',s);
fem.geom = geomcsg(fem);

```

```
% Initialize mesh

% predefined mesh size
%fem.mesh = meshinit(fem, ...
% 'hauto',3);

%custom mesh size
fem.mesh = meshinit(fem, ...
'hmaxfact',0.7, ...
'hcurve',0.4, ...
'hgrad',1.4, ...
'hcutoff',0.01, ...
'hnarrow',0.7);

% Application mode

clear appl
appl.mode.class = 'QuasiStatics';
appl.name = 'emqa';
appl.module = 'ACDC';
appl.assignsuffix = '_emqa';

clear prop
prop.elemdefault = 'Vec2';
prop.analysis = 'static';
prop.potential = 'A';
prop.gaugefix = 'off';
appl.prop = prop;

clear equ
equ.Je = 'jn_x(x,y,z)';jn_y(x,y,z)';jn_z(x,y,z)'; % the x, y, z components of the current
density given in a separate M-File (see below)
appl.equ = equ;
fem.appl1 = appl;

% Multiphysics fem = multiphysics(fem);

% Generate geometric multigrid (gmg) mesh cases
fem = meshcaseadd(fem,'mgauto','shape');

% Extend mesh
fem.xmesh = meshextend(fem);

% Solve problem
fem.sol = femstatic(fem, ...
'solcomp','tAxAyAz20','tAxAyAz21','tAxAyAz10', ...
```

```

'outcomp','tAxAyAz20','tAxAyAz21','tAxAyAz10', ...
'linsolver','fgmres', ...
'prefun','gmg', ...
'prepar','mgcycle','f','presmooth','sorgauge','presmoothpar','seconditer',2,
'postsmooth','sorugauge','postsmoothpar','seconditer',2,
'csolver','gmres','csolverpar','prefuntype','right','prefun','none', ...
'mcase',[0 1]);

% Remove generated gmg mesh cases
fem = meshcasedel(fem,[1]);

% Plot solution (Example)
postplot(fem, ...
'slicedata','normH_emqa','cont','internal', ...
'slicexspacing',0, ...
'sliceyspacing',0, ...
'slicezspacing',[0:a:b], ...
'slicemap','jet(1024)', ...
'title','Slice: Magnetic Field, norm', ...
'grid','on', ...
'campos',[-6.539699589843319,-8.522702436243039,6.702261080770996], ...
'camtarget',[0,0,0.5], ...
'camup',[0,0,1], ...
'camva',10.320623975788573);

clear appl equ fbinaryfile g1 prop s a b
%=====M-File ends=====
%=====M-File begins=====
% The current density components
function y = jn_i(x,y,z) % i = x, y or z
% If jn_i has an analytic expression, say f_i(x,y,z), it can be either included in the above
M-File or defined here
% y = f_i(x,y,z)
% If it has only numerical values then we shall interpolate it using the FastRBF method
(presented above)
global RBFjn_i
XYZI=[x;y;z];
yS=fastrbf_pointeval(RBFjn_i,XYZI); y=yS.Value;
return
%=====M-File ends=====

```

Appendix D: Solutions to The Stationary Kinematic Model

We present stationary kinematic solutions obtained by Hornig and Priest (2003) of the following incompressible resistive MHD equations:

$$-\nabla\phi + \mathbf{v} \times \mathbf{B} = \eta\mathbf{j}, \quad (15)$$

$$\nabla \cdot \mathbf{v} = 0, \quad (16)$$

$$\nabla \cdot \mathbf{B} = 0, \quad (17)$$

$$\nabla \times \mathbf{B} = \mu_0\mathbf{j}, \quad (18)$$

where, $\mathbf{E} = -\nabla\phi$, since $\nabla \times \mathbf{E} = \mathbf{0}$. Prescribing the configuration of the magnetic field as:

$$\mathbf{B} = b_0 \left(\frac{y}{L_0} \hat{\mathbf{x}} + \frac{k^2 x}{L_0} \hat{\mathbf{y}} + \hat{\mathbf{z}} \right), \quad (19)$$

which clearly satisfies the solenoidal condition (17), the electric current, on using Ampere's law (18), is given by

$$\mathbf{j} = \frac{(k^2 - 1)b_0}{L_0\mu_0} \hat{\mathbf{z}}. \quad (20)$$

Now, in order to localize the non-ideal term $\eta\mathbf{j}$ and to obtain analytical solutions for the rest of the variables, the resistivity η shall be prescribed as follow:

$$\eta = \eta_0 \exp\left(-\frac{z^2 + \gamma_k^2}{l_0^2}\right), \quad (21)$$

where,

$$\gamma_k^2 = \frac{1}{2k^2} \left((k^2 + 1) (k^2 x^2 + y^2) \cosh\left(\frac{2kz}{L_0}\right) - 2kxy \sinh\left(\frac{2kz}{L_0}\right) - (k^2 - 1) (k^2 x^2 - y^2) \right).$$

Substituting Eqs. (20) and (21), for \mathbf{j} and η , respectively, into Ohm's law (15) and solving for ϕ ,

we have

$$\phi = -\frac{b_0 \eta_0 \sqrt{\pi}}{2L_0 \mu_0} l_0 (k^2 - 1) \exp\left(-\frac{\gamma_k^2}{l_0^2}\right) \operatorname{erf}\left(\frac{z}{l_0}\right) + \phi_0. \quad (22)$$

Now, taking ϕ_0 be zero, which refers to the pure solution case, the velocity \mathbf{v} is then given by

$$\begin{aligned} \mathbf{v} &= \mathbf{v}_{\text{nonideal}} \\ &= \left(\frac{\phi}{b_0 k^2 l_0^2} \left((k^2 + 1) \left(y \cosh\left(\frac{2kz}{L_0}\right) - kx \sinh\left(\frac{2kz}{L_0}\right) \right) + (k^2 - 1) y \right) \right) \hat{\mathbf{x}} \\ &+ \left(\frac{\phi}{b_0 k l_0^2} \left((k^2 + 1) \left(y \sinh\left(\frac{2kz}{L_0}\right) - kx \cosh\left(\frac{2kz}{L_0}\right) \right) + k(k^2 - 1) x \right) \right) \hat{\mathbf{y}}, \quad (23) \end{aligned}$$

which is divergence free, as required. For the composite solution case, ϕ_0 is taking to be

$$\phi_0 = \phi_{\text{ideal}} = \frac{\varphi_0}{2k l_0^2} \left(2kxy \cosh\left(\frac{2kz}{L_0}\right) - (k^2 x^2 + y^2) \sinh\left(\frac{2kz}{L_0}\right) \right)$$

and the corresponding divergence free velocity can then be written as

$$\mathbf{v} = \mathbf{v}_{\text{nonideal}} + \mathbf{v}_{\text{ideal}}, \quad (24)$$

where,

$$\begin{aligned} \mathbf{v}_0 &= \mathbf{v}_{\text{ideal}} \\ &= \left(\frac{\varphi_0}{k b_0 l_0^2} \left(y \sinh\left(\frac{2kz}{L_0}\right) - kx \cosh\left(\frac{2kz}{L_0}\right) \right) \right) \hat{\mathbf{x}} + k \left(y \cosh\left(\frac{2kz}{L_0}\right) - kx \sinh\left(\frac{2kz}{L_0}\right) \right) \hat{\mathbf{y}}. \end{aligned}$$

Finally, the prescribed magnetic field \mathbf{B} leads to $\nabla \times (\mathbf{j} \times \mathbf{B})$. Thus, the equation of motion in the limit of slow flows:

$$-\nabla p + \mathbf{j} \times \mathbf{B} = \mathbf{0}$$

can be satisfied by taking the plasma pressure p to be

$$p = p_0 - \frac{b_0^2}{2L_0^2} (k^2 - 1) (k^2 x^2 - y^2). \quad (25)$$

Therefore, the obtained stationary kinematic solutions are in a certain limit solutions to the full resistive stationary MHD equations.

Bibliography

- Abramowitz, M. and Stegun, I. A. (1965). *Handbook of Mathematical Functions*. Dover Publications, New York.
- Al-Salti, N. and Hornig, G. (2009). On the solutions of three-dimensional non-null magnetic reconnection. *Phys. Plasmas*, 16:2101.
- Al-Salti, N. and Hornig, G. (2010). On the solutions of three-dimensional non-null magnetic reconnection ii. in preparation.
- Al-Salti, N. and Neukirch, T. (2009). Stationary magnetohydrodynamic models of three-dimensional rigidly rotating magnetized coronae. In *COOL STARS, STELLAR SYSTEMS AND THE SUN: Proceedings of the 15th Cambridge Workshop on Cool Stars, Stellar Systems and the Sun*, pages 760–763. AIP Conference Proceedings.
- Al-Salti, N. and Neukirch, T. (2010). Three-dimensional solutions of the magnetohydrostatic equations: Rigidly rotating magnetized coronae in spherical geometry. submitted.
- Al-Salti, N., Neukirch, T., and Ryan, R. (2010). Three-dimensional solutions of the magnetohydrostatic equations: Rigidly rotating magnetized coronae in cylindrical geometry. in press.
- Al-Salti, N. and Shivamoggi, B. K. (2003). Electron-inertia effects on driven magnetic field reconnection. *Phys. Plasmas*, 10:4271–4277.
- Aulanier, G., Pariat, E., Démoulin, P., and Devore, C. R. (2006). Slip-running reconnection in quasi-separatrix layers. *Sol. Phys.*, 238:347.
- Baty, H., Priest, E. R., and Forbes, T. G. (2006). Effect of nonuniform resistivity in Petschek reconnection. *Phys. Plasmas*, 13:2312.
- Biskamp, D. (2000). *Magnetic reconnection in plasmas*. Cambridge University Press, Cambridge.
- Bogdan, T. J. and Low, B. C. (1986). The three-dimensional structure of magnetostatic atmospheres. II - Modeling the large-scale corona. *Astrophys. J.*, 306:271–283.
- Boyd, T. J. M. and Sanderson, J. J. (2003). *The Physics of Plasmas*. Cambridge University Press, Cambridge.
- Craig, I. J. D. and Watson, P. G. (2003). Magnetic reconnection solutions based on a generalized ohm's law. *Sol. Phys.*, 214:131–150.
- De Moortel, I. and Galsgaard, K. (2006). Numerical modelling of 3d reconnection due to rota-

- tional footpoint motions. *Astron. Astrophys.*, 451:1101–1115.
- Donati, J.-F., Howarth, I. D., Jardine, M. M., Petit, P., Catala, C., Landstreet, J. D., Bouret, J.-C., Alecian, E., Barnes, J. R., Forveille, T., Paletou, F., and Manset, N. (2006). The surprising magnetic topology of τ Sco: fossil remnant or dynamo output? *MNRAS*, 370:629–644.
- Donati, J.-F., Morin, J., Petit, P., Delfosse, X., Forveille, T., Aurière, M., Cabanac, R., Dintrans, B., Fares, R., Gastine, T., Jardine, M. M., Lignières, F., Paletou, F., Velez, J. C. R., and Théado, S. (2008). Large-scale magnetic topologies of early M dwarfs. *MNRAS*, 390:545–560.
- Fukao, S. (1975). Topological study of magnetic field near a neutral point. *Rep. Ion. Space Res. Jap.*, 29:133–139.
- Hesse, M., Forbes, T. G., and Birn, J. (2005). On the relation between reconnected magnetic flux and parallel electric fields in the solar corona. *Astrophys. J.*, 631:1227 – 1238.
- Hesse, M. and Schindler, K. (1988). A theoretical foundation of general magnetic reconnection. *J. Geophys. Res.*, 93:5559 – 5567.
- Hornig, G. (2001). *An introduction to the geometry and topology of fluid flows*, pages 295–313. Kluwer, Dordrecht.
- Hornig, G. and Priest, E. R. (2003). Evolution of magnetic flux in an isolated reconnection process. *Phys. Plasmas*, 10:2712–2721.
- Hornig, G. and Rastätter, L. (1998). The magnetic structure of $\mathbf{b} \neq \mathbf{0}$ -reconnection. *Phys. Scripta*, T74:34–39.
- Hornig, G. and Schindler, K. (1996). Magnetic topology and the problem of its invariant definition. *Phys. Plasmas*, 3:781.
- Huba, J. D. and Rudakov, L. I. (2004). Hall magnetic reconnection rate. *Phys. Rev. Lett.*, 93:5003.
- Hussain, G. A. J., van Ballegoijen, A. A., Jardine, M., and Collier Cameron, A. (2002). The Coronal Topology of the Rapidly Rotating K0 Dwarf AB Doradus. I. Using Surface Magnetic Field Maps to Model the Structure of the Stellar Corona. *Astrophys. J.*, 575:1078–1086.
- Jardine, M. (1994). Three-dimensional steady-state magnetic reconnection. *J. Plasma Phys.*, 51:399 – 422.
- Jardine, M. (2004). Coronal stripping in supersaturated stars. *Astron. Astrophys.*, 414:L5–L8.
- Jardine, M., Barnes, J. R., Donati, J.-F., and Collier Cameron, A. (1999). The potential magnetic field of AB Doradus: comparison with Zeeman-Doppler images. *MNRAS*, 305:L35–L39.
- Jardine, M., Collier Cameron, A., and Donati, J.-F. (2002). The global magnetic topology of AB Doradus. *MNRAS*, 333:339–346.
- Jardine, M., Collier Cameron, A., Donati, J.-F., and Pointer, G. R. (2001). Prominence support in potential field configurations around rotating stars. *MNRAS*, 324:201–205.
- Jardine, M. and Unruh, Y. C. (1999). Coronal emission and dynamo saturation. *Astron. Astrophys.*, 346:883–891.
- Jardine, M. and van Ballegoijen, A. A. (2005). Slingshot prominences above stellar X-ray coro-

- nae. *MNRAS*, 361:1173–1179.
- Kaiser, R. and Salat, A. (1996). Analytic three-dimensional solutions of the magnetohydrostatic equations with twisted field lines. *Phys. Rev. Lett.*, 77:3133–3136.
- Kaiser, R. and Salat, A. (1997). New classes of three-dimensional ideal-mhd equilibria. *J. Plasma Phys.*, 57:425–448.
- Kleva, R. G., Drake, J. F., and Waelbroeck, F. L. (1995). Fast reconnection in high temperature plasmas. *Phys. Plasmas*, 2:23–34.
- Lanza, A. F. (2008). Hot Jupiters and stellar magnetic activity. *Astron. Astrophys.*, 487:1163–1170.
- Lau, Y. T. and Finn, J. M. (1990). Three dimensional kinematic reconnection in the presence of field nulls and closed field lines. *Astrophys. J.*, 350:672–691.
- Linton, M. G. and Priest, E. R. (2003). Three-dimensional reconnection of untwisted magnetic flux tubes. *Astrophys. J.*, 595:1259–1276.
- Low, B. C. (1982). Magnetostatic atmospheres with variations in three dimensions. *Astrophys. J.*, 263:952–969.
- Low, B. C. (1984). Three-dimensional magnetostatic atmospheres - Magnetic field with vertically oriented tension force. *Astrophys. J.*, 277:415–421.
- Low, B. C. (1985). Three-dimensional structures of magnetostatic atmospheres. I - Theory. *Astrophys. J.*, 293:31–43.
- Low, B. C. (1991). Three-dimensional structures of magnetostatic atmospheres. III - A general formulation. *Astrophys. J.*, 370:427–434.
- Low, B. C. (1992). Three-dimensional structures of magnetostatic atmospheres. IV - Magnetic structures over a solar active region. *Astrophys. J.*, 399:300–312.
- Low, B. C. (1993a). Three-dimensional structures of magnetostatic atmospheres. V - Coupled electric current systems. *Astrophys. J.*, 408:689–692.
- Low, B. C. (1993b). Three-dimensional structures of magnetostatic atmospheres. VI - Examples of coupled electric current systems. *Astrophys. J.*, 408:693–706.
- Low, B. C. (2005). Three-dimensional Structures of Magnetostatic Atmospheres. VII. Magnetic Flux Surfaces and Boundary Conditions. *Astrophys. J.*, 625:451–462.
- Mackay, D. H. and van Ballegooijen, A. A. (2006). Models of the Large-Scale Corona. I. Formation, Evolution, and Liftoff of Magnetic Flux Ropes. *Astrophys. J.*, 641:577–589.
- Mestel, L. (1999). *Stellar Magnetism*. Clarendon Press, Oxford.
- Morin, J., Donati, J.-F., Petit, P., Delfosse, X., Forveille, T., Albert, L., Aurière, M., Cabanac, R., Dintrans, B., Fares, R., Gastine, T., Jardine, M. M., Lignières, F., Paletou, F., Ramirez Velez, J. C., and Théado, S. (2008). Large-scale magnetic topologies of mid M dwarfs. *MNRAS*, 390:567–581.
- Neukirch, T. (1995). On self-consistent three-dimensional solutions of the magnetohydrostatic

- equations. *Astron. Astrophys.*, 301:628–640.
- Neukirch, T. (1997). Nonlinear self-consistent three-dimensional arcade-like solutions of the magnetohydrostatic equations. *Astron. Astrophys.*, 325:847–856.
- Neukirch, T. (2009). Three-dimensional analytical magnetohydrostatic equilibria of rigidly rotating magnetospheres in cylindrical geometry. *Geophys. Astrophys. Fluid Dyn.*, 103:535–547.
- Neukirch, T. and Rastätter, L. (1999). A new method for calculating a special class of self-consistent three-dimensional magnetohydrostatic equilibria. *Astron. Astrophys.*, 348:1000–1004.
- Nishida, A. (2000). Pivotal role of magnetic reconnection in the earth's magnetosphere. *Adv. Space Res.*, 26:383–392.
- Osherovich, V. A. (1985a). The eigenvalue approach in modelling solar magnetic structures. *Aust. J. Phys.*, 38:975–980.
- Osherovich, V. A. (1985b). Quasi-potential magnetic fields in stellar atmospheres. I - Static model of magnetic granulation. *Astrophys. J.*, 298:235–239.
- Parker, E. N. (1957). Sweet's mechanism for merging magnetic fields in conducting fluids. *J. Geophys. Res.*, 62:509–520.
- Parnell, C. E., Haynes, A. L., and Galsgaard, K. (2008). Recursive reconnection and magnetic skeletons. *Astrophys. J.*, 675:1656–1665.
- Parnell, C. E., Haynes, A. L., and Galsgaard, K. (2009). Magnetic separators and magnetic reconnection. in press.
- Parnell, C. E., Priest, E. R., and Golub, L. (1994). The three-dimensional structures of x-ray bright points. *Sol. phys.*, 151:57–74.
- Parnell, C. E., Smith, J. M., Neukirch, T., and Priest, E. R. (1996). The structure of three-dimensional magnetic neutral points. *Phys. plasmas*, 3:759–770.
- Petrie, G. J. D. and Neukirch, T. (1999). Self-consistent three-dimensional steady state solutions of the mhd equations with field-aligned incompressible flow. *Geophys. Astrophys. Fluid Dyn.*, 91:269–302.
- Petrie, G. J. D. and Neukirch, T. (2000). The Green's function method for non-force-free three-dimensional solutions of the magnetohydrostatic equations. *Astron. Astrophys.*, 356:735–746.
- Petschek, H. E. (1964). *Magnetic field annihilation*, pages 425–439. NASA SP-50, Washington, DC.
- Pontin, D. I. and Craig, I. J. D. (2006). Dynamic three-dimensional reconnection in a separator geometry with two null points. *Astrophys. J.*, 642:568–578.
- Pontin, D. I. and Galsgaard, K. (2007). Current amplification and magnetic reconnection at a three-dimensional null point: Physical characteristics. *J. Geophys. Res.*, 112:3103.
- Pontin, D. I., Hornig, G., and Priest, E. R. (2004). Kinematic reconnection at a magnetic null point: Spine-aligned current. *Geophys. Astrophys. Fluid Dynamics*, 98:407 – 428.

- Pontin, D. I., Hornig, G., and Priest, E. R. (2005). Kinematic reconnection at a magnetic null point: Fan-aligned current. *Geophys. Astrophys. Fluid Dynamics*, 99:77 – 93.
- Priest, E. R. (1982). *Solar Magneto-hydrodynamics*. Kluwer Academic Publishers.
- Priest, E. R. and Démoulin, P. (1995). Three-dimensional magnetic reconnection without null points. I basic theory of magnetic flipping. *J. Geophys. Res.*, 100:23443–23463.
- Priest, E. R. and Forbes, T. G. (1986). New models for fast steady-state magnetic reconnection. *J. Geophys. Res.*, 91:5579–5588.
- Priest, E. R. and Forbes, T. G. (1989). Steady magnetic reconnection in three dimensions. *Sol. Phys.*, 119:211–214.
- Priest, E. R. and Forbes, T. G. (2000). *Magnetic reconnection: MHD theory and applications*. Cambridge University Press, Cambridge.
- Priest, E. R., Hornig, G., and Pontin, D. I. (2003). On the nature of three-dimensional magnetic reconnection. *J. Geophys. Res.*, 108:SSH6–1.
- Priest, E. R. and Pontin, D. I. (2009). Three-dimensional null point reconnection regimes. *Phys. Plasmas*, 16:2101.
- Priest, E. R. and Titov, V. S. (1996). Magnetic reconnection at three-dimensional null points. *Phil. Trans. R. Soc. Lond. A*, 354:2951–2992.
- Roberts, P. H. (1967). *An Introduction to Magnetohydrodynamics*. Longmans, London.
- Ruan, P., Wiegmann, T., Inhester, B., Neukirch, T., Solanki, S. K., and Feng, L. (2008). A first step in reconstructing the solar corona self-consistently with a magnetohydrostatic model during solar activity minimum. *Astron. Astrophys.*, 481:827–834.
- Rudenko, G. V. (2001). A constructing method for a self-consistent three-dimensional solution of the magnetohydrostatic equations using full-disk magnetogram data. *Sol. Phys.*, 198:279–287.
- Ryan, R. D., Neukirch, T., and Jardine, M. (2005). A simple model for the saturation of coronal X-ray emission of rapidly rotating late-type stars. *Astron. Astrophys.*, 433:323–334.
- Salat, A. and Kaiser, R. (1995). Three-dimensional closed field line magnetohydrodynamic equilibria without symmetries. *Phys. Plasmas*, 2:3777–3781.
- Schindler, K., Hesse, M., and Birn, J. (1988). General magnetic reconnection, parallel electric fields, and helicity. *J. Geophys. Res.*, 93:5547–5557.
- Shay, M. A., Drake, J. F., and Rogers, B. N. (1999). The scaling of collisionless magnetic reconnection for large systems. *Geophys. Res. Lett.*, 26:2163–2166.
- Shivamoggi, B. K. (1986). Generalized magnetohydrostatic equilibria. *Q. Appl. Math.*, 44:487–491.
- Shivamoggi, B. K. (1993). Magnetic field reconnection driven by perturbations on boundaries. *Phys. Scr.*, 47:817–822.
- Shivamoggi, B. K. (2007). Collisionless magnetic reconnection dynamics with electron inertia and parallel electron compressibility. *J. Plasma Phys.*, 73:857–868.

- Sonnerup, B. U., Paschmann, G., Papamastorakis, I., Sckopke, N., Haerendel, G., Bame, S. J., Asbridge, J. R., Gosling, J. T., and Russell, C. T. (1981). Evidence for reconnection at the earth's magnetopause. *J. Geophys. Res.*, 86:10049–10067.
- Sweet, P. A. (1958). The neutral point theory of solar flares. In *IAU Symp. 6: Electromagnetic phenomena in cosmical plasmas*, pages 123–134. Cambridge Univ. Press, London.
- Titov, V. S., Hornig, G., and Démoulin, P. (2002). The theory of magnetic connectivity in the corona. *J. Geophys. Res.*, 107:1164.
- Townsend, R. H. D. and Owocki, S. P. (2005). A rigidly rotating magnetosphere model for circumstellar emission from magnetic OB stars. *MNRAS*, 357:251–264.
- Townsend, R. H. D., Owocki, S. P., and Groote, D. (2005). The Rigidly Rotating Magnetosphere of σ Orionis E. *Astrophys. J.*, 630:L81–L84.
- ud-Doula, A., Townsend, R. H. D., and Owocki, S. P. (2006). Centrifugal Breakout of Magnetically Confined Line-driven Stellar Winds. *Astrophys. J.*, 640:L191–L194.
- Vasyliunas, V. M. (1975). Theoretical models of magnetic field line merging, 1. *Rev. Geophys.*, 13:303–336.
- Wiegelmann, T. and Neukirch, T. (2006). An optimization principle for the computation of MHD equilibria in the solar corona. *Astron. Astrophys.*, 457:1053–1058.
- Wiegelmann, T., Neukirch, T., Ruan, P., and Inhester, B. (2007). Optimization approach for the computation of magnetohydrostatic coronal equilibria in spherical geometry. *Astron. Astrophys.*, 475:701–706.
- Wilmot-Smith, A. L., Hornig, G., and Priest, E. R. (2006). Dynamic non-null magnetic reconnection in three dimensions i. particular solutions. *Proc. Roy. Soc. A*, 462:2877–2895.
- Wilmot-Smith, A. L., Hornig, G., and Priest, E. R. (2009). Dynamic non-null magnetic reconnection in three dimensions ii. composite solutions. *Geophys. Astrophys. Fluid Dyn.*, 103:515–534.
- Woolley, M. L. (1976). Three dimensional equilibria in the magnetohydrodynamic approximation. *J. Plasma Phys.*, 15:423–430.
- Woolley, M. L. (1977). Generalized elliptic equilibria in the magnetohydrodynamic approximation. *J. Plasma Phys.*, 17:259–264.
- Yamada, M., Ji, H., Hsu, S., Carter, T., Kulsrud, R., Bretz, N., Jobs, F., Ono, Y., and Perkins, F. (1997). Study of driven magnetic reconnection in a laboratory plasma. *Phys. Plasmas*, 4:1936.
- Yeates, A. R., Mackay, D. H., and van Ballegooijen, A. A. (2008). Modelling the Global Solar Corona II: Coronal Evolution and Filament Chirality Comparison. *Sol. Phys.*, 247:103–121.
- Zhao, X. and Hoeksema, J. T. (1993). Unique determination of model coronal magnetic fields using photospheric observations. *Sol. Phys.*, 143:41–48.
- Zhao, X. and Hoeksema, J. T. (1994). A coronal magnetic field model with horizontal volume and sheet currents. *Sol. Phys.*, 151:91–105.
- Zhao, X. P., Hoeksema, J. T., and Scherrer, P. H. (2000). Modeling the 1994 April 14 Polar Crown

- SXR Arcade Using Three-Dimensional Magnetohydrostatic Equilibrium Solutions. *Astrophys. J.*, 538:932–939.
- Zweibel, E. G. and Yamada, M. (2009). Magnetic reconnection in astrophysical and laboratory plasmas. *Annu. Rev. Astron. Astrophys.*, 47:291–332.